Dynamics of concentrated colloidal suspensions

Panagiota Bogri

submitted for the degree of Doctor of Philosophy

DEPARTMENT OF MATERIALS SCIENCE AND TECHNOLOGY

UNIVERSITY OF CRETE

HERAKLION 2018

Committee:

George Petekidis [1,2] (Supervisor)

Dimitris Vlassopoulos [1,2]

Benoit Loppinet [2]

Maria Vamvakaki [1,2]

Kuriaki Chrissopoulou [2]

Konstantinos Karatasos [3]

Joris Sprakel [4]

1. Institute of Electronic and Laser (IESL), Foundation for Research and Technology (FORTH), Heraklion, Crete, Greece
2. Department of Materials Science and Technology, University of Crete, Heraklion, Greece
3. Department of Chemical Engineering, Aristotle University of Thessaloniki, Greece
4. Laboratory of Physical Chemistry and Colloid Science, Wageningen University, the Netherlands

Acknowledgments

Firstly, I would like to acknowledge my supervisor Prof. George Petekidis for facilities, funding and immense encouragement and support during all these years. I would like also to thank Prof. Kohji Ohno, Prof. Jan Vermant and Prof. Joris Sprakel for providing the samples that I used during my dissertation.

I would like to sincerely thank Andreas Pamvouxoglou, Esmaeel Moghimi and Alan Ranjit Jacob for their hearted support throughout all these years. Many special thanks go to my lab mates for the help and all the happy moments we shared and I will always remember.

I would like also to truly thank the members of the committee for the evaluation of this dissertation and the helpful advices.

Last but not least, I would like to thank all my beloved people, my parents, my husband and my brother for their never-ending love and support to complete this thesis.

This work was supported by the Thales “Complex Visco-elastic and Visco-plastic Materials: From Microscopic Structure and Dynamics to Macroscopic Flow” (Covisco), which is co-financed by the European Union (European Social Fund – ESF) and Greek national funds through the Operational Program “Education and Lifelong Learning” of the National Strategic Reference Framework (NSRF).

Abstract

Colloidal suspensions play a significant role in our daily life since they are encountered in a wide range of natural, biological and industrially relevant products, such as foams, gels, emulsions, pastes, lubricants, paints, pharmaceuticals etc. During industrial processing, these materials are imposed in shearing, which affects their microstructure and the mechanical properties of the final product as well. Thus, for the successful manipulation of these products, deep understanding and control of the interplay between structure, dynamics and rheological behavior is crucial.

This thesis focuses on the study of structure and dynamics of three classes of colloidal systems of different nature and architecture, by using various techniques, such as light scattering, rheometry and microscopy.

Firstly, we examined the structure and hydrodynamic properties of randomly oriented prolate ellipsoids of various aspect ratios suspended in aqueous solutions by using Polarized (DLS) and Depolarized Light Scattering (DDLS). Besides low ionic strength suspensions, we also explored suspensions with added salt.

Secondly, we investigated the structure and dynamics of suspensions of soft isotropic core-shell colloids with different molecular weight polymer chain grafted on a hard core, in the liquid and glassy regime. In the liquid regime, we used 3D-Dynamic Light scattering (3DDLS) to eliminate multiple scattering contributions due to high refractive index mismatch between particles and the solvent. In the glassy regime, we used Multispeckle Dynamic Light Scattering (MSDLS) to explore the kinetically arrested dynamics, by following the evolution of the slowest relaxation of the intermediate scattering function. A glass-crystal reentrant transition emerged through ageing of glassy state, which is strongly affected by the volume fraction and the polydispersity.

Finally, we studied thermosensitive core-shell colloidal systems of different softness at low ionic strength. The hybrid core-shell particles consists of a rigid

polymeric core onto which a microgel shell is affixed. In these systems, we gradually tuned the interactions from repulsive to attractive by changing the temperature below and above the LCST, in order to examine how the switch of the interactions affects the structure and dynamics in both dilute and concentrated regime. For concentrated suspensions, these temperature changes allow the switch between repulsive glasses, repulsive liquids and attractive colloidal gels. We also explored the case of screening the electrostatic interactions by increasing the ionic strength at sufficiently high salt concentrations leading to interesting aggregation phenomena. For this investigations, we employed various techniques, such as light scattering, capillary viscometry, confocal microscopy and linear and nonlinear rheology at both quiescent conditions and under shear.

Περίληψη

Τα κολλοειδή διαλύματα διαδραματίζουν ιδιαίτερα σημαντικό ρόλο στην καθημερινότητά μας, αφού τα συναντάμε σε μια πληθώρα φυσικών, βιολογικών και βιομηχανικών προϊόντων, όπως αφροί, γέλες, γαλακτώματα, πάστες, λιπαντικά υλικά, χρώματα, φαρμακευτικά προϊόντα κ.α.. Σε πολλές εφαρμογές, τα κολλοειδή διαλύματα υποβάλλονται σε διάτμηση, η οποία επηρεάζει σημαντικά την μικροδομή και τις μηχανικές ιδιότητες του τελικού προϊόντος. Συνεπώς, για τον καλύτερο δυνατό χειρισμό τέτοιων υλικών, απαιτείται η ουσιώδης κατανόηση της αλληλεπίδρασης μεταξύ δομής, δυναμικής και ρεολογικής συμπεριφοράς των κολλοειδών τόσο σε κατάσταση ηρεμίας όσο υπό διάτμηση.

Η παρούσα διδακτορική διατριβή επικεντρώνεται στη μελέτη της δομής και της δυναμικής τριών κατηγοριών κολλοειδών συστημάτων διαφορετικής αρχιτεκτονικής, μέσω της χρήσης διάφορων τεχνικών όπως σκέδαση φωτός, ρεολογίας και μικροσκοπίας.

Αρχικά μελετήσαμε τη δομή και τις υδροδυναμικές ιδιότητες υδατικών κολλοειδών διαλυμάτων που περιέχουν ελλειψοειδή σωματίδια διαφόρων λόγων διαστάσεων, χρησιμοποιώντας Πολωτική (DLS) και Αποπολωτική (DDLS) Σκέδαση Φωτός. Τα εν λόγω κολλοειδή διαλύματα μελετήθηκαν σε απουσία και παρουσία μονοσθενούς άλατος.

Εν συνεχεία, μελετήθηκε η δομή και η δυναμική κολλοειδών διαλυμάτων χαλαρών ισότροπων σωματιδίων τύπου πυρήνα-κορώνας στην περιοχή που βρίσκονται στην υγρή μορφή καθώς και στην υαλώδη κατάσταση. Τα εν λόγω κολλοειδή αποτελούνται από πολυμερικές αλυσίδες διαφόρων μοριακών βαρών που είναι συνδεδεμένες μέσω χημικών δεσμών στην επιφάνεια του πυρήνα. Στη περιοχή που τα σωματίδια βρίσκονται στην υγρή τους μορφή, χρησιμοποιήσαμε την τεχνική 3DDLS προκειμένου να εξαλείψουμε την επίδραση του φαινομένου της πολλαπλής σκέδασης, η οποία οφείλεται στη μεγάλη διαφορά δείκτη διάθλασης

μεταξύ σωματιδίων και διαλύτη. Στην υαλώδη περιοχή, χρησιμοποιήσαμε την τεχνική Multi-Speckle Dynamic Light Scattering έτσι ώστε να μελετήσουμε την «παγωμένη» δυναμική των κολλοειδών. Για το σκοπό αυτό ακολουθήσαμε την εξέλιξη του πιο αργού χρόνου χαλάρωσης της συνάρτησης αυτοσυσχέτισης. Αναλόγως του κλάσματος όγκου και της πολυδιασποράς των διαλυμάτων, παρατηρήθηκαν δομικές αλλαγές οι οποίες οδήγησαν ή όχι σε μετάβαση από την υαλώδη στην κρυσταλλική περιοχή.

Τέλος, μελετήσαμε θερμο-αποκρινόμενα κολλοειδή συστήματα που αποτελούνται από χαλαρά σωματίδια τύπου πυρήνα-κορώνας, όπου δίκτυο πολυμερικών αλυσίδων (υδρογέλη) είναι προσδεμένο χημικά σε ένα πυρήνα. Ο θερμο-αποκρινόμενος χαρακτήρας της κορώνας επιτρέπει την σταδιακή αλλαγή των αλληλεπιδράσεων μεταξύ των σωματιδίων από απωστικές ηλεκτροστατικές σε ελκτικές Van der Waals, μόνο με την εναλλαγή της θερμοκρασίας κάτω ή πάνω από την Χαμηλότερη Κρίσιμη Θερμοκρασία Διαλύματος (LCST). Κατά τον τρόπο αυτό, μελετάται η επίδραση της μεταβολής των αλληλεπιδράσεων στη δομή και τη δυναμική τόσο σε αραιά όσο και σε πυκνά διαλύματα. Στα πυκνά διαλύματα, η μεταβολή των αλληλεπιδράσεων μεταξύ των κολλοειδών οδηγεί στην μετάβαση από υαλώδη φάση σε ρευστή (και οι δύο φάσεις χαρακτηρίζονται από απωστικές αλληλεπιδράσεις) και σε κολλοειδείς γέλες (η φάση αυτή χαρακτηρίζεται από ελκτικές αλληλεπιδράσεις). Επιπρόσθετα, μελετήσαμε την περίπτωση προσθήκης υψηλής ποσότητας μονοσθενούς άλατος, ώστε να επιτύχουμε την αποτελεσματική ακύρωση των ηλεκτροστατικών απωστικών αλληλεπιδράσεων, η οποία έχει ως επακόλουθο την εμφάνιση ενδιαφερόντων φαινομένων συσσωμάτωσης των σωματιδίων. Για την πραγματοποίηση των εν λόγω μελετών χρησιμοποιήθηκαν τεχνικές σκέδασης, καθώς και ιξωδομετρία, μικροσκοπία και γραμμική και μη-γραμμική ρεολογία, τόσο σε κατάσταση ηρεμίας, όσο και υπό διάτμηση.

Contents

Summary

In Chapter 1, we give a general introduction about colloidal interactions and thermodynamic phase diagram of hard spheres and soft colloidal systems. Moreover, we briefly discuss theories and concepts which relate structure and dynamics of dilute, concentrated and arrested systems to light scattering and rheology.

In Chapter 2, we present the details about the experimental methods used in this thesis including light scattering techniques, rheometry and confocal microscopy.

In Chapter 3 we report on the investigation of structure and hydrodynamic properties of randomly oriented prolate ellipsoids of various aspect ratios suspended in aqueous solutions by Polarized (DLS) and Depolarized Light Scattering (DDLS). The range of electrostatic interparticle interactions was monitored by the second virial coefficient (A_2), a thermodynamic parameter that characterizes quantitatively the intermolecular interactions in dilute solutions. Besides salt-free suspensions, the change of interactions was also explored after the addition of monovalent salt ions.

Chapter 4 presents an experimental study of structure and dynamics of soft isotropic colloidal core-shell particles in the liquid and glassy regime. 3D-Dynamic Light scattering (3DDLS) was used for the investigation of concentrated suspensions where the multiple scattering contribution is significant. Structure and dynamics were compared with hard sphere model. In the glassy regime, where dynamics are strongly non-ergodic we used Multi-Speckle Dynamic Light Scattering (MSDLS) to monitor the evolution of the slowest relaxation time that exhibits a non-monotonic behavior with time, which is a result of structural rearrangements of the particles.

In Chapter 5, we examine the structure, dynamics and mechanical properties of electrostatically stabilized aqueous suspensions of two core-shell microgel systems with the same architecture but different softness. The thermoresponsive character of these particles allows, under specific external conditions, to gradually

tune the interactions from repulsive to attractive, providing the ability in concentrated regime to switch between glass, liquid and gel states.

Chapter 6 presents an experimental investigation of the structure, dynamics and viscoelastic properties of electrostatically stabilized aqueous suspensions of core-shell microgels, after the addition of sufficiently high quantity of monovalent salt ions. Then, the aggregation temperature emerges at which the attractive interactions become sufficiently large to overcome the screened repulsive interactions leading to interesting clustering phenomena.

In Chapter 7, we study the shear-induced flow behaviour of core-shell jammed microgels by using Orthogonal Superposition Rheometry (OSR). The characteristic crossover frequency ω_c, deduced by the linear viscoelastic spectrum under shear, is used for the scaling of the viscoelastic spectra in a master curve and provides insights for the flow mechanism in the system.

Finally general conclusions are presented about all the main findings in the thesis, providing simultaneously new ideas for future studies.

Chapter 1

Introduction

1.1 Colloids

Colloidal systems of gold particles were already known a couple of centuries ago when their nature being “extremely finely divided gold in fluid”, was realized in 1774 by Junch and Macquer (Dhont 1996). In 1861, the Scottish chemist Thomas Graham while studying diffusion classified substances into crystalloids and colloids. It was Thomas Graham who introduced the term "Colloid”, which was derived from the Greek word, “κόλλα”, meaning glue and punctuates their lack of crystallinity and low rate of diffusion (Dhont 1996). Nowadays, the term colloid is most commonly referred to the dispersed phase of a two-component system which consists of submicron particles (typically 10nm to 1000nm in at least one dimension) dispersed in a medium (liquid or gas). The particles of the dispersed phase are too small to be easily observed by an optical microscope (Russel, Saville et al. 1989, Mewis and Wagner 2012) and experiences a random-walk diffusion resulting from numerous collisions with the molecules of the liquid suspension medium. This random movement is called Brownian motion after the botanist Robert Brown who first studied it in 1827 and is driven by the thermal energy k_BT, where k_B is the Boltzmann constant and T is the temperature which sets the energy scale for all colloidal interactions. Colloids appear in many systems that we use in our daily life such as foods, biological systems, pharmaceutics, cosmetics, paints, inks and cleaning products. Therefore, the deep understanding of the physical properties of colloids is of great importance. Moreover, colloidal suspension are playing an increasingly significant role as model systems to study equilibrium and non-equilibrium state transitions in condensed matter physics (Poon 2004, Pusey 2008).

1.2 Colloidal interactions and Colloidal stability

The interparticle forces developed between colloids, suspended in a medium, can be either repulsive or attractive. The nature, the range and the balance of the repulsive and attractive interparticle forces determines the overall stability, structure and dynamics of a colloidal system. The repulsive interactions are mostly steric or electrostatic, whereas the attractive forces are mainly Van der Waals or depletion interactions.

1.2.1 Van der Waals interactions

Van der Waals interactions are short-range attractive forces which originate from the polarization of the atoms of a colloid by the atoms of another (dipole-dipole, dipole-induced dipole and induced dipole-induced dipole interactions between the colloids) (Mewis and Wagner 2012).

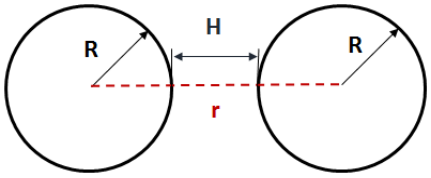

Fig. 1.1 *– Two spheres of radius R separated by distance r between their centers.*

The strength of this interaction between two identical spherical particles with radius R with respect to a particle center-to-center distance r and particles' surface-to-surface distance $H = r - 2R$ is obtained by the equation (Ohshima 2016):

$$U_A(r) = -\frac{AR}{12H} \tag{1.1}$$

where A is the Hamaker constant that is determined by material properties and depends on the polarizability of particles and the suspension medium, and can be estimated as follows (Larson 1999, Israelachvili 2011):

$$A = \frac{3}{4} k_B T \left(\frac{\varepsilon_p - \varepsilon_s}{\varepsilon_p + \varepsilon_s} \right)^2 + \frac{3 h \nu_e}{16\sqrt{2}} \frac{\left(n_p^2 - n_s^2\right)^2}{\left(n_p^2 + n_s^2\right)^{3/2}} \quad (1.2)$$

where subscripts p and s denote the particle and solvent, respectively, ε is the dielectric constant, n is the refractive index, h is Planck's constant, and ν_e is the ultraviolet absorption frequency. In dilute solutions the particles are far enough to feel this attractive potential. However, as the concentration increases such an attractive potential leads to coagulation of colloidal particles, which is often an undesirable phenomenon. Therefore, the particles need to be stabilized against coagulation. This can be done by repulsive forces that prevent colloids from aggregation (electrostatic or steric stabilization).

1.2.2 Electrostatic interactions and Electrostatic stabilization

Colloids dispersed in a polar medium, typically water, can gain charges by dissociation of acidic or basic ionisable groups or through adsorption of free ions or surfactants. The dissociated counterions are strongly bounded to the particle's surface forming an oppositely charged layer which called Stern layer. A second diffuse outer layer is comprised of loosely associated ions. These two layers are collectively called the electrostatic double layer. When the electrostatic double layer of two particles overlap it results in a repulsive interaction. The electrostatic repulsion potential can be calculated as follows (Russel, Saville et al. 1989):

$$U_R(r) = \frac{4\pi\varepsilon_r\varepsilon_o R^2 \psi_o^2}{r} \exp\left[-\kappa(r - 2R)\right] \quad (1.3)$$

where ε_r is the relative permittivity of the suspended medium, ε_o is the permittivity of the free space, ψ_o is the surface potential and κ the inverse of Debye screening length which is calculated as follows:

$$\kappa^{-1} = \sqrt{\frac{\varepsilon_r \varepsilon_o k_B T}{\sum_i (z_i e)^2 C_i}} \qquad (1.4)$$

where k_B is the Boltzmann constant, T is the absolute temperature of the suspension, N_A is Avogadro's number, e is the elementary charge, z_i is the valence of i-th species of ions of concentration C_i. Debye screening length denotes the distance beyond which electrostatic interactions can be essentially ignored, so characterizes the range of the interaction (Israelachvili 2011).

1.2.3 DLVO theory

The DLVO theory describes quantitatively the total interactions in charged colloidal suspensions and is named after Derjaguin and Landau (Derjaguin and Landau 1993) Verwey and Overbeek (Verwey, Overbeek et al. 1999) who developed it in 1940s. According to this theory, the total interaction energy of two surfaces or particles V_T is given by the summation of the Van der Waals attractive interactions $V_{VanderWaals}$ and the electrostatic repulsion $V_{Electrostatic}$ (Liang, Hilal et al. 2007):

$$V_T = V_{VanderWaals} + V_{Electrostatic} \qquad (1.5)$$

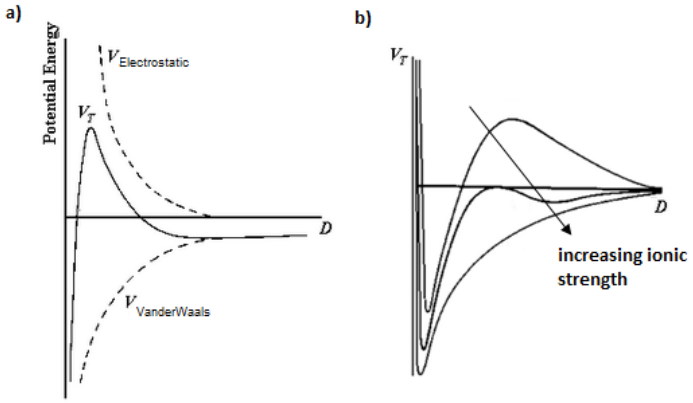

Fig. 1.2 *- a) DLVO theory by the summation of the attractive and repulsive contributions, b) the effect of ionic strength in DLVO potential.*

Steric and depletion interactions are not incorporated in the classical DLVO theory. Thus, extended DLVO theories have been introduced incorporating these non-DLVO interactions and have been reviewed by Grasso et al. (Grasso, Subramaniam et al. 2002).

1.2.4 Steric stabilization

An alternate mechanism to inhibit coagulation of colloidal suspensions caused due to Van der Waals interactions, is through inducing steric interactions by attaching (grafting or chemisorption) molecules (short polymers chains or surfactant molecules) on the surface of particles (Hiemenz 1986, Russel, Saville et al. 1989). Repulsive force of entropic origin develops when the absorbed or grafted polymeric layers on two particles start to overlap in theta or good solvent and increases rapidly as the layers are compressed. The magnitude and the range of steric repulsion depends on the quantity or coverage of polymer attached on particle surface. In the case of grafted polymer chains steric interaction depends on the grafting density and the molecular weight of the polymer. The interaction potential due to the grafted chain brush in a theta solvent can be calculated as follows (Russel, Saville et al. 1989):

$$U_{steric}(r) = n_p k_B T \left[\frac{\pi^2 N l^2}{3(r-2R)^2} + \ln\left(\frac{3(r-2R)^2}{8\pi N l^2} \right) \right] \qquad (1.6)$$

where n_p is the surface density of polymer chains, and N is the number of segments of length l per chain.

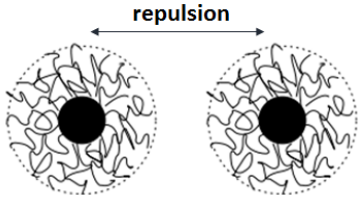

Fig 1.3 *- Schematic showing steric repulsion by linear polymer chains grafted on a particle surface.*

1.2.5 Depletion stabilization

Depletion attraction is induced between colloidal particles by addition of smaller particles (hard/soft spheres) or non-absorbing polymers to a colloidal suspension containing bigger particles. When the depletant is added to the suspension, an excluded volume is created around each particle, with the range of the radius of the depletant. When two or more particles are close enough that their excluded volumes overlap, there is a region between these particles where the small particles cannot penetrate and therefore the concentration of depletants surrounding the big particles is much larger than between the particles. This drives the creation of an unbalanced osmotic pressure, which leads to attractive depletion force that pushes the particles towards each other (Asakura and Oosawa 1954).

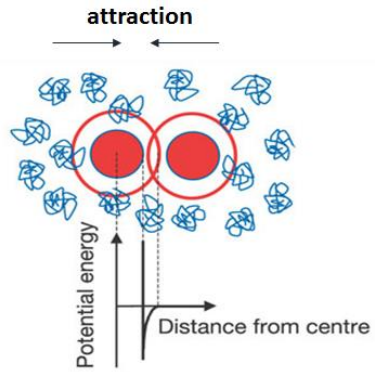

Fig. 1.4 *- Cartoon of excluded volume around each sphere into which the center of the polymer coil cannot penetrate. On approach these 'excluded volumes' overlap and the total volume available to the polymers increases, increasing their entropy (at the expense of some colloidal entropy). Asakura and Oosawa potential as a function of the interparticle distance. Adapted from (Anderson and Lekkerkerker 2002).*

The attractive potential for colloidal particles in a non-absorbing polymer solution can be calculated from the model of Asakura and Oosawa (Asakura and Oosawa 1954, Aarts, Tuinier et al. 2002). This model assumes that the colloidal particles are hard spheres and the polymer molecules behave as hard spheres toward the colloidal particles but can freely penetrate with each other. Then, the attractive potential is given by the equation:

$$\frac{U_{dep}(r)}{k_B T} = \begin{cases} +\infty & r \le \sigma \\ -\dfrac{\Pi_p}{k_B T} V_{overlap}(r) & \sigma < r \le \sigma + 2R_g \\ 0 & r > \sigma + 2R_g \end{cases} \quad (1.7)$$

where σ is the particle diameter, Π_p is the osmotic pressure of the polymer molecules and R_g is their radius of gyration. The volume of overlapping depletion zones between two colloids at a distance r is given by:

$$V_{overlap}(r) = v_p \left(\frac{\lambda}{\lambda - 1} \right)^3 \left[1 - \frac{3}{2} \left(\frac{r}{\sigma\lambda} \right) + \frac{1}{2} \left(\frac{r}{\sigma\lambda} \right)^3 \right] \quad (1.8)$$

where $v_p = (4\pi/3) R_g^3$ is the volume occupied by a polymer chain and $\lambda = 1 + 2R_g/\sigma$ (Ye, Narayanan et al. 1996).

1.3 Thermodynamic Phase Diagram

1.3.1 Hard sphere suspensions

Colloids have been used as model systems in condensed matter physics as they present a fascinating variety of phase behavior which can mimic that of simple atomic liquids and solids. The simplest model system is the hard sphere system (Pusey and Van Megen 1986). Hard-sphere potential is infinite when particles are in contact and zero when they do not, which means that the particles do not interact with each other and experience steep repulsion at contact. Thus the interaction energy is zero and the free energy contains only the entropic term. Whereas in other systems, energy and entropy always compete. Consequently, the hard sphere phase transition is driven purely by configurational entropy, which is a function of a sole parameter, the particle volume fraction, $\varphi = \frac{4}{3}\pi R^3 \rho$, where R is the particle radius, and ρ is the particle number density (Cheng, Chaikin et al. 2001).

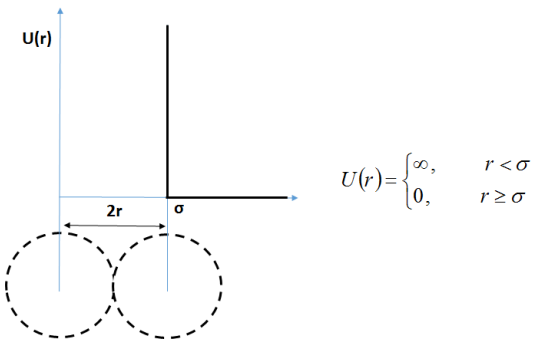

Fig. 1.5 *- Hard sphere interparticle interaction potential.*

In a dilute suspension (ϕ→0), the spheres are disordered and far from each other, like a dilute gas. Upon increasing the volume fraction, suspension exhibits liquid like order. At ϕ=0.495, the hard sphere colloids start to organize spontaneously into a crystalline phase with fluid-crystal coexistence extending up to ϕ=0.545, where it shows complete crystallization. The equilibrium crystal structure of hard spheres is found to be a face centered cubic (fcc), which is entropically favored minimum energy configuration (Pusey, Van Megen et al. 1989, Bolhuis, Frenkel et al. 1997, Woodcock 1997). Hard sphere suspensions also exhibit hexagonal close packed (hcp) structure or fcc-hcp coexistence due to their very small energy difference ($10^{-3}k_BT$) between hcp and fcc structures (Pusey, Van Megen et al. 1989, Bolhuis, Frenkel et al. 1997, Woodcock 1997). With further increase in volume fraction, the colloidal particle dynamics become slower and it undergoes kinetic arrest into a disordered and metastable state (glass) by exhibiting glass transition at ϕ=0.58. At ϕ=0.64, randomly arranged particles touch each other leading to random close packed (rcp) glassy state in hard sphere suspensions. In fcc as well as in hcp crystals, hard spheres can be packed to maximum of ϕ=0.74. The phase behavior of suspensions of colloidal particles polydisperse in size, has been found to differ from that of the monodisperse particle's case (Hansen, Zinn-Justin et al. 1991). Increasing the polydispersity, the crystallization point has been observed to shift to higher volume fractions. Suspensions of colloidal particles having size polydispersity up to ~8% are only found to exhibit crystalline ordering, whereas suspensions with larger polydispersity have been found to freeze into disordered (glassy) state.

Figure 1.6 presents the phase diagram of the monodisperse hard sphere colloidal suspensions.

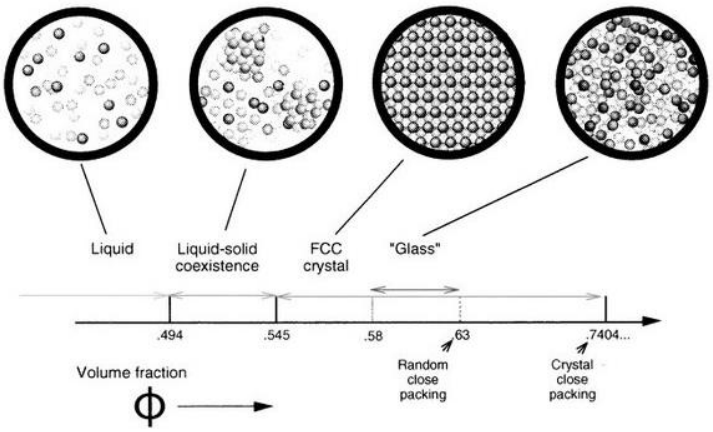

Fig. 1.6 *- The phase diagram of the monodisperse hard sphere colloidal suspension. Adapted from (Cheng, Chaikin et al. 2001).*

1.3.2 Soft particle suspensions

Soft colloidal systems consist of particles that combine polymeric with colloidal characteristics, providing a way of acquiring and tuning intermediate behaviors between short-range polymeric and long-range colloidal interactions. In fig. 1.7 various soft systems are illustrated, where, starting from a colloidal hard sphere, the interaction potential can be progressively softened with grafted hard particles, multiarm stars, microgels and polymer coils (Vlassopoulos and Fytas 2009, Vlassopoulos and Cloitre 2014). Furthermore, different architectures can be achieved, such as dendrimers, particles grafted with polymeric chains or chemical networks and colloidal micelles.

The softness tunability of a colloidal system can be quantitatively described by the pair interaction potential, which connects the structure with the properties of the colloids. As we already mentioned, hard-spheres are non-interacting at all separations beyond their radius and infinitely repulsive when they are on contact. For polymer coils in a good solvent, the potential is repulsive at all distances. Micelles, microgels and star-like systems show an intermediate interaction potential. The variation of softness for two soft particle paradigms, microgels and

star polymers, is affected by the degree of crosslinking and number of arms respectively.

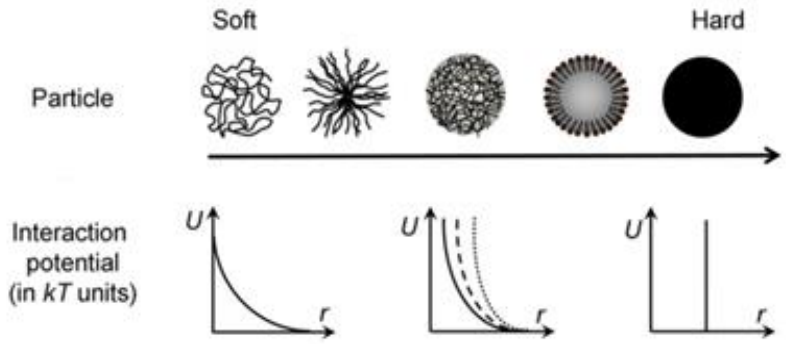

Fig. 1.7 *– Representation of intermediate systems that can be obtained between the soft (limiting case of a polymer coil) and hard (limiting case of hard sphere) interactions. Adapted from (Vlassopoulos and Cloitre 2014).*

The state diagram of soft colloids differs from that of hard spheres. Fig. 1.8 presents the phase behavior of the most significant soft systems (polymer chains, stars and soft microgels), in comparison with the behavior of monodisperse and non-interacting colloidal hard spheres.

The state diagram of both non-interacting nearly-monodisperse microgels and star-like particles undergoes the same qualitative sequence of the phase transitions with hard sphere suspensions. However, they exhibit major differences such as the actual values of the effective volume fraction marking the transitions, which depends on the softness of the particles. In general, the impact of the softness on the state diagram is significant, since the fluid phase tends to expand increasing the softness of the particles. This behavior can be connected to the behavior of the polymeric coil suspensions that remain fluid throughout the whole range of volume fractions. Moreover, the compressibility of the microgels and the interpenetration of star-like particles shift the glass and the jamming transition to higher volume fractions (Lyon and Fernandez-Nieves 2012). The star-like systems are also characterized by a large fluid region that extends up to the overlap concentration (c*), a small crystal regime and a relatively large glass-jamming region (Vlassopoulos and Cloitre 2014).

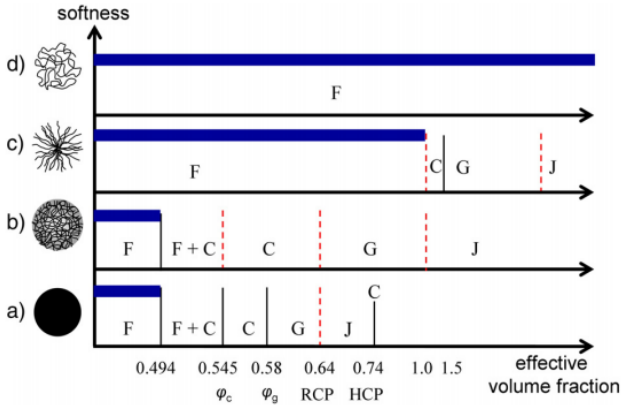

Fig. 1.8 *– Schematic one-dimensional state diagrams of nearly-monodisperse athermal soft colloidal suspensions, as function of their effective volume fraction. The numbers are characteristic values for volume fractions of hard spheres. From bottom to top the diagrams of a) hard spheres, b) microgels, c) star polymers and d) polymeric coils are shown. Letters refer to different regions: fluid (F, the blue-shaded regions), crystal (C, at φ_c= 0.545 for hard spheres), coexistence (F+C, above φ_{f+c}=0.494 for hard spheres), glass (G, at φ_g =0.58 for hard spheres), and jammed (J). RCP and HCP are the random close packing and hexagonal close packing volume fractions, which for hard spheres are determined to be 0.64 and 0.74, respectively. The solid black vertical lines represent established transitions (even if occurring at different volume fractions for different systems) whereas red dashed lines represent transitions whose universality is still debatable. The values of the volume fraction in the horizontal scale are indicative and do not respect the actual scale. Taken from (Vlassopoulos and Cloitre 2014).*

1.3.2.1 Multiarm star polymers

Star polymers represent a broad class of branched macromolecular architectures with f linear “arms” emanating from a central branching point which is referred as a “core” (Ren, McKenzie et al. 2016). A diverse range of star polymer structures that are stable and nearly monodisperse can be synthesized by controlled polymerization techniques (Roovers, Zhou et al. 1993). Their softness (number and size of arms) and their functionality can be tuned during synthesis procedure (Roovers, Zhou et al. 1993, Stiakakis, Vlassopoulos et al. 2002, Vlassopoulos and Fytas 2009).

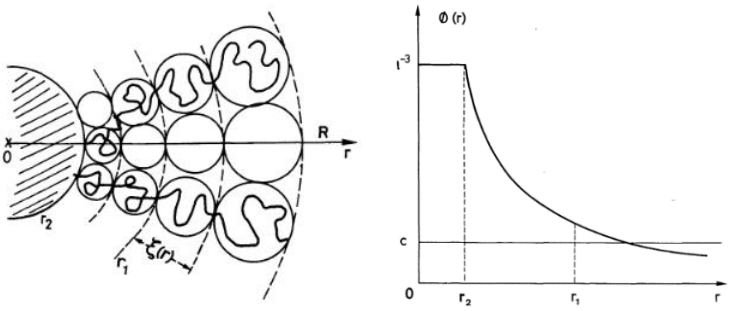

Fig. 1.9 *– Left: Graphical Representation of Daoud and Cotton model for a star polymer. Right: The density profile predicted by the model with the three different regimes. Taken from (Daoud and Cotton 1982).*

Star polymers do not present uniform monomer density distribution and can be considered as core-corona particles with core radius $r_c \sim f^{1/2}$ and softness $s = l/(l + r_c)$, where l is the corona thickness. Fig.1.9 depicts a representation of a star polymer in a good solvent, where according to the Daoud and Cotton model every branch consists of a sequence of blobs of size ξ that increases from the center of the star to the outside (Daoud and Cotton 1982). The corresponding density profile is also presented in fig.1.9, where it is possible to distinguish three different density regimes for increasing values of the distance r from the center. The inner melt-like core regime is observed for small distances ($r<r_2$) which is characterized by the constant density of the monomers, the intermediate theta-like regime ($r_2<r<r_1$), where the blobs are ideal and in the case of a dense suspension only solvent can penetrate and the outer excluded volume regime ($r>r_1$), where the blobs are swollen and in the case of dense suspensions the star-star interpenetration take place (Daoud and Cotton 1982, Vlassopoulos and Fytas 2009).

1.3.2.2 Grafted colloidal particles

Grafted spherical particles arise by the anchoring of a polymer brush shell onto the surface of a hard nanoparticle core. This architecture provides sterical stabilization against rapid aggregation and precipitation of the cores and qualitatively intermediate properties between hard sphere systems and soft

polymers. Tunability can be achieved either by varying the size of the core of the particles, which can be either organic or inorganic, or the size of the corona chains.

The theoretical model of the shell morphology established by Daoud and Cotton for star polymers is also applied successfully to these core-shell particles. Following this approach, the spherical brush grafted to the nanoparticle core is represented by a sequence of concentric, close-packed blobs similar to star polymers. The density profile of grafted particles is similar to star polymers' and consists of the regime that corresponds to the core, where the density is constant and the two regimes (intermediate theta-like and outer excluded volume regime) that correspond to the shell which are determined by the grafting density and the molecular weight of the grafted linear polymers (Grünewald, Lassenberger et al. 2015).

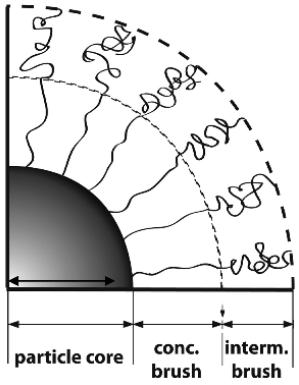

Fig. 1.10 *– Schematic representation of polymer chains grafted to a nanoparticle core.*

1.3.2.3 Colloidal micelles

Colloidal micelles are structures that arise from the self-assembly of block copolymers into micellar structures, when they are dispersed in a highly selective solvent for the one block. Their morphology and shape depend on the chain architecture, the block composition and the affinity of the solvent for the different block components. Usually, two concentric regions can be observed: an inner core of the insoluble block and an outer corona of the solvent-swollen block (Halperin, Tirrell et al. 1992) which is similar to that of stars. Micelles differ from stars in the fact that the core of micelles is usually larger compared to stars and is separated

from the corona due to enthalpic repulsion. Another significant difference compared to stars is that micelles are formed due to physical reasons, whereas the star formation results by chemical grafting, a fact that renders dubious the stability of the micelles (Vlassopoulos and Fytas 2009). For providing stability to the micelles, the blocks of the core should be in a melt state, above T_g. The density profile of the star-like micelles follows the Daoud-Cotton model.

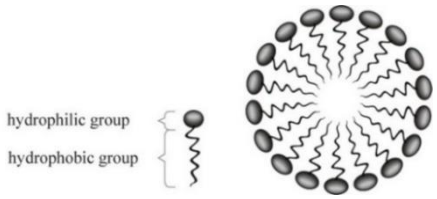

Fig. 1.11– *Representation of a colloidal spherical micelle.*

1.3.2.4 Microgels

Microgel particles constitute a significant class of soft particles which consist of chemically crosslinked polymer chains with typical size range from 10 to 1000nm. They can be sterically or charged stabilized particles with an inhomogeneous density distribution of crosslinks and free dangling chains at the surface, which may also be charged. The spatial distribution of crosslinks inside the microgel determines the local microstructure of the particles that can be either homogeneous or core-shell. Because of their architecture, microgels are partially impenetrable, but at the same time inherently soft and deformable. Microgels are ideal for a vast range of applications because of their ability to swell and de-swell in response to changes in the physicochemical conditions of the external environment, such as pH, temperature, solvent quality and light (Bonham, Faers et al. 2014), affecting directly the softness of the particles that can switch from soft-like to hard-like one. Furthermore, microgels whose interactions can be tuned by an external trigger can in principle be switched between different physical states which allows the study in detail of phase transitions (Appel, Fölker et al. 2016). The most widely studied responsive microgels are composed of the environmentally responsive polymer poly(N-isopropylacrylamide) (PNIPAM), which undergoes a temperature induced phase transition at around 31^{o}C that is reversible (Jones and Lyon 2003).

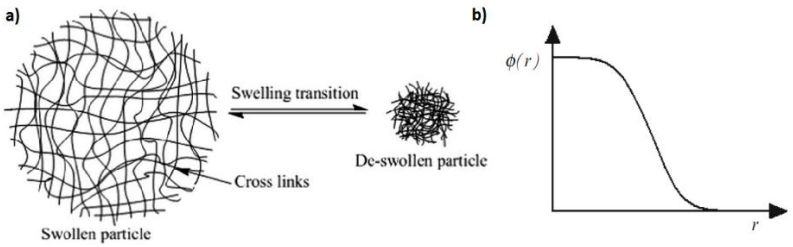

Fig. 1.12 *– a) Representation of a microgel particle and b) distribution of monomer density profile φ(r).*

1.4 Structure and Dynamics

1.4.1 Form factor and single particle properties

The shape and the size of an individual colloidal particle can be determined in a dilute suspension by the form factor P(q) via the quantification of intra-particle correlations in the reciprocal space. For spheres the form factor P(q) is calculated by the equation:

$$P(q) = V^2 \left[\frac{\sin(qR) - (qR)\cos(qR)}{(qR)^3} \right]^2 \tag{1.9}$$

where R and V is the radius and the volume of the sphere respectively and q the scattering vector.

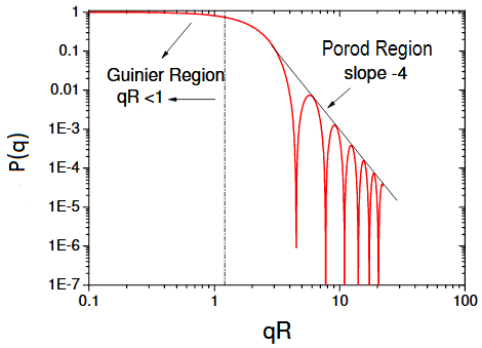

Fig. 1.13 *– The form factor for a hard sphere depicting the Guinier region for qR <1 and Porod region for high qRs.*

Hard sphere's form factor at qR<1 is characterized by the Guinier region response, whereas at high qR range by the Porod region one that exhibits

characteristic interference oscillations with an overall q^{-4} dependence. (Guiner, Fournet et al. 1955).

The form factor of soft colloids, such as star-like particles, polymer grafted colloids and microgels, displays correlation lengths describing their inherent inhomogeneous density profile ϕ(r). These systems can be approximated by the equation:

$$P(q)=\left[\int_0^\infty 4\pi r^2\phi(r)\frac{\sin(qr)}{qr}dr\right]^2 \Big/ \int_0^\infty 4\pi r^2\phi(r)dr \qquad (1.10)$$

The softest case of linear polymers, are characterized by the Debye form of P(q) with maximum at q=0 and power law dependence $-q^2$ at high qR_g, where R_g is the polymer radius of gyration (Higgins and Benoît 1994).

Size and shape of colloids in dilute suspensions can also be determined by the translational diffusion coefficient D_0 expressed by the Stokes-Einstein equation:

$$D_o = k_B T / 6\pi\eta R \qquad (1.11)$$

which describes the Brownian motion of a single particle in a liquid medium due solely to the thermal fluctuations of the molecular movements around the particles. The translational diffusion coefficient D_0 can be extracted by dynamic light scattering and can be used for proving the consistency of the scattering results.

The mean square displacement for hard sphere colloids at dilute regime is associated with the particle self-diffusion coefficient D_0 through the equation:

$$\left\langle \Delta R(\tau)^2 \right\rangle = 6D_0\tau \qquad (1.12)$$

1.4.2 Structure factor and dynamic interparticle properties

At sufficiently high volume fractions, the interactions between the particles are no longer negligible and hence the diffusion of one particle is influenced by the

presence of its neighbors. Thus, the spatial correlations between different mesoscopic particles are expressed by the static structure factor $S(q) \sim I(q)/P(q)$, where $I(q)$ is the total scattering intensity.

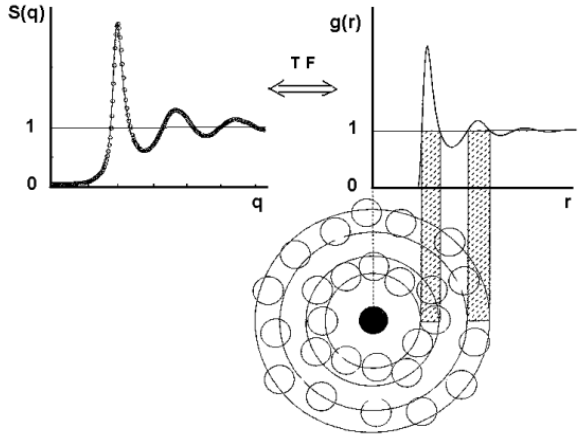

Fig. 1.14 *– Structure factor S(q) and pair correlation function g(r) for hard spheres, which can be extracted by S(q) by performing a numerical Fourier transformation and expresses the probability of finding neighboring particles at specific separation distances. The peak of both S(q) and g(r) corresponds to the position of the first neighbors and the successive peaks to next close neighbors. Adapted from (Bretonnet 2011).*

This onset of the aforementioned interactions between the particles, marks also the alteration of dynamics, which can be probed by the intermediate scattering function C(q,t) that measures the spatiotemporal correlations of the thermal volume fraction fluctuations. Moreover, dynamics are affected by hydrodynamic interactions H(q) through the relation $D(q)=D_0H(q)/S(q)$, where D_0 is the diffusion coefficient in infinite dilution limit.

The measurement of C(q,t) at low qR-values yields the cooperative diffusion D_C, which describes the relaxation of a concentration gradient and depends on the osmotic compressibility [~1/S(qR→0)]. Apart from cooperative diffusion, there is self-diffusion process as well. The self-diffusion coefficient D_s describes the fluctuating trajectory of a tracer particle among other particles and can be obtained by a time average of the position correlation function. Alternatively, D_s can also be measured for monodisperse hard sphere suspensions at finite concentrations, at

high qR where S(q)→1, when the interactions can be ignored. At infinite dilution, D_C and D_s coincide with D_0, but differ for more concentrated suspensions. We should also mention that both cooperative and self-diffusion coefficients depend on the thermodynamic interactions of the colloidal suspension (expressed by S(q)) and hydrodynamic interactions H(q) and exhibit distinctly different dependence on q and ϕ (Pusey and Tough 1982, Bowen and Mongruel 1998).

1.5 Arrested Phases

1.5.1 Colloidal glasses

Upon increasing the volume fraction, colloidal systems tend to reach a frozen state (glassy state), where due to the particles' crowding or the presence of strong interparticle interactions (repulsive or attractive), the movements of the particles are constrained. Generally, the particles of a colloidal glass hold some freedom for local Brownian motions but are unable to diffuse over large lengths. Due to this localization, colloidal glasses at rest are amorphous solids. Moreover, these systems are far from the equilibrium configuration and exhibit ageing phenomena, since in the process of attaining equilibrium configuration, their properties keep changing with waiting time t_w. Hard-sphere like colloidal glasses are also characterized by non-ergodicity and nearly time-dependent MSD (Van Megen and Underwood 1994), enhanced storage modulus due to significant increase of the viscosity (Mason and Weitz 1995), spatial and dynamic heterogeneity (Weeks and Weitz 2002, Chen, Weeks et al. 2003).

Understanding the slow dynamics in non-equilibrium systems is a longtime challenge in physics. In fig. 1.15, we can see all the possible colloidal systems in glassy regime from hard sphere glasses (either repulsive or attractive ones) to soft star glasses and the extreme case of glasses of linear flexible polymers. Hard sphere suspensions of high volume fraction form glass. Then the "cage model" is defined, when in short time scale a single particle is trapped among its neighboring particles in such a way that it maintains its original position almost unchanged, resulting in the formation of an effective cage that restricts its macroscopic motion (Pusey 1991). In

such a non-ergodic state, this structural arrest of the colloidal glass leads to the non-fully relaxation decay of the intermediate scattering function for the experimental time scale, a fact supported also with theory and simulations (Pusey and van Megen 1987). Local motions of the particle inside its cage are associated with the β-relaxation or fast relaxation. The escape of the particle from its cage is associated with a-relaxation, which takes place in longer time scales and determines the flow of the glass.

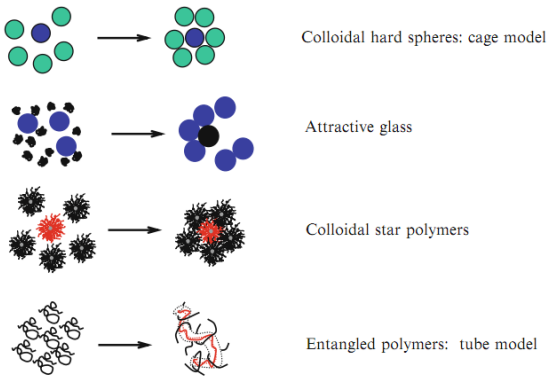

Fig. 1.15 *– Schematic representation of various glassy systems. The first three systems can be described by the general cage model, whereas the last one by the tube model for entanglements. Taken from (Vlassopoulos and Fytas 2009).*

For colloids of intermediate softness, a modified cage model can be considered which includes an extra relaxation step during the relaxation mechanism that is absent to hard sphere cage model. The soft particles are trapped among their neighbors similar to the hard sphere cage model, but due to their inherent structure, they can deform (mainly microgels) and interpenetrate (mainly polymer-grafted particles and star-like polymers) forming some entanglements of the outer blobs. Then, in order to escape from their cage and macroscopically flow, they should also disentangle from their neighbors. Due to deformability and interpenetration, the particles in soft glasses are more densely packed forming glasses at higher effective volume fractions.

In the limiting case of glasses of long chain polymers which is above the entanglement limit, the topological constraints of the neighbors (entanglements) confine a chain within a so-called tube. The dynamics of this dense system is related

to the escape of this chain from its tube, the so-called reptation (Doi and Edwards 1988).

As we already mentioned, colloidal glasses, in order to reach the equilibrium configuration, undergo ageing where their properties change with waiting time. During an ageing process at early times the system is able to access at least part of the energy states by thermally overcoming barriers and getting out of local minima. However, as time passes, the system falls each time into a deeper minima which is more difficult to avoid. Consequently, the kinetics of the system during ageing become slower and slower in such a way that the system cannot reach the thermodynamic equilibrium. During ageing, the viscosity of the system increases and the diffusion coefficient of the particles decreases. This suggests that the trapping of particles in cages formed by neighbors in real space is equivalent to the arrest of the system in a local minimum of the free energy landscape (Cipelletti and Ramos 2005).

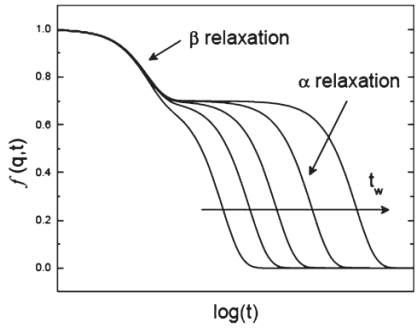

Fig. 1.16 *– Prediction of the mode coupling theory of the dynamic structure factor $f(q,t)$. Two relaxation times are presented: β for the fast relaxation and α for the slow relaxation, which becomes slower due to the progressive freezing of the intensity fluctuation of the glass with the waiting time t_w. Adapted from (Pujala 2014).*

Soft colloids, such as multiarm stars and polymer grafted glasses, present an unexpected speed up of the short-time diffusion which is connected with a spontaneous crystallization of an ageing glass with no out-of-cage diffusive motion (fig. 1.17). This speed up of dynamics can be rationalized with the assumption that the star glass eventually evolves toward a crystal at long times. In this case ordering leads on average to locally enhanced free volume resulting in faster particle dynamics (Stiakakis, Wilk et al. 2010).

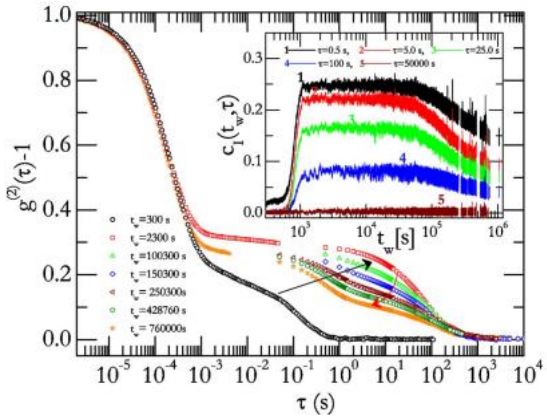

Fig. 1.17 *– Time evolution of the correlation function of the scattering intensity $g^{(2)}(\tau)-1$ in a 6.3%wt. (1.26c*) solution of multiarm stars in tetradecane after a temperature jump from T=15 to 25°C measured at q=0.024nm^{-1} / ϑ=90°. The arrows indicate the initial slowing down and subsequent speed up of the dynamics. Waiting times are indicated. Inset: corresponding degree of correlation for few sample times as a function of time. Taken from (Stiakakis, Wilk et al. 2010).*

1.5.2 Gelation

At low volume fractions, without the existence of attractions, a colloidal suspension consists of dispersed mobile particles. The implementation of weakly short-range attraction between particles leads to the formation of mobile clusters. Increasing the attraction strength, the clusters occupy an increasingly larger volume fraction up to the point at which their motions are arrested and large inhomogeneities (voids) are created. The maximum heterogeneity is formed at the gelation point (Koumakis, Moghimi et al. 2015). If the attraction strength increases further, heterogeneity decreases and more homogeneous structures are formed (Dibble, Kogan et al. 2006). The increase of the attraction strength can occur either by adding non-absorbing linear polymers or by alternating physicochemical properties of the external environment (pH, temperature) of stimuli-responsive suspensions.

1.6 Rheology

1.6.1 Linear Viscoelastic response

When applying oscillatory shear in the linear regime of strains, the microstructural properties of the probed material are not affected by the imposed shear and the measured viscoelastic properties reflect the state at rest. Then the variation of the oscillation frequency, at linear regime, allows us to study the viscoelastic properties at different time scales and obtain a better insight into the microscopic properties of the probed material.

A Dynamic Frequency Sweep (DFS) probes the elastic (G') and viscous (G'') moduli of a colloidal suspension in the linear regime at various frequencies, where the strain is constant for each frequency applied. The linear viscoelastic moduli determine the response of a suspension to small oscillatory shears which weakly perturb the equilibrium structure. At low frequencies, the shear induced perturbations are relaxed by Brownian motion, a phenomenon that dissipates energy and making the suspension be predominantly viscous. However, at higher frequencies, the perturbations can no longer be relaxed in the period of oscillation. This change of the equilibrium configuration results in energy storage and hence in an increase of the elastic component. There is a characteristic frequency, between the low and the high ones, which is determined by the ratio of the convection rate due to shear to the diffusional relaxation rate (the Peclet number $Pe = R^2\dot{\gamma}/D_s$, where R is the radius of the particle, $\dot{\gamma}$ the shear rate and D_s the short-time diffusion coefficient which is dependent on the particle volume fraction) (Mason and Weitz 1995).

For hard sphere suspensions, at low volume fractions the loss modulus is larger than the storage modulus, denoting that the suspension is a colloidal fluid. Increasing the volume fraction and approaching the colloidal glass transition, an onset of dominant storage modulus is observed which is almost frequency independent and marks the alteration of the rheological response from viscoelastic liquid behavior to solid-like behavior. This solidification of the suspensions occurs due to packing constrains that hinder the particles' motion. The evolution of the

viscoelastic spectra leading to solidification has been studied in detail for both hard spheres (Mason and Weitz 1995, Koumakis, Schofield et al. 2008) and soft particles (Senff, Richtering et al. 1999, Deike, Ballauff et al. 2001, Crassous, Siebenbürger et al. 2006, Carrier and Petekidis 2009, Siebenbürger, Fuchs et al. 2009, Cloitre 2011, Crassous, Casal-Dujat et al. 2013, Basu, Xu et al. 2014) and is directly affected by the softness of the particles.

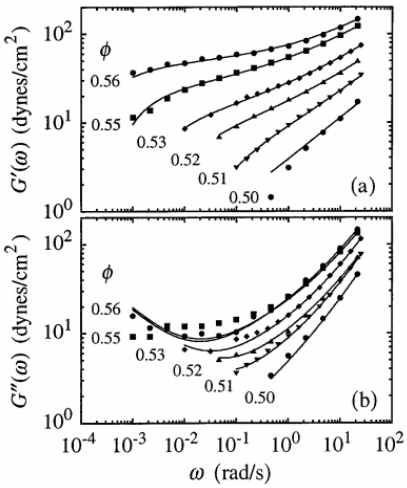

Fig. 1.18 *– Frequency dependence of the (a) storage and (b) loss moduli for different volume fractions of PMMA-HAS hard spheres. All measurements were performed at low strain to be in the linear regime. The solid lines represent MCT predictions. Adapted from (Mason and Weitz 1995).*

The frequency dependence of the storage and loss moduli for hard sphere suspensions as a function of volume fraction is presented in the fig. 1.18 (Mason and Weitz 1995).

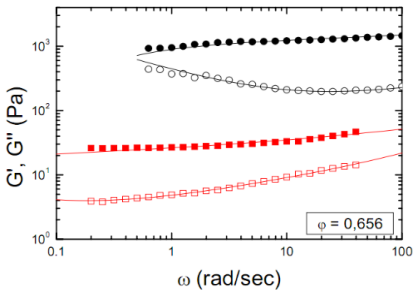

Fig. 1.19 *– Linear dynamic frequency sweeps of a glass (black circles) and its shear induced crystal (red squares) showing G' and G''. Lines are Mode Coupling Theory (MCT) fits. Taken from (Koumakis, Schofield et al. 2008).*

The linear viscoelastic behavior of a glassy hard sphere suspension and its shear induced crystal is depicted in fig. 1.19. Both glass and crystal show a solid-like response in a large range of frequencies, characteristic of a structurally frozen system. In the glass, the elastic modulus has a slightly increasing slope, which may be attributed to increased particle motions in small frequencies comparing to the higher ones, whereas the viscous modulus exhibit a minimum that expresses the transition from in-cage motion to out-of-cage motion at a characteristic time $t_{min}=2\pi/\omega$. The shear induced crystal show weaker elastic and viscous moduli than the glass due to ordering and hence larger available space per particle at the same volume fraction (Koumakis, Schofield et al. 2008).

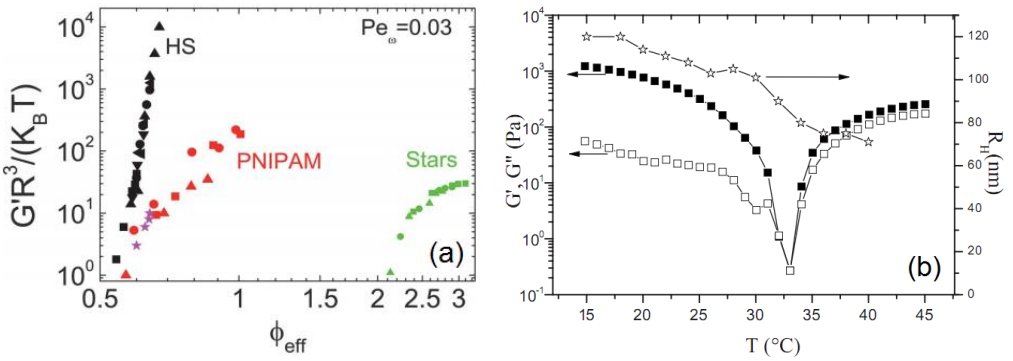

Fig. 1.20 *– (a) Storage modulus G' as a function of φ_{eff} at a specific time scale of Pe_ω=0.03 ($Pe_\omega=\omega t_B=\omega R^3 6\pi\eta/k_BT$) for hard spheres, microgels and star-like micelle. Taken from (Koumakis, Pamvouxoglou et al. 2012), (b) Left axis: Storage (filled squares) and loss (open squares) moduli versus temperature at 1Hz and strain amplitude γ=1% of concentrated thermosensitive core-shell microgels. Right axis: hydrodynamic radius of the microgels versus temperature. Adapted from (Carrier and Petekidis 2009)*

The softness of the probed particles affects the viscoelastic properties of the colloidal suspensions. Typical representatives of soft particles are multiarm star polymers and star-like micelles, which exhibit a strong interpenetration at high volume fraction, and microgel particles which show deformability. In general, the transition to the glassy state for soft systems is observed at a volume fraction (ϕ_{eff}) higher than that of hard spheres (see fig. 1.20a). Often, these soft systems exhibit thermoreversible liquid-to-solid transition since the temperature affects the solvent

quality, which results in the change of the particle size and thus the change of the ϕ_{eff} (Senff, Richtering et al. 1999, Kapnistos, Vlassopoulos et al. 2000, Loppinet, Stiakakis et al. 2001, Purnomo, van den Ende et al. 2008, Carrier and Petekidis 2009, Scheffold, Díaz-Leyva et al. 2010).

1.6.2 Yielding and Flow properties

Concentrated suspensions of colloidal particles behave as typical yield-stress fluids that respond either like elastic solids at rest or when the applied stress/strain is below a critical stress/strain called "yield stress/strain", or like a viscous fluids when a stress/strain is higher than the yield value of the material is applied.

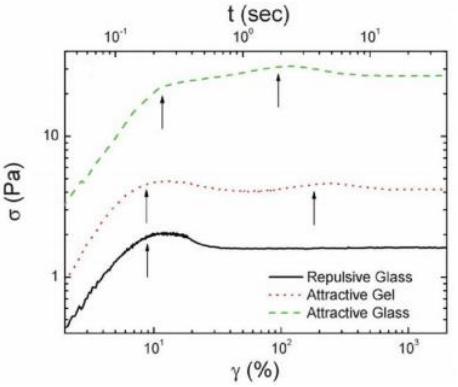

Fig. 1.21 *– Step rate experiments showing stress response versus strain/time performed at shear rate of $0.5s^{-1}$ for a repulsive glass of φ=0.6, an attractive glass of φ=0.6 and a gel of φ=0.4 with attraction strength $U_{dep}(2R)=-23.5k_BT$. Arrows indicate single and double yielding for repulsive and attractive glass/gel respectively. Taken from (Koumakis and Petekidis 2011).*

In a start-up shear flow experiment, a constant shear is imposed and stress versus time or strain is measured. Hard sphere repulsive glass exhibit a single stress overshoot in start-up shear flow, reflecting a single yielding mechanism that corresponds to cage breaking and the transition from an elastic deformation to a steady state plastic or viscous flow. Moreover, the stress response has been related to an elastic energy storage mechanism which causes an increase of stress before the peak and a dissipative energy release mechanism after the peak leading to shear-induced flow and structural anisotropy, manifested mainly by a decrease of the maximum of the pair-distribution function in the extension axis (Koumakis, Laurati et

al. 2012, Koumakis, Laurati et al. 2016). In contrast to hard sphere repulsive glasses, both attractive glass and gel show two distinct peaks in start-up shear flow. For the attractive glass, the first yielding mechanism is attributed to the short length scale bond breaking, whereas the second one to the breaking of the cages. For colloidal gels, the first yielding is related to the breaking of bonds that connect the clusters, while the second one to the breaking of the clusters to smaller pieces (Koumakis and Petekidis 2011, Laurati, Egelhaaf et al. 2011).

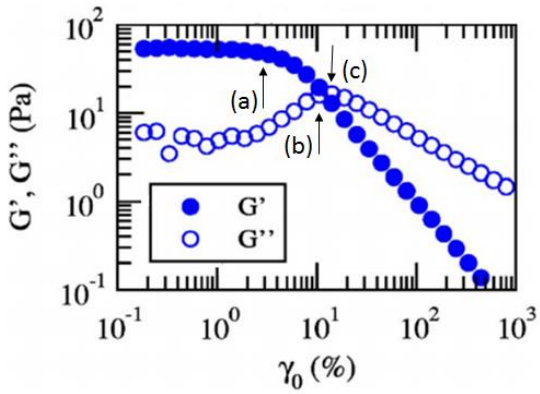

Fig. 1.22 *– Dynamic Strain Sweep for a glass at ω=1rad/s showing the elastic (solid circles) and viscous (open circles) moduli for φ=0.60. Replotted from (Pham, Petekidis et al. 2008). The arrows denote the various definitions of the yield strain.*

A Dynamic Strain Sweep (DSS) test probes the elastic (G') and viscous (G'') moduli of a colloidal suspension, by keeping constant the frequency and varying the strain applied. Similarly with start-up shear flow experiment, in DSS experiments the colloids show the yielding mechanism they follow depending on their interactions and their volume fraction. In the fig. 1.22, an example of DSS test for hard sphere glasses of purely repulsive interactions at low frequency is depicted (Pham, Petekidis et al. 2008). At low strains, the viscoelastic properties remain constant with the elastic modulus G' being greater that the viscous modulus G'', defining the linear regime, where the cage is only slightly distorted. As strains increase about 1-2% strain amplitude, G' starts decreasing, while G'' passes through a maximum before decreasing as well.

The transition of a colloidal glass from a viscoelastic solid to a viscoelastic liquid is called yielding and is microscopically related to the breaking of the cage formed by the neighbor particles. There are different ways to define the yielding point from a DSS experiment (see arrows marked in the fig. 1.22). Hence, we define strain (a) as the onset of yielding, where the linear properties start changing and non-linearity becomes apparent. At the crossover point (b), the elastic modulus is equal to the viscous one marking the point that the system transits from a viscoelastic solid into a viscoelastic liquid. Finally, the point (c) where the peak of G'' takes place is associated with the strain that the viscous loss during the cage breaking procedure is maximum.

It is interesting to highlight that hard sphere repulsive glasses show complex response in oscillatory shear flow depending on the frequency of oscillation. Under certain frequencies, a hard sphere glass also yields in two-step process where the first one is related to the Brownian-motion-assisted cage escape while the second one associated with the escape through shear-induced collisions (Koumakis, Brady et al. 2013).

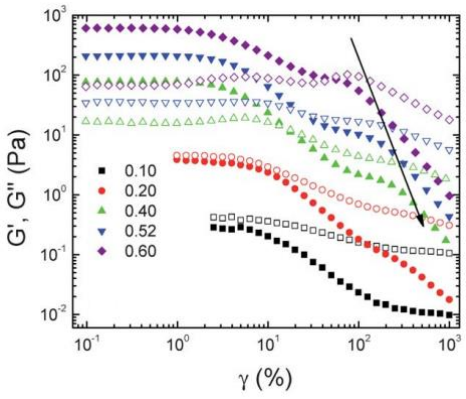

Fig. 1.23 *– Dynamic strain sweep performed at ω=10rad/s for five different volume fractions with equal attraction strength U_{dep}=-23.5k_BT.The arrow shows the shift of the second peak of G'' with decreasing volume fraction. Adapted from (Koumakis and Petekidis 2011).*

Dynamic strain sweep is also consistent with the start-up shear flow experiment in the case of attractive glasses and colloidal gels. The two-yielding mechanism for various particle volume fractions is apparent in fig. 1.23, where both

G’ and G’’ exhibit two distinct shoulders that signify the two-step yielding process. The second yield process, which for the gels is related to the breaking of clusters to smaller pieces, shows a strong dependence on the volume fraction. Moreover, the position of the second G’’ peak moves to larger values as the volume fraction is decreased due to the fact that at lower volume fractions larger clusters are present. Therefore, the yield strain needed in order to break the larger clusters is also larger (Koumakis and Petekidis 2011).

Similar to hard sphere repulsive glasses, soft colloidal systems such as multiarm stars (Helgeson, Wagner et al. 2007), microgels (Le Grand and Petekidis 2008, Carrier and Petekidis 2009, Koumakis, Pamvouxoglou et al. 2012, Appel, Fölker et al. 2016), concentrated emulsions (Mason, Lacasse et al. 1997, Paredes, Michels et al. 2013) or block copolymer micelles (Koumakis, Pamvouxoglou et al. 2012) with repulsive interactions exhibit yielding flow related to the “caging effect” and a typical shear-thinning behavior of a colloidal glass. However, in the case of multiarm star polymers, except for the fast and the slow relaxation modes that are connected to cage effect, the interdigitation of arms contributes to an additional relaxation mode resulting from the disengagement of the star arms (fig. 1.24) (Helgeson, Wagner et al. 2007).

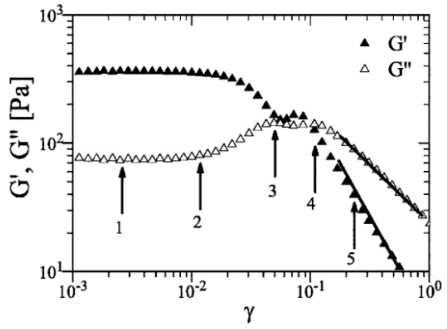

Fig. 1.24 *– Dynamic strain sweep performed of multiarm PBD stars of 2.1c* in squalene at an oscillatory frequency of ω=0.05rad/s. The arrows depict: (1) the linear viscoelastic regime, (2) onset of nonlinear deformation, (3) shear yielding, (4) second maximum of G’’ and (5) shear thinning. Taken from (Helgeson, Wagner et al. 2007).*

So far we reported the yielding as an onset of the flow of colloidal suspensions as the applied stress is increased. It is also interesting to refer to the

flow behavior of colloidal suspensions as the flow rate is decreased. Steady shear experiments (flow curves) probes the stress σ when steady state is reached as a function of constant shear rates $\dot{\gamma}$ applied. Fig. 1.25 depicts representative flow behaviors for various particle volume fractions for both hard sphere (Siebenbürger, Fuchs et al. 2009) and soft systems with repulsive interactions, such as microgels (Cloitre, Borrega et al. 2003, Carrier and Petekidis 2009, Siebenbürger, Fuchs et al. 2009, Basu, Xu et al. 2014, Pellet and Cloitre 2016), concentrated emulsions (Paredes, Michels et al. 2013) and multiarm star polymers (Erwin, Cloitre et al. 2010).

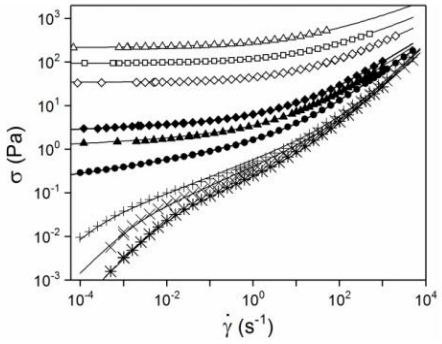

Fig. 1.25 *– Flow curves of microgel suspensions with increasing volume fraction (from bottom to top) in the viscous regime (crosses), entropic glass regime (full symbols), and jammed regime (open symbols). Continuous lines are fits with the Carreau-Yasuda equation (viscous suspension), generalized Herschel-Bulkley equation (entropic glass), and Herschel-Bulkley (jammed glass). Replotted from (Erwin, Cloitre et al. 2010).*

Dilute suspensions exhibit a purely viscous behavior that can be modelled with the Carreau-Yasuda equation:

$$\sigma(\dot{\gamma}) = \dot{\gamma}\left[\eta_\infty + (\eta_0 - \eta_\infty)\left(1 + (\dot{\gamma}\tau_0)^\alpha\right)^b\right] \qquad (1.13)$$

where η_0 and η_∞ are the low and high shear rate limits of viscosity respectively, τ_0 is the longest relaxation time which marks the onset of shear thinning and α and b are fitting parameters.

At high concentrations (jammed glass regime), the low shear regime is characterized by a flat plateau and the stress conforms to the Herschel-Bulkley equation:

$$\sigma(\dot{\gamma}) = \sigma_y + k\dot{\gamma}^n \tag{1.14}$$

where σ_y is the bulk yield stress, k a material-dependent constant and n an exponent typically ranging between 0.4 and 0.7.

At intermediate concentrations (entropic glass regime), the generalized Herschel-Bulkley equation involves a linear combination of a constant yield stress and two power law variations:

$$\sigma(\dot{\gamma}) = \sigma_y + k'\dot{\gamma}^p + k\dot{\gamma}^n \tag{1.15}$$

where k, k', n and p are parameters (Pellet and Cloitre 2016).

Finally, there is also the case of Bingham model which consists of the simplest idealization of a shear-thinning pseudo-plastic fluid that behaves as an elastic solid below the yield stress and as a Newtonian fluid above the yield stress:

$$\sigma(\dot{\gamma}) = \sigma_y + \mu\dot{\gamma} \tag{1.16}$$

where σ_y the yield stress, $\dot{\gamma}$ the shear rate and μ the Bingham or plastic viscosity (Yoshimura and Prud'homme 1987).

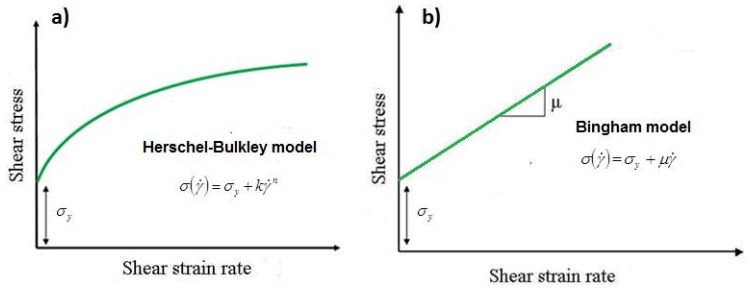

Fig. 1.26 *– Schematic representation of Herschel-Bulkley and Bingham fluid models.*

References:

Aarts, D. G., et al. (2002). "Phase behaviour of mixtures of colloidal spheres and excluded-volume polymer chains." Journal of Physics: Condensed Matter **14**(33): 7551.

Anderson, V. J. and H. N. Lekkerkerker (2002). "Insights into phase transition kinetics from colloid science." Nature **416**(6883): 811-815.

Appel, J., et al. (2016). "Mechanics at the glass-to-gel transition of thermoresponsive microgel suspensions." Soft Matter **12**(9): 2515-2522.

Asakura, S. and F. Oosawa (1954). "On interaction between two bodies immersed in a solution of macromolecules." The Journal of Chemical Physics **22**(7): 1255-1256.

Basu, A., et al. (2014). "Rheology of soft colloids across the onset of rigidity: scaling behavior, thermal, and non-thermal responses." Soft Matter **10**(17): 3027-3035.

Bolhuis, P. G., et al. (1997). "Entropy difference between crystal phases." Nature **388**(6639): 235-236.

Bonham, J., et al. (2014). "Non-aqueous microgel particles: synthesis, properties and applications." Soft Matter **10**(47): 9384-9398.

Bowen, W. R. and A. Mongruel (1998). "Calculation of the collective diffusion coefficient of electrostatically stabilised colloidal particles." Colloids and Surfaces A: Physicochemical and Engineering Aspects **138**(2): 161-172.

Bretonnet, J.-L. (2011). Thermodynamic Perturbation Theory of Simple Liquids. Thermodynamics-Interaction Studies-Solids, Liquids and Gases, InTech.

Carrier, V. and G. Petekidis (2009). "Nonlinear rheology of colloidal glasses of soft thermosensitive microgel particles." Journal of Rheology (1978-present) **53**(2): 245-273.

Cheng, Z., et al. (2001). "Phase diagram of hard spheres." Materials & Design **22**(7): 529-534.

Cipelletti, L. and L. Ramos (2005). "Slow dynamics in glassy soft matter." Journal of Physics: Condensed Matter **17**(6): R253.

Cloitre, M. (2011). "Yielding, flow, and slip in microgel suspensions: from microstructure to macroscopic rheology." Microgel Suspensions: Fundamentals and Applications: 283-309.

Cloitre, M., et al. (2003). "Glassy dynamics and flow properties of soft colloidal pastes." Physical review letters **90**(6): 068303.

Crassous, J. J., et al. (2006). "Thermosensitive core-shell particles as model systems for studying the flow behavior of concentrated colloidal dispersions." The Journal of Chemical Physics **125**(20): 204906.

Crassous, J. r. m. J., et al. (2013). "Structure and dynamics of soft repulsive colloidal suspensions in the vicinity of the glass transition." Langmuir **29**(33): 10346-10359.

Daoud, M. and J. Cotton (1982). "Star shaped polymers: a model for the conformation and its concentration dependence." Journal de Physique **43**(3): 531-538.

Deike, I., et al. (2001). "Rheology of thermosensitive latex particles including the high-frequency limit." Journal of Rheology **45**(3): 709-720.

Derjaguin, B. and L. Landau (1993). "Theory of the stability of strongly charged lyophobic sols and of the adhesion of strongly charged particles in solutions of electrolytes." Progress in Surface Science **43**(1-4): 30-59.

Dhont, J. K. (1996). An introduction to dynamics of colloids, Elsevier.

Dibble, C. J., et al. (2006). "Structure and dynamics of colloidal depletion gels: Coincidence of transitions and heterogeneity." Physical Review E **74**(4): 041403.

Erwin, B. M., et al. (2010). "Dynamics and rheology of colloidal star polymers." Soft Matter **6**(12): 2825-2833.

Grasso, D., et al. (2002). "A review of non-DLVO interactions in environmental colloidal systems." Reviews in Environmental Science and Biotechnology **1**(1): 17-38.

Grünewald, T. A., et al. (2015). "Core–Shell Structure of Monodisperse Poly (ethylene glycol)-Grafted Iron Oxide Nanoparticles Studied by Small-Angle X-ray Scattering." Chemistry of Materials **27**(13): 4763-4771.

Guiner, A., et al. (1955). "Small angle scattering of X-rays." J. Wiley & Sons, New York.

Halperin, A., et al. (1992). Tethered chains in polymer microstructures. Macromolecules: Synthesis, Order and Advanced Properties, Springer**:** 31-71.

Hansen, J. P., et al. (1991). Liquids, Freezing and Glass Transition: Les Houches Session 51., 3-28 Juillet 1989, North Holland.

Helgeson, M. E., et al. (2007). "Viscoelasticity and shear melting of colloidal star polymer glasses." Journal of Rheology **51**(2): 297-316.

Hiemenz, P. C. (1986). Principles of colloid and surface chemistry, M. Dekker New York.

Higgins, J. S. and H. Benoît (1994). Polymers and neutron scattering, Clarendon press Oxford.

Israelachvili, J. N. (2011). Intermolecular and surface forces, Academic press.

Jones, C. D. and L. A. Lyon (2003). "Shell-restricted swelling and core compression in poly (N-isopropylacrylamide) core− shell microgels." Macromolecules **36**(6): 1988-1993.

Kapnistos, M., et al. (2000). "Reversible thermal gelation in soft spheres." Physical review letters **85**(19): 4072.

Koumakis, N., et al. (2013). "Complex oscillatory yielding of model hard-sphere glasses." Physical review letters **110**(17): 178301.

Koumakis, N., et al. (2012). "Yielding of hard-sphere glasses during start-up shear." Physical review letters **108**(9): 098303.

Koumakis, N., et al. (2016). "Start-up shear of concentrated colloidal hard spheres: Stresses, dynamics, and structure." Journal of Rheology **60**(4): 603-623.

Koumakis, N., et al. (2015). "Tuning colloidal gels by shear." Soft Matter **11**(23): 4640-4648.

Koumakis, N., et al. (2012). "Direct comparison of the rheology of model hard and soft particle glasses." Soft Matter **8**(15): 4271-4284.

Koumakis, N. and G. Petekidis (2011). "Two step yielding in attractive colloids: transition from gels to attractive glasses." Soft Matter **7**(6): 2456-2470.

Koumakis, N., et al. (2008). "Effects of shear induced crystallization on the rheology and ageing of hard sphere glasses." Soft Matter **4**(10).

Larson, R. G. (1999). The structure and rheology of complex fluids, Oxford university press New York.

Laurati, M., et al. (2011). "Nonlinear rheology of colloidal gels with intermediate volume fraction." Journal of Rheology (1978-present) **55**(3): 673-706.

Le Grand, A. and G. Petekidis (2008). "Effects of particle softness on the rheology and yielding of colloidal glasses." Rheologica Acta **47**(5-6): 579-590.

Liang, Y., et al. (2007). "Interaction forces between colloidal particles in liquid: Theory and experiment." Advances in colloid and interface science **134**: 151-166.

Loppinet, B., et al. (2001). "Reversible thermal gelation in star polymers: An alternative route to jamming of soft matter." Macromolecules **34**(23): 8216-8223.

Lyon, L. A. and A. Fernandez-Nieves (2012). "The polymer/colloid duality of microgel suspensions." Annual review of physical chemistry **63**: 25-43.

Mason, T., et al. (1997). "Osmotic pressure and viscoelastic shear moduli of concentrated emulsions." Physical Review E **56**(3): 3150.

Mason, T. and D. Weitz (1995). "Linear viscoelasticity of colloidal hard sphere suspensions near the glass transition." Physical review letters **75**(14): 2770.

Mewis, J. and N. J. Wagner (2012). Colloidal suspension rheology, Cambridge University Press.

Ohshima, H. (2016). "Van Der Waals Interaction Between Colloidal Particles." Encyclopedia of Biocolloid and Biointerface Science 2V Set: 1087-1094.

Paredes, J., et al. (2013). "Rheology across the zero-temperature jamming transition." Physical review letters **111**(1): 015701.

Pellet, C. and M. Cloitre (2016). "The glass and jamming transitions of soft polyelectrolyte microgel suspensions." Soft Matter **12**(16): 3710-3720.

Pham, K., et al. (2008). "Yielding behavior of repulsion-and attraction-dominated colloidal glasses." Journal of Rheology **52**(2): 649-676.

Poon, W. (2004). "Colloids as big atoms." Science **304**(5672): 830-831.

Pujala, R. K. (2014). Dispersion stability, microstructure and phase transition of anisotropic nanodiscs, Springer.

Purnomo, E. H., et al. (2008). "Glass transition and aging in dense suspensions of thermosensitive microgel particles." Physical review letters **101**(23): 238301.

Pusey, P. (2008). "Colloidal glasses." Journal of Physics: Condensed Matter **20**(49): 494202.

Pusey, P. and R. Tough (1982). "Dynamic light scattering, a probe of Brownian particle dynamics." Advances in colloid and interface science **16**(1): 143-159.

Pusey, P. and W. Van Megen (1986). "Phase behaviour of concentrated suspensions of nearly hard colloidal spheres." Nature **320**(6060): 340-342.

Pusey, P., et al. (1989). "Structure of crystals of hard colloidal spheres." Physical review letters **63**(25): 2753.

Pusey, P. N. and W. van Megen (1987). "Observation of a glass transition in suspensions of spherical colloidal particles." Physical review letters **59**(18): 2083.

Ren, J. M., et al. (2016). "Star Polymers." Chemical Reviews **116**(12): 6743-6836.

Roovers, J., et al. (1993). "Regular star polymers with 64 and 128 arms. Models for polymeric micelles." Macromolecules **26**(16): 4324-4331.

Russel, W. B., et al. (1989). Colloidal dispersions, Cambridge university press.

Scheffold, F., et al. (2010). "Brushlike interactions between thermoresponsive microgel particles." Physical review letters **104**(12): 128304.

Senff, H., et al. (1999). "Rheology of a temperature sensitive core− shell latex." Langmuir **15**(1): 102-106.

Siebenbürger, M., et al. (2009). "Viscoelasticity and shear flow of concentrated, noncrystallizing colloidal suspensions: Comparison with mode-coupling theory." Journal of Rheology **53**(3): 707-726.

Stiakakis, E., et al. (2002). "Kinetic arrest of crowded soft spheres in solvents of varying quality." Physical Review E **66**(5): 051804.

Stiakakis, E., et al. (2010). "Slow dynamics, aging, and crystallization of multiarm star glasses." Physical Review E **81**(2): 020402.

Verwey, E. J. W., et al. (1999). Theory of the stability of lyophobic colloids, Courier Corporation.

Vlassopoulos, D. and M. Cloitre (2014). "Tunable rheology of dense soft deformable colloids." Current Opinion in Colloid & Interface Science **19**(6): 561-574.

Vlassopoulos, D. and G. Fytas (2009). From polymers to colloids: Engineering the dynamic properties of hairy particles. High Solid Dispersions, Springer**:** 1-54.

Woodcock, L. (1997). "Entropy difference between the face-centred cubic and hexagonal close-packed crystal structures." Nature **385**(6612): 141.

Ye, X., et al. (1996). "Depletion interactions in colloid-polymer mixtures." Physical Review E **54**(6): 6500.

Yoshimura, A. and R. Prud'homme (1987). "Response of an elastic Bingham fluid to oscillatory shear." Rheologica Acta **26**(5): 428-436.

Chapter 2

Experimental methods

2.1 Photon Correlation Spectroscopy

Photon Correlation Spectroscopy (PCS) or Dynamic Light Scattering (DLS) is a very popular technique for the characterization of colloidal suspensions in single-scattering regime, since it provides a wealth of structural and dynamical information on mesoscopic length scales (Berne 1976, Russel, Saville et al. 1989). In the classical theory of light scattering experiment, the light from a laser source passes through a polarizer that defines the polarization of the incident beam and then impinges on the scattering medium, which most of the radiation being transmitted and a small portion being scattered. The scattered light then passes through an analyzer, which selects a given polarization, and finally enters a detector (photomultiplier tube). The position of the detector defines the scattering angle θ. Moreover, the intersection of the incident beam and the beam intercepted by the detector defines the scattering volume V. Then, the scattered intensity can be related to the structure of the particles, whereas the intensity fluctuations reveal the dynamical motion of particles over an extended range of time scales.

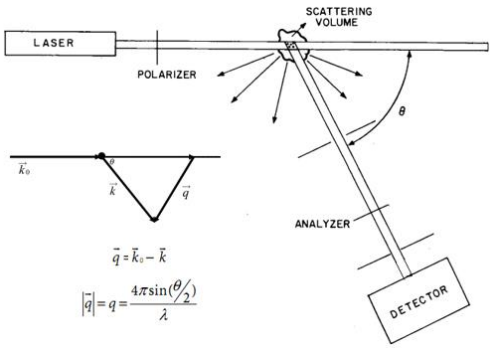

Fig. 2.1 *– Schematic representation of light scattering experiment. The scattering vector* $\vec{q} = \vec{k}_0 - \vec{k}$ *is defined by the geometry. Since the scattered wave has essentially the same wavelength as the incident wave* $k_0 = k = 2\pi n/\lambda$*, it follows the law of cosines that* $q = 2k\sin(\vartheta/2)$*. Taken from (Berne and Pecora 2000).*

The basic theory of light scattering was developed more than a half century ago by Rayleigh, Mie, Smoluchowski, Einstein and Debye (Chu 2007). Based on Einstein's theory, light scattering is a result of local fluctuations in the dielectric constant of the medium, which originate from the constant translational and rotational motion of molecules. Then, the instantaneous dielectric constant of a given subregion of the illuminated volume, which depends on the positions and orientations of the molecules, will fluctuate and thus give rise to light scattering (Einstein 1910).

The scattering of light can be considered as the redirection of light when the incident light ray, which consists of an electromagnetic (EM) wave, encounters an obstacle or non-homogeneity that in our case is the scattering particle. The mode of the interaction of light with the particle depends on the electronic structure of the particle's material as determined by its quantum mechanical properties. If the energy of the incident photon ($h\omega_0/2\pi$, where h is the Planck's constant) is equal to the difference in energy between two states in the system, then the photon might be absorbed by the system. As an oscillating electric field, light distorts the distribution of the charges in the system, which when they are accelerated emit radiation in the form of scattered light. If there is no exchange of energy between the photon and the system, then the frequency of the scattered light, ω_s, is equal to the frequency of the incident light ω_0, a process referred to as elastic scattering. On the contrary, if energy is exchanged between the photon and the system, ω_s differs from ω_0 and then the process is referred to as inelastic light scattering (Schmitz and Phillies 1991). The characteristic length scale of an elastic light scattering experiment is determined by the wavelength λ of the light used to probe the system and is proportional to $\propto 2\pi/q$. Here q denotes the scattering vector given by $q = (4\pi n/\lambda)\sin(\theta/2)$, where n is the refractive index of the solvent.

Photon Correlation spectroscopy entails the "mathematical translation" of the temporal intensity fluctuations of the scattered light in a single coherence area into the temporal normalized autocorrelation function of the scattered intensity,

using a digital correlator. The time-dependent scattered intensity is multiplied with itself after it has been shifted by a distance τ in time and then they are averaged over the total measurement time. For scattering particles suspended in a medium which undergo Brownian motion, the normalized autocorrelation function of the scattered intensity should be a single exponential decay according to the equation:

$$g^{(2)}(q,\tau)=\frac{\langle I(q,t)I(q,t+\tau)\rangle}{\langle I(q,t)^2\rangle} \quad (2.1)$$

while the respective normalized autocorrelation function of the electric field is written:

$$g^{(1)}(q,\tau)=\frac{\langle E(q,t)E^*(q,t+\tau)\rangle}{\langle E(q,t)^2\rangle} \quad (2.2)$$

Under the assumption of a Gaussian distribution of the scattering intensity profile, $g^{(2)}(q,\tau)$ is related to the electric field autocorrelation function $g^{(1)}(q,\tau)$ through the Siegert relation (Berne 1976):

$$g^{(2)}(q,\tau)=1+f^*\left(ag^{(1)}(q,\tau)\right)^2=1+f^*|C(q,\tau)|^2 \quad (2.3)$$

where *f** is the coherence factor, α the fraction of the scattered intensity with dynamics inside the correlator's window and C(q,τ) the normalized correlation function. In experimental practice, several coherence areas or speckles are detected simultaneously. Therefore, the intercept of the normalized intensity correlation function (coherence factor *f**) deviates from the theoretically expected value of unit, which corresponds to the case of one speckle detected.

In the simplest case of dilute suspension of monodisperse spherical particles, C(q,τ) is used to deduce the relaxation time τ related to the q-independent

translational diffusion coefficient D according to: $C(q,\tau)=\exp(-t/\tau)=\exp(-q^2 D\tau)$. Then the hydrodynamic radius R_H is obtained according to the Stokes-Einstein relation (Berne 1976, Brown 1993, Pusey and Tough 2002):

$$D=\frac{k_B T}{6\pi\eta R_H} \tag{2.4}$$

where k_B is Boltzmann's constant, T the temperature and η the viscosity.

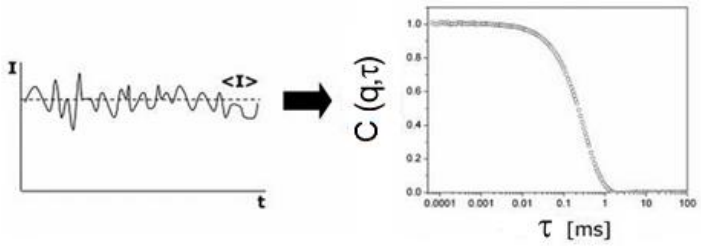

Fig. 2.2 *– Temporal fluctuations of the scattered intensity and normalized intensity autocorrelation function, which should single-exponential decaying from 1 to 0.*

The experimental setup used in this thesis is a typical photon correlation spectrometer, equipped by a 130mW/532nm wavelength He-Ne laser, an automated ALV goniometer that varies the scattering angle, a photomultiplier tube as a detector and an ALV-5100 digital corellator. For this set-up, the coherence factor is equal to *f**=0.36.

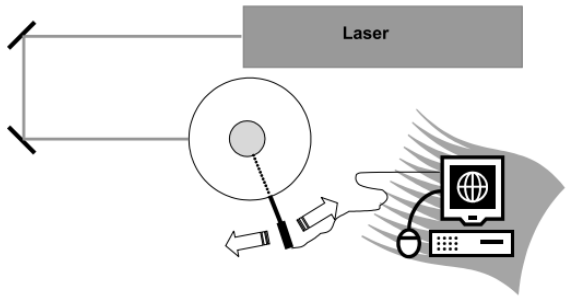

Fig. 2.3 *– Sketch of standard light scattering experimental setup. Adapted by (Schärtl 2007).*

Once the autocorrelation function is obtained, we can use the Kohlrausch-Williams-Watts (KWW) function (stretched-exponential function) in order to fit

relaxation processes that are for the determination of the translational diffusion coefficient of each process:

$$C(q,\tau) = A\exp\left[-\left(t/\tau_{WW}\right)^{\beta}\right] \quad (2.5)$$

where τ_{ww} is a characteristic relaxation time, β is the stretching exponent ranging between 0 and 1 and A the amplitude of the correlation function.

Another technique for extracting the translational diffusion coefficient once the autocorrelation data have been generated, is the so-called "cumulant analysis" given by Koppel (Koppel 1972). Cumulant analysis is used for analysing the experimental data of more complicated systems compared to the monodisperse ones, obtained by samples with small size polydispersities. One can write:

$$\ln C(q,t) = -K_1 t + \frac{1}{2}K_2 t^2 - \frac{1}{3!}K_3 t^3 + \frac{1}{4!}K_4 t^4 - \ldots \quad (2.6)$$

where $K_n = \left((-1)^n \ln C(q,t)\right)_{\tau=0}$ is the n^{th} cumulant of C(q,t). The first cumulant $K_1 = q^2\langle D\rangle$ yields the average translational diffusion coefficient and the corresponding inverse average hydrodynamic radius. The higher cumulant are referred to polydisperse samples, with the second cumulant K_2 being a measure of the variance of the distribution, while K_3 and K_4 measures of the asymmetry of the distribution. When the experimental data are good at small times, we can determine the coefficient K_1 from the explicit form for the first cumulant is $K^1=q^2D$ and finally estimate the translational diffusion coefficient D.

2.2 3D – Dynamic Light Scattering (3DDLS)

As we already mentioned, Photon Correlation Spectroscopy is a powerful technique for the study of colloidal suspensions. However, in concentrated suspensions, the conventional PCS experiment frequently fails due to strong multiple scattering contributions. Therefore, another light scattering technique was

developed in order to overcome these measurement limitations, the so-called 3D Dynamic Light Scattering (3DDLS) technique (Schätzel 1991, Overbeck, Sinn et al. 1997, Urban and Schurtenberger 1998, Urban and Schurtenberger 1998, Urban 1999), which effectively isolates the singly scattered light and suppresses any undesired multiple scattering contributions. In 3DDLS technique, two scattering experiments are performed simultaneously on the same scattering volume (with two laser beams, initial wave vectors k_{i1} and k_{i2} and two detectors positioned at final wave vectors k_{f1} and k_{f2}) and cross-correlating the signals which seen by the two detectors (Urban and Schurtenberger 1998). More specifically, the two incident and the two detected light paths are placed at an angle θ/2 above and below the plane of symmetry of the scattering experiment. The initial (k_{i1},k_{i2}) and final (k_{f1},k_{f2}) wave vector pairs are rotated by some angle about the common scattering $q=q_1=q_2$ for the two scattering processes 1-1 and 2-2, whereas the two other scattering processes 1-1 and 2-2 detected in this experiment have different scattering vectors. These additional scattering processes will contribute to the background only, which means that the maximum intercept for the 3D experiment is one quarter ($\beta_T^2 = 0.25$) of the value obtained for autocorrelation or other cross-correlation schemes such as the two-color method ($\beta_T^2 = 1$) (Pusey 1999). The reason for this reduction is that scattered light from the first (second) beam can also impinge onto the second (first) detector. Thus the cross-correlation function can be written as:

$$g_c^{(2)}(\tau) = \frac{\left\langle I_1^i(0) I_2^i(\tau) \right\rangle + \left\langle I_1^i(0) I_2^{ii}(\tau) \right\rangle + \left\langle I_1^{ii}(0) I_2^i(\tau) \right\rangle + \left\langle I_1^{ii}(0) I_2^{ii}(\tau) \right\rangle}{\left\langle I^2 \right\rangle} \qquad (2.7)$$

where the Arabic numbers denote the detector, whereas the Roman numbers the incident beam. The undesired contributions coming from the “wrong” incident beams that are still detected by the photomultipliers, are decorrelated and produce different scattering vectors $q_1 \neq q_2$. In the equation above only the second term gives correlated contributions to $g_c^{(2)}(\tau)$. Hence, the equation below is used which uses the

factor β_{tot}^2 that includes any correction that should be taken into consideration in a cross-correlation experiment.

$$g_c^{(2)}(\tau) = \frac{3\langle I_1 \rangle \langle I_2 \rangle + \langle I_1^i(0) I_2^{ii}(\tau) \rangle}{\langle I_1^i + I_1^{ii} \rangle \langle I_2^i + I_2^{ii} \rangle} = \frac{3}{4} + \frac{1}{4}\left[1 + \beta^2 [C(q,\tau)]\right] = 1 + \beta_{tot}^2 [C(q,\tau)] \quad (2.8)$$

where $\beta_{tot}^2 = \beta^2 \beta_{OV}^2 \beta_{MS}^2 \beta_T^2$ is the correction factor, with β^2 being the "coherence factor", which is related to coherence area and depends on the detection optics (similar to f* referred in DLS experiments), β_{OV}^2 the "overlap factor" that is connected to the fact that the scattering volumes seen by the two detectors are slightly different, $\beta_{MS}^2 = \frac{\left(g^{(2)}(q,\tau=0)-1\right)_{conc}}{\left(g^{(2)}(q,\tau=0)-1\right)_{dilute}} = \frac{\beta_{conc}^2}{\beta_{dilute}^2}$ the "multiple scattering factor" that is determined as the ratio of the amplitude of the cross-correlation function for the concentrated sample to the amplitude of the correlation function for a dilute sample and β_T^2 the "technique" factor connected to the "wrong" light collected by the detectors ($\beta_T^2 = 0.25$ for the 3DDLS set-up used for the experiments) (Pusey 1999).

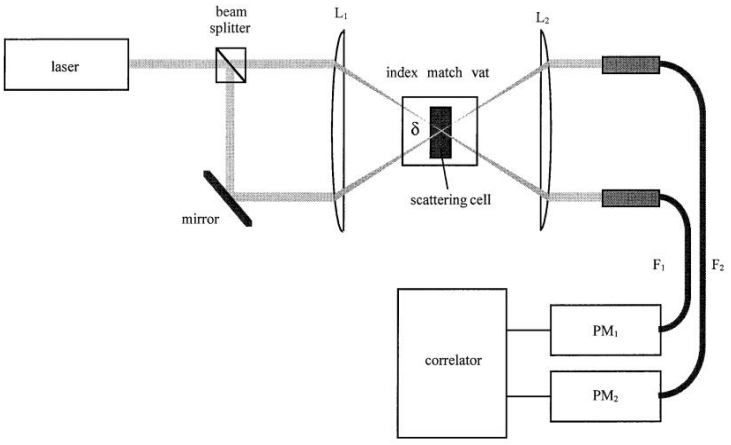

Fig. 2.4 – *Schematic representation of the experimental setup for 3D cross-correlation.*

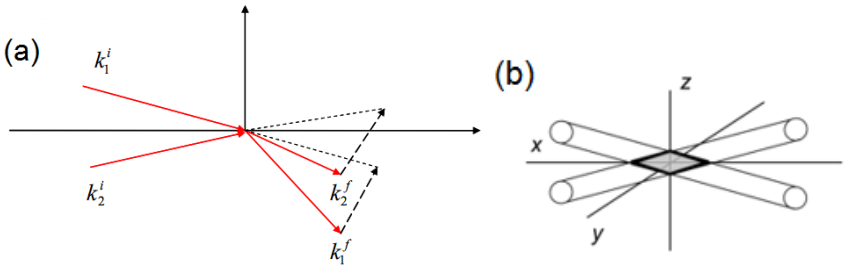

Fig. 2.5 – *(a) Schematic representation of the three dimensional dynamic light scattering light path. (b) Sketch of the scattering volume.*

At high concentrations, the interactions between the particles are not negligible and can be examined by the static structure factor S(q). For calculating the structure factor S(q) the scattering loss parameters such as the correction factor β_{tot}^2 and the sample transmission should be taken into consideration based on the equation:

$$S(q) = \frac{I_{conc}^{total}(q) c_{dilute} T_{dilute}}{I_{dilute}(q) c_{conc} T_{conc}} \tag{2.9}$$

where c is the concentration of the suspension and T the transmission values.

The single scattering intensity $I_{conc}^{S}(q)$ is calculated by multiplying the normalized scattering intensity of the concentrated sample with the correction factor β_{MS} :

$$I_{conc}^{S}(q) = \sqrt{\beta_{MS}^2} I_{conc}(q) = \beta_{MS} I_{conc}^{total}(q) \tag{2.10}$$

Several research groups (Overbeck, Sinn et al. 1997, Aberle, Hülstede et al. 1998, Urban and Schurtenberger 1998, Urban and Schurtenberger 1998) have established that quite turbid samples down to 5% transmission can be successfully measured with this technique.

2.3 Multi – Speckle Dynamic Light Scattering (MSDLS)

Dynamic Light Scattering is a well-established technique for investigating the dynamics of a wide variety of systems. In a DLS experiment, the quantity of interest is the ensemble-averaged temporal autocorrelation function of fluctuations of the light scattered by the studied suspension. As we have already mentioned, a typical setup includes a laser source, a goniometer and a detector which usually is a photomultiplier tube whose signal is fed to an electronic correlator and collects light from a single coherence area (speckle) (Berne 1976). To obtain good statistical accuracy, it is necessary to extensively time-average the correlator output. For ergodic samples, the time averaging directly yields the desired ensemble average. However, this approach is not applicable for non-ergodic systems where time and ensemble averaging are no longer equivalent due to the fact that density fluctuations are frozen and so dynamics is so slow that the averaging time becomes too long. Moreover, in such systems (colloidal glasses and polymeric or colloidal gels) interesting dynamics often occurs at length scales as large as several microns which corresponds to very small angles and very slow dynamics (Cipelletti and Weitz 1999).

In order to overcome these problems, a modification of the conventional dynamic light scattering set-up was introduced by Bartch et al. (Bartsch, Frenz et al. 1997) replacing the photomultiplier tube used conventionally as detector by a charge-coupled device (CCD) camera. This technique is called Multi-Speckle Dynamic Light Scattering (MSDLS) and is implemented in suspensions that are both in single and DWS regime. MSDLS allows the monitoring of the intensity fluctuations of many independent speckles simultaneously, calculation of the time-averaged intensity autocorrelation function $g^{(2)}(q,\tau)$ for each speckle and then construction of the ensemble-averaged intermediate scattering function for all the speckles measured (Bartsch, Frenz et al. 1997).

The MSDLS experimental setup which used for our experiments is homemade and is schematically presented in the fig. 2.6. In this setup, there are two different detection units for detecting the scattered light. Arm 1 holds the CCD camera, while arm 2 the conventional photomultiplier tube. The sample is placed at the center of

the vat in a way that the laser beam passes through the centre of the cell. The cell is immersed in an index matching liquid (decalin) to avoid reflections. The temperature controlling unit is built at the bottom part of the vat.

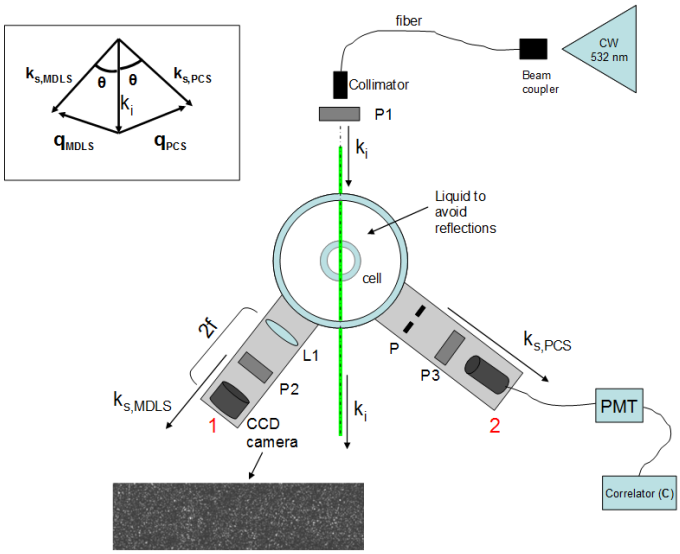

Fig. 2.6 – *Schematic representation of the MSDLS set-up used in the experiments of this thesis.*

A green CW Nd-Yag laser (coherent) beam with a wavelength of λ=532 nm is used in this setup. The beam is vertically polarized and passes through a beam coupler-fiber (single mode-polarization maintaining) collimator system, which is placed close to the goniometer. The polarization of the incident and the scattered beam is vertical to the scattering plane and can be tuned by the polarizers P1, P2 and P3. After the collimator, the incident beam passes through the polarizer P1 and is scattered from the cell. As it is already mentioned, on arm 2 there is a photomultiplier tube, which collects the scattering light at scattering angle θ and through the correlator (ALV-5000 E), calculates the autocorrelation function of the scattering intensity. On arm 1, a CCD camera is mounted. Before the CCD camera there is a polarizer P2, a pinhole that defines the speckle size (d=2.5mm) and a lens at distance 2*f from the camera for imaging the speckles at a magnification of M=1. This arrangement provides the possibility of direct measurement of a large number of speckles at the same scattering angle (bright spots on the image above).

The sensor of the CCD camera contains multiple pixels, each one of them works as a photon detector. Moreover, there is appropriate software which

calculates the auto-correlation function instead of a hardware correlator. This software processes a series of images from the CCD camera which are saved in the hard disk drive of a computer and later analysed to produce the correlation function at different waiting times.

The measurements in this setup are long and thus it is of great importance the achievement of temperature stability. Small differences in temperature during slow dynamics and aging measurements may affect the experiment (Cipelletti and Ramos 2005). Therefore, the vat is connected to a temperature controlling system with heating and cooling abilities, which is controlled by a temperature controller. The fluctuation of the temperature inside the vat is $\Delta T \sim 0.03^{o}C$. The vat consists of an optical glass cylindrical pot, which is mounted inside a ceramic cylinder and is filled with an index matching liquid (decalin) for avoiding undesirable reflections and ensuring temperature stability in the cell. In the copper cylinder, three ceramic thermal cylinders are implanted in order to heat isotropically the glass vat, which are also controlled by a temperature controller. Under the copper cylinder, a liquid cooling systems is installed, which is connected to a temperature controlling bath. This temperature controlling system is very stable at a temperature range from $5^{o}C$ up to $90^{o}C$ providing $\pm 0.05^{o}C$ accuracy.

Software Correlator – Calculation of autocorrelation function:

During the MSDLS experiment a series of images with different speckle pattern are saved in the hard drive of the computer. The time difference between the images depends on the frame rate of the CCD camera that is used during the experiment. These images are uncompressed bitmap files (raw files). The CCD camera that is used is a 8-bit digital camera (Basler A301f) with a CCD area of 649(H)x486(V). For most experiments the used region is of 300(H)x60(V), whereas the used frame rates range between 2 and 82frames/sec depending on the experiment. This means that our images are arrays of 300 columns by 60 rows, with integer values from 0 to 255. The software that is used for capturing and saving images is “Streampix” (NorPix). In order to calculate the correlation of the images, a

program copies the pixel intensity of each frame to the RAM or the hard disk of the computer. Then, the intensity of each pixel p can be written as a function of time t as $I_p^{raw}(t)$. The dark counts of each pixel are also taken into account by performing the experiment with the same frame rate, but without illuminating the sample. For obtaining the average intensity of dark counts for each pixel, a number of frames (~100) is averaged. The instantaneous value of the scattered intensity measured by the p^{th} pixel at time t used to calculate the autocorrelation function $I_p(t) = I_p^{raw}(t) - \langle I_p^{dark} \rangle$ (Cipelletti and Ramos 2005). $I_p(t)$ is used to calculate the degree of correlation $c_I(t,\tau)$ of the scattered intensity of two images separated by lag time τ, where the $\langle ... \rangle_p$ is taken over all CCD pixels (fig. 2.7). The degree of correlation $c_I(t,\tau)$ is calculated by multiplying two frames (the first at t and the second at t+ τ) and summing up the results from all pixels by the number of the pixels $\left(\langle I_p(t) I_p(t+\tau) \rangle_p \right)$:

$$c_I(t,\tau) = \frac{\langle I_p(t) I_p(t+\tau) \rangle_p}{\langle I_p(t) \rangle_p \langle I_p(t+\tau) \rangle_p} \qquad (2.11)$$

We should highlight that no time average is needed; the degree of correlation depends on both the lag time τ between the two images analysed and the time t at which the first image of the pair is taken.

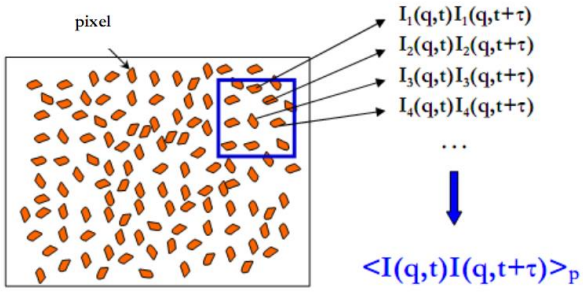

Fig. 2.7 – *Schematic representation for calculating the autocorrelation function of the scattered intensity in a MSDLS experiment.*

The use of asymmetric normalization ($\langle I_p(t)I_p(t+\tau)\rangle_p$) in the degree of correlation instead of ($\langle I_p(t)\rangle_p^2$) provides more reliable results when the intensity of the incident beam has long time fluctuations. For that reason we use a fiber to guide the laser beam to the sample (see fig. 2.6), the use of which is important in order to avoid the laser beam point instabilities, which are crucial in MSDLS setup. This instability comes from small fluctuations in the propagation direction of the laser beam. As long as the center of the speckle pattern is around the direction of the propagated beam and is recorded in the CCD camera, small changes in propagation direction will change artificially the position of the speckles in the speckle pattern. Therefore, the intensity of each pixel will change and lead to an artificial drop in the degree of correlation $c_I(t,\tau)$.

In MSDLS, the $c_I(t,\tau)$ provides the real ensemble average of the normalized autocorrelation function of the scattering field by the equation:

$$\left(|C(q,t)|^2 = \frac{\left(\langle c_I(t,\tau)\rangle_t - 1\right)}{f^*} \right) \tag{2.12}$$

where ensemble is a small time average typically of 10-100s, because each frame consists of 18000 pixels. Therefore, $c_I(t,\tau)$ is a snapshot of the system dynamics and thus such method is very useful for studying non-ergodic dynamics and ageing phenomena.

2.4 Diffusive Wave Spectroscopy (DWS)

Diffusing-Wave Spectroscopy (DWS) is the extension of conventional dynamic light scattering to very strongly multiply scattered samples. All light scattering techniques entail the measurement of the temporal intensity fluctuations of the scattered light in a single coherence area (speckle spot) and the calculation of the temporal autocorrelation function of the scattered intensity, which provides information about dynamics and thereby information about physical properties of

the medium (Weitz, Zhu et al. 1992, Weitz, Zhu et al. 1993). In DWS technique, the photons are scattered many times before they reach the detector. In this limit, the direction of light is totally randomized. For this highly multiple scattering regime, the propagation of photon through the sample can be adequately described as a simple diffusion process, where the details of each single scattering event are no longer relevant. This photon diffusion process is characterized by the so-called transport mean free path l^*, which is the average distance that a photon travels in the sample before its direction of propagation is randomized (Pine, Weitz et al. 1988, Pine, Weitz et al. 1990, Weitz, Zhu et al. 1992). In DWS the wave vector dependence is lost and the measured relaxation times highly depend on the experimental scattering geometry (transmission or backscattering), rather than the actual scattering angle, as well as on the number of scattering events n, the geometry of the incident beam and the intrinsic dynamics of the sample (Maret and Wolf 1987, Pine, Weitz et al. 1988, Weitz, Zhu et al. 1993).

To analyze the experimental data obtained with DWS requires the calculation of the correlation function of the multiply scattered light. As we already mentioned, in DWS we exploit the fact that a long path involves many scattering events and approximate each individual scattering event by an average scattering event. Then, the total correlation function is determined by summing the contributions of the individual paths, weighed by the probability that a diffusing photon follows that path:

$$g^{(1)}(\tau) = \int_0^\infty P(s)\exp\left(-\left(2\tau/\tau_0\right)s/l^*\right)ds \qquad (2.13)$$

where τ is the delay time, $\tau_0 = \left(k_0{}^2 D_0\right)^{-1}$ is the characteristic diffusion time, $k_0=2\pi/\lambda$ is the incident wave vector, P(s) is the probability that the light travels a path of length s and l^* the transport mean free path. Physically the equation of $g^{(1)}(q,\tau)$ reflects the fact that a diffusion path of length s corresponds to a random walk of s/l^* steps and decays on average $\exp\left(-2\tau/\tau_0\right)$ per step. Thus, $g^{(1)}(q,\tau)$ contains a

wide distribution $g^{(1)}(q,\tau)$ of decay times, with the most rapid decay times coming from the longest paths (Pine, Weitz et al. 1988).

In the transmission geometry, the correlation function of the scattered electric field can be approximated by (Weitz, Zhu et al. 1993):

$$g^{(1)}(\tau)=\sqrt{g^{(2)}(\tau)-1}\cong\exp\left(-\frac{1}{6}nk_0{}^2\left\langle\Delta r^2(\tau)\right\rangle\right)=\exp\left(-\frac{4\pi^2L^2D_0\tau}{l^{*2}\lambda^2}\right) \qquad (2.14)$$

where $n=\left(L/l^*\right)^2$ is the number of scattering events (L is the thickness of the suspension and l^* the transport mean free path) and $\left\langle\Delta r^2(\tau)\right\rangle=6D_0\tau$ the mean square displacement of a particle in single-scattering regime.

For our experiments we used a homemade DWS setup in transmission geometry equipped by green CW Nd-Yag laser (Coherent) beam with a wavelength of λ=532 nm. The beam is vertically polarized and passes through a beam coupler – fiber (single mode – polarization maintaining) – collimator system. After the collimator the incident beam passes through a polarizer, which tunes vertically the polarization and is scattered from the sample in the square cell. Then the scattered light passes through a polarizer and then is detected by the detector unit which is placed at angle 180°, relative to the incident beam. So, in this transmission geometry, the light is incident on the one side of the sample and is detected from the other side.

Firstly, a PMT is used as a detector unit, which collects the scattering light at θ=180° after having been vertically polarized with a polarizer and a digital multi-tau (ALV-5000 E) calculates the autocorrelation function of the scattering intensity. For measuring the autocorrelation function of the intensity of non-ergodic cases, the PMT detector is replaced by a CCD camera, which contains multiple pixels, each one of them works as a single photon detector. As we already described in MSDLS technique, the CCD camera monitors the intensity fluctuations of many independent speckles simultaneously. Then through a software that is used instead of correlator, the time-averaged intensity autocorrelation function $g^{(2)}(q,\tau)$ is calculated for each

speckle and the ensemble-averaged intermediate scattering function for all the speckles measured is finally constructed.

Accurate and fast control of the temperature is achieved by Peltier elements connected with the holder of the cell.

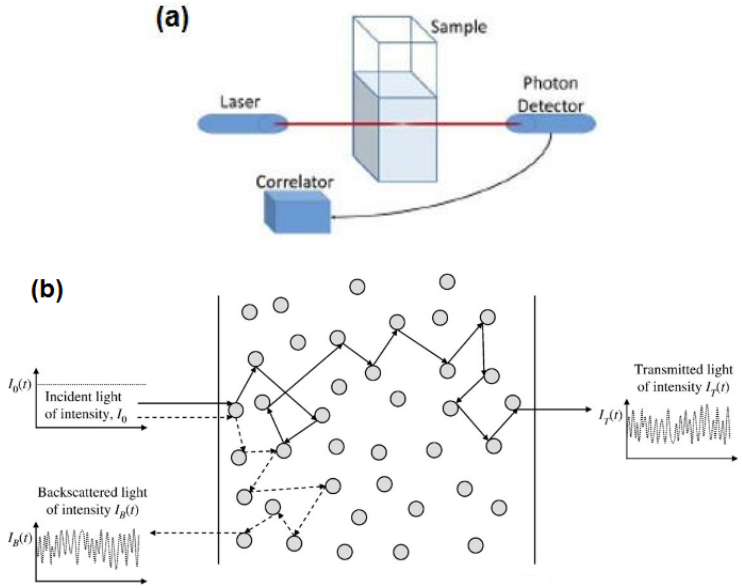

Fig. 2.8 – *(a) Schematic Diffusive Wave Spectroscopy (DWS) setup in transmission geometry, (b) a beam of light on the dispersed phase medium is multiply scattered by the moving particles before exiting the medium to be collected by light intensity detectors; the light exits from the face on which the incident beam enters is the backscattered light, while that which leaves through the opposite face is the transmitted one. Adapted from (Zivkovic, Biggs et al. 2008).*

2.5 Rheology fundamentals

Rheology is a branch of physics, which studies of the deformation and flow of materials in response to an applied stress or strain. The term originates from the Greek word «ροή», which means flow. Ideal solids store energy and provide a spring-like, elastic response, whereas ideal liquids dissipate energy through viscous flow. For more complex viscoelastic materials, both solid-like and liquid-like behaviour are detected depending on the time scale of experiment and the structural relaxation time of material. Rheometry is the measuring technology used to determine rheological properties.

2.5.1 Simple shear

The fundamental concepts of rheology and rheometry will be derived from fig. 2.9 that presents the ideal case of a simple flow condition, where a simple fluid exists in between two flat rigid surfaces. In a simple shear, a force F_x is applied on the top plate that is moved with a velocity V_x, whereas the bottom plate is stationary. The adhesion between the fluid and the surfaces is assumed to be strong enough that there is "no slip" effects at either surfaces. The two plates are separated by a distance h that corresponds to the thickness of the fluid.

Fig. 2.9 *- Schematic representation of an ideal velocity profile for an ideal fluid flow in between two plates. The top plate moving with velocity V and the bottom plate is stationary. The two plates are separated by a distance h.*

In "no slip" condition, the velocity gradient along the y-axis is constant and is given by:

$$\frac{dV_x}{dy} = \frac{V}{h} = \dot{\gamma} = \frac{d\gamma}{dt} = const. \qquad (2.15)$$

where $\dot{\gamma}$ is the shear rate and γ=Δx/h is the shear strain, which is defined as the displacement of the top plate Δx relative to the thickness of the sample h.

We also define shear stress $\sigma_{xy}=F_x/A$, which is the force applied F_x per unit area with x denoting the direction of shear stress and y denoting the plane normal to which the force is acting. In an ideal liquid the velocity gradient or shear rate determines the internal stresses. According to Newton's constitutive equation for

fluids the shear stress is proportional to the shear rate and the proportionality constant determines the viscosity of the fluid $\eta = \sigma_{xy} / \dot{\gamma}$.

If the fluid between the surfaces is an ideal elastic solid, Hooke's law is applicable. Then, the shear stress is proportional to the strain or the deformation and the proportionality constant is the shear modulus of the solid G= σ_{xy} /γ. Since the stress has units of force/area and the strain is dimensionless, the shear modulus has units force/area too.

Materials such as polymers and colloidal suspensions are viscoelastic, meaning that they present intermediate properties between Newtonian liquids and Hookean solids, behaving as liquids at certain applied rates and solids at others.

2.5.2 Oscillatory shear

A different kind of flow profile can be applied to the top moving plate namely oscillatory. In this profile, the strain applied is as seen in fig. 2.10(a) and is mathematically expressed as $\gamma = \gamma_0 \sin(\omega t)$, where ω is the frequency of oscillation, t is the time of oscillation and γ_0 is the maximum amplitude of strain. The shear rate is defined as derivative of strain:

$$\frac{d\gamma}{dt} = \dot{\gamma} = \dot{\gamma}_0 \cos(\omega t) = \gamma_0 \omega \cos(\omega t) \qquad (2.16)$$

with $\dot{\gamma}_0 = \gamma_0 \omega$ the maximum amplitude of shear rate within a cycle as seen in fig. 2.10(b).

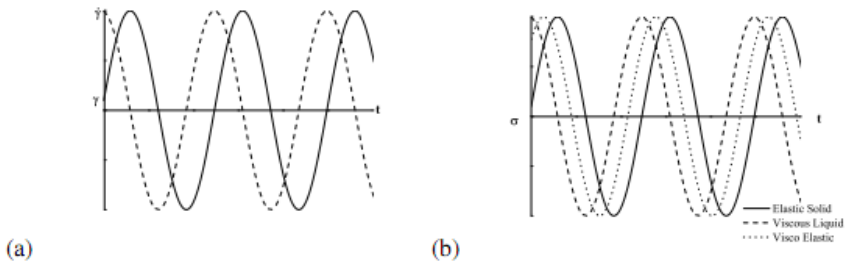

Fig. 2.10 *- (a) Strain and shear rate during oscillatory shear and (b) Stress response for the oscillatory strain for an ideal elastic solid, a viscous fluid and a viscoelastic material.*

If the material studied is an ideal elastic solid which follows Hooke's law, σ=Gγ the stress response will be:

$$\sigma(t) = G\gamma(t) = G\gamma_0 \sin(\omega t) \tag{2.17}$$

where the stress is perfectly in-phase with the strain.

On the other hand, if the material investigated is a Newtonian fluid where $\sigma = \eta\dot{\gamma}$, the oscillatory stress response will be related to the shear rate through Newton's law:

$$\sigma(t) = \eta\dot{\gamma}(t) = \eta\dot{\gamma}_0 \cos(\omega t) \tag{2.18},$$

which denotes that the Newtonian fluid oscillates with the same angular frequency ω, but is out-of-phase with the strain by π/2. For viscoelastic materials, the stress response can be written as a function of strain as follows:

$$\sigma(t) = \sigma_0 \sin(\omega t + \delta) \tag{2.19}$$

where δ is the phase angle difference between the stress and the applied oscillating strain. In general δ can be frequency dependent with any value in the range 0<δ<π/2. Hookean solids and Newtonian fluids correspond to the limits allowed for the phase angle with the Hookean solids having δ=0, whereas Newtonian fluids δ=π/2 at all frequencies. When the strain amplitude of γ_0 is small, the material is in the linear regime of shear. In this case, since the stress response σ(t) is sinusoidal with the same frequency as the strain, we can separate the stress into two orthogonal functions that oscillate with the same frequency, one in-phase with the strain and the other out-of-phase with the strain by π/2. So:

$$\sigma(t) = \gamma_0 \left(G'(\omega)\sin(\omega t) + G''(\omega)\cos(\omega t) \right) \tag{2.20}$$

where $G' = \frac{\sigma_0 \cos\delta}{\gamma_0}$ is the storage modulus and $G'' = \frac{\sigma_0 \sin\delta}{\gamma_0}$ the loss modulus. The storage modulus represents the elastic properties of materials, whereas the loss modulus describes the ability of materials to dissipate energy. Hence, for G'>G'' solid-like response is detected, whereas for G'<G'' liquid-like response dominates. Soft solid materials typically indicate G'>G'' on the experimental time window with a slow increase of the storage modulus with frequency, while loss modulus exhibits a minimum (Mason and Weitz 1995). Contrary, a liquid-like response is characterized by a simple Maxwell model which describes well the linear viscoelastic behaviour with the frequency as $G' \sim \omega^2$, the loss modulus scales with the frequency as $G'' \sim \omega$, while the crossover frequency, ω_c, where G'=G'', signifies an internal long time relaxation process in the system. The low-frequency liquid-like region in which G' and G'' obey these power law is called the terminal regime (Ferry 1980).

The loss tangent is defined as the ratio of the loss modulus to the storage modulus and given by:

$$\tan\delta = \frac{G''}{G'} \tag{2.21}$$

Also, the storage and the loss moduli can be written as the real and imaginary parts of the complex modulus:

$$G^*(\omega) = G'(\omega) + iG''(\omega) \tag{2.22}$$

Hence oscillatory shear contributes in extracting the elastic and viscous components of the viscoelastic samples.

In large amplitude oscillatory shear experiment, the moduli G' and G'' are measured even at strain amplitudes where there large anharmonic contributions. In this case, the above definition fails to sufficiently describe the storage and loss

moduli and then other representation methods are required which take into consideration the higher harmonics' contribution (Ewoldt, Hosoi et al. 2008, Hyun, Wilhelm et al. 2011, Rogers, Erwin et al. 2011, Poulos, Stellbrink et al. 2013, Jacob, Deshpande et al. 2014).

A measure of the importance of Brownian and shear-induced motions is given by the dimensionless Peclet number:

$$Pe = \dot{\gamma} t_B \tag{2.23}$$

where $\dot{\gamma}$ is the shear strain rate and t_B is the Brownian relaxation time (the time needed for a particle to diffuse distance proportional to its own radius). In dilute suspensions, $t_B = R^2/D_0$, where R is the particle radius and $D_0 = k_B T/6\pi\eta R$ is the Stokes-Einstein diffusivity of a non-interacting particle in a medium with viscosity η. Thus:

$$t_B = 6\pi\eta\, R^3/k_B T \tag{2.24}$$

In concentrated suspensions, the short-time self-diffusion is not equal to the diffusion of dilute regime, rather it is reduced due to hydrodynamic interactions (Sierou and Brady 2001). The hydrodynamic effects are important and should be taken into consideration, since the actual Brownian time of the colloidal suspensions scales all other resulting times, when examining the effects of shear. Hence, we can distinguish two Brownian times and/or Peclet numbers. The first, which is called "bare", refers to the dilute regime and its Brownian time can be calculated by the particle radius and solvent viscosity. The second one which is called "dressed", which takes into consideration the hydrodynamic interactions between particles and reflects the smaller short-time self-diffusion coefficient, $D_s(\phi)$. The calculation of the dressed Pe requires the knowledge of the ϕ-dependence of $D_s(\phi)/D_0$ (Pusey 1991).

2.6 Rheometry

2.6.1 Cone and Plate geometry

Cone and Plate is one of the most commonly used geometries in rheometry for investigation of suspension rheology because the velocity and therefore the shear rate $\dot{\gamma}$ is constant all along the geometry (fig. 2.11). When the angle of the cone is small (α≤0.1rad) the shear rate $\dot{\gamma} = \omega/\alpha$, where ω is the rotational speed in rad/s^{-1} and α the angle of the cone in rad, depends on the tangential velocity and the local distance between the plates. The shear stress of a cone and plate geometry is calculated as:

$$\sigma = \frac{3T}{2\pi R^3} \tag{2.25}$$

where T is the torque experienced by the geometry and R is the radius of the geometry (Mewis and Wagner 2012).

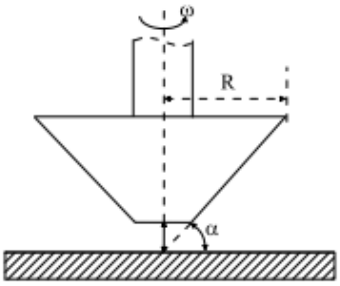

Fig. 2.11 – *Cone and plate geometry.*

In our experiments, we used the Rheometric Scientific (TA) strain-controlled rheometer, with dual transducer (measuring torque range: 0.004-10gr·cm with the first transducer and 0.004-100gr·cm with the second one). For eliminating the solvent evaporation during the measurements, a homemade trap was used which was “sealed” by a low-molecular poly(dimethylsiloxane) of low viscosity (5cP).

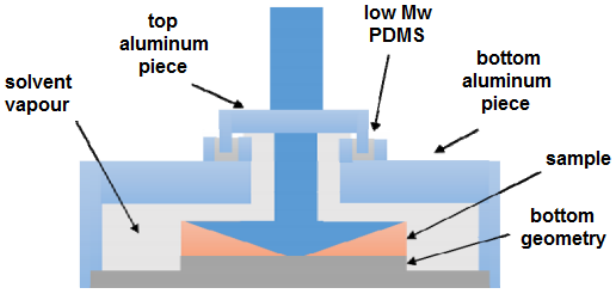

Fig. 2.12 *- Schematic representation of the homemade trap used in measurements with TA ARES strain-controlled rheometer.*

2.6.2 Orthogonal Superposition setup

For Orthogonal Superposition measurements performed at ETH (Zurich), where we used a double-walled Couette flow cell adapted in a strain-controlled rheometer (ARES-G2, TA Instruments) (fig 2.13) (Colombo, Kim et al. 2017). This geometry consists of two motors, one in the horizontal direction and another one in the vertical direction. The horizontal motor performs shear experiments similar to an ordinary Couette geometry, whereas the vertical motor imposes only oscillation in the vertical direction. The horizontal and vertical transducers are separate and housed in the top part of the system. The inner cylinder of the double-walled Couette acts as a reservoir for the sample removing all instabilities arising due to the vertical oscillation. The blue and the hatched light grey regions in fig. 2.13d indicate the volume occupied by the sample. The flow cell is designed to minimize the back-flow of material in the measurement gaps (0.5mm), due to pumping effect caused by the oscillatory motion of the bob in the z direction during orthogonal superposition measurements (Vermant, Moldenaers et al. 1997). To reduce the backflow in the gap, there are openings in the inner wall of the cup, allowing the sample to flow in and out of the large central reservoir during measurements.

The orthogonal storage and loss moduli are calculated by the equations:

$$G' = \frac{1}{A}\left(\frac{F_0}{z_0}\cos\phi - K + (m + \beta A\rho)\omega^2\right) \tag{2.26}$$

and

$$G'' = \frac{1}{A}\left(\frac{F_0}{z_0}\sin\phi - \xi\omega\right) \tag{2.27}$$

where $A = \frac{4\pi h}{\ln\left(\frac{R_b}{R_a}\right)}$ and $\beta = \frac{R_b^2}{2}\left(\frac{\left(\frac{R_b}{R_a}\right)^2 - 1}{2\ln\left(\frac{R_b}{R_a}\right)} - \left(1 + \ln\left(\frac{R_b}{R_a}\right)\right)\right)$ are geometric factors,

whereas R_b is the average radius of the oscillating cylinder, $R_\alpha = R_b - w$ and w is the width of the gap, F_0/z_0 is the force amplitude divided by the height amplitude of the oscillating cylinder and ϕ is the phase difference between the strain input and stress output in the vertical direction. Finally, m,K and ξ are the parameters describing the vertical transducer (Vermant, Moldenaers et al. 1997).

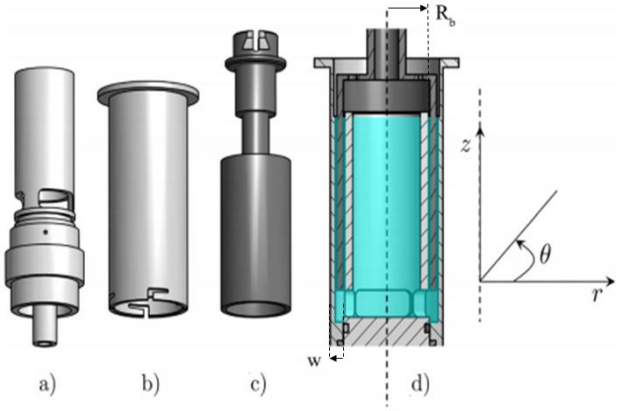

Fig. 2.13 – *Double-wall Couette cell for Orthogonal Superposition Rheometry. a) The inner and b) the outer part of the cup, c) the measuring bob and d) the cross section of the assembled cell in measuring position. The sample filling is presented in blue/light grey with the large reservoir in the center. Adapted from (Colombo, Kim et al. 2017).*

2.7 Laser Scanning Confocal Microscopy

Optical microscopy is widely used in many systems where the domain of interest lies in the submicron to micron range. These include biological systems such as cells or tissue as well as areas of soft physics, such as complex fluids and colloidal dispersions. Since the important length scales are of the order of the wavelength of

visible light, microscopy provides a powerful tool to obtain real-space and real-time information about the complex mechanisms that govern these systems (Wilson 1995).

A laser scanning confocal microscope (LSCM) incorporates the ideas of point-by-point illumination of the sample and elimination of out-of-focus glare (Spring and Inoué 1997, Semwogerere and Weeks 2005). In fig. 2.14 a confocal microscope and its main internal components are presented. Laser light (blue line) is directed by a dichroic mirror towards a pair of mirrors that scan the light in x and y. The light then passes through the microscope objective and excites the fluorescent sample. The fluoresced (light green) light from the sample passes back through the objective and is descanned by the same mirrors used to scan the sample. The light then passes through the dichroic mirror through a pinhole placed in the conjugate focal (hence the term confocal) plane of the sample. This pinhole contributes to the rejection of all the out-of-focus light arriving from the sample. The light that emerges from the pinhole is finally measured by a detector such as a photomultiplier tube (Habdas and Weeks 2002, Prasad, Semwogerere et al. 2007).

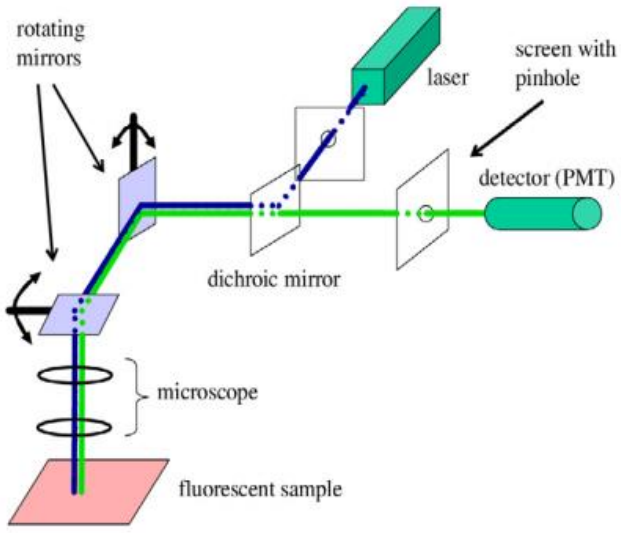

Fig. 2.14 - *Schematic representation of a basic setup of a confocal microscope. The screen with the pinhole lies in the back focal plane of the sample with respect to the objective, thus rejecting most out-of-focus light. The rotating mirrors scan the sample pixel by pixel and the rate-limiting step for obtaining an image. Adapted from (Prasad, Semwogerere et al. 2007).*

In confocal microscopy, there is never a complete image of the sample, because at any instant only one point is observed. Thus, for visualization the detector is attached to a computer, which reconstructs the 2D image plane one pixel at a time. The image created by the confocal microscope is a thin planar region of the sample, which in general is referred to as optical sectioning. Out-of-plane unfocused light has been rejected, resulting in a better-resolved image. Moreover, a 3D reconstruction of the sample can be done by combining a series of such optical sections at different depths.

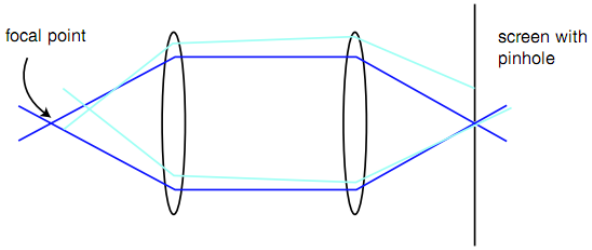

Fig. 2.15 *- Rejection of out-of -focus light. All light from the focal point that reaches the screen is allowed through, whereas light away from the focal point is mostly rejected. Adapted from (Semwogerere and Weeks 2005).*

A confocal microscope has some limitations and often compromises should be done in order to optimize the performance. Similar to a conventional optical microscope, the resolution of a confocal microscope is limited due to diffraction of light (Spring and Inoué 1997). Furthermore, the optical sectioning capability depends strongly on the size of the pinhole. The smaller the size of the pinhole, the less the number of photons that arrive at the detector from the sample, fact that may lead to a reduced signal-to-noise ratio (Wilson 1995). The speed of most confocal microscopes is also limited by the rate at which the mirrors can scan the entire sample plane. Typically this speed can range from 0.1 to 30Hz (Prasad, Semwogerere et al. 2007). Another significant limitation is the choice of fluorophores, which is influenced by several factors. For instance, the used fluorophores should be sensitive enough for the given excitation wavelength and not chemically affect the probed sample, a fact that has influence on the position of the peaks of the excitation and emission spectra (Sheppard and Shotton 1997). A major problem is photobleaching

according to which the used fluorophores fade away (irreversibly) when exposed to excitation light (Chen, Swedlow et al. 1995).

The experiments of this thesis performed by VT-Eye confocal system of VisiTech, equipped by a single mode diode laser of 100mW (emission wavelength λ=488nm), a Nikon eclipse Ti-U inverted microscope used with a 100x oil immersion objective and a scanning head, which consists of an Acousto Optical Deflector (AOD) in x-axis, a standard galvanic mirror in the y-axis and a highly sensitive photomultiplier tube (detector). The use of an AOD provides the ability of ultra-fast scanning (up to 10fps at 1024x1024 resolution) and high resolution confocal image acquisition. The vertical (z) position of the objective is controlled by a piezo-based focusing attachment. Temperature changes of the samples achieved by a homemade cooling/heating device which consists of Peltier elements.

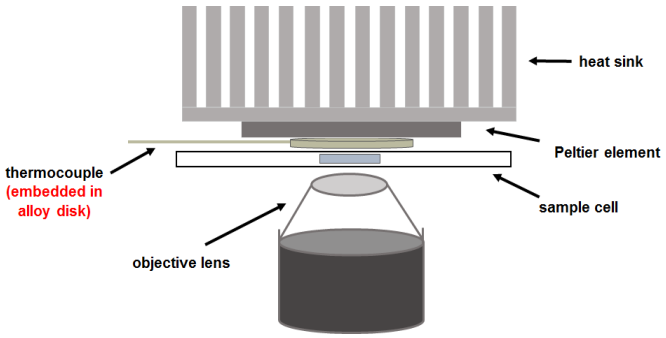

Fig. 2.16 *- Schematic representation of the cooling/heating system used in confocal microscopy.*

2.8 Rheo – Confocal Microscopy

Rheo-Confocal Microscopy constitutes a powerful tool in soft material physics, which provides the opportunity of the study of microstructure of a soft system during rheological measurements. The combination of light microscopy and rheology allows the visualization of the influence of shear and deformation forces on the sample's microstructure. The instrumentation of this technique is quite challenging since the experimental device should combine high resolution, high magnification, real space, time resolved spatial information in three dimensions with simultaneous high resolution mechanical deformations. Precision measurements of the structure and mechanical properties of soft systems require submicron spatial

resolution and nanonewton-meter torque resolution (Dutta, Mbi et al. 2013). These requirements can be fulfilled by combining two independent commercial set-ups, a confocal microscope with a commercial stress-controlled rheometer.

The confocal rheometer system, used for the visualization of samples under shear of this thesis, consists of a stress-controlled MCR302 rheometer of Anton Paar mounted on VT-Eye confocal system of VisiTech described in last paragraph. A custom stainless steel cup is mounted to the rheometer platform and positions a metallic bottom plate that has a slotted opening to provide optical access from below for the inverted microscope. In the slotted opening, a glass cover-slip of the same shape and size is rigidly glued. For the rheological tests we used a measuring system tool in cone-plate geometry from Anton Paar, which is 150mm long in order to reach the coverslip.

This design ensures the autonomous functionality of the two set-ups when joined together and permits their easier disconnection when needed to operate independently. For changing the temperature of the samples we used a homemade cooling/heating device which consists of a water bath.

2.9 Surface charge density determination of charged colloids

The interparticle forces developed between colloids, suspended in a medium, can be either repulsive or attractive. The nature, the range and the balance of these repulsive and attractive interparticle forces characterize the overall stability, structure and dynamics of a colloidal system. Electrostatic repulsive interactions (Coulombic interactions) constitute the physical mechanism in order to stabilize colloidal systems against colloidal aggregation, dispersed in a polar medium, typically water.

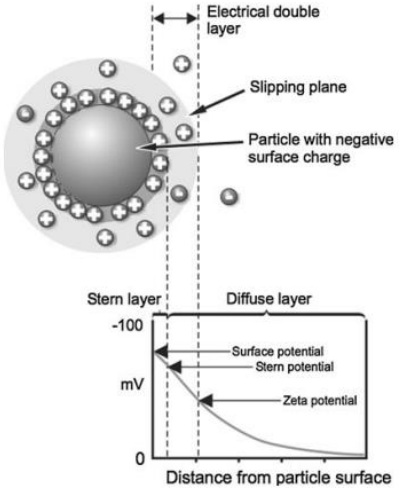

Fig. 2.17 – *Schematic representation of Stern and Diffuse layers. Adapted from (Freire, Domingues et al. 2011)*

Charged colloidal particles contain ionisable groups on their surfaces, some of which dissociate when particles are dispersed in a polar medium. The counterions discharged into the liquid move away from particles in Brownian motion, remaining though in their field of force. The result is an electrical double layer surrounding the particle that consists of a region of counterions strongly bound to its surface, called Stern layer, and a second diffuse outer layer that is comprised of loosely associated ions. As the particles moves, there exists a boundary (slipping plane) between the ions in the diffuse layer that move with the particle and ions that remain with the bulk dispersant. The electrostatic potential ψ at this "slipping plane" boundary is the zeta potential ζ. Zeta potential is therefore a function of the surface charge of the particle and the nature and composition of the surrounding medium (Israelachvili 2011). In the diffuse layer, the variation of potential ψ with distance is connected by the charge density in the system through Poisson's equation (Ghosh):

$$\nabla^2\psi = \frac{d^2\psi}{dx^2} = -\frac{\sigma}{\varepsilon\varepsilon_0} \qquad (2.28)$$

where σ is the surface charge density, ε is the dielectric constant of the medium and ε0 is the permittivity of the free space.

The estimation of the surface charge density σ (ionic conductivity) can be used for the quantification of the range of the Coulombic interaction and the calculation of the Debye screening length κ^{-1} of the particles, which denotes the distance beyond which interactions can be essentially ignored (Benenson, Harris et al. 2006). Based on Poisson's equation and Boltzmann distribution law, Benenson et al. (Benenson, Harris et al. 2006) connected the surface charge with the concentration of ions in the surface of the particle through the equation:

$$\sigma = e\sum_i \mu_i C_i \tag{2.29}$$

where e is the elementary electron charge, μ_i is the ion mobility and C_i is the concentration of i-th type of ion. The Debye screening length is given by the equation:

$$\kappa^{-1} = \left(\varepsilon_0 \varepsilon_r k_B T \Big/ \sum_i (z_i e)^2 C_i \right)^{1/2} \tag{2.30}$$

where ε_0 is the permittivity of free space (vaccum), ε_r is the relative permittivity of the suspended medium, k_B is the Boltzmann constant, T is the absolute temperature of the suspension, e is the elementary charge, z_i is the valence of i-th species of ions of concentration C_i (Israelachvili 2011).

Chapter 3 of this dissertation focuses on the study of aqueous suspensions of PS sulfate-stabilized spheroids. This particles contain three different ionic species: $SO4^{-2}$, H^+ and OH^-. The concentrations of ions H+ and OH- are calculated from the measured pH value as $C_{H^+} = 10^{-pH}$ and $C_{OH^-} = 10^{pH-14}$ respectively. Then, by knowing the mobility of all the mentioned ions $\mu_{H^+} = 3.623 \cdot 10^{-7}\, m^2/sV$, $\mu_{OH^-} = 2.05 \cdot 10^{-7}\, m^2/sV$ and $\mu_{SO_4^{-2}} = 8.29 \cdot 10^{-8}\, m^2/sV$, we use the equation, which relates the ionic conductivity with the concentration of the ions in order to estimate

the only unknown value which is $C_{SO_4^{-2}}$ (Haynes 2014, Saha, Bandyopadhyay et al. 2015).

Experimentally, surface charge density was taken by Zetasizer Nano ZS90 by Malvern Instruments equipped by a red-laser λ=633nm. Zetasizer Nano ZS90 uses a combination of two measurement techniques, Electrophoretic Light Scattering (ELS) and Laser Doppler Velocimetry, in order to measure the velocity of a particle in a medium when an electrical field is applied and then using the viscosity and the dielectric constant of the sample, to quantify the zeta potential and hence the surface charge density.

More specifically, the application of an external voltage causes the charged particles to move towards one of the electrodes; a negative particle moves to the anode and a positive one to the cathode. The moving particles scatter the incident light at a frequency F_2, which is Doppler shifted with respect to the incident frequency F_1. Since the frequency of light is high (10^{14}Hz), the shift in frequency can only be measured by an optical mixing or interferometry. This is done using a pair of mutually coherent laser beams derived from a single source and following similar path lengths. The scattered light from the particles is combined with the reference beam to create intensity variations. At the crossing point of the beams, interference fringes are formed, the spacing of which will give rise to a certain frequency component in the scattered light as a particle passes through the fringes. The value of this frequency component is determined by the mobility of the particles.

Fig. 2.18b shows an example where a reference beam of frequency F_1 is combined with scattered light arising from moving particles. This scattered light has a frequency F_2. Combining the two frequencies together gives rise to a modulated beam due to constructive and destructive effects which has a much smaller, measurable frequency. This “beat” frequency Δf is the difference between F_1 and F_2 and is used to determine the mobility of the particles.

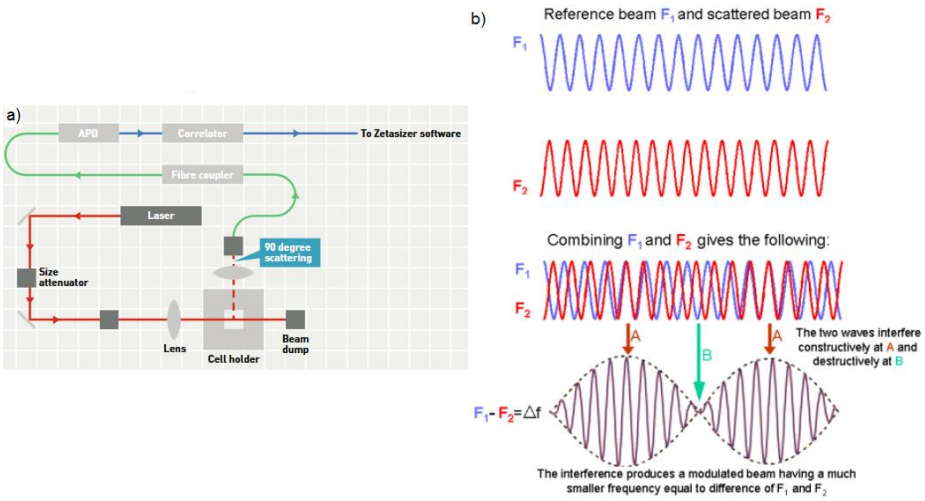

Fig. 2.18 – *a) Schematic representation of components of Zetasizer Nano ZS90 and b) schematic diagram illustrating how the combination of a reference beam (F_1) and a scattered beam (F_2) gives rise to a beat frequency.*

References:

Aberle, L. B., et al. (1998). "Effective suppression of multiply scattered light in static and dynamic light scattering." Applied Optics **37**(27): 6511-6524.

Bartsch, E., et al. (1997). "Multi-speckle autocorrelation spectroscopy—a new strategy to monitor ultraslow dynamics in dense and nonergodic media." Optical Methods and Physics of Colloidal Dispersions: 40-48.

Berne, B. (1976). J. and Pecora, R.," Dynamic Light Scattering, Wiley, New York.

Berne, B. J. and R. Pecora (2000). Dynamic light scattering: with applications to chemistry, biology, and physics, Courier Corporation.

Brown, W. (1993). Dynamic light scattering: the method and some applications, Oxford University Press, USA.

Chen, H., et al. (1995). The collection, processing, and display of digital three-dimensional images of biological specimens. Handbook of biological confocal microscopy, Springer**:** 197-210.

Chu, B. (2007). Laser light scattering: basic principles and practice, Courier Corporation.

Cipelletti, L. and L. Ramos (2005). "Slow dynamics in glassy soft matter." Journal of Physics: Condensed Matter **17**(6): R253.

Cipelletti, L. and D. Weitz (1999). "Ultralow-angle dynamic light scattering with a charge coupled device camera based multispeckle, multitau correlator." Review of scientific instruments **70**(8): 3214-3221.

Colombo, G., et al. (2017). "Superposition Rheology and Anisotropy in Rheological Properties of Sheared Colloidal Gels." Journal of Rheology.

Dutta, S., et al. (2013). "Development of a confocal rheometer for soft and biological materials." Review of scientific instruments **84**(6): 063702.

Einstein, A. (1910). "Theory of the opalescence of homogeneous and of mixed liquids in the neighborhood of the critical region." Ann. Physik **33**: 1275-1298.

Ewoldt, R. H., et al. (2008). "New measures for characterizing nonlinear viscoelasticity in large amplitude oscillatory shear." Journal of Rheology (1978-present) **52**(6): 1427-1458.

Ferry, J. D. (1980). Viscoelastic properties of polymers, John Wiley & Sons.

Freire, J. M., et al. (2011). "Using zeta-potential measurements to quantify peptide partition to lipid membranes." European Biophysics Journal **40**(4): 481-487.

Ghosh, P. "Electrostatic Double Layer Force: Part II."

Habdas, P. and E. R. Weeks (2002). "Video microscopy of colloidal suspensions and colloidal crystals." Current Opinion in Colloid & Interface Science **7**(3): 196-203.

Haynes, W. M. (2014). CRC handbook of chemistry and physics, CRC press.

Hyun, K., et al. (2011). "A review of nonlinear oscillatory shear tests: Analysis and application of large amplitude oscillatory shear (LAOS)." Progress in Polymer Science **36**(12): 1697-1753.

Israelachvili, J. N. (2011). Intermolecular and surface forces, Academic press.

Jacob, A. R., et al. (2014). "Large amplitude oscillatory shear of supramolecular materials." Journal of non-newtonian fluid mechanics **206**: 40-56.

Koppel, D. E. (1972). "Analysis of macromolecular polydispersity in intensity correlation spectroscopy: the method of cumulants." The Journal of Chemical Physics **57**(11): 4814-4820.

Maret, G. and P. Wolf (1987). "Multiple light scattering from disordered media. The effect of Brownian motion of scatterers." Zeitschrift für Physik B Condensed Matter **65**(4): 409-413.

Mason, T. and D. Weitz (1995). "Linear viscoelasticity of colloidal hard sphere suspensions near the glass transition." Physical review letters **75**(14): 2770.

Mewis, J. and N. J. Wagner (2012). Colloidal suspension rheology, Cambridge University Press.

Overbeck, E., et al. (1997). "Approaching the limits of multiple scattering decorrelation: 3D light-scattering apparatus utilising semiconductor lasers." Optical Methods and Physics of Colloidal Dispersions: 117-120.

Pine, D., et al. (1988). "Diffusing wave spectroscopy." Physical review letters **60**(12): 1134.

Pine, D., et al. (1990). "Diffusing-wave spectroscopy: dynamic light scattering in the multiple scattering limit." Journal de Physique **51**(18): 2101-2127.

Poulos, A. S., et al. (2013). "Flow of concentrated solutions of starlike micelles under large-amplitude oscillatory shear." Rheologica Acta **52**(8-9): 785-800.

Prasad, V., et al. (2007). "Confocal microscopy of colloids." Journal of Physics: Condensed Matter **19**(11): 113102.

Pusey, P. (1991). Liquids, freezing and the glass transition, North-Holland: Amsterdam.

Pusey, P. (1999). "Suppression of multiple scattering by photon cross-correlation techniques." Current Opinion in Colloid & Interface Science **4**(3): 177-185.

Pusey, P. and R. Tough (2002). Neutrons, X-Rays and Light: Scattering Methods Applied to Soft Condensed Matter; Lidner, P., Zemb, T., Eds, North Holland, Elsevier: Amsterdam.

Rogers, S. A., et al. (2011). "A sequence of physical processes determined and quantified in LAOS: Application to a yield stress fluid." Journal of Rheology (1978-present) **55**(2): 435-458.

Russel, W. B., et al. (1989). Colloidal dispersions, Cambridge university press.

Saha, D., et al. (2015). "Dynamic light scattering study and DLVO analysis of physicochemical interactions in colloidal suspensions of charged disks." Langmuir **31**(10): 3012-3020.

Schärtl, W. (2007). Light scattering from polymer solutions and nanoparticle dispersions, Springer Science & Business Media.

Schätzel, K. (1991). "Suppression of multiple scattering by photon cross-correlation techniques." Journal of modern optics **38**(9): 1849-1865.

Schmitz, K. S. and G. D. Phillies (1991). "An introduction to dynamic light scattering by macromolecules." Physics Today **44**: 66.

Semwogerere, D. and E. R. Weeks (2005). "Confocal microscopy." Encyclopedia of Biomaterials and Biomedical Engineering **23**: 1-10.

Sheppard, C. and D. Shotton (1997). "Confocal fluorescence microscopy." Confocal Laser Scanning Microscopy; Springer-Verlag New York Inc.: New York: 61-70.

Sierou, A. and J. F. Brady (2001). "Accelerated Stokesian dynamics simulations." Journal of Fluid Mechanics **448**: 115-146.

Spring, K. and S. Inoué (1997). Video microscopy: the fundamentals, New York: Plenum Press.

Urban, C. (1999). Development of fiber optic based dynamic light scattering for a characterization of turbid suspensions, Herbert Utz Verlag.

Urban, C. and P. Schurtenberger (1998). "Characterization of turbid colloidal suspensions using light scattering techniques combined with cross-correlation methods." Journal of colloid and interface science **207**(1): 150-158.

Urban, C. and P. Schurtenberger (1998). Dynamic light scattering in turbid suspensions: An application of different cross-correlation experiments. Trends in Colloid and Interface Science XII, Springer**:** 61-65.

Vermant, J., et al. (1997). "Orthogonal superposition measurements using a rheometer equipped with a force rebalanced transducer." Review of scientific instruments **68**(11): 4090-4096.

Weitz, D., et al. (1992). Principles and applications of diffusing-wave spectroscopy. Structure and Dynamics of Strongly Interacting Colloids and Supramolecular Aggregates in Solution, Springer**:** 731-748.

Weitz, D. A., et al. (1993). "Diffusing-wave spectroscopy: The technique and some applications." Physica Scripta **1993**(T49B): 610.

Wilson, T. (1995). The role of the pinhole in confocal imaging system. Handbook of biological confocal microscopy, Springer**:** 167-182.

Zivkovic, V., et al. (2008). "Particle dynamics in a dense vibrated fluidized bed as revealed by diffusing wave spectroscopy." Powder Technology **182**(2): 192-201.

Chapter 3

Structure and dynamics of ellipsoidal particles in dilute regime

Polarized (DLS) and Depolarized Light Scattering (DDLS) were employed to study the structure and dynamics of randomly oriented prolate ellipsoids of different aspect ratios suspended in aqueous solutions. The experiment yielded the size and shape distribution, and hydrodynamic properties through the estimation of translational and rotational diffusion coefficients. The range of electrostatic interparticle interactions was inferred by the second virial coefficient measured in both low ionic strength suspensions (salt-free solutions) and the presence of monovalent salt ions of (KCl at C_s=0.5mM).

3.1 Introduction

Anisotropic particles are extensively used in many biological and industrial applications. The non-spherical shape, either being simpler or more complex, impels the particles to diffuse in a different way compared to spheres, leading to coupling of translational to rotational motion. Therefore, the deep understanding of the mechanism of diffusion of anisotropic colloids, through the investigation of hydrodynamic properties of anisotropic particles is crucial. The physics behind particle anisotropy was firstly explored by Perrin et al. (Perrin 1934, Perrin, Bruhat et al. 1936) more than 80 years ago, who thoroughly studied dynamics of prolate and oblate ellipsoids in infinite-dilution limit. Afterwards, the translational and rotational diffusion coefficients of various colloidal anisotropic particles such as ellipsoids (Matsuoka, Morikawa et al. 1996, Quirantes, Ben-Taleb et al. 1996), rods (Van Bruggen, Lekkerkerker et al. 1998, Lehner, Lindner et al. 2000, De Souza Lima, Wong et al. 2003, Koenderink, Aarts et al. 2003, Kroeger, Deimede et al. 2007, Brogioli, Salerno et al. 2009) and platelets (Jabbari-Farouji, Eiser et al. 2004), have thoroughly studied either by experiment (Flamberg and Pecora 1984, Kanetakis and Sillescu 1996, Phalakornkul, Gast et al. 2000, Koenderink, Zhang et al. 2003, Hoffmann, Lu et al. 2008, Hoffmann, Wagner et al. 2009, Plum, Steffen et al. 2009, Shetty, Wilkins et al. 2009), simulation (Heyes, Nuevo et al. 1998), and theory (Pecora 1972, Hu and Zwanzig 1974, Aragon and Pecora 1977, Takagi and Tanaka 2001, Nägele 2002).

An important category of anisotropic colloids is ellipsoidal particle which can be either prolate (ellipsoids which consist of a long major semi-axis α and a short minor semi-axis b, with $\rho=\alpha/b>1$) or oblate (ellipsoids which consist of a short major semi-axis α and a long minor semi-axis b, with $\rho=\alpha/b<1$). Hydrodynamic properties of randomly oriented prolate ellipsoids has been the subject of numerous experimental studies using light scattering and microscopy. Dubin et al. estimated the shape of enzyme lysozyme molecules by combining the rotational and the translational diffusion coefficients extracted by polarized and depolarized scattered light using high resolution Fabry-Perot interferometers and considering a hydrodynamic equivalent of a prolate ellipsoid in revolution (Dubin, Clark et al. 1971). Quirantes et

al. employed depolarized light scattering for the determination of the particle size and shape and the study of rotational diffusion of ellipsoidal hematite (α-Fe_2O_3) particles (Quirantes, Ben-Taleb et al. 1996). Moreover, Matsuoka et al. used polarized and depolarized light scattering for the coupling of translational and rotational motions of electrostatically charged polystyrene latex spheroids, whose size and shape defined by Transmission Electron Microscopy (TEM) (Matsuoka, Morikawa et al. 1996). Dai et al. employed depolarized light scattering for exploring the time dependence of the size, shape and concentration of ordered ellipsoidal polystyrene-polyisoprene diblock copolymer grains (Dai, Balsara et al. 1996). Bantchev et al. also used depolarized light scattering for the study of particle size and dynamics of dilute solutions of polytetrafluoroethylene (PTFE) latex spheroids in glycerin/water mixture, which present strong depolarization signal mainly due to optically anisotropy of the partially crystalline PTFE material (Bantchev, Russo et al. 2006). Han et al. used digital video microscopy for investigating the Brownian motion of isolated PMMA ellipsoids in water and elucidating the effects of coupling between translational and rotational motion (Han, Alsayed et al. 2006, Han, Alsayed et al. 2009).

In this work, we present the study of size and shape distribution of randomly oriented prolate ellipsoids of various aspect ratios and the estimation of hydrodynamic properties through the light scattering technique. The new contribution of this study is the investigation of the dependence of ellipsoids' concentration on both polarized and depolarized scattered intensity and the estimation of the interparticle interactions at both low and high ionic strength aqueous suspensions.

3.2 Materials

Prolate ellipsoidal particles of various aspect ratios are prepared by uniaxial stretching of monodisperse polystyrene (PS) CML latex 0.4μm spheres according to the Keville et al. technique (Keville, Franses et al. 1991, Coertjens, Moldenaers et al. 2014). The spheroids are suspended in nano-purified water produced by a Milli-Q

system. In this chapter, PS latex spheres and spheroids of various aspect ratios (1.8:1, 2.3:1, 3:1 and 6.9:1) were investigated in dilute regime.

The spheroid systems studied are stabilized in aqueous suspension by Coulombic repulsive interactions, which dominate over Van der Waals attractive ones and prevent colloidal aggregation. As we have already discussed, the range of the Coulombic interaction can be quantified by estimating the surface charge densities σ (ionic conductivity) and the Debye screening length κ^{-1} of the particles, which denotes the distance beyond which interactions can be essentially ignored (Benenson, Harris et al.). The ionic conductivity measured by Zetasizer Nano ZS90 by Malvern Instruments equipped by a red-laser λ=633nm. Zetasizer Nano ZS90 uses a combination of two measurement techniques, Electrophoresis and Laser Doppler Velocimetry, in order to extract surface charge densities.

Benenson et al. (Benenson, Harris et al. 2006) introduced the relation between the surface charge density and concentration of ions in the surface of the particle:

$$\sigma = e\sum_i \mu_i C_i \tag{3.1}$$

where e is the elementary electron charge, μ_i is the ion mobility and C_i is the concentration of i-th type of ion. The Debye screening length is given by the equation:

$$\kappa^{-1} = \left(\varepsilon_0 \varepsilon_r k_B T \Big/ \sum_i (z_i e)^2 C_i \right)^{1/2} \tag{3.2}$$

where ε_0 is the permittivity of free space (vaccum), ε_r is the relative permittivity of the suspended medium, k_B is the Boltzmann constant, T is the absolute temperature of the suspension, e is the elementary charge, z_i is the valence of i-th species of ions of concentration C_i (Israelachvili 2011).

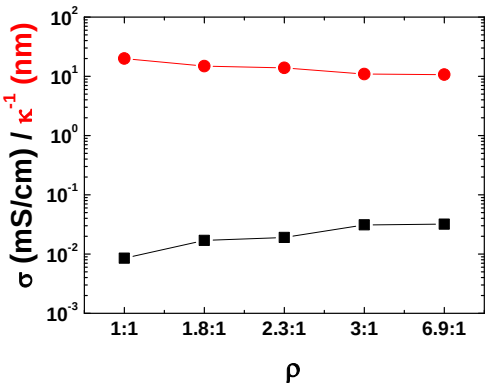

Fig. 3.1 *- Measured ionic conductivity and calculated values for Debye screening length of PS ellipsoids of various aspect ratios (ρ=1.8, 2.3, 3 and 6.9).*

Fig. 3.1 shows the ionic conductivity σ measured for suspensions of various aspect ratios and the estimated Debye screening length κ^{-1}. Increasing the aspect ratio, the κ^{-1} decreases denoting the redistribution of the initial amount of electrostatic charges in the surface of the particles depending on the different aspect ratio.

3.3 Characterization methods

The particles were investigated in dilute regime, using various experimental techniques, in order to investigate the size and shape distribution, dynamic properties and the interactions between the particles.

3.3.1 Field Emission Scanning Electron Microscopy (FESEM)

Microscopy is the only method in which the individual particles are directly observed and measured (Allen 2013). Therefore, FESEM used for collecting sufficient statistics for structural and shape characterization of the particles and estimating the polydispersity of the spheroids obtained by stretching procedure.

3.3.2 Photon Correlation Spectroscopy

3.3.2.1 Static Light Scattering (SLS)

The second virial coefficient is a thermodynamic parameter that provides information about intermolecular interactions. Positive values of the second virial coefficient A_2 indicate predominantly repulsive interparticle interactions, whereas negative values reflect predominantly attractive interactions (George and Wilson 1994, Neal, Asthagiri et al. 1999, Saluja, Fesinmeyer et al. 2010).

In order to obtain experimentally the second virial coefficient we used static light scattering technique (SLS). The SLS data were processed by the classical Zimm treatment (Zimm 1948):

$$\frac{Kc}{R_{VV}} = \frac{1}{M_w} + 2A_2c \tag{3.3}$$

where M_w is the solute molecular weight (g/mol), c is the solute concentration (g/ml), R_{vv} is the reduced scattered intensity or the Rayleigh ratio which depends on the geometry of the instrument (Morawetz 1973), A_2 the second virial coefficient (mol·ml/g^2) and K is a constant defined by the optical properties of the system:

$$K = \frac{4\pi^2 n_0^2}{N_A \lambda^4}\left(\frac{dn}{dc}\right)^2 \tag{3.4}$$

where N_A is the Avogadro's number, n_0 is the refractive index of the solvent, (dn/dc) is the refractive index increment for the particle/solvent pair, λ the wavelength of the incident laser light in vacuum (Utiyama 1972, Wilson 2003). The procedure for determining A_2 requires the measurement of the intensity of scattered light of the suspension, normalized by the power of the laser beam, the solvent used, the particle concentration and the scattering strength of particles in a specific solvent.

Once the experimental data are plotted according to the equation (3.3), from the values of the slope and the intercept and the molecular weight (M_w =2.13·10^{10}g/mol) we can extract the second virial coefficient A_2.

3.3.2.2 Polarized (DLS) and Depolarized (DDLD) Dynamic Light Scattering

When a suspension of particles of infinite dilution is illuminated by a coherent light source, translational, rotational and internal motions lead to fluctuations of the intensity of the scattered light (Gilányi, Varga et al. 2000, Bowen 2002, Bantchev, Russo et al. 2006, Tinke, Govoreanu et al. 2006, Akbari, Tavandashti et al. 2011). Then, the signal is decimated into intervals and time correlated to extract the intensity autocorrelation function $g^{(2)}(q,\tau)$, which is directly related to the electric field autocorrelation function $g^{(1)}(q,\tau)$ and the normalized correlation function $C(q,\tau)$ through the Siegert relation (Berne 1976, Schärtl 2007):

$$g^{(2)}(q,\tau) = 1 + g^{(1)}(q,\tau)^2 = 1 + f^* \left| C(q,\tau) \right|^2 \qquad (3.5)$$

where f^* is the coherence factor. All the light scattering measurements carried out with ALV-5100 correlator and goniometer, equipped by a 130mW/532nm wavelength He-Ne laser at temperature 20°C, where f^*=0.36.

In DLS the incident light is usually vertically polarized (VV). For spheres, the scattered light is dominated by the vertically polarized contribution. To the contrary, non-spherical shape of spheroids creates optical anisotropy and then the scattered light contains horizontally polarized (VH) contribution as well (De Souza Lima, Wong et al. 2003, Bantchev, Russo et al. 2006, Hoffmann, Wagner et al. 2009). The horizontally polarized contribution is captured by Depolarized Dynamic Light Scattering (DDLS), where the scattered light is measured through a horizontally oriented polarizer.

In the dilute regime where interactions between particles are negligible, DLS technique yields information about the translational dynamics of the optically anisotropic particles in solution by measuring the translational diffusion coefficient,

whereas in DDLS method translational and rotational dynamics are coupled between them by measuring the rotational diffusion coefficient (internal dynamics) as well. For anisotropic particles containing a rotation axis of higher symmetry (e.g. ellipsoid in revolution or rod-like molecule), the correlation function for polarized (VV) and depolarized (VH) geometries is given by the equations respectively:

$$g_{VV}^{(1)}(q,\tau) = Na^2 \exp\left(-D_T q^2 \tau\right) + \frac{4}{3} N\beta^2 \exp\left[-\left(D_T q^2 + 6\Theta_r\right)\tau\right] \quad (3.6)$$

and

$$g_{VH}^{(1)}(q,\tau) = N\beta^2 \exp\left[-\left(D_T q^2 + 6\Theta_r\right)\tau\right] \quad (3.7)$$

where N is the number of particles in the scattering volume, $a = \frac{1}{3}\left(a_{II} + 2a_{\perp}\right)$ is the isotropic part of the polarizability of the molecule that takes into consideration the parallel and perpendicular to the molecular symmetry axis component of the polarizability, while $\beta = a_{II} - a_{\perp}$ is the anisotropic part of the polarizability (optical anisotropy). The first term of the polarized correlation function $g_{VV}^{(1)}(q,\tau)$ corresponds to the isotropic fluctuations of the polarizability tensor, which is proportional to α^2 and the second to the contribution of the depolarized scattering ($4/3 I_{VH}$). Thus, the $g_{VV}^{(1)}(q,\tau)$ depends on both the polarized ($\Gamma_{VV} = D_T q^2$) and the depolarized component ($\Gamma_{VH} = D_T q^2 + 6\Theta_r$). However, the depolarized correlation function $g_{VH}^{(1)}(q,\tau)$ depends only on the rotation of the anisotropic molecule, since the translational one is eliminated (Alms, Bauer et al. 1973, Berne 1976, Brown 1993).

Perrin related the hydrodynamic properties with geometrical size and shape of an ellipsoidal particle by introducing a hydrodynamic model, which assumes that the spheroid may be treated as a macroscopic particle dispersed in a continuous medium. Moreover it assumes “stick boundary conditions”, which stipulates that at

the surface of the particle the solvent velocity is zero relative to the particle velocity. Thus, he determined the translational diffusion coefficient for ellipsoidal particles to be (Perrin 1934, Perrin, Bruhat et al. 1936, Berne 1976, Aragon and Pecora 1977):

$$D_T = \frac{k_B T}{6\pi\eta a} G(\rho) \tag{3.8}$$

where α is the major semi-axis, b the minor semi-axis, ρ is the axial ratio (ρ=α/b), η is the shear viscosity of the solution and G(ρ) is a function of the axial ratio which for prolate ellipsoids (ρ>1), has the form:

$$G(\rho) = \left(1 - 1/\rho^2\right)^{-1/2} \ln\left[\rho\left(1 + \left(1 - 1/\rho^2\right)^{1/2}\right)\right] \tag{3.9}$$

As we already mentioned, DDLS technique studies the rotational motion of anisotropic particles in solution. For an ellipsoid of revolution of major semi-axis α and minor semi-axis b, Perrin has shown that the rotational diffusion coefficient characterizing the rotation of the symmetry axis is (Matsuoka and Ise , Perrin 1934, Perrin, Bruhat et al. 1936, Berne 1976, Charles and Johnson Jr 1981, Chonde and Krieger 1981, Nagy and Keller 1989, Brown 1993, Ho, Ottewill et al. 1993):

$$\Theta_r = \frac{3k_B T}{16\pi\eta a^3}\left[\frac{\left(2 - 1/\rho^2\right)G(\rho) - 1}{1 - 1/\rho^4}\right] \tag{3.10}$$

3.4 Results - Discussion

3.4.1 Particle Characterization

Figure 3.2a depicts the Field Emission Scanning Electron Microscopy (FESEM) image of the initial PS latex spheres, whereas images of Fig. 3.2b-d depict the stretched spheroids. Through image analysis of a large amount of 2D images of FESEM we extracted a representative distribution of the aspect ratio of the ellipsoids, where we found that the PS latex spheres are quite monodisperse.

Moreover, the higher the aspect ratio of the spheroids the higher the polydispersity of the aspect ratio (Table 3.a).

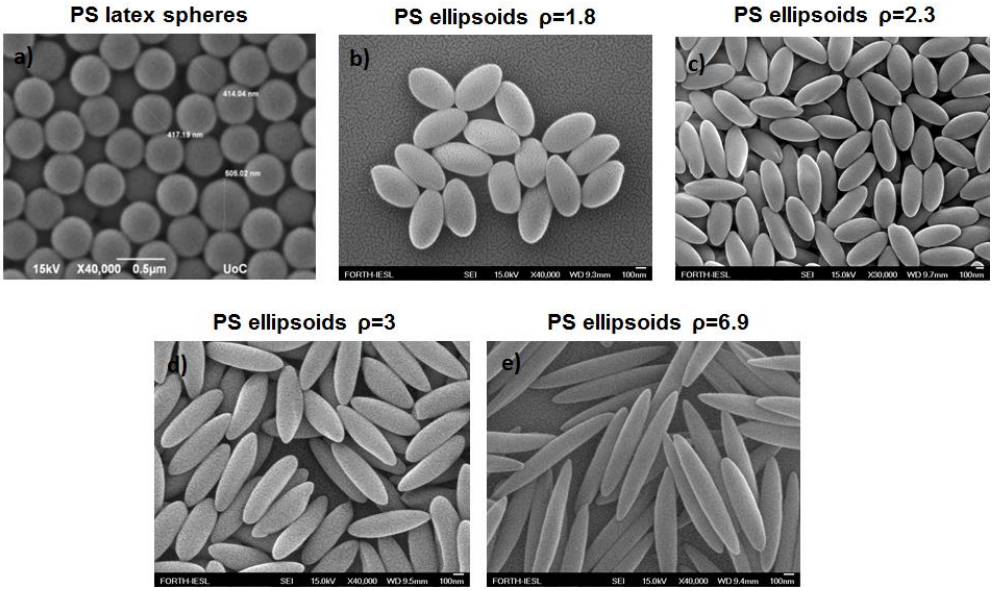

Fig. 3.2 – *Typical FESEM images for a) PS CML latex spheres (Invitrogen), PS ellipsoids for aspect ratios b) 1.8, c) 2.3, d) 3 and e) 6.9.*

FESEM						DLS				
ρ_{FESEM}	*a(nm)*	*b(nm)*	*PD (%)*	$D_{T\ FESEM}$ (10^{-8} cm2/s)	$\Theta_{r\ FESEM}$ (s^{-1})	ρ_{DLS}	*a(nm)*	*b(nm)*	$D_{T\ DLS}$ (10^{-8} cm2/s)	$\Theta_{r\ DLS}$ (s^{-1})
1	200	200	4	1.08	-	1	200	200	1.04	-
1.8	320	177	11	0.91	9.5	1.97	349	177	0.99	7.7
2.3	375	163	12	0.92	8	2.4	393	163	0.91	5.8
3	414	138	13	0.95	6.6	3.3	454	138	0.94	6.4
6.9	773	112	16	0.75	2.2	6.69	750	112	0.74	3

Table 3.a – *Aspect Ratio values ρ, sizes a and b of the semi-axis, polydispersity, translational diffusion coefficient and rotational diffusion coefficient determined by FESEM and the same properties determined by dynamic light scattering.*

Table 3.a summarizes the characteristics values for various aspect ratios extracted both by FESEM and light scattering; the aspect ratio ρ, the long major semi-axis α and the short minor semi-axis b and the polydispersity. The translational and rotational diffusion coefficients are also presented which were estimated by Perrin's formulas for characteristics both obtained from FESEM and light scattering.

The light scattering values reported in table 3.a resulted from the analysis of the experimental data presented afterwards.

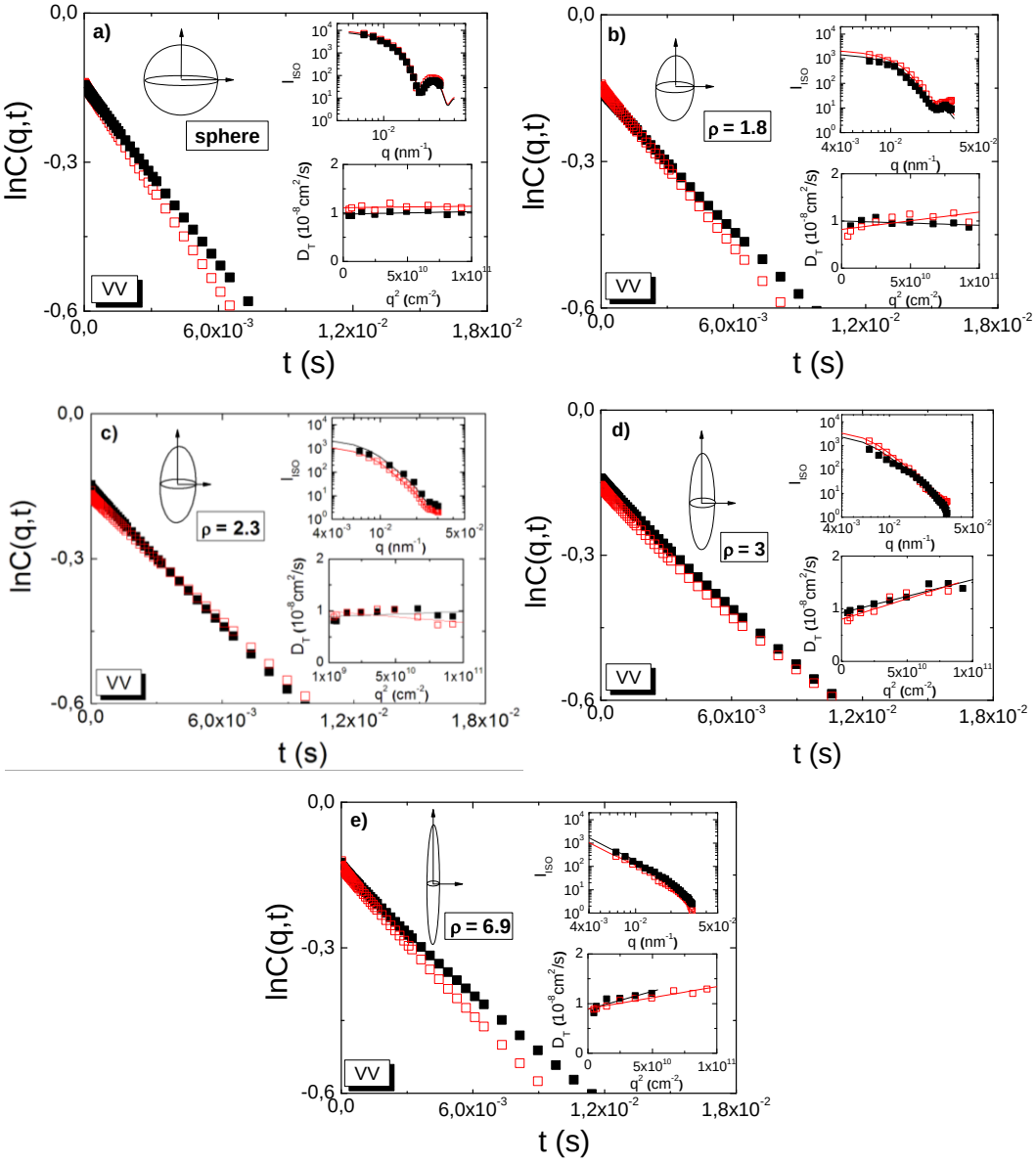

Fig. 3.3 *- Normalized intensity autocorrelation functions of the polarized (VV) scattered light in angle 30° (q=0.00815nm^{-1}) for aspect ratios a) sphere, b) 1.8, c) 2.3, d) 3 and c) 6.9 for mass concentration c=6.3·10^{-7}g/ml. Black full symbols correspond to salt-free solutions, whereas red open symbols to solutions with salt concentration 0.5mM of KCl.*

Upper inset: Normalized scattered intensity as a function of scattering vector q. Solid lines correspond to fittings with form factor theory for prolate ellipsoids. Lower inset: Diffusion coefficient for salt-free solutions (black full symbols) and salt solutions (red open symbols).

In fig. 3.3, we present the experimental data for polarized (VV) DLS measurements for the same concentration of both salt-free and salt-present dilute suspensions ($c=6.3\cdot10^{-7}$g/ml) for the PS latex sphere and the four aspect ratios of PS spheroids (ρ=1.8, 2.3, 3 and 6.9). The analysis which used for extracting the normalized autocorrelation functions from the experimental data is the cumulant analysis (first cumulant) discussed in chapter two (Koppel 1972, Berne 1976, Berne and Pecora 2000), where it is obvious that dynamics between salt-free and salt solutions dynamics are quite similar, but not identical. This means that although the concentration in both cases is dilute enough to be described as a system where interaction can be neglected, there are still residual interactions that affect the dynamics due to long-range Coulombic forces.

The experimental data of the polarized scattered intensity for sphere and aspect ratio ρ=1.8 were fitted with the theoretical Form Factor for homogeneous spheres (Pedersen 1997):

$$F(q,R)=\frac{4\pi}{3}R^3\frac{3(\sin(qR)-qR\cos(qR))}{(qR)^3} \tag{3.11}$$

where q is the scattering vector and R is the radius of the sphere) .

For aspect ratios ρ=2.3 and 3 we used the theoretical Form Factor formula for prolate ellipsoids of revolution of major semi-axis α and minor semi-axis b (Zhao, Pearce et al. 1995):

$$F(q)=\frac{9\pi}{2}\int_0^{\pi/2}\frac{\left[J_{3/2}(u)\right]^2}{u^3}\cos(\theta)d\theta \tag{3.12}$$

where $u=qa\left(\cos^2(\theta)+\frac{b^2}{a^2}\sin^2(\theta)\right)^{1/2}$ and $J_{3/2}(u)$ is the 3/2-order Bessel function: $J_{3/2}(u)=\left(\frac{2u}{\pi}\right)^{1/2}\left(\frac{\sin(u)}{u^2}-\frac{\cos(u)}{u}\right)$.

For highest measured aspect ratio ρ=6.9, we used the theoretical Form Factor for cylinders of revolution of diameter 2R and height 2H:

$$F(q)=\int_0^{\pi/2}\frac{\sin^2\left(qH\cos(\theta)\right)}{q^2H^2\cos^2(\theta)}\frac{4J_1^2\left(qR\sin(\theta)\right)}{q^2R^2\sin^2(\theta)}\sin(\theta)d\theta \qquad (3.13)$$

(Fournet 1951, Guiner, Fournet et al. 1955). In all probed cases, we observe that there is consistency between theory and experiments.

For the PS latex spheres, the translational diffusion coefficient for both salt-free and salt-present solutions is q-independent, as expected for suspensions of infinite dilution. For aspect ratios ρ=1.8 and 2.3, D_T for low ionic strength solutions is purely q-independent, while in the presence of salt we observe a slight deviation from q-independency denoting the impact of screening the repulsive interactions. At higher aspect ratios (ρ=3 and 6.9) for salt-free dispersions, the translational diffusion coefficient shows a small q-dependency which is slightly more prominent at suspensions with salt, reflecting the creation of small agglomerates due to screening of electrostatic interactions.

As we already mentioned, in DLS experiments the non-spherical shape of spheroids creates optical anisotropy, with the scattered light containing both vertically and horizontally polarized contributions. Fig. 3.4 depicts the normalized autocorrelation functions of the electric field of the depolarized scattered light at angle 30^o for salt-free and salt-present solutions of low concentration ($c=6.3\cdot10^{-7}$g/ml) for four different aspect ratios of prolate ellipsoids (ρ=1.8, 2.3, 3 and 6.9). For aspect ratio ρ=1.8, the Brownian motion for the salt solution is slightly faster than the samples without salt, corresponding to slightly smaller particle size which is attributed to the screening of strong electrostatic interactions. However, the relaxation of the normalized autocorrelation functions of salt-present suspensions for the aspect ratios ρ=2.3, 3 and 6.9 is slightly slower denoting the existence of small agglomerates (doublets and triplets) after the addition of KCl.

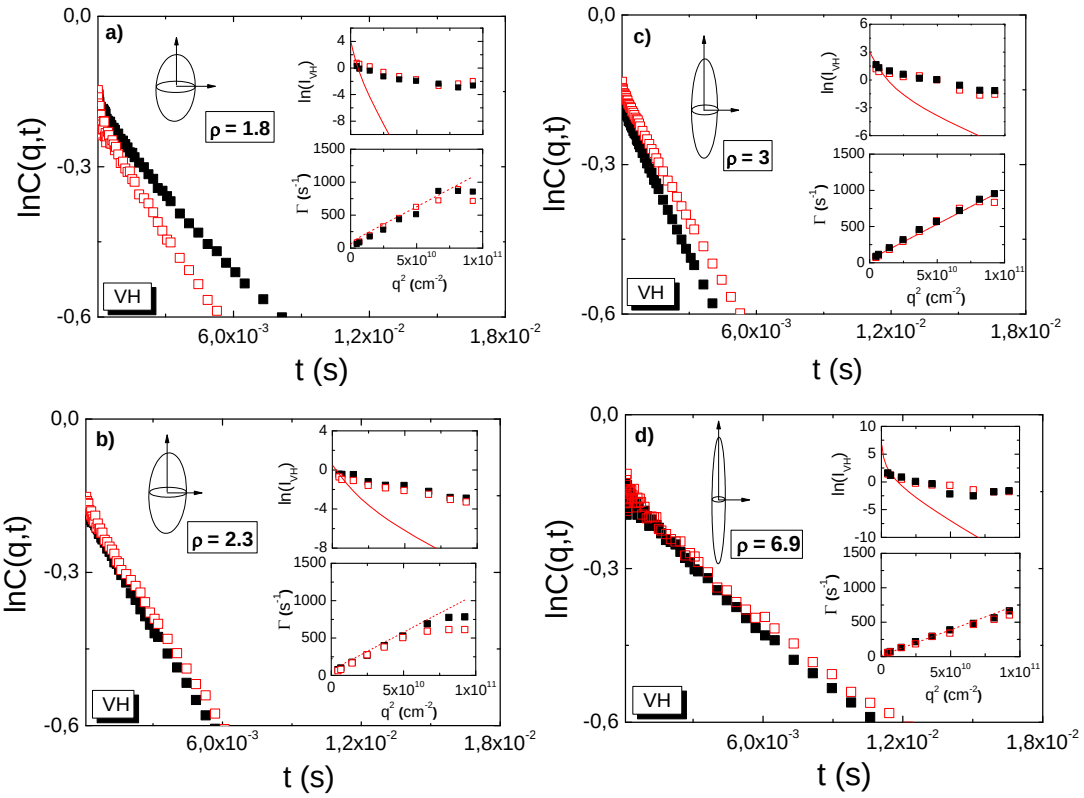

Fig. 3.4 *- Normalized field autocorrelation functions of the depolarized (VH) scattered light at angle 30° (q=0.00815nm^{-1}) for various aspect ratios a) 1.8, b) 2.3, c) 3 and d) 6.9 for mass concentration c=6.3·10^{-7}g/ml. Black full symbols correspond to salt-free solutions, whereas red open symbols to solutions with salt concentration 0.5mM of KCl.*

Upper inset: Normalized scattered intensity as a function of scattering vector q. Red solid line corresponds to form factor for prolate ellipsoids for specific ρ taking into consideration L the length of the major semi-axis, whereas W the length of the minor one. Lower inset: Relaxation rate as a function of q^2 for various aspect ratios for salt-free and salt solutions. Dash lines depict the theoretical relaxation rate taking into consideration the theoretical values of D_T and Θ_r for the specific ρ.

The depolarized scattered intensity experimental data of fig 3.4 were fitted by Born approximation for depolarized scattered intensity in single scattering limit, I(θ) for randomly oriented prolate ellipsoids for the specific aspect ratios (Stein and Wilson 1962, Newstein, Garetz et al. 1995, Dai, Balsara et al. 1996):

$$I(\theta) = K\phi W^2 L\left[C(\theta) + D(\theta)\right] \qquad (3.14)$$

where K is an optical constant, ϕ is the volume fraction occupied by ellipsoids, L is the length along the optical axis, W the diameter perpendicular to the optical axis, and functions C(θ) and D(θ) are given by:

$$C(\theta)=\exp\left[-\frac{q^2W^2}{4}\right]\int_0^{\pi} da\sin^5(a)\exp\left[-\beta(a)\right]I_0\left[\beta(a)\right] \tag{3.15}$$

$$D(\theta)=-\exp\left[-\frac{q^2W^2}{4}\right]\int_0^{\pi} da\sin^5(a)\exp\left[-\beta(a)\right]I_1\left[\beta(a)\right] \tag{3.16}$$

where $q=4\pi\sin(\theta/2)/\lambda$, $\beta(a)=(q^2W^2/8)\left[L^2/W^2-1\right]\sin^2(a)$ and I_m is the modified Bessel function of order m (Dai, Balsara et al. 1996). We observe that the approximation for the depolarized scattered intensity of randomly oriented prolate ellipsoids fails to describe the experimental data.

Plotting the relaxation rate Γ versus q^2, the rotational diffusion coefficient Θ_r can be determined from the intercept $q^2\rightarrow 0$ and the translational diffusion coefficient D_T from the slope of the curve ($\Gamma=D_Tq^2+6\Theta_r$) (Berne and Pecora 2000). For both salt-free and salt solutions of aspect ratios ρ=1.8 and 2.3, the theory overestimates the rotational diffusivity Θ_r due to charge interactions. However, for salt-free solutions of ρ=3 and 6.9, the decay rate is completely consistent with the theoretical values, whereas in salt-suspension the rate is slightly lower, due to the screening of the Coulombic interactions that lead to small agglomerates (doublets and triplets) and decrease of the overall rotational diffusivity. Furthermore, for all aspect ratios studied (ρ=1.8, 2.3, 3 and 6.9), in both salt-free and salt suspensions, at q=0.0285nm^{-1} and q=0.0304 nm^{-1} there is divergence of the trend of the relaxation rate which constitutes polydispersity effect (Morawetz 1973).

Fig. 3.5a and 3.5b shows the translational and rotational diffusion coefficient determined experimentally and extracted by theory assuming the size from FESEM for both salt-free and salt solutions of all the probed aspect ratios. We observe that there is satisfactory consistency between experimental data and theoretical

predictions, except for the rotational diffusion coefficient of ρ=1.8 and 2.3, where the values of experimental Θ_r are smaller compared to theory.

Fig. 3.5c and 3.5d depict the polarized I_{ISO} and the depolarized I_{VH} scattered intensities at q→0 respectively, as a function of aspect ratio. The I_{ISO} normalized by the lowest particle's concentration ($c=6.3\cdot10^{-7}$g/ml) is almost constant for various aspect ratios for both salt-free and salt suspensions, denoting that the light scattering experiments are performed in the regime of infinite dilution, where essentially all particles scatter the same as they have almost identical volume and molecular weight. Both for salt-free and salt-present solutions, the I_{VH} increases by increasing the aspect ratios, which is in agreement with the expected increase of the optical anisotropy with increasing aspect ratio.

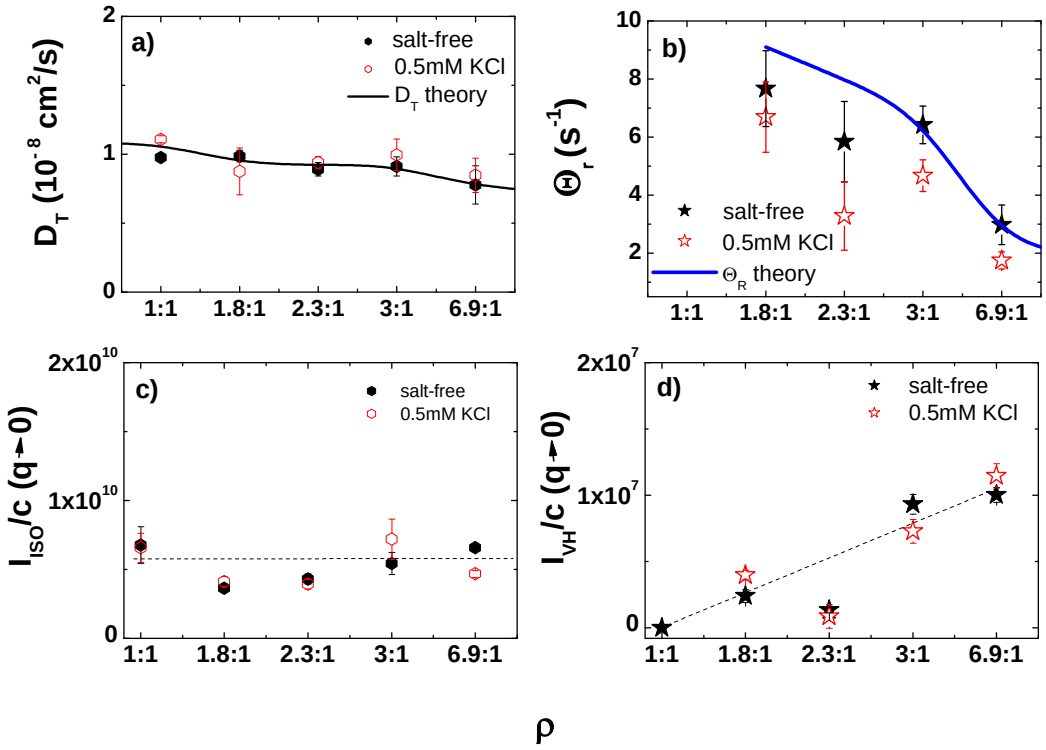

Fig. 3.5 *- a) Translational (circles) and b) Rotational diffusion coefficients (stars) at lowest volume fraction (φ→0) as a function of aspect ratios for salt-free solutions (black full symbols) and solutions with 0.5mM of KCl (red open symbols). Solid lines correspond to theory for translational (black solid line) and rotational diffusion (blue solid line).*

c) Normalized polarized scattering intensity $I_{ISO}(q\to0)$ and d) normalized depolarized scattering intensity $I_{VH}(q\to0)$ as a function of aspect ratio ρ for particle concentration $c=6.3\cdot10^{-7}$g/ml.

3.4.2 Volume fraction dependence of normalized scattered intensity in dilute regime and interactions between particles

The light scattering measurements were performed at really low volume fractions where interactions between particles are negligible. In order to prove this, we can estimate an "effective overlap volume fraction" ϕ*, which is equal to the ratio between the volume of the particles and the cube of the particle's diameter. Then the ϕ* is calculated to range between 0.5 for the sphere to 0.012 for the highest aspect ratio (ρ=6.9). Thus, the probed range of volume fractions ($3 \cdot 10^{-5}$ – $6 \cdot 10^{-7}$) is deeply in the dilute regime.

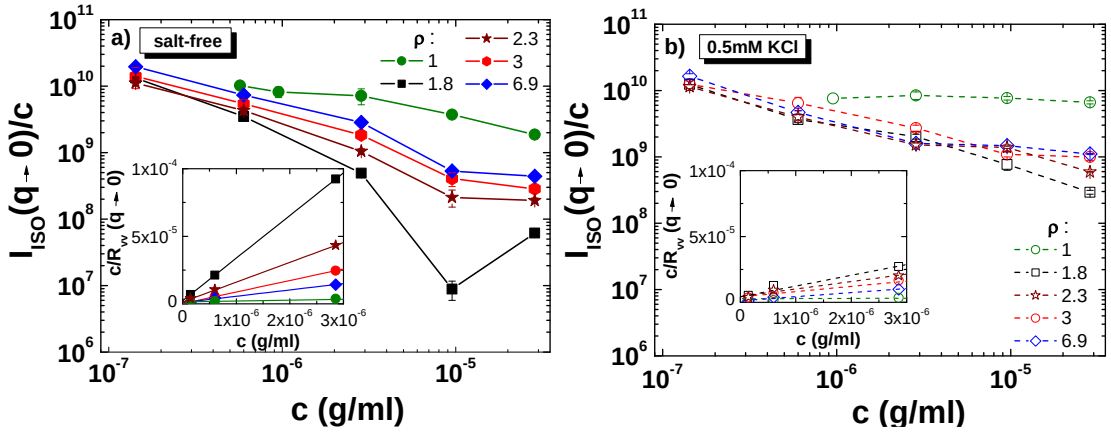

Fig. 3.6 *- a) Normalized polarized scattering intensity $I_{ISO}(q\to 0)$ divided by mass concentration as a function of volume fraction φ for salt free solutions for various aspect ratios ρ.*

b) $I_{ISO}(q\to 0)/c$ as a function of φ for solutions with salt concentration 0.5mM of KCl

Insets: a) Typical plots of SLS experimental data (T=293K) according to eq. 1 for salt-free solutions and b) Salt solutions with salt concentration 0.5mM of KCl. The variation of the virial coefficient (extracted by the slope of the linear fittings) with aspect ratio ρ is obvious.

Fig. 3.6 presents the volume fraction dependence of the polarized scattered intensity extrapolated to q→0, normalized by the mass concentration. For salt-free case of aspect ratio ρ=1.8, there is a prominent minimum of the normalized scattering intensity at volume fraction $\phi=10^{-5}$. We should highlight that all measurements at this specific volume fraction were repeated multiple times revealing the reproducibility of this minimum. The long-range electrostatic interactions probably impose preferential positions of the particle in the suspension, leading in this way in the creation of "pseudo-organized" structures. At aspect ratios

ρ=2.3, 3 and 6.9 the minimum still exists at ϕ=10^{-5}, but is less pronounced. In all the cases, this minimum disappears completely when the salt is added and therefore we can consider it as a result of long-range Coulombic interactions.

To make contact with the macroscopic properties of the systems we should note that the static structure factor in the q→0 limit is related to the osmotic compressibility through $S(0) = k_B T\left(\frac{\partial \phi}{\partial \Pi}\right)_T$, where Π is the osmotic compressibility (Pecora 2013). For semi-dilute and concentrated regime the theoretical prediction of S(0) for hard spheres is given through $S(0) = \frac{(1-\phi)^4}{(1+2\phi)^2 + \phi^3(\phi-4)}$ (Holmqvist, Mohanty et al. 2012). Fig. 3.7a shows the S(0) for various aspect ratios, including also the comparison with the HS theory. We observe that upon increasing the volume fraction, the spheroids exhibit a qualitatively similar trend of decrease compared to HS's behavior even at so low volume fractions, where we expect S(0) to be volume fraction independent. This fact denotes that even in dilute regime there are long-range interactions that are significant enough. From surface charge density measurements we calculated the Debye screening length, which denotes the distance beyond which interactions can be essentially ignored. For the simplest case of spheres the Debye screening length is around κ^{-1}=20nm (fig. 3.1), which means that electrostatic interactions correspond to an effective size of R=220nm (~10% bigger than the actual one). However, this effective size does not constitute evidence of the existence of that significant long-range interactions. Alternatively, we tried to estimate an effective size for the case of sphere corresponding to the long-range interactions resulting from the calculations for S(0). Therefore, we shifted the sphere's experimental data in the horizontal axis in a way that the data will collapse with the theory for HS. By the shifting we extracted that this effective size is 900% bigger than the actual one, denoting that the corresponding Debye screening length is around κ^{-1}=1800nm. Hence, the measured and the estimated electrostatic interactions do not converge between them.

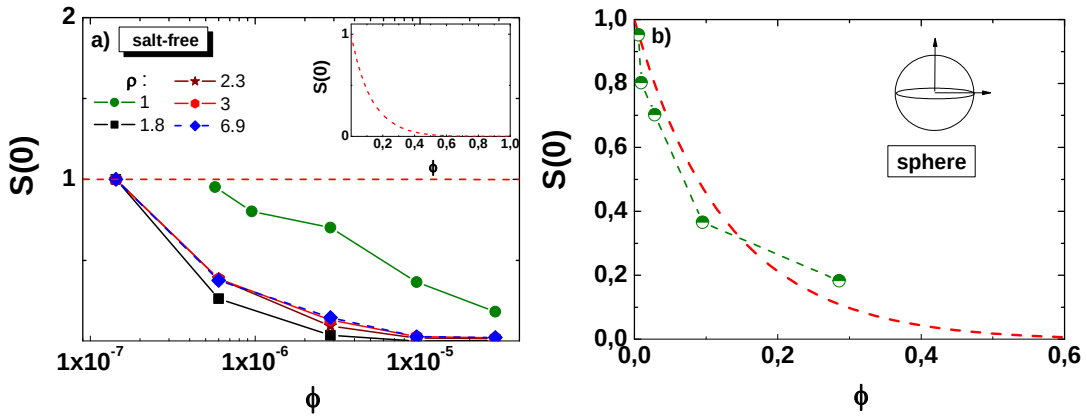

Fig. 3.7 *– a) Volume fraction dependence of S(0) for various aspect ratios for salt-free solutions. Red dashed line is the HS's theoretical prediction. Inset: the HS's theoretical prediction at higher volume fractions and b) sphere's horizontal shift.*

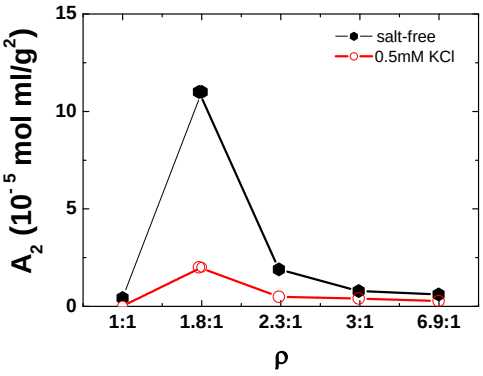

Fig. 3.8 - *Second virial coefficient A_2 calculated by the experimental data presented in inset plots of fig. 3.6 for both salt-free and salt suspensions.*

The second virial coefficient A_2 is a thermodynamic parameter that characterizes the intermolecular interactions in dilute solutions by reflecting the magnitude of interactions (Valente, Payne et al. 2005). Positive values of A_2 indicate predominantly repulsive intermolecular interactions, while negative values reflect predominantly attractive interactions (Neal, Asthagiri et al. 1999). The inset plot in fig. 3.6 presents the inverse reduced scattered intensity R_{VV} (Rayleigh ratio) as a function of volume fraction. Then, from the slope and the intercept of the plots according to the equation (3.3) and the particles' molecular weight (M_w $=2.13\cdot10^{10}$g/mol), we calculated the second virial coefficient A_2 for PS latex spheres and various aspect ratios of spheroids for both salt-free and salt-present solutions

(fig. 3.8). In all probed cases, the slope is positive, indicative of repulsive interactions between the particles in the aqueous suspensions. After the addition of the salt, the slope decreases, denoting the screening of the electrostatic interactions. However, the screening is partial since the slope does not go to zero.

Afterwards, fig. 3.9 depicts the volume fraction dependence of the depolarized scattered intensity at q→0 extracted by DDLS experiments. The prominent minimum at $\phi=10^{-5}$ that we observed in polarized DLS measurements for ρ=1.8, 2.3, 3 and 6.9, does not exist anymore both in salt-free and salt solutions. Moreover, the scattering intensity, normalized with the particle concentration exhibit a linear volume fraction dependence with slightly negative slope which denotes that the particles are not randomly oriented and their relative position tends to become perpendicular to another.

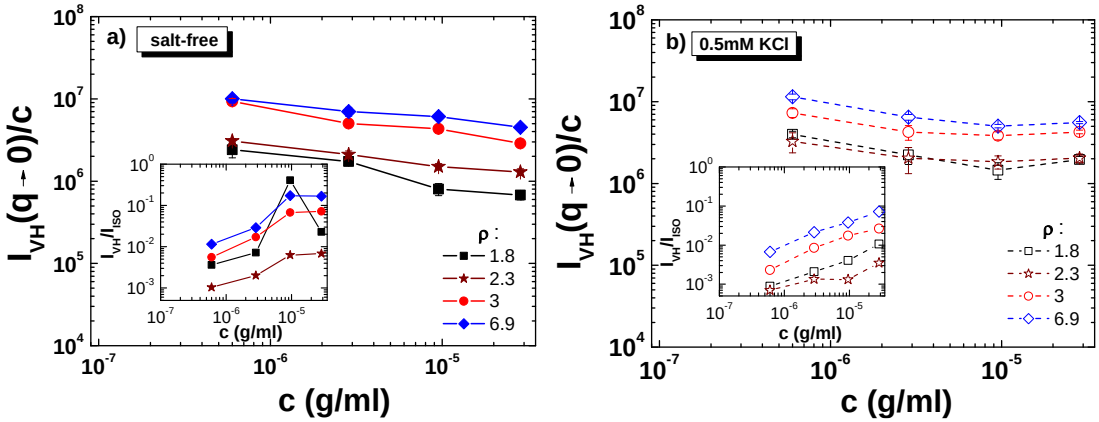

Fig. 3.9 *– a) Normalized depolarized scattering intensity $I_{VH}(q\to 0)$ divided by mass concentration as a function of volume fraction φ for salt free solutions for various aspect ratios ρ and b) $I_{VH}(q\to 0)/c$ as a functions of φ for solutions with salt concentration 0.5mM of KCl.*

Insets: depolarization ratio I_{VH}/I_{ISO} for various aspect ratios for salt-free and salt solutions.

The depolarized scattered intensity can be characterized by the depolarized ratio I_{VH}/I_{ISO} (Jernigan and Flory 1967, Berne 1976). According to the theory of light scattering by single small particles, the maximum value of depolarization ratio cannot exceed 1/3 which is the value for rods (Hulst and van de Hulst 1957, Kerker 1969, Khlebtsov, Melnikov et al. 2005, Khlebtsov, Khanadeev et al. 2008). The inset plot of fig. 3.9 depicts the volume fraction dependence of the experimentally

calculated depolarization ratio. At volume fraction $\phi=10^{-5}$ of aspect ratio $\rho=1.8$, where we observe the systematic divergence in vertical polarization for salt-free solutions, the experimental depolarization ratio exceeds about 22% the theoretical limit of 1/3.

3.5 Conclusions

In this chapter, FESEM was employed in order to obtain the size of shape distribution of PS spheres and PS prolate ellipsoids of various aspect ratios. Afterwards, DLS and DDLS techniques were used for the characterization of the size and the study of hydrodynamic properties for both salt-free aqueous solutions of various aspect ratios of PS spheroids and suspensions containing monovalent salt ions of KCl. The size values which were extracted by FESEM and LS technique are quite close. However, the combination of the two techniques can ensure the extraction of more accurate information. The SLS experimental data of polarized scattered intensity of particles are consistent with the corresponding theoretical predictions, whereas the corresponding data for the depolarized scattered intensity fail to get described by theory for randomly oriented prolate ellipsoids. The translational diffusion coefficients exhibit satisfactory agreement with the theory developed by Perrin. However, the predictions for rotational diffusion coefficient overestimates the values for the smaller aspect ratios ($\rho=1.8$ and 2.3), while describes successfully the higher aspect ratios ($\rho=3$ and 6.9). SLS technique was also used for the investigation of the interactions developed between particles, through the second virial coefficient A_2 for salt-free solutions, and how they change upon the addition of salt. Moreover, we observed that the long-range electrostatic interactions are responsible for the formation of “pseudo-organized” structure at a specific volume fraction ($\phi=10^{-5}$), which disappear after the addition of KCl. Finally, the estimation of static structure factor at $q\rightarrow0$ limit, S(0), which compared with HS predictions, supported the idea of existence of long-range interactions much stronger than what the measurement of surface charge densities and the quantification of Debye screening length revealed.

References:

Akbari, B., et al. (2011). "Particle Size Characterization of Nanoparticles–A Practicalapproach." Iranian Journal of Materials Science and Engineering **8**(2): 48-56.

Allen, T. (2013). Particle size measurement, Springer.

Alms, G., et al. (1973). "Depolarized Rayleigh scattering and orientational relaxation of molecules in solution. III Carboxylic acids." The Journal of Chemical Physics **59**(10): 5321-5328.

Aragon, S. and R. Pecora (1977). "Theory of dynamic light scattering from large anisotropic particles." The Journal of Chemical Physics **66**(6): 2506-2516.

Bantchev, G. B., et al. (2006). "Simple multiangle, multicorrelator depolarized dynamic light scattering apparatus." Review of scientific instruments **77**(4): 043902.

Benenson, W., et al. (2006). Handbook of physics, Springer Science & Business Media.

Benenson, W., et al. Handbook of Physics, 2002, Springer-Verlag, New York.

Berne, B. (1976). J. and Pecora, R.," Dynamic Light Scattering, Wiley, New York.

Berne, B. J. and R. Pecora (2000). Dynamic light scattering: with applications to chemistry, biology, and physics, Courier Corporation.

Bowen, P. (2002). "Particle size distribution measurement from millimeters to nanometers and from rods to platelets." Journal of Dispersion Science and Technology **23**(5): 631-662.

Brogioli, D., et al. (2009). "Characterization of anisotropic nano-particles by using depolarized dynamic light scattering in the near field." Optics express **17**(3): 1222-1233.

Brown, W. (1993). Dynamic light scattering: the method and some applications, Oxford University Press, USA.

Charles, S. and D. A. Johnson Jr (1981). Gabriel laser light scatter ing, New York: Dover Publications, Inc.

Chonde, Y. and I. Krieger (1981). "Emulsion polymerization of styrene with ionic comonomer in the presence of methanol." Journal of Applied Polymer Science **26**(6): 1819-1827.

Coertjens, S., et al. (2014). "Contact angles of microellipsoids at fluid interfaces." Langmuir **30**(15): 4289-4300.

Dai, H., et al. (1996). "Grain growth and defect annihilation in block copolymers." Physical review letters **77**(17): 3677.

De Souza Lima, M. M., et al. (2003). "Translational and rotational dynamics of rodlike cellulose whiskers." Langmuir **19**(1): 24-29.

Dubin, S. B., et al. (1971). "Measurement of the rotational diffusion coefficient of lysozyme by depolarized light scattering: configuration of lysozyme in solution." The Journal of Chemical Physics **54**(12): 5158-5164.

Flamberg, A. and R. Pecora (1984). "Dynamic light scattering study of micelles in a high ionic strength solution." The Journal of Physical Chemistry **88**(14): 3026-3033.

Fournet, G. (1951). "Scattering functions for geometrical forms." Bull. Soc. Fr. Min. Crist. **74**: 39-113.

George, A. and W. W. Wilson (1994). "Predicting protein crystallization from a dilute solution property." Acta Crystallographica Section D: Biological Crystallography **50**(4): 361-365.

Gilányi, T., et al. (2000). "Characterisation of monodisperse poly (N-isopropylacrylamide) microgel particles." Physical Chemistry Chemical Physics **2**(9): 1973-1977.

Guiner, A., et al. (1955). "Small angle scattering of X-rays." J. Wiley & Sons, New York.

Han, Y., et al. (2009). "Quasi-two-dimensional diffusion of single ellipsoids: Aspect ratio and confinement effects." Physical Review E **80**(1): 011403.

Han, Y., et al. (2006). "Brownian motion of an ellipsoid." Science **314**(5799): 626-630.

Heyes, D. M., et al. (1998). "Translational and rotational diffusion of model nanocolloidal dispersions studied by molecular dynamics simulations." Journal of Physics: Condensed Matter **10**(45): 10159.

Ho, C., et al. (1993). "Monodisperse ellipsoidal polystyrene latex particles: Preparation and characterisation." Polymer international **30**(2): 207-211.

Hoffmann, M., et al. (2008). "Dumbbell-shaped polyelectrolyte brushes studied by depolarized dynamic light scattering." The Journal of Physical Chemistry B **112**(47): 14843-14850.

Hoffmann, M., et al. (2009). "3D Brownian diffusion of submicron-sized particle clusters." ACS nano **3**(10): 3326-3334.

Holmqvist, P., et al. (2012). "Structure and dynamics of loosely cross-linked ionic microgel dispersions in the fluid regime." Physical review letters **109**(4): 048302.

Hu, C. M. and R. Zwanzig (1974). "Rotational friction coefficients for spheroids with the slipping boundary condition." The Journal of Chemical Physics **60**(11): 4354-4357.

Hulst, H. C. and H. C. van de Hulst (1957). Light scattering by small particles, Courier Corporation.

Israelachvili, J. N. (2011). Intermolecular and surface forces, Academic press.

Jabbari-Farouji, S., et al. (2004). "Ageing dynamics of translational and rotational diffusion in a colloidal glass." Journal of Physics: Condensed Matter **16**(41): L471.

Jernigan, R. and P. Flory (1967). "Optical Anisotropy of Chain Molecules. Theory of Depolarization of Scattered Light with Application to n-Alkanes." The Journal of Chemical Physics **47**(6): 1999-2007.

Kanetakis, J. and H. Sillescu (1996). "Simultaneous measurement of rotational and translational diffusion by forced Rayleigh scattering. Colloid spheres in suspension." Chemical physics letters **252**(1-2): 127-134.

Kerker, M. (1969). The scattering of light, Academic Press, New York.

Keville, K., et al. (1991). "Preparation and characterization of monodisperse polymer microspheroids." Journal of colloid and interface science **144**(1): 103-126.

Khlebtsov, B. N., et al. (2008). "Observation of extra-high depolarized light scattering spectra from gold nanorods." The Journal of Physical Chemistry C **112**(33): 12760-12768.

Khlebtsov, N. G., et al. (2005). "Can the light scattering depolarization ratio of small particles be greater than 1/3?" The Journal of Physical Chemistry B **109**(28): 13578-13584.

Koenderink, G. H., et al. (2003). "Rotational dynamics of colloidal tracer spheres in suspensions of charged rigid rods." The Journal of Chemical Physics **119**(8): 4490-4499.

Koenderink, G. H., et al. (2003). "On the validity of Stokes–Einstein–Debye relations for rotational diffusion in colloidal suspensions." Faraday Discussions **123**: 335-354.

Koppel, D. E. (1972). "Analysis of macromolecular polydispersity in intensity correlation spectroscopy: the method of cumulants." The Journal of Chemical Physics **57**(11): 4814-4820.

Kroeger, A., et al. (2007). "Equilibrium length and shape of rodlike polyelectrolyte micelles in dilute aqueous solutions." Macromolecules **40**(1): 105-115.

Lehner, D., et al. (2000). "Determination of the translational and rotational diffusion coefficients of rodlike particles using depolarized dynamic light scattering." Langmuir **16**(4): 1689-1695.

Matsuoka, H. and N. Ise "Chemtract, 4, 53 (1993)." Google Scholar.

Matsuoka, H., et al. (1996). "Rotational diffusion of ellipsoidal latex particles in dispersion as studied by depolarized dynamic light scattering." Colloids and Surfaces A: Physicochemical and Engineering Aspects **109**: 137-145.

Morawetz, H. (1973). "Light scattering from polymer solutions, M. B. Huglin, Ed., Aca-demic Press Inc., London, 1972. 885 pp. $45.00." Journal of Polymer Science: Polymer Letters Edition **11**(1): 68-69.

Nägele, G. (2002). "Viscoelasticity and diffusional properties of colloidal model dispersions." Journal of Physics: Condensed Matter **15**(1): S407.

Nagy, M. and A. Keller (1989). "Ellipsoidal polymer particles with predesigned axial ratio." Polymer communications **30**(5): 130-132.

Neal, B., et al. (1999). "Why is the osmotic second virial coefficient related to protein crystallization?" Journal of Crystal Growth **196**(2): 377-387.

Newstein, M., et al. (1995). "Light scattering and microscopy from block copolymers with cylindrical morphology." Macromolecules **28**(13): 4587-4597.

Pecora, R. (1972). "Quasi-elastic light scattering from macromolecules." Annual review of biophysics and bioengineering **1**(1): 257-276.

Pecora, R. (2013). Dynamic light scattering: applications of photon correlation spectroscopy, Springer Science & Business Media.

Pedersen, J. S. (1997). "Analysis of small-angle scattering data from colloids and polymer solutions: modeling and least-squares fitting." Advances in colloid and interface science **70**: 171-210.

Perrin, F. (1934). "Mouvement brownien d'un ellipsoide-I. Dispersion diélectrique pour des molécules ellipsoidales." Journal de Physique et le Radium **5**(10): 497-511.

Perrin, F., et al. (1936). "Brownian motion of an ellipsoid. II. Free rotation and depolarisation of fluorescence: translation and diffusion of ellipsoidal molecules." J Phys Rad **7**: 1-11.

Phalakornkul, J., et al. (2000). "Rotational dynamics of rodlike polymers in a rod/sphere mixture." The Journal of Chemical Physics **112**(14): 6487-6494.

Plum, M. A., et al. (2009). "Probing dynamics at interfaces: resonance enhanced dynamic light scattering." Optics express **17**(12): 10364-10371.

Quirantes, A., et al. (1996). "Determination of size/shape parameters of colloidal ellipsoids by photon correlation spectroscopy." Colloids and Surfaces A: Physicochemical and Engineering Aspects **119**(1): 73-80.

Saluja, A., et al. (2010). "Diffusion and sedimentation interaction parameters for measuring the second virial coefficient and their utility as predictors of protein aggregation." Biophysical journal **99**(8): 2657-2665.

Schärtl, W. (2007). Light scattering from polymer solutions and nanoparticle dispersions, Springer Science & Business Media.

Shetty, A. M., et al. (2009). "Multiangle depolarized dynamic light scattering of short functionalized single-walled carbon nanotubes." The Journal of Physical Chemistry C **113**(17): 7129-7133.

Stein, R. S. and P. R. Wilson (1962). "Scattering of light by polymer films possessing correlated orientation fluctuations." Journal of Applied Physics **33**(6): 1914-1922.

Takagi, S. and H. Tanaka (2001). "Phase-coherent light scattering spectroscopy. II. Depolarized dynamic light scattering." The Journal of Chemical Physics **114**(14): 6296-6302.

Tinke, A., et al. (2006). "Particle size and shape characterization of nano and submicron liquid dispersions." Am Pharm Rev **9**(6): 1-5.

Utiyama, H. (1972). "Calibration and correction factors." Light Scattering from Polymer Solutions. MB Huglin, editor. Academic Press, London.

Valente, J. J., et al. (2005). "Colloidal behavior of proteins: effects of the second virial coefficient on solubility, crystallization and aggregation of proteins in aqueous solution." Current pharmaceutical biotechnology **6**(6): 427-436.

Van Bruggen, M., et al. (1998). "Long-time translational self-diffusion in isotropic and nematic dispersions of colloidal rods." Physical Review E **58**(6): 7668.

Wilson, W. W. (2003). "Light scattering as a diagnostic for protein crystal growth—A practical approach." Journal of structural biology **142**(1): 56-65.

Zhao, J., et al. (1995). "Micelles formed by a model hydrogen-bonding block copolymer." Macromolecules **28**(6): 1972-1978.

Zimm, B. H. (1948). "Apparatus and methods for measurement and interpretation of the angular variation of light scattering; preliminary results on polystyrene solutions." The Journal of Chemical Physics **16**(12): 1099-1116.

Chapter 4

Structure and dynamics of soft core-shell particles from dilute to glassy regime

This chapter refers to the study of structure and dynamics in suspensions of soft isotropic colloidal core-shell particles in the concentrated and glassy regime. The core-shell particles consist of PMMA chains of different molecular weight grafted on a hard silica core (P2_41k and P2-126k). The particles are suspended in a mixture of two solvents in order to achieve the refractive index matching of the solvent with the shell and thus minimize multiple scattering contributions that arise when increasing the effective volume fraction. In the concentrated regime, we used 3D Dynamic Light Scattering technique (3DDLS) to measure static and dynamic properties. The diffusion coefficient data D(q) were measured near and around the structure factor S(q) peak and interpreted through comparison with hard sphere models.

In the glassy regime, where the dynamics are strongly non-ergodic, Multispeckle Dynamic Light Scattering technique (MSDLS) was utilized to follow ageing, which strongly depends on the effective volume fraction (c/c). In the whole glassy regime, the evolution of the degree of correlation as a function of the waiting time shows a non-monotonic behavior which is also reflected in the slowest relaxation time. This behavior is a consequence of structural rearrangements of the particles that, depending on c/c* and the polydispersity, may lead to crystallization of the system. Hence the phase behavior reveals a liquid, a liquid-crystal coexistence followed by a crystalline phase, while at large concentrations metastable glasses states are detected.*

4.1 Introduction

This experimental study aims in understanding the structure and dynamics in suspensions of soft colloidal core-shell particles up to liquid-crystal coexistence and glassy regime. The core-shell particles consist of PMMA chains of specific molecular weight grafted on a hard silica core. The particles are suspended in a mixture of two solvents in order to achieve the refractive index matching of the solvent with the shell.

In the concentrated regime where due to refractive index mismatch and large particle number density which induce multiple scattering contributions, 3D Dynamic Light Scattering technique (3DDLS) was used to allow the detection of single particle dynamics. The data were interpreted through comparison with hard sphere theories. In the glassy regime, where the dynamics are strongly non-ergodic, it was used the Multispeckle Dynamic Light Scattering technique (MSDLS). Through this technique, it is also possible to monitor the ageing of the suspension as a function of waiting time and its transition from the glassy to the crystal regime.

The comprehension of the physics of concentrated colloidal suspensions and more specifically the relation between the structure and the dynamics constitutes a topic that many scientific groups have studied by both experimental and theoretical work (Pusey 1991).

Permeable colloids may be represented by different types of fuzzy-sphere particles where the internal structure allows solvent to pass through it and may even change with concentration and/or temperature. This kind of suspensions can be found in a great variety of synthesized particles. A well-studied permeable system consists of cross-linked poly(N-iso-propylacrylamide) network particles (PNIPAM microgel spheres) immersed in an aqueous (or mixtures with organic solvents) solvent, which are highly thermosensitive and exhibit large and reversible volume changes as a function of temperature. Eckert and Richtering (Eckert and Richtering 2008)studied the short-time dynamics of PNIPAM in DMF who observed the slowing down of the dynamics in the q-region around the maximum of the structure factor peak $S_{max}(q)$, which is quite similar to the HS behaviour. Another category of permeable soft particles are core-shell particles with a rigid, impermeable spherical

core and an outer polymeric coat (shell). The shell provides steric stabilization (under theta or good solvent conditions) against Van der Waals attraction and prevent the particles from aggregating. Petekidis et al. studied the short-time dynamics of core-shell particles which consists of a hard silica core with grafted PDMS chains immersed in a 50-50 mixture of toluene and heptane (Petekidis, Gapinski et al. 2004). They observed that dynamics slow down near the peak of S(q) in a weaker way than HS do. Sigel et al. studied the short-time dynamics of giant colloidal micelles, which consist of polystyrene (PS) core with tethered polyisoprene (PI) chains and PI core with tethered PS chains in decane and dimethylacetamide (DMA), preferential solvents for I block and S block, respectively (Sigel, Pispas et al. 1999). They argued that PS-PI micelles present absence of thermodynamic slowing down of the dynamics around the peak of S(q), as a result of the nonlocal mobility due to the interacting tethered chains. However, the relaxation time was not determined from the initial slope, but rather with Contin analysis. Robert, Wagner et al. studied the dynamic behaviour of charge-stabilized poly-perfluoropentyl-methacrylate in water/glycol mixture. This group observed that increasing the volume fraction, the peak of S(q) shifts to higher qRs, because of the reduction of the interparticle distances and the short-time diffusion $D_0/D(q)$ is greater than S(q), a fact that is a result of indirect hydrodynamic interactions (Robert, Wagner et al. 2008). On the other hand there are polymeric systems, Chrissopoulou et al. studied the dynamics of SI diblock copolymers in toluene, a nonselective good solvent, and compared them with polymer blends. For copolymers the slowing down of short-time dynamics occurs around the peak of S(q) ($q \to q^*$), as microphase separation is approached, whereas for the intermolecular mixtures (binary polymer blends), the slowing down of the dynamics takes place in the thermodynamic limit ($q \to 0$) as they approach the macrophase separation (Chrissopoulou, Pryamitsyn et al. 2001).

At even higher concentrations, colloidal suspensions can form “colloidal glasses”. Glassy state is a metastable non-ergodic amorphous state, in which the particles’ motion is constrained due to their neighbors’ cages. However, they retain some freedom for local Brownian motions which are unable to diffuse over large

distances (Pusey and Van Megen 1986, Pusey 1991). The slow dynamics of out-of-equilibrium soft materials has been studied for a wide variety of systems, ranging from hard spheres to more complicated materials. Generally, in glassy regime dynamics are not completely frozen, with the structural relaxations taking place in very long timescales. Ageing is an inherent feature of glassy samples, where the properties of out-of-equilibrium system continuously change with time as a the system evolves towards its equilibrium configuration (Cipelletti and Ramos 2005, El Masri, Brambilla et al. 2009). Typically, during ageing the dynamics becomes progressively slower, with the system spending more and more time in deeper energy states it visits. The mechanism, for slow dynamics and ageing in some soft glassy systems, is the relaxation of internal stresses (Cipelletti and Ramos 2005). Molecular dynamic (MD) simulations in hard sphere glasses suggest that a spontaneous crystallization can occur on time scales that a glass is ageing (Zaccarelli, Valeriani et al. 2009).

Studies on star polymers by Monte Carlo simulations and theory (Watzlawek, Likos et al. 1999, Foffi, Sciortino et al. 2003) report a variety of crystal phases. The first experimental report came from Stiakakis et al. (Stiakakis, Wilk et al. 2010) with multiarm star polymers, where slowing down of dynamics and structure monitored by Multispekle Dynamic Light Scattering (MSDLS) and Small Angle Neutron Scattering (SANS) respectively. Finally, a glass-crystal transition was revealed through gradual speed up of dynamics leading to a final steady state at long times. Here, we also examine slow dynamics and ageing phenomena in core-shell particles using the MSDLS technique.

4.2 Materials

Hybrid core-shell particles (PMMA-SiPs), which consists of silica (SiP) core and shell of polymethylmethacrylate (PMMA) grafted chains were synthesized by surface-initiated atom transfer radical polymerization (ATRP) of MMA, by Kohji Ohno et al. (Ohno, Morinaga et al. 2005). The mean diameter of the silica core is 130 nm with a relative standard deviation of 10%. The weight-average molecular weights

$\overline{M_w}$ of the grafted polymer chains 41kg/mol (P2_41k), 126kg/mol (P2_126k) and 402kg/mol (P2_402k) with polydispersity indices 1.25, 1.24 and 1.15 respectively. The surface grafting density of the SiP's varies between 0.55-0.65chains/nm^2, which means that every particle has 34500 grafted chains per particle.

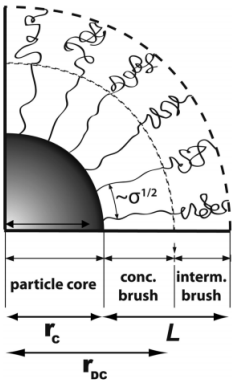

Fig. 4.1 *– Top: Schematic representation of the hybrid particle cross section indicating the various polymer brush regimes; concentrated brush regime (CPB) and intermediate brush regime (SDPB). Bottom: Particle's refractive index as a function of distance r from the center of the particle. Attached by (Voudouris, Choi et al. 2009)*

As the grafting density, of the polymer chains in the shell of the hybrid particles, is high, two regions can be distinguished: (1) the Concentrated Polymer Brush regime (CPB), where the polymer chains are stretched due to excluded volume effect and (2) the intermediate brush regime (SDPB), which is characterized by reduced polymer grafting density and the polymer conformation changes by increasing the distance from the core (fig. 4.1). For spherical particle brushes, increasing the distance r from the particle surface, the effective polymer density decreases according to $\sigma_{eff} = \sigma_0 \left(\frac{r_C}{r} \right)^2$, where r_C is the particle core radius and σ_0 is the surface grafting density at the core surface, a transition from the concentrated to the intermediate brush regime is expected at a critical distance r_{DC}. This follows the Daoud-Cotton model for star polymers, where $r_{DC} = 2\nu r_0 \left(\pi\sigma^* \right)^{0.5}$, with $\sigma^* = \sigma_0 a^2$ expressing the dimensionless surface coverage (a is the monomer length) and ν the excluded-volume parameter that is about b/a (b is the Kuhn length) for athermal

solvents (Daoud and Cotton 1982). Then, when f chains are grafted on the surface of the particle core, $\sigma_0 = \frac{f}{4\pi r_0^2}$ and $r_{DC} \approx bf^{0.5}$ is the size of the core and the concentrated brush regime (CPB) where the excluded-volume effect is screened, respectively. The ratio r_C/L, where $L = \frac{R_N}{\sqrt{6}}$ and R_N is the end to end distance in good solvent, indicates the particle "softness", which varies depending on the polymer M_w and solvent. When a system behaves as a hard sphere, then $r_C/L \approx 1$ (Voudouris, Choi et al. 2009).

In order to achieve refractive index matching (n=1.489) with the shell at λ=633nm, the particles are dispersed in a mixture of solvents; mixture of solvents 1,2-Dichloroethane (DE) (50% vol) and o-Dichlorobenzene (DCB) (50% vol) was used for P2-126k, whereas a mixture of o-dimethoxy benzene (Veratrole) and Dimethyl Formamide (DMF) for P2-41k and P2-402k. Toluene is also a good solvent for PMMA and therefore used in some studies.

Sample name	R_H (nm)	Number of chains / nm² (σ_o)	Number of chains / particle (f)	r_C / L	r_C / R_H	σ_{eff} outer blob
P2-41k (ver-DMF)	133	0.55	34500	1.58	1	0.138
P2-41k (toluene)	123	0.55	34500	1.58	1.08	0.154
P2-126k (DE-DCB)	205	0.65	34500	0.78	0.62	0.065
P2-126k (ver-DMF)	204	0.65	34500	0.78	0.62	0.068
P2-402k (ver-DMF)	420	0.65	34500	0.39	0.305	0.016
P2-402k (toluene)	470	0.65	34500	0.39	0.27	0.012

Table 4.a *– Characteristic values of Silica-grafted PMMA core-shell particles.*

Table 4.a summarizes the characteristics values like hydrodynamic radius, surface density, grafting density, particle softness and effective density of the outer blobs for different soft systems of the same series. Most of these systems were studied by 3DDLS and MSDLS by Pamvouxoglou et al. (Pamvouxoglou A., PhD thesis, 2014). In this chapter, we will present only the additional studies on the system P2-

41k in ver-DMF and some experimental data of P2-41k in toluene in fluid regime. Moreover, we report the experimental investigation of P2-126k in ver-DMF in glassy regime.

The particles are permeable and not rigid. Hence, in order to determine the effective volume fraction ϕ_{eff} for the system P2-41k in ver-DMF, we measured the relative viscosity η_r for various particle concentrations in dilute regime using the LOVIS/DMA 4100M viscometer by Anton Paar. Then, an effective volume fraction ϕ_{eff} was calculated via the Einstein-Batchelor's equation $\eta_r = 1 + 2.5\phi_{eff} + 5.9\phi_{eff}^2$ assuming HS response. The ϕ_{eff} can be also substituted by kc, where c is the mass concentration of the dispersion in wt/wt and k is a shift factor for converting the mass concentration to the ϕ_{eff}, which describes the volume change of the permeable particles. The effective volume fraction values are presented in comparison with the ratio c/c* extracted by TGA experiment, where $c^* = (3M_w)/(4N_A \pi R_H^3)$ is the overlap concentration. For P2-41k in ver-DMF is $c^* = 41.8\%\, g/g$.

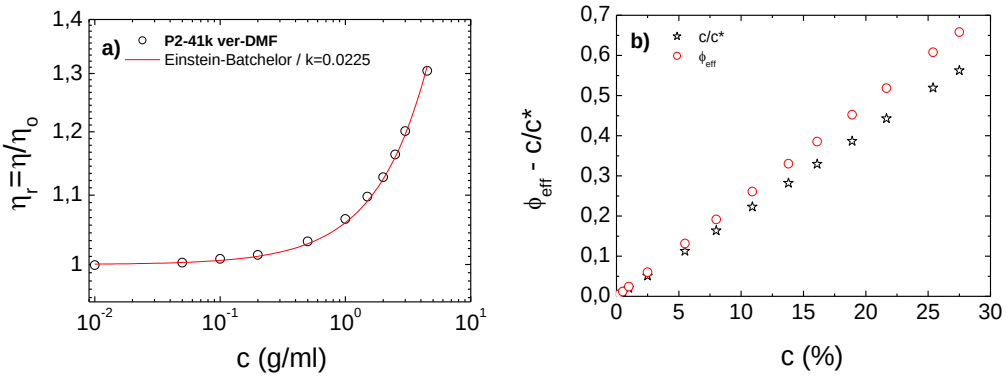

Fig. 4.2 *– a) Relative viscosity as a function of concentration in dilute regime for P2-41k in ver-DMF at T=20°C and fitting of the experimental data with Einstein-Batchelor equation and b) effective volume fraction determined through viscometry and c/c* for mass concentration range 0.1- 27.5%.*

4.3 Results - Discussion

4.3.1 Dilute regime: Dynamic properties, Form factor and interactions

Dynamic light scattering technique was used in dilute regime in order to extract the hydrodynamic properties of the probed systems. Fig. 4.3 depicts the correlation functions at θ=30° (q=0.00815nm^{-1}) for system P2-41k suspended in toluene and the solvent mixture (ver-DMF).

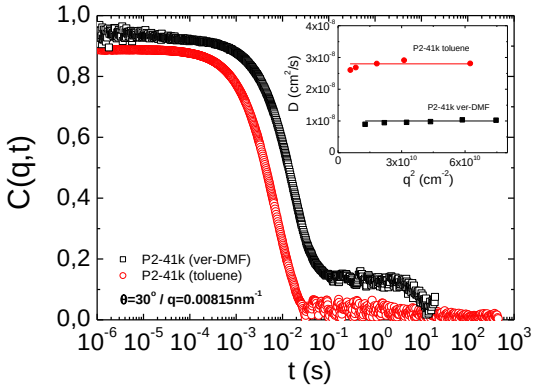

Fig. 4.3 – *Correlation functions for ϑ=30°/q=0.00815nm^{-1} for system P2-41k in toluene and solvent mixture ver-DMF. Inset: Diffusion coefficient for the two different solvents.*

In the dilute regime the static light scattering intensity depicts the particle's form factor F(q). Fig. 4.4a presents the form factor for various systems of different softness coming from different M_w of the polymer chains grafted in silica core. For fitting the F(q), which is strongly q-dependent for all systems, we used a model that refers to core-shell structures consisting of a homogeneous core and a inhomogeneous shell (Förster, Apostol et al. 2010). This model assumes that the shell has an algebraic density profile $\phi \sim r^{-a}$, i.e. a scaling law typical for polymer brushes (fig. 4.4b). The value of parameter α depends on the geometry (spherical, cylindrical or planar polymer brush) and the solvent quality. A value of α=0 corresponds to a homogeneous shell. For spherical polymer brushes this parameter has typical values between 1 (theta solvent) and 4/3 (good solvent) (Förster, Apostol et al. 2010). This model takes also into consideration the scattering contributions from both the core and the fuzzy shell and depends on the contrast variation Δn between core, shell and solvent. The equation that describes the particle form factor is the following:

$$F(q)=\left(\frac{3(\sin(qR)-qR\cos(qR))}{(qR)^3}\exp\left(-\frac{\sigma^2 q^2}{2}\right)\right)^2 \qquad (4.1)$$

where σ denotes the width of the fuzzy particle surface (Förster, Apostol et al. 2010).

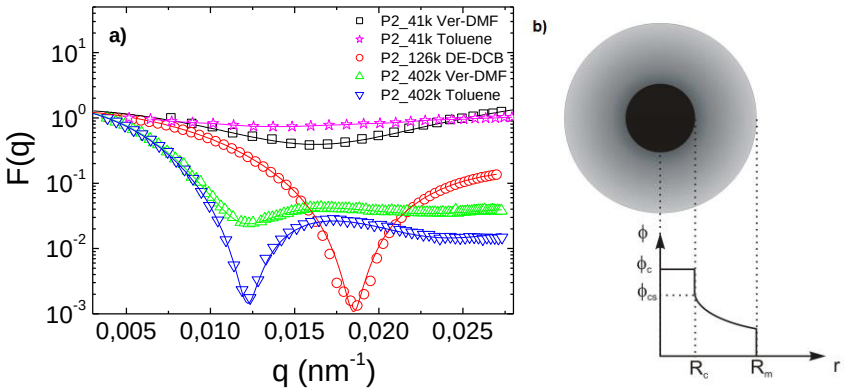

Fig. 4.4 – *a) Particle's form factor as a function of scattering wavevector for various systems of different softness. Experimental data fitted with homogeneous core and inhomogeneous shell model. By fitting with this model radii of 130nm (P2-41k ver-DMF), 173nm (P2-41k toluene), 194nm (P2-126k DE-DCB), 396nm (P2-402k ver-DMF) and 382nm (P2-402k toluene) were calculated and b) Schematic of density profile for model of homogeneous core and inhomogeneous shell.*

Table 4.b shows the parameters used to calculate the form factor with this model.

Sample name	P2-41k (ver-DMF)	P2-41k (toluene)	P2-126k (DE-DCB)	P2-402k (ver-DMF)	P2-402k (toluene)
M_w (kg/mol)	41	41	126	402	402
n_{core}	1.479	1.479	1.479	1.479	1.479
$n_{solvent}$	1.489	1.496	1.489	1.489	1.496
$r_{DC}=bf^{0.5}$	134	134	134	134	134
r_c	65	65	65	65	65
σ_{core}	0.05	0.12	0.1	0.05	0.05
R_{tot} (nm)	133	119	194	396	382
R_H (nm)	133	123	205	420	470
$h=R_H-r_c$	71.5	54	127	355	405
Δn	-0.095	-0.031	-0.0322	-3.01e-03	-2.7e-03

Table 4.b *– Parameters used to fit the form factor with the homogeneous core and inhomogeneous shell model and particle characteristics extracted from SLS and DLS experiments.*

The form factor for P2-41k (firg. 4.4a) exhibits a minimum at q=0.016nm^{-1} in both ver-DMF and toluene (black squares and magenta stars respectively). Hard Sphere model assumes that the first minimum of single-scattering form factor F(q) is

at qR=4.49 (Berne 1976, Segre, Behrend et al. 1995), according to which the P2-41k in both solvents at q=0.016nm^{-1}, corresponds to an overall effective HS radius of R=277nm. In toluene solution, the minimum is weaker compared to the solvent mixture of ver-DMF. However, the fitting with the homogeneous core and inhomogeneous shell model gives a total radius of 130nm in ver-DMF and 173nm in toluene.

Moreover, for obtaining information about intermolecular interactions between particles, we use the second virial coefficient A_2, which is extracted by static light scattering experimental data through the Zimm method (Zimm 1948). According to Zimm method, the second virial coefficient A_2 (in (mol·ml/g^2)) is determined by the equation $\frac{Kc}{R_{vv}} = \frac{1}{M_w} + 2A_2c$, where M_w is the solute molecular weight (g/mol), c is the solute concentration (g/ml), R_{VV} the excess Rayleigh ratio and K is a constant defined by the optical properties of the system (Utiyama 1972).

Positive second virial coefficient A_2 values indicate the presence of repulsive interactions between solute molecules, while negative values reflect attractive interactions (George and Wilson 1994, Saluja, Fesinmeyer et al. 2010). For P2-41k in both ver-DMF and toluene we measure a positive A_2 (fig. 4.5) with values 7.82·10^{-7}ml·mol/g^2 and 9.74·10^{-7}ml·mol/g^2 respectively.

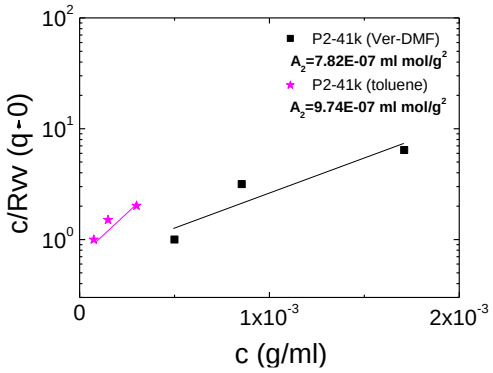

***Fig. 4.5** – Typical plots of SLS experimental data according to equation $Kc/R_{vv} = 1/M_w + 2A_2c$ for system P2-41k suspended in toluene and ver-DMF. In all cases A_2>0 denoting repulsive interactions.*

4.3.2 Concentrated regime: Static and Dynamic properties

In concentrated suspensions, the conventional light scattering technique fails due to strong multiple scattering contributions. Therefore, in order to study the dynamic and static properties of colloidal suspensions in concentrated regime, we used the 3Dimensional Dynamic light scattering technique (3DDLS), which effectively isolates the singly scattered light and suppresses any undesired multiple scattering contributions.

In general, when the light is singly scattered by a colloidal suspension, the scattering intensity is given by the equation: I(q)=S(q)F(q), where S(q) is the structure factor, which reflects the interparticle spatial correlations and F(q) is the single particle form factor. However, for concentrated suspensions, multiple scattering contributions are significant and then the scattering loss parameters should also be taken into account. Hence, the scattering intensity measured by 3DDLS, is extracted by the equation: $S(q) = \frac{I_{conc}^{total}(q) c_{dilute} T_{dilute}}{I_{dilute}(q) c_{conc} T_{conc}}$, where $I_{conc}^{S}(q) = \beta_{MS} I_{conc}^{total}(q)$ with $\beta_{MS}^2 = \frac{\left(g^{(2)}(q,\tau=0)-1\right)_{conc}}{\left(g^{(2)}(q,\tau=0)-1\right)_{dilute}} = \frac{\beta_{conc}^2}{\beta_{dilute}^2}$ the "multiple scattering factor" that is determined as the ratio of the amplitude of the cross-correlation function for the concentrated sample to the amplitude of the correlation function for a dilute sample.

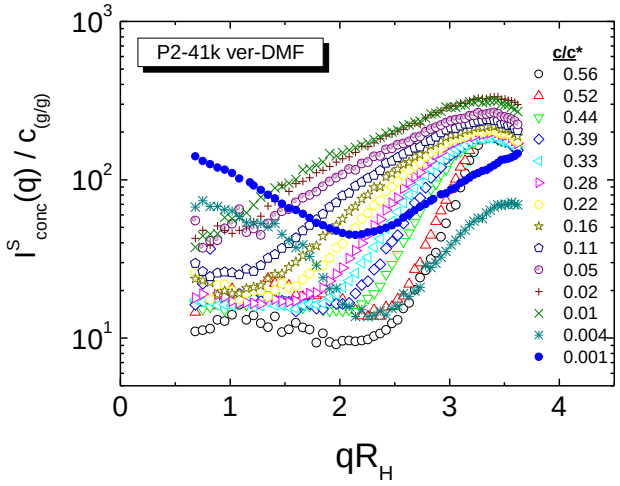

***Fig. 4.6** – Normalized single scattering intensity as a function of qR_H at different volume fractions.*

Fig. 4.6 presents the evolution of the single scattering intensity normalized by the mass concentration $I^{S}_{conc}(q)/c_{(g/g)}$, for P2-41k suspended in the solvent mixture ver-DMF, as a function of qR_H at different effective volume fractions. At higher volume fractions (0.56c/c*), the scattering intensity shows a strong maximum at qR_H~3.25 corresponding closely to the first peak of S(q). Decreasing the volume fractions the interparticle distances increase, leading to decrease of the interparticle interactions and shift of the maximum value towards lower q's ($q = 2\pi/r_{interparticle}$). At low q's, increasing volume fraction, the normalized scattering intensity decreases, indicating an increasing osmotic compressibility, which suppresses the creation of concentration fluctuations as concentration increases.

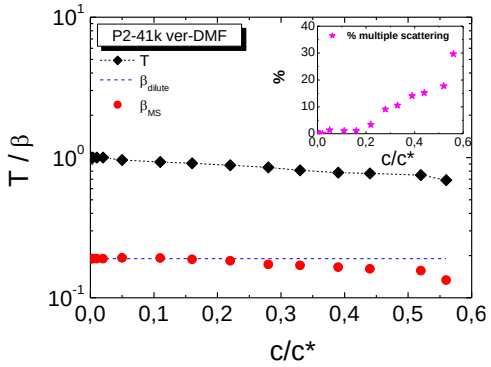

Fig. 4.7 – *Transmission of light T, intercept β and inset: %percentage of multiple scattering for various volume fractions.*

Fig. 4.7 shows the measured values of transmission of light through the samples for various volume fractions. For dilute regime (ϕ_{eff}<0.05c/c*) the transmission is equal to 1, whereas in more concentrated regime (ϕ_{eff} ≥0.05 c/c*), where there is the onset of multiple scattering contributions, the transmission of light is less than one. More specifically, increasing the effective volume fraction, the multiple scattering contributions increase and the transmission values decrease. Furthermore, for calculating the percentage [%] of multiple scattering for each volume fraction, we used the intercept of the normalized correlation function for each concentration (β_{MS}) taking into consideration the intercept ($\beta_{dilute} = 0.19$) of the dilute-reference sample (0.001c/c*).

$$\%Multiplescatteringpercentage = \frac{|\beta_{dilute} - \beta_{MS}|}{\beta_{dilute}} 100$$

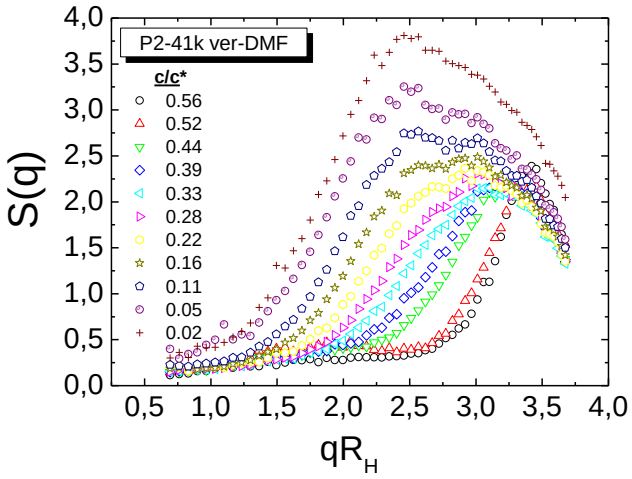

Fig. 4.8 – *Static structure factor S(q) as a function of qR_H for various effective c/c* for P2-41k.*

In fig. 4.8, we present the structure factor S(q) for the system P2-41k suspended in ver-DMF for various volume fractions, which reflects the interactions between particles and is proportional to the normalized single scattering intensity of a concentrated sample divided by the single particle form factor in the absence of particle-particle interactions. At higher volume fraction (0.56 c/c*), the peak position of structure factor is at qR=3.42, which is close to the peak position of S(q) for concentrated suspensions of hard spheres for volume fraction less than 0.49 c/c* (qR=3.5 for volume fractions < 0.494) (Van Megen, Ottewill et al. 1985), indicating a behaviour close to the hard sphere one. However, there is a slight difference with HS behaviour that is perhaps attributed to the fact that in the outer blob of the soft core-shell particles, there are dangling chain ends that introduce weak long-range repulsions at distances beyond R_H and keep the particles at larger distances between them. Moreover, the calculation of the effective volume fraction perhaps introduces some divergence too. The amplitude of the peak of S(q), which indicates the ordering of the system at inter-particle distance equal to the cage size, shows a non-monotonic behaviour with volume fraction. Moreover, at the limit of low scattering

wavevectors ($q \to 0$), increasing the volume fraction the osmotic compressibility increases ($S(0) = k_B T \left(\frac{\partial \phi}{\partial \Pi} \right)_T$) (Holmqvist, Mohanty et al. 2012).

Below, the experimental static structure factor are fitted by the Percus – Yevick approximation for Hard Spheres in order to assess how close the response is to that of HS's (Pusey, Fijnaut et al. 1982). Fig. 4.9 presents the fitting for the three highest measured volume fractions (0.56, 0.52 and 0.44 c/c*) for various polydispersity values. We observe that for 0.56 and 0.52 c/c* the fitting is quite good for qR>2.5 for polydispersity σ=0.14, whereas for 0.44 c/c* for σ=0.1. However, at lower qR-values the discrepancy is rather high with the experimental data being quite higher than the theoretical model.

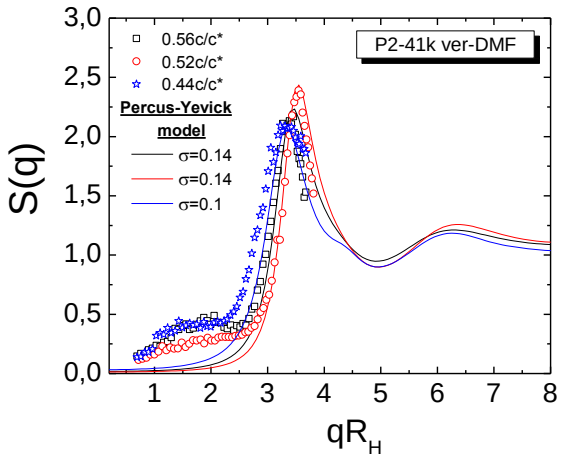

Fig. 4.9 – *Percus – Yevick approximation for the three highest volume fractions 0.56, 0.52 and 0.44 c/c* for P2-41k in ver-DMF.*

Fig. 4.10 depicts the Percus-Yevick approximations for volume fractions lower than 0.44c/c* (0.39, 0.33, 0.28 and 0.22c/c*), where we observe that it fails to describe the experimental data.

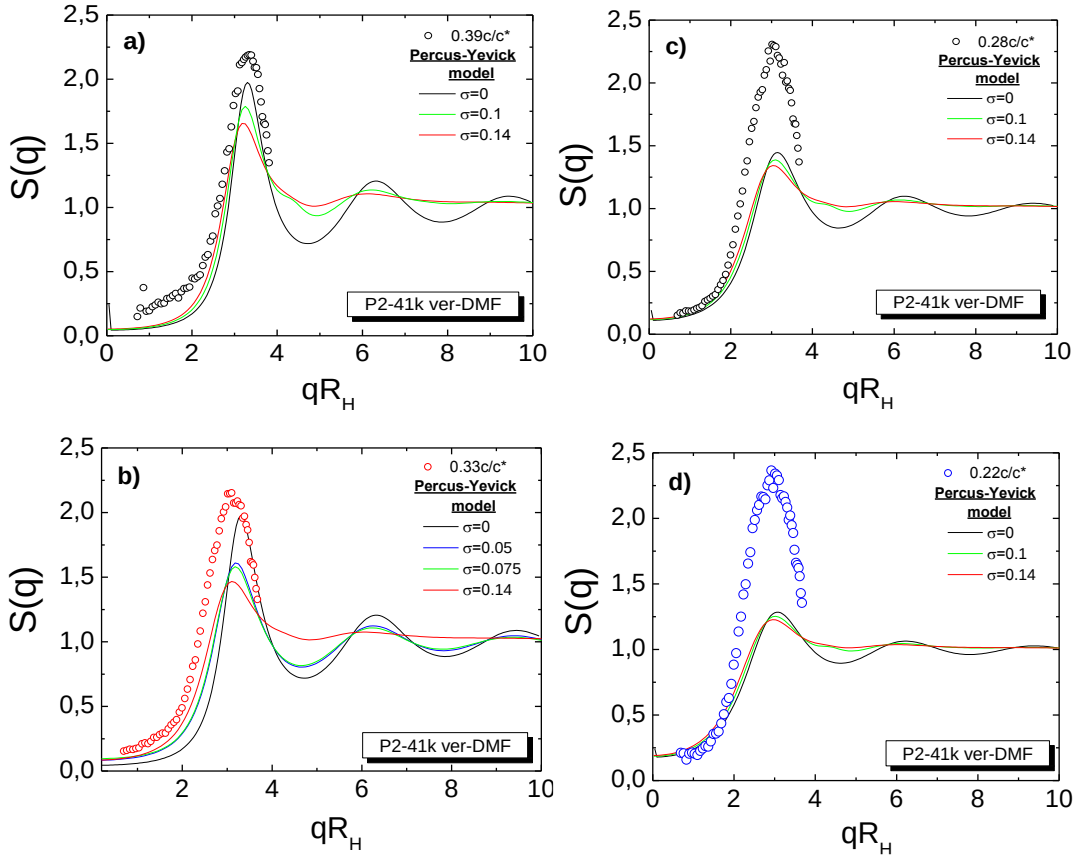

Fig. 4.10 – *Percus–Yevick approximation for various volume fractions.*

The qR_H position of the peak of structure factor reflects the distance between a particle and its first neighbours and it has a volume fraction dependency which is presented in the fig. 4.11. The mapping of the $q_{peak}R_H$ position of the peak of S(q) provides information about the interactions of this system. For comparison, it is also presented the $q_{peak}R_H$ for hard spheres, which was calculated using Percus-Yevick approximation in the liquid regime and the corresponding prediction in the case of charged spheres with long-range repulsive interactions, where the first neighbour particle-particle distance scales as $\phi^{-1/3}$. As we observe, the system P2-41k exhibits a similar volume fraction dependence with hard spheres.

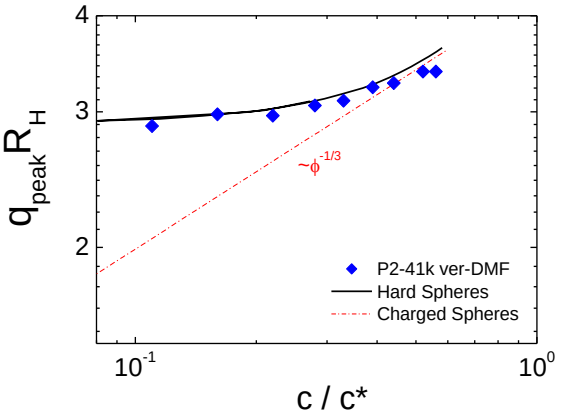

Fig. 4.11 – *Volume fraction dependence of peak position of S(q) and comparison of the experimental data with hard sphere and charge spheres' behaviour.*

Fig. 4.12a depicts the amplitude of the peak of S(q) as a function of volume fraction, which represents the probability of two neighbouring particles to be at distance $2\pi/q_{peak}$ and expresses how well defined the formed cage is. Hard sphere theory predicts that increasing the volume fraction the peak of S(q) increases as well, reaching the maximum amplitude of 2.85 in the liquid state (Hansen-Verlet criterion) (Hansen and Verlet 1969) while, beyond this value the sample acquires a crystal structure. However, here increasing the volume fraction, the soft core-shell particles tend to shrink leading to cancellation effects and variation of the form factor F(q), which results in inaccurate calculation of S(q) from the equation: $S(q)=\frac{I_{conc}^{total}(q)c_{dilute}T_{dilute}}{I_{dilute}(q)c_{conc}T_{conc}}$. This is probably the reason why the amplitude of the peak of S(q) for P2-41k is almost volume fraction independent.

The value of the structure factor S(q) at low q's is related to the osmotic compressibility through $S(0)=k_BT\left(\frac{\partial\phi}{\partial\Pi}\right)_T$, where Π is the osmotic compressibility (Pecora 2013) and is determined by the interaction potential between the particles. For semi-dilute and concentrated regime, the theoretical prediction of S(0) for hard spheres is given through $S(0)=\frac{(1-\phi)^4}{(1+2\phi)^2+\phi^3(\phi-4)}$ (Holmqvist, Mohanty et al. 2012). Fig. 4.12b shows the values of S(q) at low q's as a function of volume fraction.

We should mention that the value of S(q→0) was determined at the lowest measured q-value, which was at $qR_H \sim 0.69$. As we observe, the system follows within error the theory for hard spheres with regard to S(q→0).

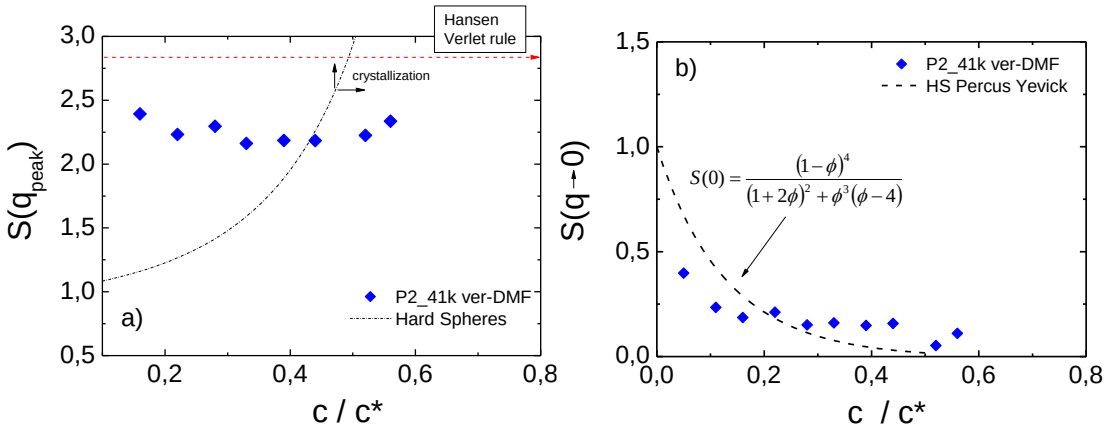

Fig. 4.12 *– a) Volume fraction dependence of the amplitude of peak of S(q). Dotted line denotes the Hard sphere prediction and the horizontal dashed line corresponds to Hansen-Verlet limit for HS crystal and b) Volume fraction evolution of S(q) at q→0. Dashed line represents HS theory.*

In contrast to the static intensity, dynamics are not affected by the possible changes of the single particle form factor F(q). Therefore, the dynamics measured by 3DDLS technique represent the relaxation of concentrated fluctuations at different q's through the cooperative or self-diffusion mechanisms. Fig. 4.13 shows typical normalized correlation functions of the scattered electric field C(q,t) from system P2-41k suspended in ver-DMF at various volume fractions for the highest possible measured wavevector ($q=0.0268nm^{-1}/\theta=130^o/qR_H=3.56$). We observe that increasing the volume fraction, the relaxation time becomes slower. Moreover, even at higher volume fractions, the correlation function decays almost as a single exponential, contrary to the hard spheres' behaviour, where a second slower mode is evolving related to the out-of-cage diffusion process.

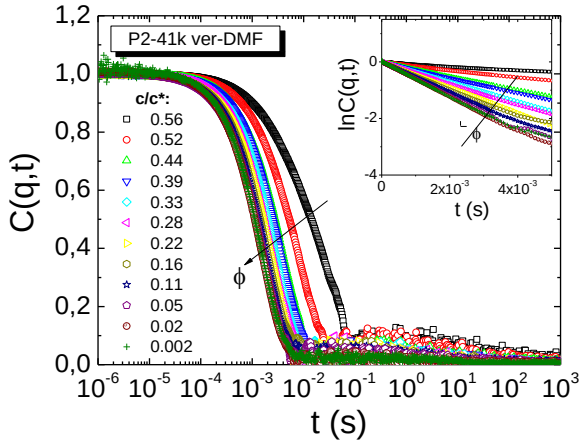

Fig. 4.13 – *Correlation function of time at different volume fractions (q=0.0268nm^{-1}/ϑ=130°). Inset: Same experimental data in ln-lin plot, which indicates the initial short-time decay.*

In the dilute regime, the dynamics are diffusive with a q-independent diffusion coefficient D(q). On the contrary, in the concentrated regime, the diffusion process is strongly affected by both hydrodynamic interactions between particles and the structural arrangements of the particles dictated by thermodynamics, which are reflected by S(q) according to the equation $D(q)=D_0H(q)/S(q)$. Thus, the diffusion coefficient D(q) is q-dependent, presenting a minimum value at the peak of S(q), which is connected with a slowing down of the dynamics due to the formed cage by the first neighbours. However, due to the small size of the particles, the qR_H regime probed is limited. Hence, the full information about the diffusion behaviour of the system is not accessible, as we cannot access high qR's where self-diffusion can be measured. Fig. 4.14a presents the volume fraction dependence of the normalized diffusion coefficient $D(q)/D_0$ as a function of qR_H for system P2-41k, where the influence of structure factor S(q) and hydrodynamic interactions H(q) are depicted. The D(q) is obtained by the initial (short-time) decay of the temporal correlation function C(q,t). For the normalization, we used the diffusion coefficient D_0 of a dilute/reference sample (0.001c/c*). At higher volume fractions (0.56 – 0.39 c/c*), we observe strong q-dependence with a clear minimum, which becomes less pronounced decreasing the volume fraction towards the dilute regime which is characterized by q-independence. Fig. 4.14b presents the volume fraction dependence of $D(q)/D_0$ as a function of qR_H for the larger particle P2-126k in ver-

DMF. For comparison reasons, hard sphere calculations at two volume fractions (0.46/solid and 0.2/dashed lines) according to Beenakker and Mazur's theory (Beenakker and Mazur 1984) are also presented at both fig. 4.14a and 4.14b. For both systems, the minimum of $D(q)/D_0$ is observed at similar qR values with those predicted for hard spheres, but for higher c/c*. We should also mention that the HS prediction for ϕ=0.2 overestimates the behaviour of the core-shell particles for c/c*=0.22. At low qR regime, the experimental data have much lower values of $D(qR \to low)$ than theory, possibly due to some particle clustering which leads to a decrease of D(q). Another possible reason of this discrepancy is the presence of stronger long range repulsions due to polymeric shell of the particles, which leads to a decrease of $1/[S(qR \to 0)]$ and of $D(qR \to 0)$ like in the case of PDMS-grafted silica particles studied by Petekidis et al. (Petekidis, Gapinski et al. 2004).

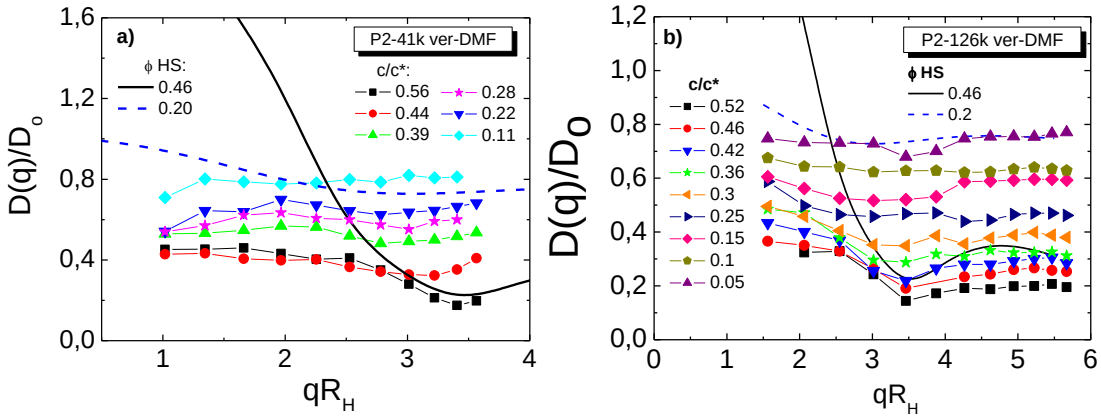

Fig. 4.14 – *Normalized diffusion coefficient $D(q)/D_0$ extracted by cumulant fits to the experimental data for the initial exponential decay for a) P2-41k and b) P2-126k in ver-DMF . Solid and dotted lines: Beenakker and Mazur calculation for hard spheres for volume fractions 0.46 and 0.2 (Beenakker and Mazur 1984).*

The effect of softness and permeability can be investigated by the structural cage diffusion coefficient $D_S(q_{peak})$, which is determined at the peak of structure factor S(q). At wavevector $q=q_{peak}$, dynamics and structures on a length scale comparable to the nearest-neighbour interparticle distance are probed (Segre, Behrend et al. 1995). Fig. 4.15a depicts the normalized $D_S(q_{peak})/D_0$ for various systems of different softness (P2-41k, P2-126k and P2-402k) as a function of c/c*,

which is compared with the theory of Segre et al. for the peak position of the structure factor for hard spheres (structural cage diffusion coefficient):

$$\frac{D_S(q_{peak})}{D_0} = \frac{1}{1 - 2\phi_{eff} + 5\phi_{eff}^2 - 200\phi_{eff}^3 + 347\phi_{eff}^4} \qquad (4.2)$$

where D_0 is the diffusion coefficient of the dilute sample (0.001c/c*) and ϕ_{eff} the effective volume fraction. This theory is valid for volume fractions until 0.1 <c/c*<0.5 (Segre, Behrend et al. 1995).

Fig. 4.15b depicts the normalized structural diffusion coefficient $D_S(q_{peak})/D_0$ as a function of the reduced free volume per particle $V/V_0=\pi/6\phi$, according to model introduced by Segre et al., where $V_0=(2R)^3$ (Segre, Behrend et al. 1995). The extrapolation of the reduced free volume to zero indicates the random close packing volume fraction, where the short-time structural diffusion coefficient $D_S(q_{peak})$, which expresses the motion at the length-scale of the cage, is zero. Hence, the random close packing volume fraction for P2-41k is $\Phi_{RCP}\approx0.95$, which is higher than the correspondent value for hard spheres ($\Phi_{RCP}\approx0.64$) (Segre, Behrend et al. 1995).

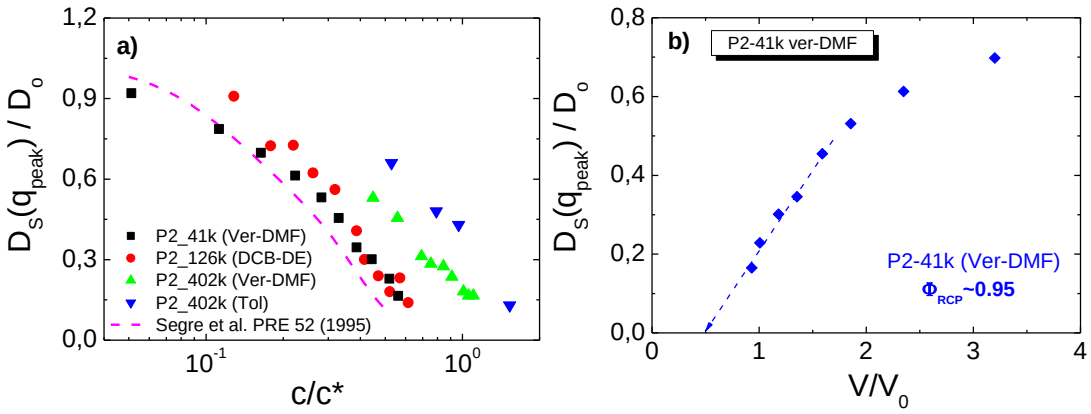

Fig. 4.15 – *a) Normalized diffusion coefficient $D_S(q_{peak})/D_0$ at the peak of S(q) for various systems of same nature but different softness. Solid line represents the model for hard spheres and b) $D_S(q_{peak})/D_0$ as a function of the reduced volume per particle for system P2-41k. The arrows indicate the RCP of the system.*

The dynamics at the limit of $qR \to 0$ represents the cooperative motion of the particles. Fig. 4.16 shows the normalized cooperative diffusion coefficient $D(qR \to 0)/D_0$ as a function of the volume fraction for the lowest qR measured. We compared the experimental data with Batchelor's theory for cooperative diffusion coefficient for hard spheres. In general, increasing the volume fraction, the cooperative diffusion coefficient is expected to increase due to the impact of thermodynamics and the decrease of $S(qR \to 0)$ reflecting the increasing osmotic compressibility of the sample. For the P2-41k, $D(qR \to 0)$ decreases with volume fraction in contrast to the expected HS behaviour. This is attributed either to large errors introduced due to the use of the lowest qR measured (q=0.00513nm^{-1} / qR_H=0.68), or clustering or stronger long range repulsions due to polymeric shell of the particles, resulting in a decreased $D(qR \to 0)$.

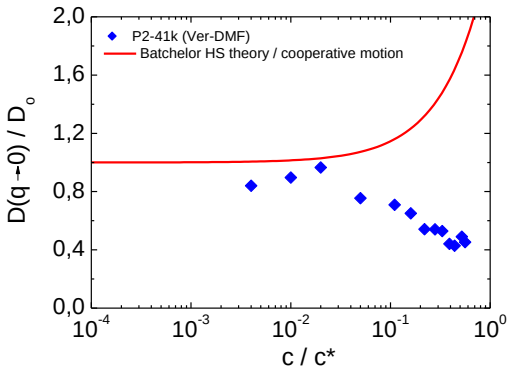

Fig. 4.16 – *Normalized cooperative diffusion coefficient as a function of volume fraction for P2-41k in ver-DMF. Solid line represents the Batchelor's HS theory for cooperative diffusion coefficient.*

4.3.3 Glassy regime

Increasing the volume fraction we enter the glassy regime, where dynamics are strongly non-ergodic. For the investigation of slow dynamics in this regime, we used the Multispeckle Dynamic Light Scattering technique (MSDLS).

4.3.3.1 Dynamic properties

Below, we explored the dynamics of the core-shell systems P2-41k and P2-126k used for the 3DDLS experiments, in the glassy regime. Both systems are suspended in the mixture of solvents veratrole-DMF. P2-41k was studied at volume

fractions 0.81 and 0.77c/c*, whereas the system P2-126k at 0.75 and 0.68c/c*. The samples were placed in NMR cells in order to minimize multiple scattering contributions. The rejuvenation was performed by mixing the probed sample with a stainless steel ball immersed in the solution.

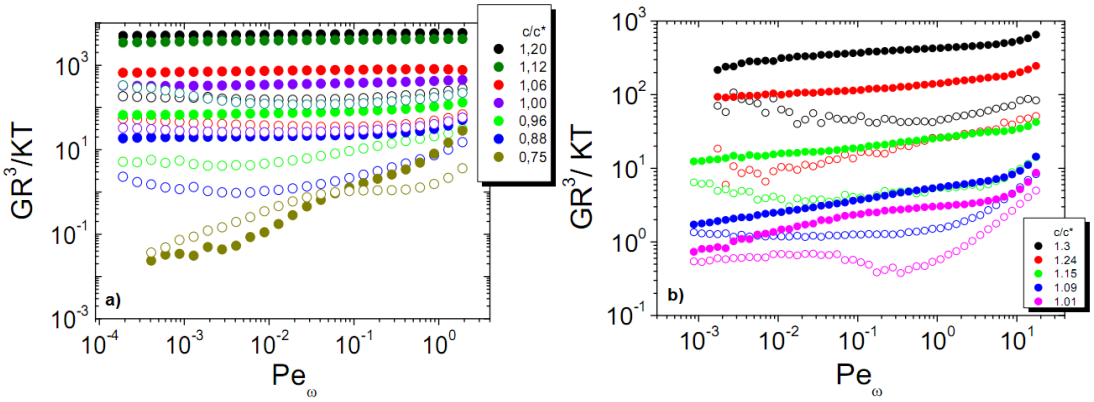

Fig. 4.17 – *Dynamic frequency sweeps for various volume fractions for a) P2-41k in ver-DMF solvent mixture and b) P2-126k in veratrole solvent. Solid symbols represent G' and open symbols G''. Adapted from PhD thesis of A. Pamvouxoglou.*

Linear viscoelastic measurements for P2-41k at c/c* close to the ones that we study, which were performed from A. Pamvouxoglou during his PhD thesis (Pamvouxoglou A., PhD thesis, chapter 5, fig. 5.6, p.141, 2014) (fig. 4.17a), reveal that the volume fraction 0.88c/c* is at the glassy regime presenting a typical glassy behaviour with G'>G'' at all probed angular frequencies. In contrast, at 0.75c/c* multiple relaxation processes are observed with a solid-like behaviour at high frequencies and a liquid-like one at intermediate and low ones. However, at low frequencies, the storage and the viscous moduli do not obey to the power law dependence implying the tendency of the sample to acquire again a solid-like behaviour at even lower frequencies that are not experimentally accessible.

Correspondent rheological measurements have not been done for P2-126k in mixture of solvents ver-DMF, allowing us the direct comparison between light scattering and rheological measurements. Nevertheless, the system P2-126k has been studied in linear viscoelastic regime in veratrole solvent by A. Pamvouxoglou (Pamvouxoglou A., PhD thesis, chapter 5, fig. 5.7, p.142, 2014) (fig. 4.17b), who

explored volume fractions between 1.3-1c/c*. In this range the system exhibits a glassy behaviour. The volume fractions that we study in ver-DMF are 0.75 and 0.68c/c*. Attempting to make an indirect comparison, the probed volume fractions perhaps are glasses or supercooled liquids near-glass regime with slow dynamics.

Fig 4.18 presents the angular dependence of the system P2-41k for 0.81c/c* and 0.77c/c*, which took place at time t_w=244s and t_w=60s respectively after rejuvenation. For 0.81c/c*, the correlations functions of time consist of three separate correlation functions merged all together, one taken from the fiber (PMT) (single speckle detection) and two from the camera at different frame rates (82 and 2fp/s), whereas for 0.77c/c*, the correlation functions were fully measured by PMT. In both cases, a double stretched exponential fit was used to fit the two relaxation processes. At 0.81c/c*, a quite strong non-ergodic plateau is noticed, while slow dynamics are of the order of 10s. At 0.77c/c*, a weak non-ergodic plateau is observed with slow dynamics being one order less than 0.81c/c*. Nevertheless, as we already mentioned, both volume fractions are in glassy regime.

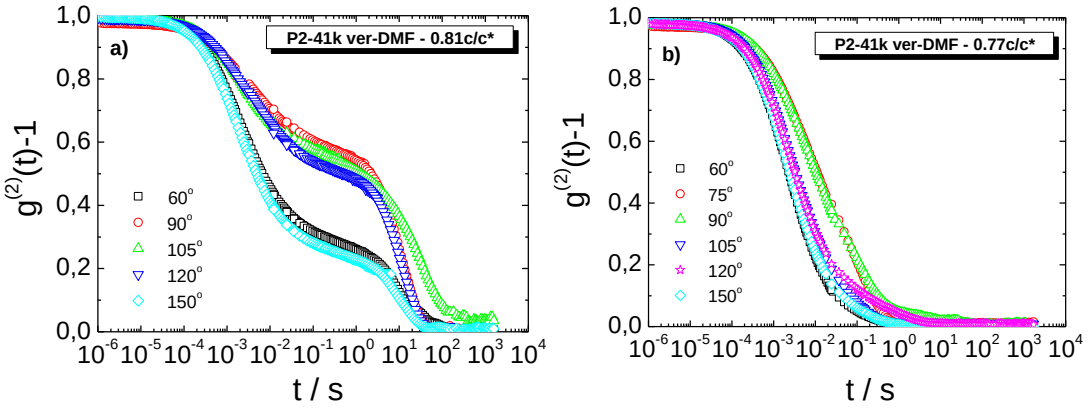

Fig 4.18 *- Angular dependence of the intermediate scattering function for P2_41k at a) 0.81c/c* and b) 0.77c/c* after rejuvenation.*

As we already mentioned in the 3DDLS experiments performed in the liquid state, the peak position of S(Q) of the highest measured volume fraction (0.56c/c*) and therefore the minimum of D(q) (D(q)~1/S(q)) for systems P2-41k is around qR=3.39 (q=0.025nm^{-1} / θ=116°). Fig. 4.19a and 4.19b depicts the normalized short-time diffusion coefficient $D(q)/D_o$, extracted by the relaxation processes at different

angles, for the fast process, which is related to the in-cage diffusion. We observe that $D(q)/D_o$ is strongly q-dependent for both volume fractions 0.81 and 0.77c/c*, presenting a slowing down around the point that corresponds to the peak position of S(q) for the liquid state.

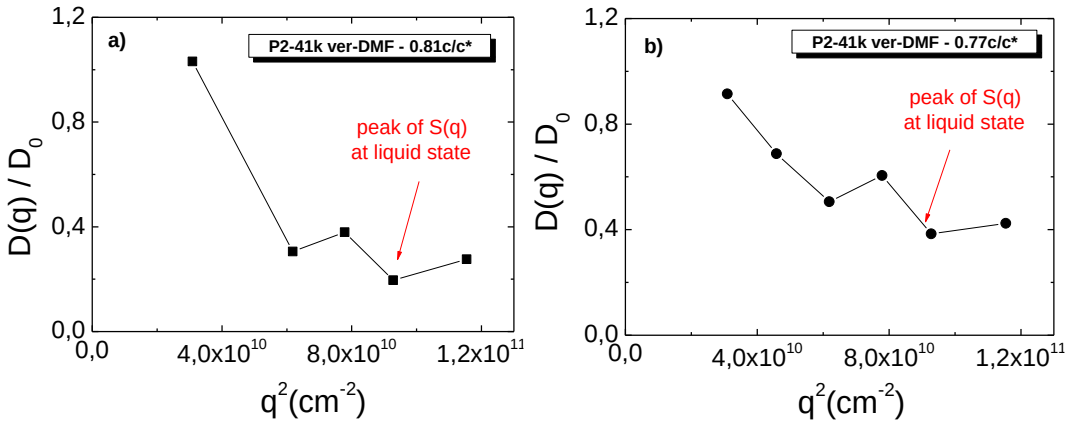

Fig 4.19 – *Normalized short-time self-diffusion $D(q)/D_o$ for the fast process at different q's for a) 0.81 and b) 0.77c/c*.*

Fig. 4.20 depicts the long-time self-diffusion coefficients extracted by the slow processes at different angles for both 0.81 and 0.77c/c* of P2-41k. Black symbols refers to the diffusion coefficient that uses the average relaxation time $\tau_{av} = (\tau/\beta) * \Gamma(1/\beta)$, where β is the stretching exponent factor and Γ(x) the gamma function, while red symbols refer to the slowest relaxation time τ extracted by KWW fit. We observe that long-time diffusion coefficient presents q-dependence too.

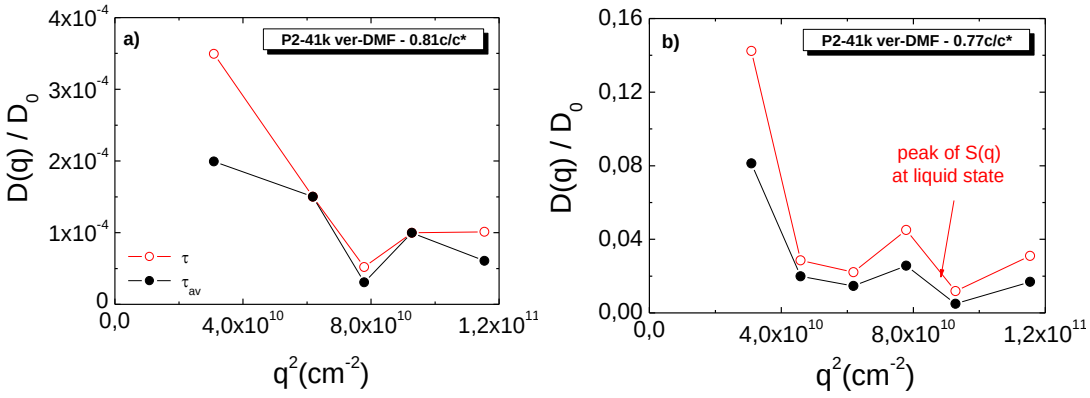

Fig 4.20 – *Normalized long-time self-diffusion $D(q)/D_o$ for the slow process at different q's for a) 0.81 and b) 0.77c/c*.*

4.3.3.2 Ageing

We also followed ageing in the glassy regime, where both systems exhibit non-stationary dynamics with time. The dynamics in glassy regime becomes gradually slower as the sample ages until it reaches its equilibrium configuration, spending more and more time in the metastable states it visits. For P2-41k, monitoring the evolution of the slowest relaxation time through MSDLS, we observed a glass-crystal re-entrant transition. A similar transition was also observed for system P2-126k after long-time from rejuvenation due to high polydispersity.

Firstly, we measured the time evolution of the degree of correlation $c_I(t_w,\tau)$ for volume fractions 0.81 and 0.77c/c* of system P2-41k in mixture of solvent Ver-DMF as a function of the waiting time t_w after rejuvenation.

In general, for a system in steady state the degree of correlation is steady increasing the waiting time. When the $c_I(t_w,\tau)$ increases with time, the relaxation process slows down. For 0.81c/c* (fig. 4.21a), the degree of correlation $c_I(t_w,\tau)$ reaches a stable state at around t_w~10^4s. Until then, the dynamics slows down, as the system gets kinetically trapped in deeper energy minima and the particles are constrained more efficiently by their neighbours. After t_w~340000s (~4 days) the particles acquire a more ordered structure which leads to locally enhanced free volume resulting in faster particle dynamics similarly to what has been observed in star polymers (Stiakakis, Wilk et al. 2010). Then the system reaches a second and possibly final steady state that is related to crystal formation at long times, also visible by bare eye (see fig. 4.24). For volume fraction 0.77c/c*, we see (fig. 4.21b) that the $c_I(t_w,\tau)$ reaches a stable state at around t_w~1500s. Similarly to the higher volume fraction, until then, the slow relaxation process keeps slowing down. Once, the transient stable state is reached, the dynamics is steady with time. At waiting time around t_w~1500s, the degree of correlation $c_I(t_w,\tau)$ starts decreasing, denoting a speed up of the relaxation that leads to the second and final steady state.

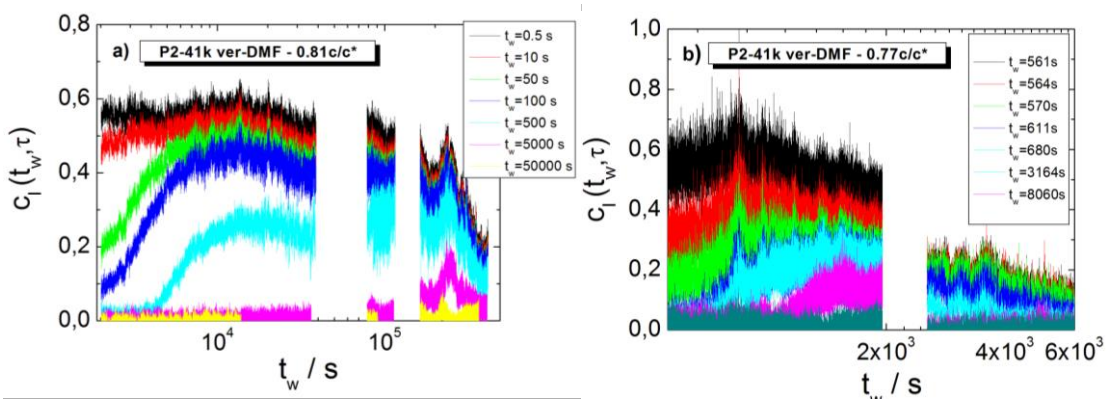

Fig 4.21 – *Degree of correlation at different delay times for P2_41k for a) 0.81 and b) 0.77c/c*.*

The intermediate scattering functions extracted by the degree of correlation for 0.81 and 0.77c/c* are depicted in fig. 4.22a and 4.22b respectively. In both cases the intermediate scattering function consists of two modes, where the first one is related to the motion of the particles inside the cages formed by their neighbours whereas the second one with their out-of-cage motion. We can notice that for 0.81c/c* the fast modes changes with sample ageing, whereas for 0.77c/c* remain unchanged.

Similarly to the behaviour of the degree of correlation, for volume fraction 0.81c/c*, we observe that increasing the waiting time the intermediate scattering function slows down until waiting time t_w~340000s. Then, the dynamics speed up, leading to the crystal formation which is homogeneous through all the sample's volume. For 0.77c/c*, the intermediate scattering function slows down until around t_w~1542s and then dynamics becomes faster, denoting the onset of the crystal growth. We should mention that, at 0.77c/c*, a liquid-crystal coexistence is observed, with crystalline regime obtaining the biggest volume of the sample, whereas the liquid area is restricted in a small area in the upper part of the sample (see fig. 4.24b).

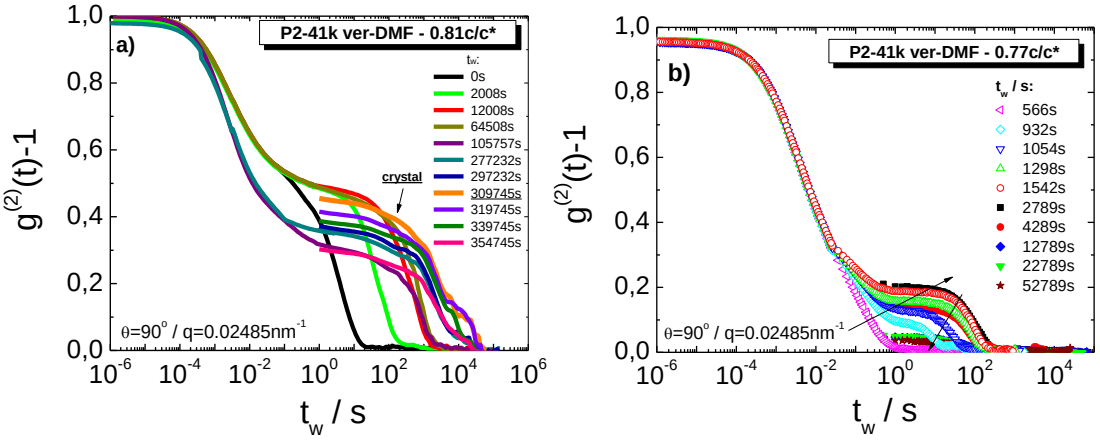

Fig 4.22 – *The intermediate scattering function at ϑ=90°/q=0.02487nm^{-1}/qR$_H$=3.31 for a) 0.81 and b) 0.77c/c*.*

Fig. 4.23 presents the changes of the amplitude of the non-ergodic plateau as the time elapses. For 0.81c/c*, the non-ergodic plateau drops and then passes through a peak, which corresponds to the onset of crystallization, before decrease again. For 0.77c/c* where the crystallization is much faster compared to 0.81c/c*, the amplitude of the non-ergodic plateau exhibits a peak that denotes the crystal growth and then decreases reaching the final stable state.

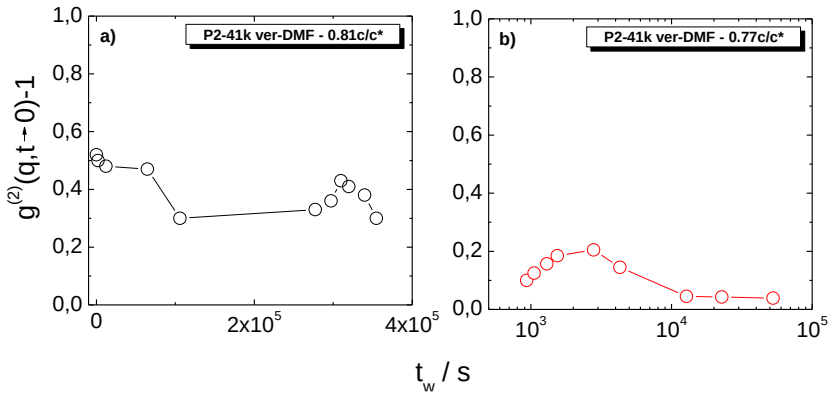

Fig 4.23 – *The amplitude of the non-ergodic plateau of the intermediate scattering function at ϑ=90°/q=0.02487nm^{-1}/qR$_H$=3.31 for a) 0.81 and b) 0.77c/c*.*

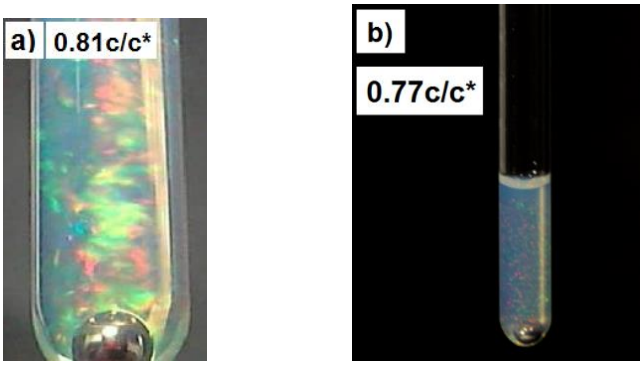

Fig. 4.24 – *a) Crystal formation for 0.81c/c* after t_w~340000s and b) 0.77c/c* after t_w~1542s from rejuvenation.*

Fig. 4.25 depicts the evolution of the slowest relaxation time (τ_{slow}), at q=0.025nm^{-1}, which is extracted by the fitting of the intermediate scattering function with a stretched KWW fit.

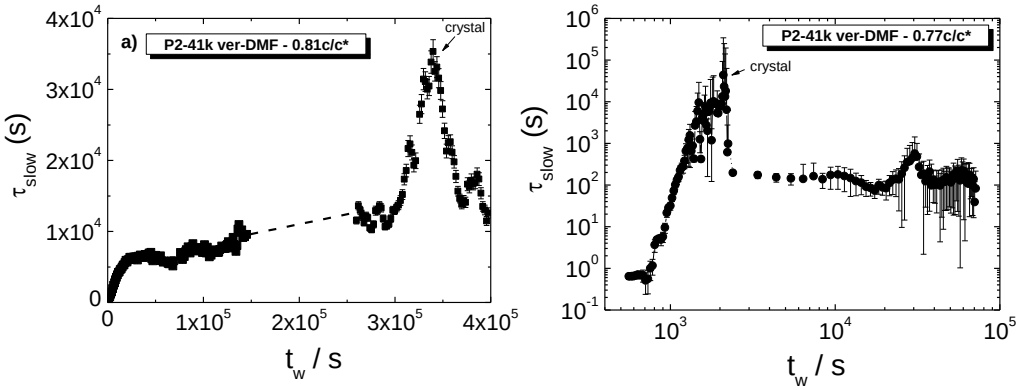

Fig. 4.25 – *The evolution of the slowest relaxation time (t_{slow}), at q=0.025nm^{-1} for a) 0.81 and b) 0.77c/c*.*

Fig. 4.26 shows the evolution of the intermediate scattering function of the system P2-41k, in mixture of solvents veratrole-DMF, for various volume fractions from dilute to glassy regime. Increasing the volume fraction, the relaxation slows down. It is also presented the evolution of the dynamics for 0.77c/c* and 0.81c/c* after rejuvenation and after the spontaneous crystallization.

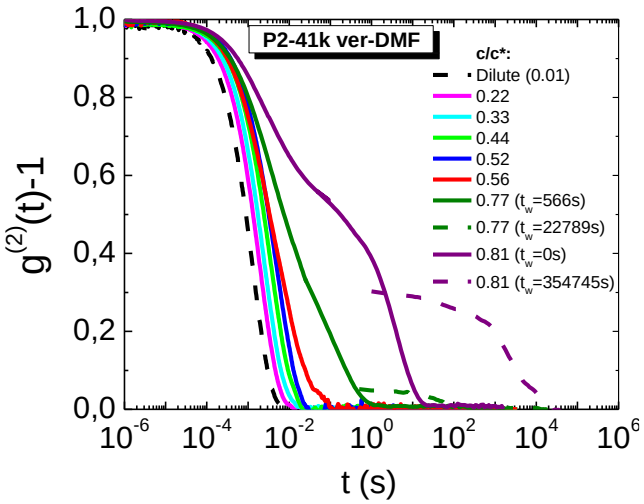

Fig. 4.26 - *Intermediate scattering functions for P2_41k in veratrole-DMF in the volume fraction range 0.22-0.81c/c*. 3DDLS technique is used up to 0.56c/c* and MSDLS for 0.77 and 0.81c/c*. The correlation function for a dilute P2-41k sample is shown with a black dashed line for comparison.*

Dynamics and ageing of the system P2-126k in ver-DMF were also investigated. Similar to system P2-41k, we monitored the evolution of the slowest relaxation time in order to explore dynamics at 0.75 and 0.68c/c* and detect the existence or not of a glass-crystal re-entrant transition.

The degree of correlation used in order to extract the intermediate scattering functions for volume fractions 0.75 and 0.68c/c*, which are presented in fig. 4.27a and 4.27b respectively. For volume fraction 0.75c/c*, we observe that increasing the waiting time the intermediate scattering function slows down until t_w~84667s, where a stable state is reached, while the non-ergodic plateau decreases significantly. This stable state is temporary since dynamics start slowing down again between t_w~373000-1330000s. Then dynamics speed up until t_w~1500000s where second stable state is reached. Contrary to P2-41k, the system P2-126k does not seem to reach a crystal state at the specific explored time-window. The “frozen” particles of this system age towards deeper energy landscape minima, reaching temporary states that they can locally diffuse faster. A possible reason for the lack of crystallization is polydispersity which is 16% according to the fitting of the form factor in dilute regime with the homogenous core/inhomogeneous shell model. When the polydispersity is sufficiently high enough (>8%), it provokes destabilization

of the crystal and hence the crystallization seems to be completely supressed (Zaccarelli, Valeriani et al. 2009). Another reason is the time of the monitoring of the dynamics, which probably is not long enough in order to observe crystal growth.

For 0.68c/c*, the intermediate scattering function speeds up just after the rejuvenation until around t_w~24500s, where a "temporal" stable state is reached, while the contrast dramatically drops without any visual signs for formation of crystal. Similar to 0.77c/c*, the particles may acquire the maximum local ordering for the investigated time window, with high polydispersity hindering the long-range crystallization.

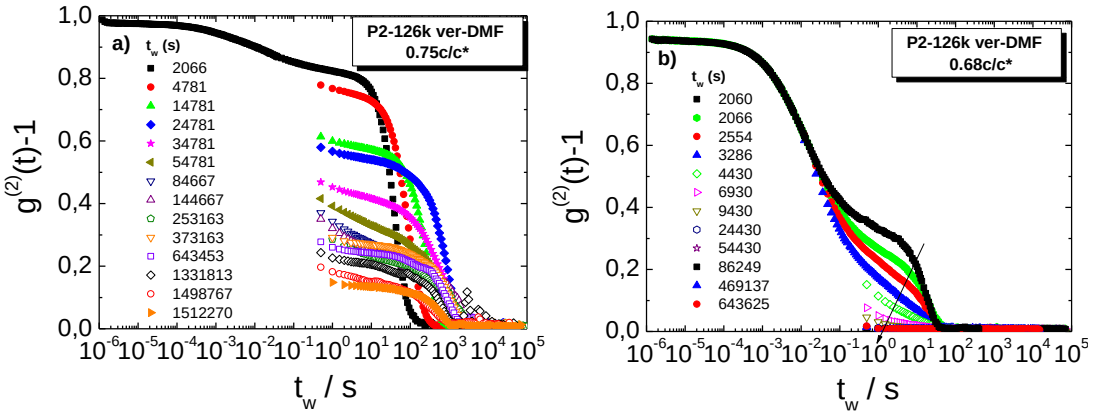

Fig 4.27 – *The intermediate scattering function at ϑ=90°/q=0.02487nm^{-1}/qR_H=3.31 for a) 0.75 and b) 0.68c/c*.*

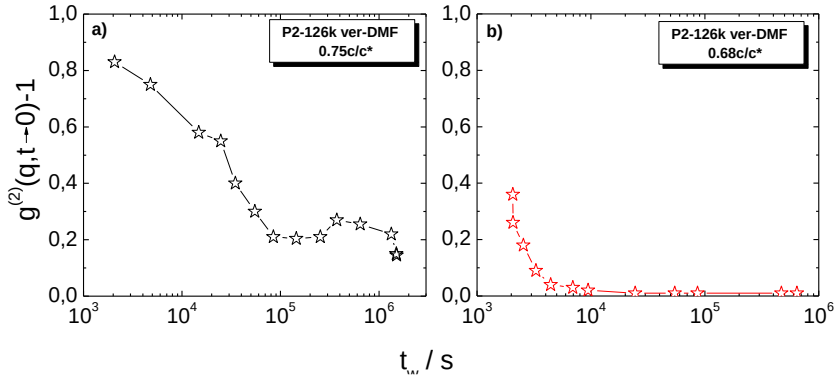

Fig 4.28 – *The amplitude of the non-ergodic plateau of the intermediate scattering function at ϑ=90°/q=0.02487nm^{-1}/qR_H=3.31 for a) 0.75 and b) 0.68c/c*.*

Fig. 4.28 shows the waiting time dependence of the amplitude of the non-ergodic plateau. For 0.75c/c*, the non-ergodic plateau drops reaching the

"temporal" stable state that we also observed before and probably is not the last one. Then the non-ergodic plateau strengthens before weakening again and reaching another state. For 0.68c/c*, we observe a continuous collapse of the plateau before reaching the stable state.

After 6 months from rejuvenation, at 0.68c/c* of P2-126k in ver-DMF, a liquid-crystal coexistence is finally detected, with crystalline area obtaining the biggest volume of the sample and being inhomogeneous, probably due to size segregation, whereas the liquid regime was restricted in a smaller area in the upper part of the sample (see fig. 4.29).

Fig 4.29 – *Crystal formation for 0.68c/c* of P2-126k in ver-DMF after almost 6 months from rejuvenation.*

4.4 Conclusions

Liquid regime:

3D Dynamic Light Scattering technique was used for the investigation of structure and dynamics of a wide range of concentrated suspensions of grafted polymer core-shell colloidal particles. In the dilute regime, we characterized the particles in terms of size, inter-particle interactions and the determination of the effective volume fraction. In concentrated suspensions, structural properties of core-shell particles deviate from hard spheres probably due to form factor changes that do not allow us to measure properly the S(q).

Apart from static properties, dynamic properties were also investigated. Until volume fraction 0.56c/c*, the correlation function remains single exponential,

contrary to the hard spheres' behaviour, where a second and slower mode is appeared which is related to the out-of-cage diffusion process. Moreover, the concentration dependence of the structural diffusion coefficient studied, presenting a minimum around the peak position of the S(q) and contrasted with theoretical predictions for hard spheres. Finally, the random close packing volume fraction was determined around $\Phi_{RCP}\approx 0.95$ by plotting the structural diffusion coefficient as a function of free volume at the limit of $D_s(q_{\min} \to 0)$ which is much higher than the RCP of hard spheres.

Glassy regime / Ageing:

Multispeckle Dynamic Light Scattering technique (MSDLS) was used to investigate the transient evolution of the dynamics at glassy regime, which is due to strong residual stresses and interpenetration. The slowest relaxation time increases with waiting time, since in glassy regime the particles are in almost "frozen" cages which age towards deeper energy landscape minima. In both P2-41k and P2-126k systems, which represent monodisperse and polydisperse case respectively, the structural rearrangements led to creation of larger free volume locally via progressive ordering of the particles and thus crystallization. The polydispersity though slows down significantly the evolution of the phenomenon and affects the homogeneity of the final crystal.

References:

Beenakker, C. and P. Mazur (1984). "Diffusion of spheres in a concentrated suspension II." Physica A: Statistical Mechanics and its Applications **126**(3): 349-370.

Berne, B. (1976). J. and Pecora, R.," Dynamic Light Scattering, Wiley, New York.

Chrissopoulou, K., et al. (2001). "Dynamics of the Most Probable Composition Fluctuations of "Real" Diblock Copolymers near the Ordering Transition." Macromolecules **34**(7): 2156-2171.

Cipelletti, L. and L. Ramos (2005). "Slow dynamics in glassy soft matter." Journal of Physics: Condensed Matter **17**(6): R253.

Daoud, M. and J. Cotton (1982). "Star shaped polymers: a model for the conformation and its concentration dependence." Journal de Physique **43**(3): 531-538.

Eckert, T. and W. Richtering (2008). "Thermodynamic and hydrodynamic interaction in concentrated microgel suspensions: Hard or soft sphere behavior?" The Journal of Chemical Physics **129**(12): 124902.

El Masri, D., et al. (2009). "Dynamic light scattering measurements in the activated regime of dense colloidal hard spheres." Journal of Statistical Mechanics: Theory and Experiment **2009**(07): P07015.

Foffi, G., et al. (2003). "Structural arrest in dense star-polymer solutions." Physical review letters **90**(23): 238301.

Förster, S., et al. (2010). "Scatter: software for the analysis of nano-and mesoscale small-angle scattering." Journal of Applied Crystallography **43**(3): 639-646.

George, A. and W. W. Wilson (1994). "Predicting protein crystallization from a dilute solution property." Acta Crystallographica Section D: Biological Crystallography **50**(4): 361-365.

Hansen, J.-P. and L. Verlet (1969). "Phase transitions of the Lennard-Jones system." physical Review **184**(1): 151.

Holmqvist, P., et al. (2012). "Structure and dynamics of loosely cross-linked ionic microgel dispersions in the fluid regime." Physical review letters **109**(4): 048302.

Ohno, K., et al. (2005). "Synthesis of monodisperse silica particles coated with well-defined, high-density polymer brushes by surface-initiated atom transfer radical polymerization." Macromolecules **38**(6): 2137-2142.

Pecora, R. (2013). Dynamic light scattering: applications of photon correlation spectroscopy, Springer Science & Business Media.

Petekidis, G., et al. (2004). "Dynamics of core-shell particles in concentrated suspensions." Physical Review E **69**(4): 042401.

Pusey, P. (1991). Liquids, freezing and the glass transition, North-Holland: Amsterdam.

Pusey, P., et al. (1982). "Mode amplitudes in dynamic light scattering by concentrated liquid suspensions of polydisperse hard spheres." The Journal of Chemical Physics **77**(9): 4270-4281.

Pusey, P. and W. Van Megen (1986). "Phase behaviour of concentrated suspensions of nearly hard colloidal spheres." Nature **320**(6060): 340-342.

Robert, A., et al. (2008). "Dynamics in dense suspensions of charge-stabilized colloidal particles." The European Physical Journal E: Soft Matter and Biological Physics **25**(1): 77-81.

Saluja, A., et al. (2010). "Diffusion and sedimentation interaction parameters for measuring the second virial coefficient and their utility as predictors of protein aggregation." Biophysical journal **99**(8): 2657-2665.

Segre, P., et al. (1995). "Short-time Brownian motion in colloidal suspensions: Experiment and simulation." Physical Review E **52**(5): 5070.

Sigel, R., et al. (1999). "Structural relaxation of dense suspensions of soft giant micelles." Physical review letters **83**(22): 4666.

Stiakakis, E., et al. (2010). "Slow dynamics, aging, and crystallization of multiarm star glasses." Physical Review E **81**(2): 020402.

Utiyama, H. (1972). "Calibration and correction factors." Light Scattering from Polymer Solutions. MB Huglin, editor. Academic Press, London.

Van Megen, W., et al. (1985). "Measurement of the wave-vector dependent diffusion coefficient in concentrated particle dispersions." The Journal of Chemical Physics **82**(1): 508-515.

Voudouris, P., et al. (2009). "Effect of shell architecture on the static and dynamic properties of polymer-coated particles in solution." Macromolecules **42**(7): 2721-2728.

Watzlawek, M., et al. (1999). "Phase diagram of star polymer solutions." Physical review letters **82**(26): 5289.

Zaccarelli, E., et al. (2009). "Crystallization of hard-sphere glasses." Physical review letters **103**(13): 135704.

Zimm, B. H. (1948). "Apparatus and methods for measurement and interpretation of the angular variation of light scattering; preliminary results on polystyrene solutions." The Journal of Chemical Physics **16**(12): 1099-1116.

Chapter 5

Structure, dynamics and mechanical properties of thermosensitive core-shell microgels

We present an experimental study of structure, dynamics and mechanical properties of electrostatically stabilized aqueous suspensions of microgels. Two different microgel systems used which comprise of a rigid core, onto which a PNIPAM shell crosslinked by 5%wt of MBAM, is affixed that is responsible for the introduction of the thermoresponsive character to microgels. Both systems have the same core size but different shell size allowing the comparison of the effect of particle softness on their dynamics and mechanical properties. When the temperature is below the Lower Critical Solution Temperature (T<LCST) the PNIPAM shell swells because of good solvent conditions, while for temperatures above the LCST, the shell collapses due to unfavourable conditions created by hydrogen bonding between amide groups and the aqueous solvent.

We used dynamic and static light scattering in dilute regime in order to determine the temperature dependent hydrodynamic radius R_H of the core-shell microgels and get a better insight into the intermolecular interactions developed between them. The thermoresponsive character of these particles allows, under specific conditions, to gradually tune the interactions from repulsive to attractive, providing the ability in concentrated regime to switch between glass, liquid and gel states. Diffusive wave spectroscopy was used for probing dynamics of highly multiple scattering suspensions and monitoring ergodic (liquid state) to non-ergodic (glass or gel state) transitions. Moreover, confocal laser scanning microscopy at rest used for

direct visualization of the structural ordering at various temperatures although imaging, due to multiple scattering, was not possible beyond few first layers. Finally, rheology was employed to study the linear and non-linear viscoelastic properties of the microgels in these three different states.

5.1 Introduction

The physical state of a colloidal suspension is strongly affected by the volume fraction of the particles and the inter-particle interactions. The simplest case is that of colloidal hard spheres that are governed by entropy which is directly related to the particle volume fraction (Pusey 1991). A wider variety of phases, such as fluids, gels, crystals and glasses can be created by introducing enthalpic contributions, either repulsive or attractive (Pusey and Van Megen 1986, Pusey and van Megen 1987, Mason and Weitz 1995, Gasser, Weeks et al. 2001, Chen and Schweizer 2004, Zaccarelli 2007, Pusey 2008). Last decade, the focus of soft matter community has moved to soft colloids which consist of a class of particles where the average interparticle distance can be smaller than the particle diameter and correspondingly the effective interaction potential shows a finite repulsion at or beyond contact (Mohanty, Paloli et al. 2014).

Cross-linked microgels constitute a subclass of soft particles that their nature lies between that of hard sphere colloids and ultra-soft polymeric colloids such as star polymers (Likos, Löwen et al. 1998, Laurati, Stellbrink et al. 2007). Microgels can undergo reversible volume phase transitions upon variations of external stimuli, such as temperature, pH and solvent quality (Bonham, Faers et al. 2014).

Thermosensitive microgels facilitate the control of various colloidal properties by means of temperature. The most widely studied water-swellable microgel system is poly(N-iso-propylacrylamide) (PNIPAM) which is readily synthesized by free-radical precipitation polymerization (Pelton and Chibante 1986). PNIPAM undergoes thermally induced de-swelling when the solution temperature is increased above the lower critical solution temperature (LCST~32^{o}C) (Schild 1992, Saunders and Vincent 1999). Water behaves as a good solvent through hydrogen

bonding with the amide groups at temperatures below the LCST. However, this hydrogen bonding with water is increasingly disrupted upon temperature increase, causing water to act as a poorer solvent and gradually leading to collapse of the particles at temperatures above the LCST (Saunders and Vincent 1999). This remarkable shrinking of microgels with increasing temperature, which has been extensively studied (Wu and Zhou 1995, Saunders and Vincent 1999, Gilányi, Varga et al. 2000, Gan and Lyon 2001, Wu, Huang et al. 2003, Wu, Zhou et al. 2003, Ballauff and Lu 2007), favors the manipulation of the effective volume fraction ϕ_{eff} of microgel suspensions by simple temperature changes, while the mass concentration and thus the number density is kept constant (Senff and Richtering 1999). This advantage is used in almost any experimental technique, where the sample is prepared in fluid-like state at low volume fraction by imposing high temperature and subsequently quenched to the solid-like states by decreasing the temperature and thus inflating the microgels and reaching higher volume fraction. This protocol ensures the elimination of all previous history, caused by shear or mechanical deformation of the suspension (Cloitre, Borrega et al. 2000, Crassous, Siebenbürger et al. 2006, Rogers, Vlassopoulos et al. 2008, Sessoms and Bischo 2009).

Another major property of thermosensitive microgels is the temperature control of the particle-particle interaction potential (Wu, Huang et al. 2003, Stieger, Pedersen et al. 2004). The interaction potential is repulsive at temperatures below the LCST, while becomes attractive at temperatures above the LCST. Apart from temperature, the particle interaction potential strongly depends on the crosslinking density. At low crosslinking densities, microgels are highly soft exhibiting a behavior similar to polymer suspensions, while at high crosslinking densities microgels are more rigid and almost impenetrable similar to hard spheres. Finally, at intermediate crosslinking densities, microgels start to resemble the behavior of multiarm star polymers or block copolymer micelles (Wolfe and Scopazzi 1989, Senff and Richtering 1999).

These unique physical properties of microgels allow them showing a much richer phase behavior comparing to hard spheres. Their ability to compress and

partially interpenetrate, facilitate the packing to effective volume fractions far above close packing fraction, ϕ_{cp}, resulting in interesting structural and dynamical properties (Mattsson, Wyss et al. 2009, Sessoms and Bischo 2009, Zhang, Xu et al. 2009, Scheffold, Díaz-Leyva et al. 2010, Paloli, Mohanty et al. 2013). A concentrated microgel suspension at room temperature, where the particles are swollen, is dominated by short-range repulsive interactions, presenting a solid-like behavior due to increased spatial constraints. Increasing the temperature, the effective volume fraction decreases due to shrinking of the particles and at the LCST a solid-liquid transition is observed as particles are free to move. At temperatures above the LCST, the interaction potential changes from repulsive to attractive leading to a liquid-solid transition due to an incipient phase separation and the formation of a percolated network. Various experimental techniques such as rheology (Senff and Richtering 1999, Senff, Richtering et al. 1999, Carrier and Petekidis 2009, Sessoms and Bischo 2009, Appel, de Lange et al. 2015, Appel, Fölker et al. 2016), scattering techniques (Dingenouts, Norhausen et al. 1998, Stieger, Lindner et al. 2004, Stieger, Pedersen et al. 2004, Sessoms and Bischo 2009, Scheffold, Díaz-Leyva et al. 2010) and confocal microscopy (Royall, Williams et al. 2008, Kodger and Sprakel 2013, Paloli, Mohanty et al. 2013, Mohanty, Paloli et al. 2014, Yunker, Chen et al. 2014, Appel, de Lange et al. 2015) have been used in order to explore thoroughly the internal structure of the microgel particles during the phase transitions in a temperature range where the systems transform from a liquid to a glass of from a glass to a colloidal gel. Moreover, many investigations have extensively studied the flow behavior of microgel suspensions well below and above the LCST and the flow-induced microstructural changes (Buscall 1994, Senff and Richtering 1999, Deike, Ballauff et al. 2001, Stieger, Richtering et al. 2004). At low volume fractions, microgels display a Newtonian response to shear, whereas at high concentrations they shear thin as other colloidal systems (Wolfe and Scopazzi 1989).

5.2 Materials

We used temperature-sensitive composite core-shell particles which consists of a rigid fluorescently labeled (Nile red) trifluorethyl methacrylate (TFEMA) core of 85nm radius, onto which a Poly(*N*-isopropylacrylamide) (PNIPAM) shell is affixed. The composition of the microgel shell determines the thermosensitive behavior of the composite particles (Liu, Fraylich et al. 2009). The composite microgels are electrostatically stabilized by sulfonate groups at their periphery and suspended in water. Two systems of composite particles with similar thermoresponsive characteristics and different shell size and therefore different softness, are synthesized in two step-procedure according to the process described by (Appel, de Lange et al. 2015). In the shell of both systems, NIPAM is copolymerized by 5%wt. N, N'-methylenebis(acrylamide) (MBAM), TFEMA/PNIPAM, which introduces a thermoresponsive character to microgels. The total size of the particles of the first system is around D~900nm at T=20^{o}C, whereas the diameter of the second one around D~500nm (samples in deep red color in Table 5.a). The PNIPAM network of the shell decreases in size as the temperature increases due to temperature dependence of the solvent quality. For T<LCST the network is swollen because of good solvent conditions, whereas for T>LCST, the solvent quality is poor due to unfavorable hydrogen bonding between amide groups and the aqueous solvent leading to shrinking of the shell and consequently shrinking of the particles' size in total .

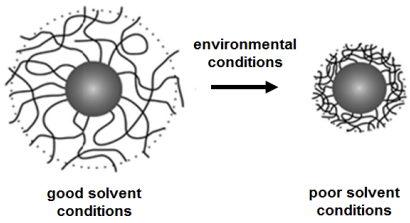

Fig. 5.1 *–Schematic representation of a hybrid microgel particle*

Sample name	D_{core} (nm)	$D_{H@20°C}$ (nm)	Crosslinking density (%)	Fluorescent label	Chapter report
TFEMA / PNIPAM 900nm	170	900	5	Nile red	chapter 5
TFEMA / PNIPAM 500nm	170	500	5	Nile red	chapter 5
TFEMA / PNIPAM 880nm	170	880	5	Nile red	chapters 6 , 7
TFEMA / PNIPAM-co-AAc 1300nm	170	1300	1	Nile red	chapter 8

Table 5.a *– Characteristic values of TFEMA core- PNIPAM shell hybrid systems studied in this thesis. Deep red colour refers to systems reported in this chapter.*

5.3 Results - Discussion

5.3.1 Particle Characterization

The physical mechanism used to stabilize the particles in the aqueous suspensions and prevent colloidal aggregation is electrostatic repulsion. The repulsive forces are sufficiently strong to prevent the particles from diffusing close to each other and dominate over the short-range Van der Waals attractive forces which lead to aggregation. The range of the electrostatic interactions can be quantified by estimating the surface charge densities σ and the Debye screening length κ^{-1} of the particles, as discussed earlier in chapter 3. Hence, ionic conductivity measurements were performed by a Zetasizer Nano ZS90 by Malvern Instruments equipped by a red-laser λ=633nm. Fig. 5.2 presents the temperature dependence of surface charge densities σ for both systems and the estimated Debye screening length κ^{-1}. Upon the temperature increase and the correspondent particle shrinking, the charges in the periphery of the particles redistribute resulting in a slight decrease of the Debye screening length. Taking into consideration the overall size of the systems and the estimated κ^{-1}, we conclude that the electrostatic stabilization for TFEMA/PNIPAM 900nm is slightly weaker than for TFEMA/PNIPAM 500nm.

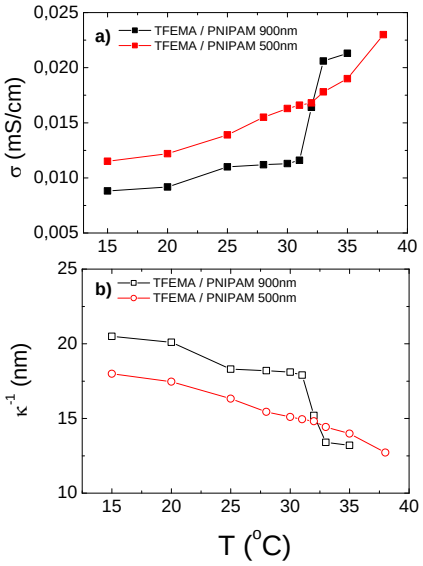

Fig. 5.2 *- Ionic conductivity σ and Debye screening length κ^{-1} as a function of temperature for both systems.*

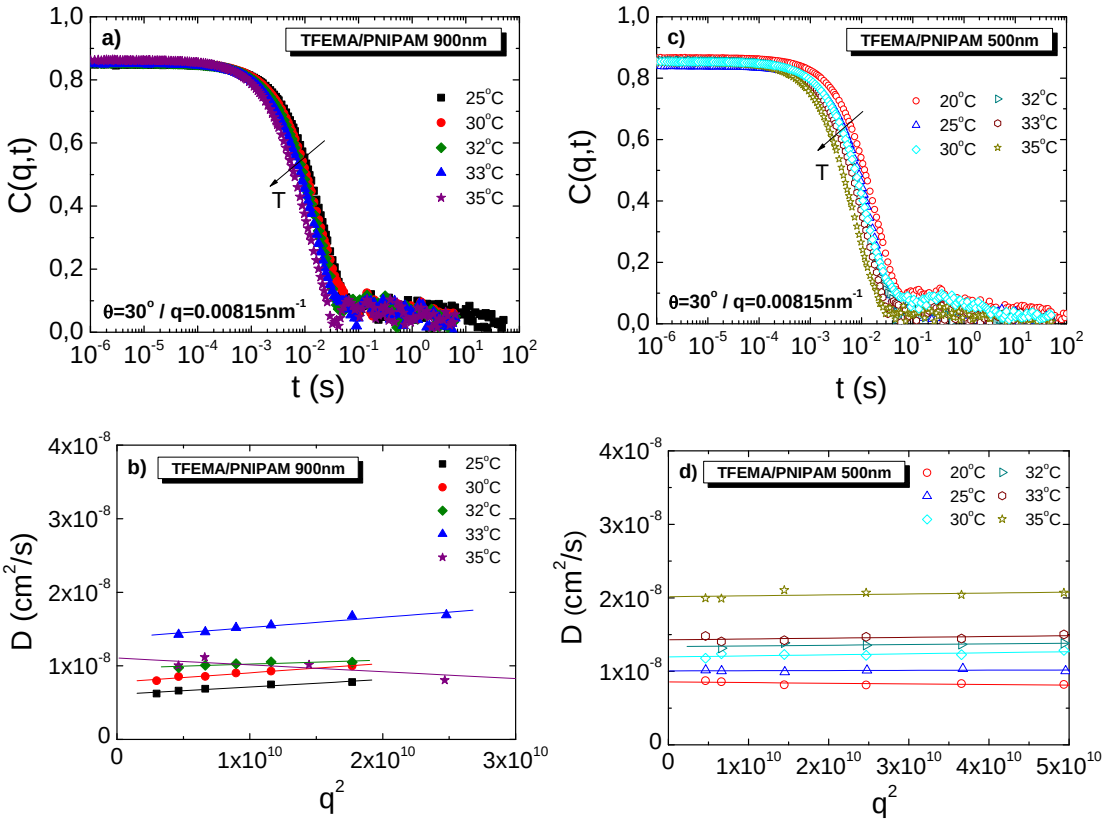

Fig. 5.3 – *Correlation functions for ϑ=30°/q=0.00815nm^{-1} for various temperatures for a) TFEMA/PNIPAM 900nm and c) TFEMA/PNIPAM 500nm and diffusion coefficient for various temperatures b) TFEMA/PNIPAM 900nm and d) TFEMA/PNIPAM 500nm.*

We used Dynamic Light Scattering (DLS) to determine the overall size of core-shell microgels in dilute regime. Fig. 5.3a and 5.3c depict the correlation functions for a 30° angle (q=0.00815nm^{-1}) at different temperatures for both systems studied, whereas fig. 5.3b and 5.3d show the temperature dependence of the diffusion coefficient. After determining the D(q→0) we calculate the temperature dependence of the hydrodynamic radius R_H of both TFEMA/PNIPAM systems in dilute regime (fig. 5.4). We should also mention that the viscosity changes upon temperature have been taken into consideration for the calculation of R_H. Increasing the temperature, the particle size decreases, because the solvent quality decreases as well due to an increasing preference for the PNIPAM chains to form intramolecular hydrogen bonds. Above the LCST, attractive interactions are expected between the polymer chains of the microgel which lead to phase separation (Appel, de Lange et al. 2015). From fig. 5.3 there is not any clear indication of the presence of attractive interactions above the LCST, since we refer to particle concentration at infinite dilution limit, where the particles are so far between them that they do not interact with each other.

The particle size also depends on the cross-linking density of the shell and the copolymerization which used during synthesis. The extent of swelling can be determined from changes in the hydrodynamic radius measured by DLS by estimating the de-swelling ratio α (Saunders and Vincent 1999):

$$\alpha = \frac{V_{collapsed}}{V_{swollen}} = \left(\frac{R_H^{38^o C}}{R_H^{15^o C}} \right)^3 \qquad (5.1)$$

where $R_H^{15^o C}$ is the hydrodynamic radius in fully swollen state, whereas $R_H^{38^o C}$ in the fully collapsed one. Despite the fact that the cross-linking density and copolymerization is similar for both systems, the de-swelling ratio for the larger system is about 57%, whereas for the smaller one about 46%.

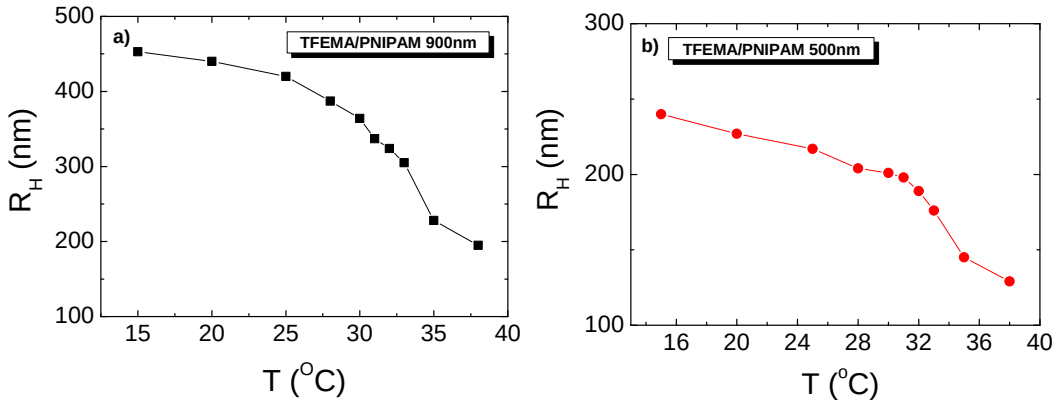

Fig. 5.4 – *Hydrodynamic radius R_H as a function of temperature for particles a) TFEMA/PNIPAM 900nm and b) TFEMA/PNIPAM 500nm.*

In the dilute regime, static light scattering intensity yields the particle form factor F(q), which gives us information about the overall shape, structure and size through fitting with appropriate model. Here, we used a core-shell model consisting of a homogeneous core and an inhomogeneous shell. This model assumes that the shell has an algebraic density profile $\phi \sim r^{-a}$ (fig. 5.5c). The value of parameter α depends on the geometry (spherical, cylindrical or planar polymer brush) and the solvent quality. It takes also into consideration the scattering contributions from both the rigid core and the fuzzy shell and the contrast variations Δn between core, shell and solvent according to the equation (4.1) reported in chapter 4.

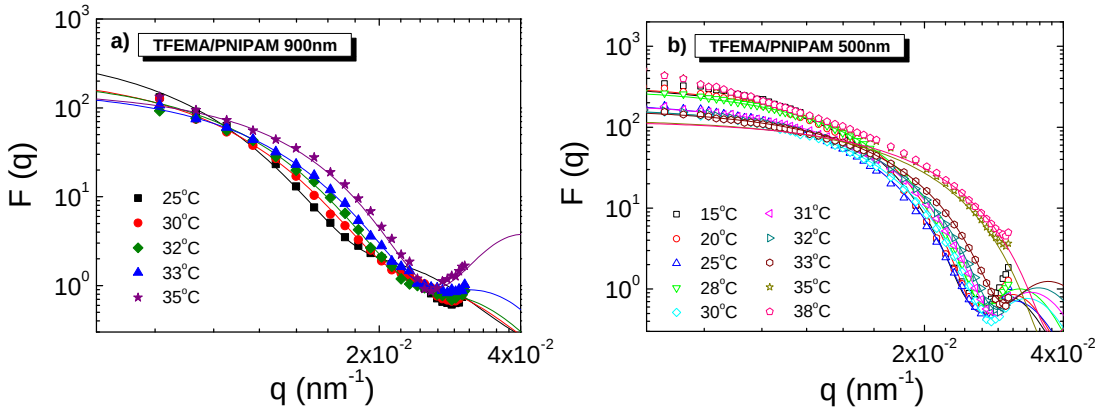

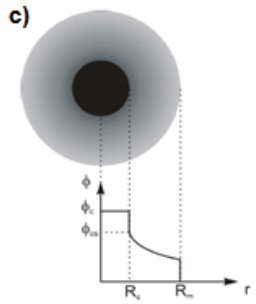

Fig. 5.5 - *Particle's form factor as a function of scattering wavevector for a) TFEMA/PNIPAM 900nm and b) TFEMA/PNIPAM 500nm. Experimental data fitted with homogeneous core and inhomogeneous shell model, c) schematic of density profile for model of homogeneous core and inhomogeneous shell.*

The thermodynamic properties of colloidal suspensions are determined by the molecular interactions involving both solvent and solute particles. A quantitative understanding of this relationship is important for the characterization of the system and its manipulation at high concentrations (Neal, Asthagiri et al. 1998). Therefore, we examined the second virial coefficient A_2, a thermodynamic parameter that characterizes the intermolecular interactions in dilute solutions by counting the total magnitude of interactions (Valente, Payne et al. 2005). The most popular method for the estimation of the second virial coefficient is static light scattering technique (SLS), where we extract the A_2 according to Zimm method (Zimm 1948). Positive values of A_2 indicate predominantly repulsive intermolecular interactions, whereas negative values indicate that attractive interactions dominate (Neal, Asthagiri et al. 1999).

Fig. 5.6 presents the inversed scattering intensity extracted by SLS as a function of particle concentration for various temperatures for both systems. From the values of the slope, the intercept and the molecular weight we extract the second virial coefficient A_2 (Velev, Kaler et al. 1998, Bockstaller, Köhler et al. 2001). At T<LCST, the slope of the inverse scattering intensity, for TFEMA/PNIPAM 900nm particles is higher comparing to the smaller ones, denoting the presence of stronger repulsive interactions between solute particles for this system depending on the

temperature. On the other hand, at T<LCST, the slope of the bigger particles is lower indicating weaker attractive interactions at this regime.

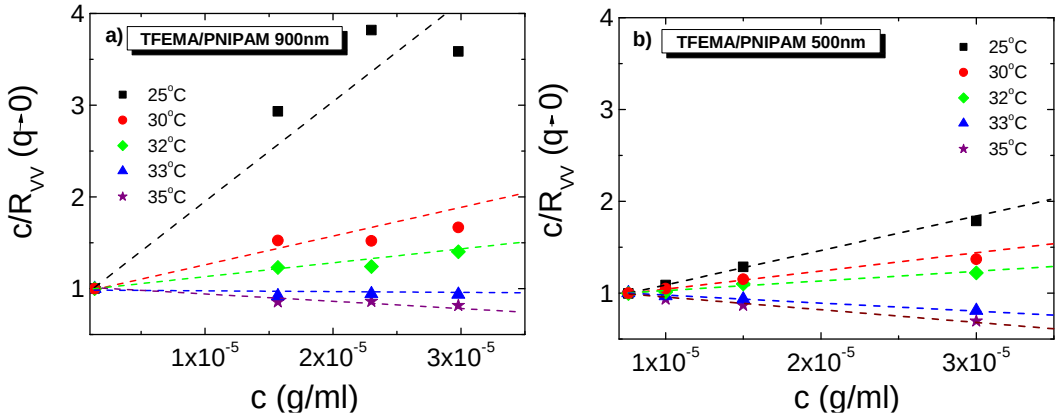

Fig. 5.6 *–Typical plots of SLS experimental data for various temperatures for particles a) TFEMA/PNIPAM 900nm and b) TFEMA/PNIPAM 500nm.*

Since, the molecular weight is not known for both systems, the values of A_2 are estimated for various temperatures as a function of M_w (fig.5.7). For the larger system the repulsive interactions are stronger than the smaller one and hence the slope is more abrupt.

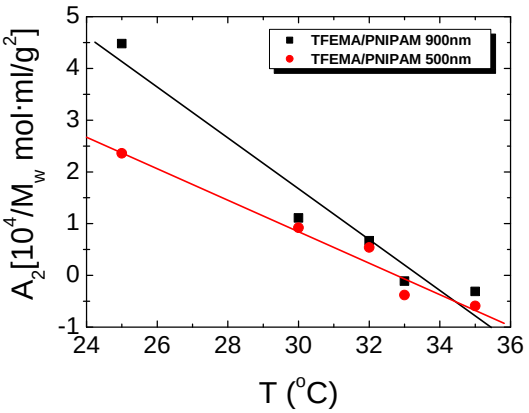

Fig. 5.7 *– Estimation of second virial coefficient A_2 through the experimental SLS data for particles a) TFEMA/PNIPAM900nm and b) TFEMA/PNIPAM 500nm.*

As we already mentioned, an important property of thermoresponsive microgels is that an effective volume fraction ϕ_{eff} can be utilized and easily controlled by temperature, while the mass concentration and thus the number density is kept constant. A simple method to determine the effective volume fraction

of such permeable colloidal suspensions is the measurement of the relative viscosity η_{rel} for a series of dilute solutions, which can be related to the effective volume fraction through the Batchelor-Einstein's expression $\eta_{rel} = 1 + 2.5\phi_{eff} + 5.9\phi_{eff}^2$. This method has been already described in chapter 4 (Senff and Richtering 1999, Senff and Richtering 2000, Deike, Ballauff et al. 2001). Fig. 5.8 presents the relative viscosity as a function of the mass concentration for various temperatures. The viscosity measurements were performed by a LOVIS/DMA 4100M Anton Paar viscometer. A strong temperature dependence can be seen, which is due to the shrinkage of the particles with increasing temperature. All experimental data were fitted according to Batchelor-Einstein's expression, with ϕ_{eff} substituted by $\phi_{eff}=kc$. The k shift factors obtained for each temperature are summarized in table 5.b.

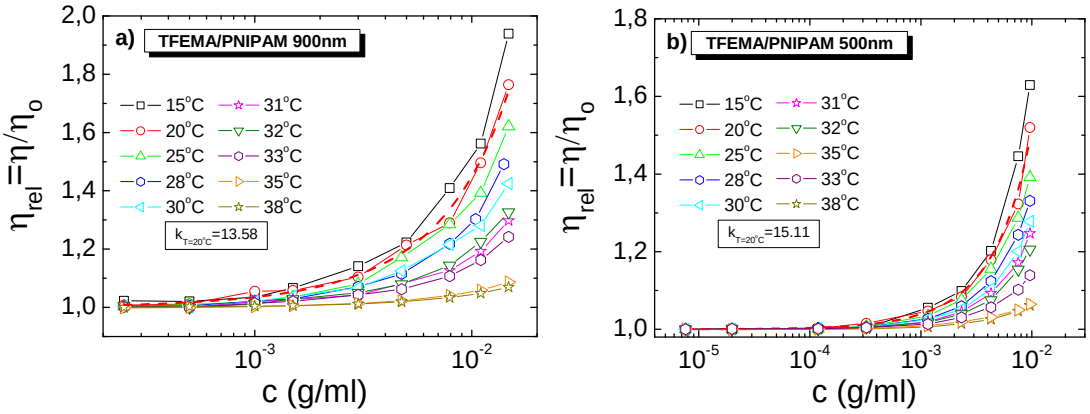

Fig. 5.8 – *Relative viscosity η_{rel} as a function of mass concentration for various temperatures for both systems and fitting with Batchelor-Einstein's expression at 20°C.*

Alternatively, ϕ_{eff} can be also estimated for more temperatures by renormalizing the $\phi_{eff}(20^oC)$ by the hydrodynamic radius of the particles $R_H(T)$, according to the equation:

$$\phi_{eff}(T) = \phi_{eff}(20^oC) \cdot \left(\frac{R_H(T)}{R_H(20^oC)} \right)^3 \qquad (5.2)$$

Moreover, the effective volume fraction ϕ_{eff}, estimated by applying the Batchelor-Einstein's expression in the experimental viscosity data at each temperature, can be used in order to extract an effective size. Then, we can check if the temperature dependence of the viscosity experimental data is in agreement with the DLS / SLS, by comparing the obtained effective size with the DLS / SLS $R_H(T)$. In fig. 5.9a, we observe that the temperature dependence of the size variation of the bigger TFEMA/PNIPAM microgels extracted by capillary viscometry is consistent to that obtained by DLS and SLS experiments. However, for temperatures below LCST, the experimental data for the smaller microgels (fig. 5.9b) extracted by SLS experiments, slightly deviate from the results obtained by DLS and viscometry experiments which are quite similar, whereas for T>LCST, DLS experimental data present a higher deviation from the SLS and viscometry measurements.

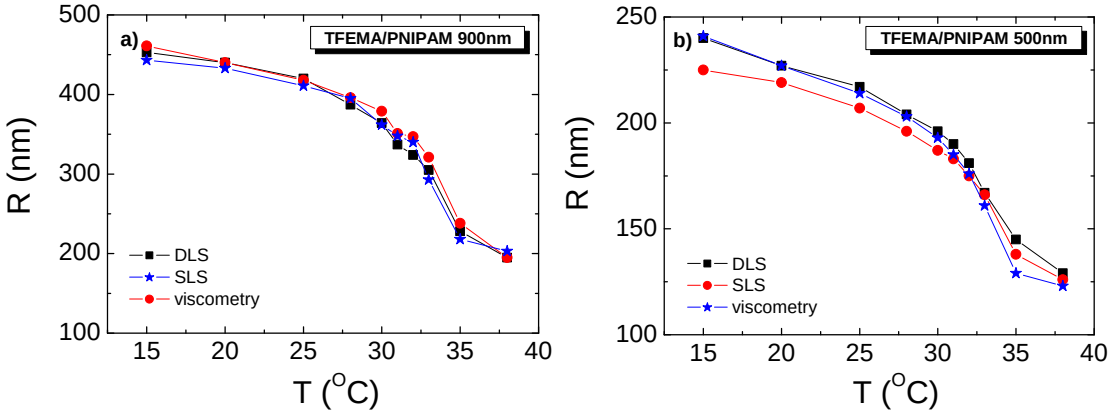

Fig. 5.9 *– Estimation of R for various T(°C) extracted by DLS and SLS technique and capillary viscometry for systems a) TFEMA/PNIPAM 900nm and b) TFEMA/PNIPAM 500nm.*

Tables 5.b and 5.c summarize the characteristic values like hydrodynamic radius extracted by DLS, effective radius extracted by SLS and viscometry, effective volume fraction and shift factor k for both under investigation microgel systems.

TFEMA / PNIPAM 900nm						
T (°C)	R_H (nm) (DLS)	ϕ_{eff} (DLS/Senff et al.)	k	R_H (nm) (viscometry)	ϕ_{eff} (viscometry)	R (nm) (SLS)
15	453	1.25	15.8	461	1.31	443
20	440	1.15	13.6	440	1.15	433
25	420	0.99	11.6	418	0.99	411
28	387	0.78	9.9	396	0.83	395
30	364	0.65	8.7	379	0.73	362
31	337	0.52	6.2	351	0.58	348
32	324	0.46	6.9	347	0.56	340
33	305	0.38	5.3	321	0.44	293
35	228	0.16	2.2	238	0.18	218
38	195	0.1	1.7	195	0.1	203

Table 5.b – *Estimation of R_H and φ_{eff} extracted by DLS technique and R_H and φ_{eff} extracted by capillary viscometry for TFEMA/PNIPAM 900nm.*

TFEMA / PNIPAM 500nm						
T (°C)	R_H (nm) (DLS)	ϕ_{eff} (DLS/Senff et al.)	k	R_H (nm) (viscometry)	ϕ_{eff} (viscometry)	R (nm) (SLS)
15	240	1.27	18.1	241	1.285	225
20	227	1.07	15.1	227	1.073	219
25	217	0.94	12.6	214	0.894	207
28	204	0.78	10.9	203	0.773	196
30	201	0.75	9.3	193	0.662	187
31	198	0.71	8.3	185	0.591	183
32	189	0.62	7.2	176	0.513	175
33	176	0.5	5.3	160	0.376	166
35	145	0.28	2.7	129	0.188	138
38	129	0.19	2.4	123	0.169	126

Table 5.c – *Estimation of R_H and φ_{eff} extracted by DLS technique and R_H and φ_{eff} extracted by capillary viscometry for TFEMA/PNIPAM 500nm.*

5.3.2 Structure and Dynamics

For hard spheres, increasing the volume fraction there is a transition from a disordered fluid to a crystal phase through an intermediate fluid-crystal coexistence regime, and then to a disordered amorphous glassy state, where the positions of the particles are uncorrelated. For volume fractions higher than random close packing, the particles are forced into contact in a jammed state. The state diagram can be influenced quantitatively and qualitatively by various parameters such as polydispersity and softness of the particles. For soft systems, compressibility (microgels) and interpenetration (star-like systems) allows accessibility to volume fractions well above jamming transition (Vlassopoulos and Cloitre 2014). Spherical microgels with a solid core and a thermosensitive shell can be used as colloidal atoms in soft matter physics to mimic transitions from equilibrium phases such as crystals and liquids to non-equilibrium phases such as glasses and gels and vice versa (Crassous, Siebenbürger et al. 2006, Crassous, Siebenbürger et al. 2008). Hence, understanding the details of microgel structure and dynamics at the various states, is important.

Here the structure and particle dynamics were investigated extensively for concentrated suspensions of microgels TFEMA/PNIPAM 900nm and TFEMA/PNIPAM 500nm. Different values of ϕ_{eff} were achieved by varying the temperature between T=15-38^{o}C. For both systems, at low temperatures, ϕ_{eff} values are higher than 1, which possibly occurs due to the compressibility and partial chain interpenetration of the outer blob of the shell.

Many optical techniques such as light scattering and optical microscopy can be used to study colloidal systems experimentally. These two techniques provide complementary information. Experimental data inferred from scattering techniques are in Fourier space and averaged over the whole scattering volume. On the other hand, optical microscopy yields real-space data of a small part of the suspension. Confocal Laser Scanning Microscopy (CLSM) consists of an advanced version of optical microscopy, which is often used to investigate the structure and dynamics of colloidal suspensions in real-space. Confocal microscopy's function hinges on two

principles: illumination of a small sample volume and rejection of the vast majority of out-of-focus light (Prasad, Semwogerere et al. 2007, Hunter and Weeks 2012). Images are recorded using a confocal fluorescence microscope of VisiTech (VT-Eye confocal system) equipped by a single mode diode laser of 100mW (emission wavelength λ=488nm) and a Nikon eclipse Ti-U inverted microscope using a 100x oil immersion objective. Temperature was controlled by a homemade cooling/heating system using Peltier elements.

The core of microgel particles is labelled by Nile red dye, so that we observe only the fluorescent cores of total size around 170nm and not the non-fluorescent shells. We should also mention that the core size is below the setup resolution, resulting in bad imaging quality which in combination with the jammed states that we study prohibit the acquisition of dynamics. Fig. 5.10 shows the changes observed in the structure for various temperatures for system TFEMA/PNIPMA 900nm (c=0.0845g/ml - ϕ_{eff}=1.25 at 15^{o}C). At low temperatures (T<LCST), we observe that the system TFEMA/PNIPMA 900nm exhibits a well-ordered state which corresponds to crystal. This can be easily understood from Fourier Transformation, where the Bragg peaks are in well-defined positions. Due to multiple scattering it was not possible imaging beyond few first layers, remaining thus close to the glass surface that perhaps is responsible for the crystallization effect. According to this assumption, if there was the ability to image the bulk, then an amorphous state probably could be observed which denotes the existence of a glassy/semi-crystal state. Increasing the temperature (32^{o}C) the suspension is liquefied and there are no Bragg peaks appeared in specific positions. At temperatures above LCST i.e. 38^{o}C, PNIPAM becomes insoluble and phase separates from its aqueous solvent. Then, attractive interactions induced by PNIPAM (Kodger and Sprakel 2013) lead to the formation of a percolated network among the particles. This temperature induced gelation is completely reversible.

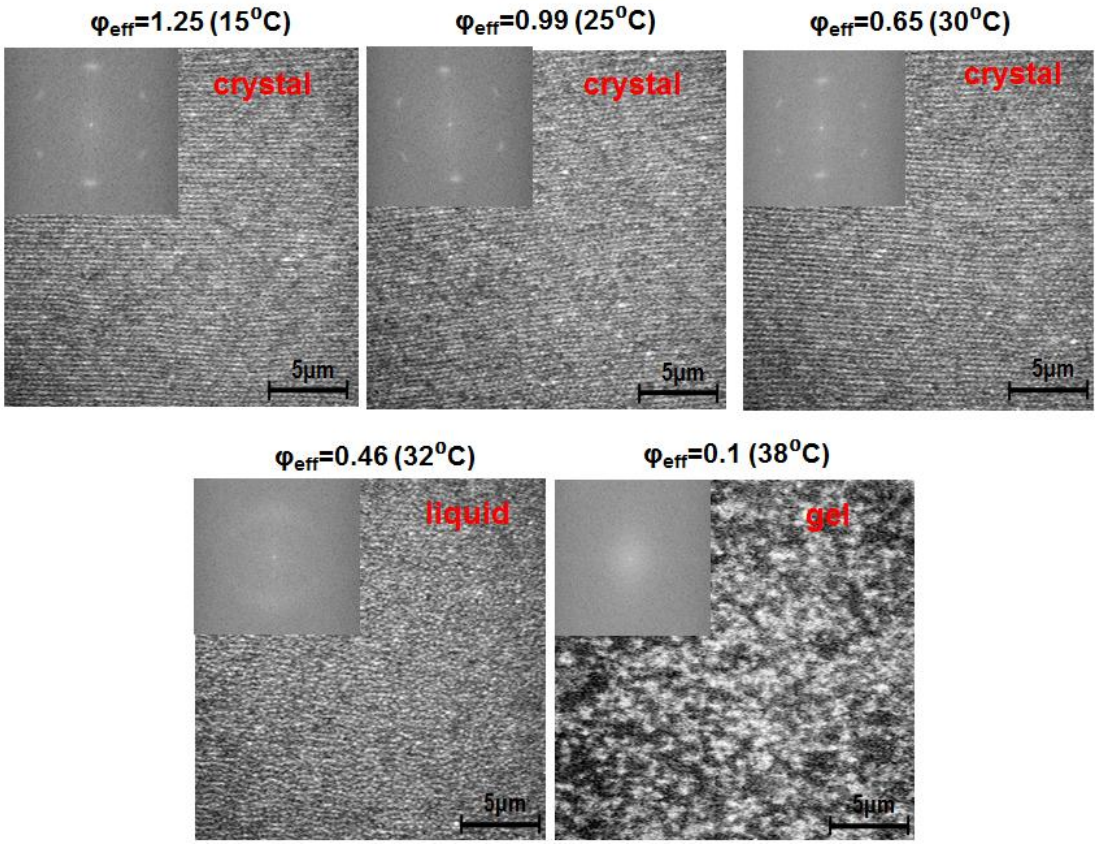

Fig. 5.10 – *2D Confocal Microscopy images for various T of concentrated sample c=0.0845g/ml of TFEMA/PNIPAM 900nm.*

The system TFEMA/PNIPAM 900nm was also studied in lower mass concentration (c=0.07g/ml - ϕ_{eff}=1.11 at 15°C), where the behavior was similar to c=0.0845g/ml. Below the LCST, increasing the temperature we observe the gradual liquefaction of the crystal, whereas the gel formation for temperatures above the LCST.

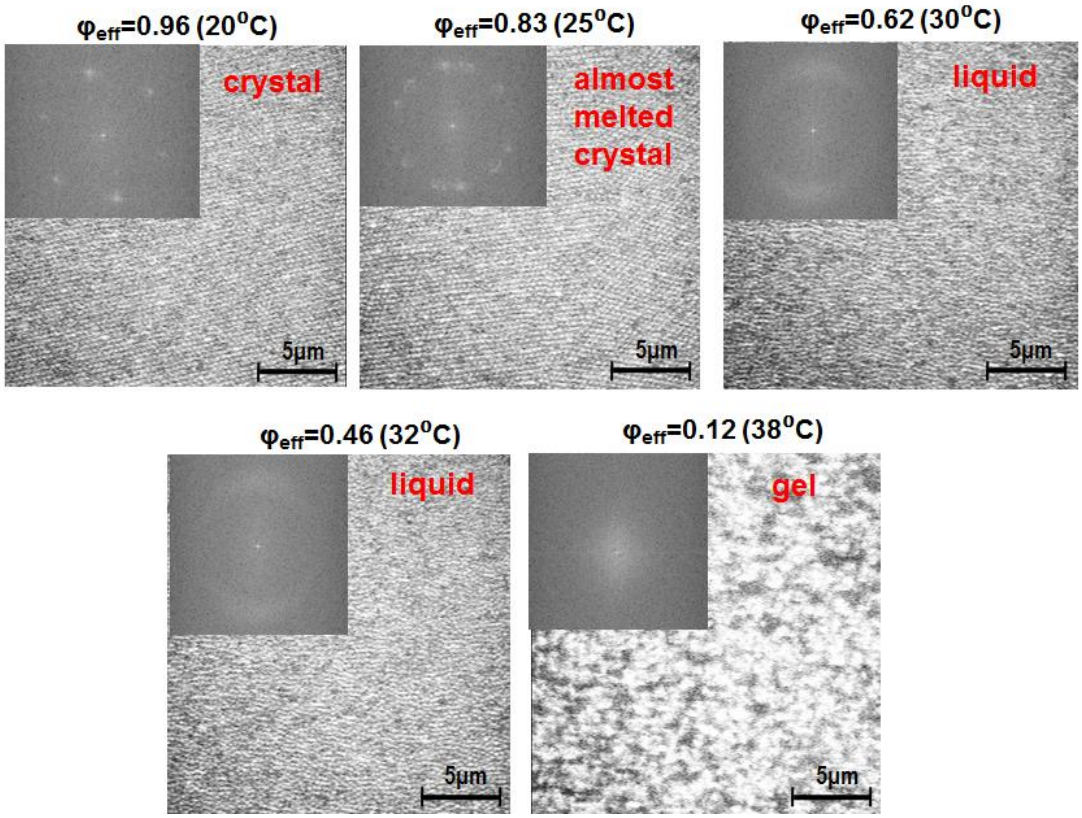

Fig. 5.11 – *2D Confocal Microscopy images for various T of concentrated sample c=0.07g/ml of TFEMA/PNIPAM 900nm.*

We also study the temperature influence on the structure of an even diluter suspension of TFEMA/PNIPAM 900nm at c=0.0423g/ml (ϕ_{eff}=0.57 at 20°C) between the temperature range of T=20-55°C. Increasing the temperature above LCST, a percolated gel state arises. However, from the 2D confocal microscopy images (fig. 5.12), we can observe that increasing further the temperature there are no significant changes in gel microstructure.

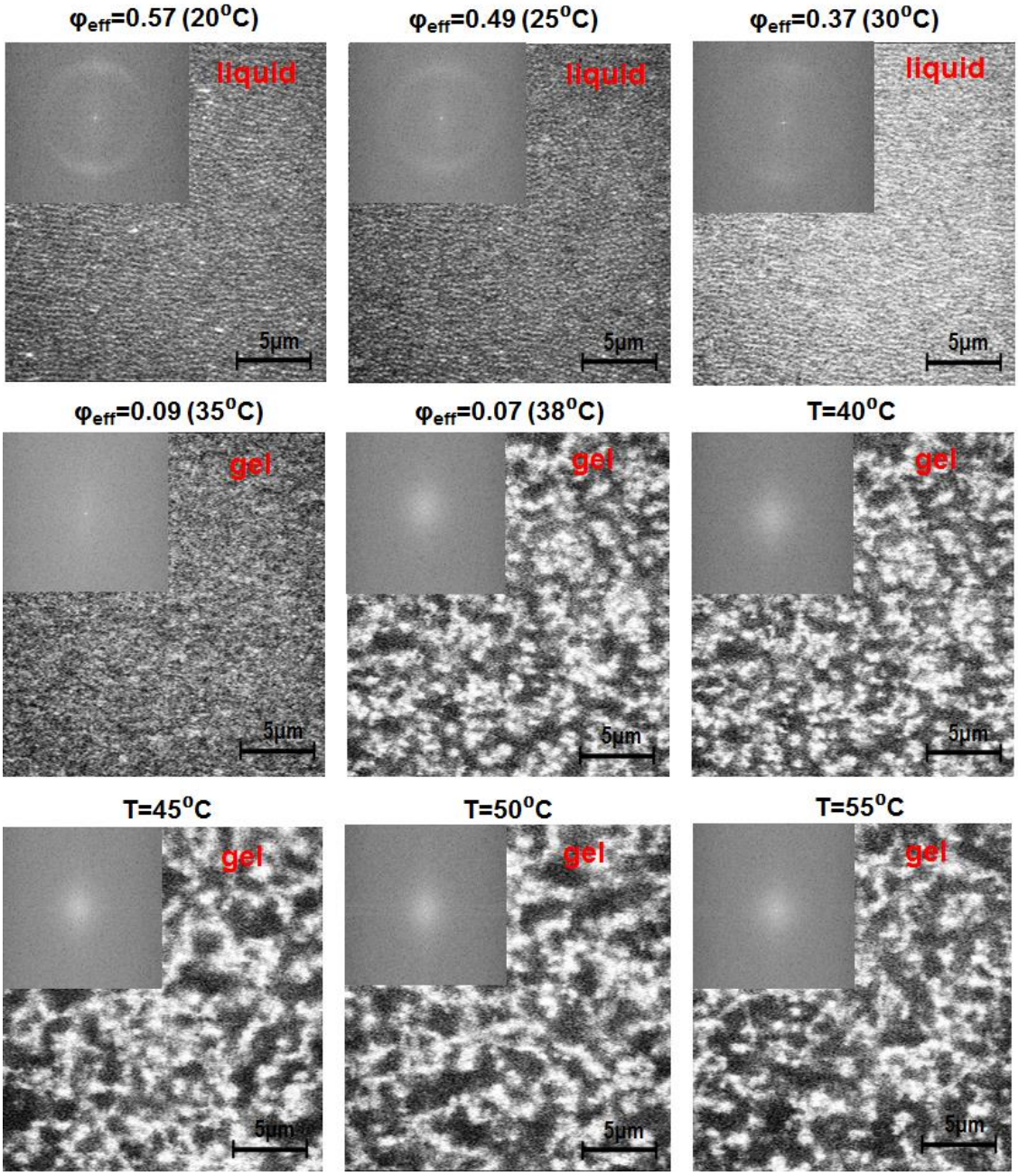

Fig. 5.12 *– 2D Confocal Microscopy of concentrated sample TFEMA/PNIPAM 900nm (c=0.0423g/ml) images for T>LCST.*

Fig. 5.13 depicts, the confocal images for the system TFEMA/PNIPMA 500nm (c=0.071g/ml - ϕ_{eff}=1.27 at 15°C). Increasing the temperature above LCST, a sea of floating clusters arises. This behavior occurs because in the absence of salt there are remains of repulsive interactions coming from electrostatic stabilization, which partially prohibits the effective formation of a network.

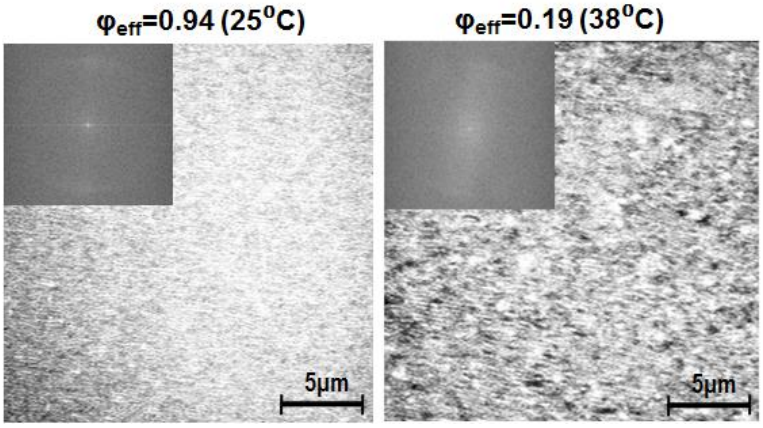

Fig. 5.13 – *2D Confocal Microscopy images for various T of concentrated sample c=0.071g/ml of TFEMA/PNIPAM 500nm.*

Diffusive wave spectroscopy (DWS) was used for probing dynamics of highly multiple scattering suspensions and monitoring ergodic (liquid state) to non-ergodic (glass or gel state) transitions, where dynamics are of length scales that are unattainable using conventional scattering techniques (Weitz, Zhu et al. 1993, Mason and Weitz 1995). DWS technique assumes that light traversing the sample behaves like a random walk. For the experiments we used a homemade DWS setup in transmission geometry equipped by green CW Nd-Yag laser (Coherent) beam with a wavelength of λ=532 nm. Firstly, a PMT is used as a detector unit for capturing fast dynamics and then a CCD camera for accessing slow dynamics. Accurate and fast control of the temperature was achieved by Peltier elements connected with the holder where the cell of 10mm thickness was placed.

Dynamics of two different mass concentrations (c=0.0845g/ml and c=0.07g/ml) for the system TFEMA/PNIPAM 900nm and one mass concentration for the system TFEMA/PNIPAM 500nm (c=0.07g/ml) investigated by DWS at different temperatures and thus different volume fractions. Fig. 5.14a depicts the temperature dependence of the intermediate scattering function, once the steady state is reached. At low temperatures (T<LCST) it presents a strong non-ergodic plateau, which is characteristic of a kinetically arrested state that is formed due to the “caging effect”, where the particle diffusion is restricted within a cage formed by its nearest neighbors. In all cases probed, the intermediate scattering function finally

decays to zero. Increasing temperature the effective volume fraction decreases with the non-ergodic plateau becoming continuously weaker and at the LCST the intermediate scattering function singly exponentially decays to zero denoting the existence of an ergodic state. At temperatures above the LCST, attractive interactions dominate leading the suspension to coagulation. At this extent, the decay of the intermediate scattering function progressively shifts to longer correlation times due to the slower motion of the clusters formed during aggregation and a plateau is presented denoting the formation of a percolated network among the particles (gelation). The behavior which was observed in confocal microscopy (fig. 5.10) is in agreement with what we see in DWS.

Fig. 5.14b exhibits the conversion of the correlation function to the mean square displacement (MSD) of the particles. This conversion requires knowledge of the transport mean free path l^*, a measure of sample turbidity, which was obtained from a static transmission measurement relative to a sample of known transport mean free path. Then, by measuring the ratio of the transmitted intensity of a reference sample to the transmitted intensity of the unknown sample, we calculated the l^* of the unknown sample. As a reference sample, we used polystyrene latex spheres of total size 385nm suspended in water. To determine the value of l^*_{ref}, we measured the transmission intensities for various sample thicknesses of the reference sample in a transmission geometry. Then through the equation (5.3) we determined the value $l^*_{ref} \approx 0.11cm$ for all thicknesses measured. Alternatively, we also estimated the l^*_{ref} by measuring the correlation function of the electric field of the reference sample for the same sample thicknesses in the same transmission geometry. These correlation functions were fitted by KWW model with the number of scattering events $n = \left(L/l^*_{ref}\right)^2$ being the only parameter in the fit, yielding at the end the reference value of $l^*_{ref} \approx 0.11cm$ for all thicknesses probed. So, the two methods which used are in agreement between them.

Afterwards, we measured the transmitted intensity of the reference T_{ref} and the unknown sample T in transmission geometry for sample thickness $L = 4mm$. Then, taking the ratio of the equations below, we calculated the transport mean free path of the unknown sample $l^* = 47\mu m$:

$$T_{ref} \propto \frac{l^*_{ref} / L}{1 + 4l^*_{ref} / 3L} \tag{5.3}$$

and

$$T \propto \frac{l^* / L}{1 + 4l^* / 3L} \tag{5.4}$$

Once, the transport mean free path is estimated the time dependent mean square displacements of the system TFEMA/PNIPAM 900nm is calculated by numerically inverting the field correlation functions using the l^* according to the equation (2.14) (Brown 1993, Weitz, Zhu et al. 1993). Fig. 5.14b displays the evolution of the MSD for various temperatures as a function of the time normalized by Brownian time t_B. At temperatures below the LCST, the MSD is characterized by a nearly diffusive behaviour at short-times that at intermediate times is spatially constrained by "caging" due to crowding which is manifested as a plateau. At even longer times, the decay in the correlation function, reveals the breakage of the cages, and the free motion of individual particles. Close to LCST, the mean square displacement is characterized by an almost linear increase at shortest times denoting the diffusive motion of the particles. At temperatures above the LCST, at short and intermediate time region the mean square displacement slows down due to obstacles appeared due to clustering, while a diffusive process is recovered at long times.

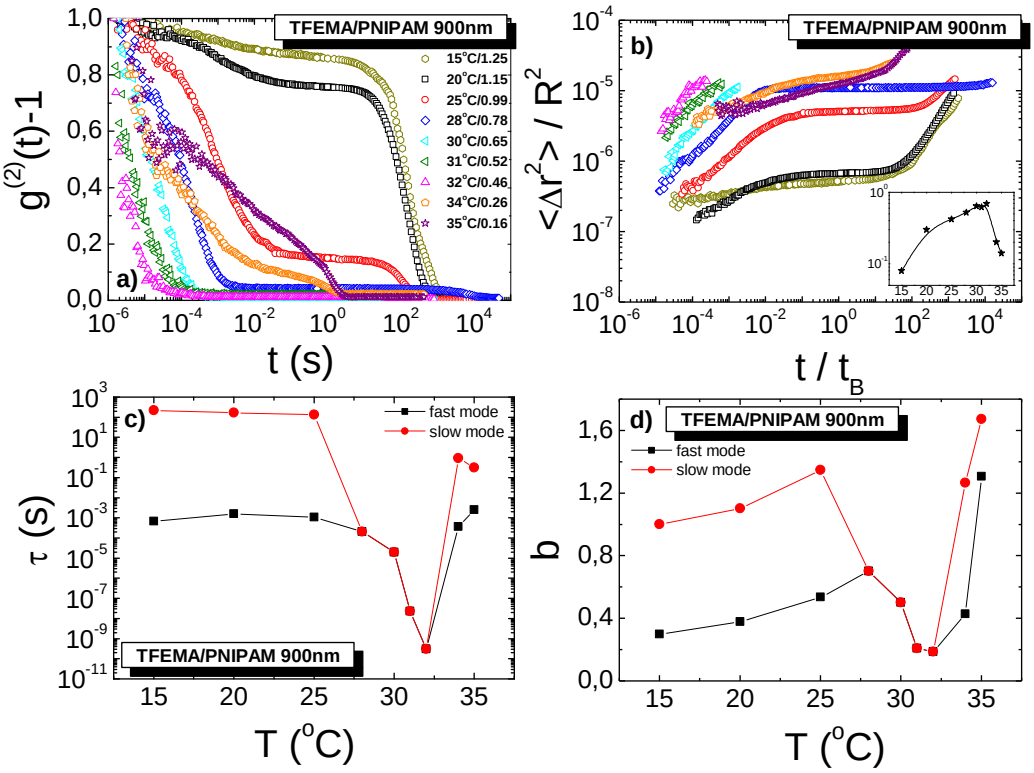

Fig. 5.14 – *a) Intermediate scattering function for various temperatures and various effective volume fractions of concentrated sample c=0.0845g/ml - TFEMA/PNIPAM 900nm. b) Mean square displacement, measured by DWS – Inset: the slope of the short-time increase, c) temperature dependence of relaxation time and d) stretching exponent extracted by KWW fitting of intermediate scattering function.*

Moreover, fig. 5.14c shows the relaxation time as a function of temperature for the c=0.0845g/ml of TFEMA/PNIPAM 900nm at all volume fractions tuned by temperature, whereas fig. 5.14d presents the corresponding stretching exponents b. Both relaxation time and stretching exponent extracted by fitting the intermediate scattering functions by stretched exponential decay model (KWW). We observe that increasing the temperature both relaxation time and stretching exponent drop for both fast and slow mode and then increase again, denoting a transition from a viscoelastic glass (non-ergodic behavior) to a viscoelastic liquid (ergodic behavior) and then to a viscoelastic solid again (gel state).

We also present the DWS experimental results (fig. 5.15) for mass concentration c=0.07g/ml of TFEMA/PNIPAM 900nm, where we observe similar

solid-liquid-solid transitions to the higher concentration c=0.0845g/ml. We mention also that the DWS response is consistent with the confocal imaging (fig. 5.11).

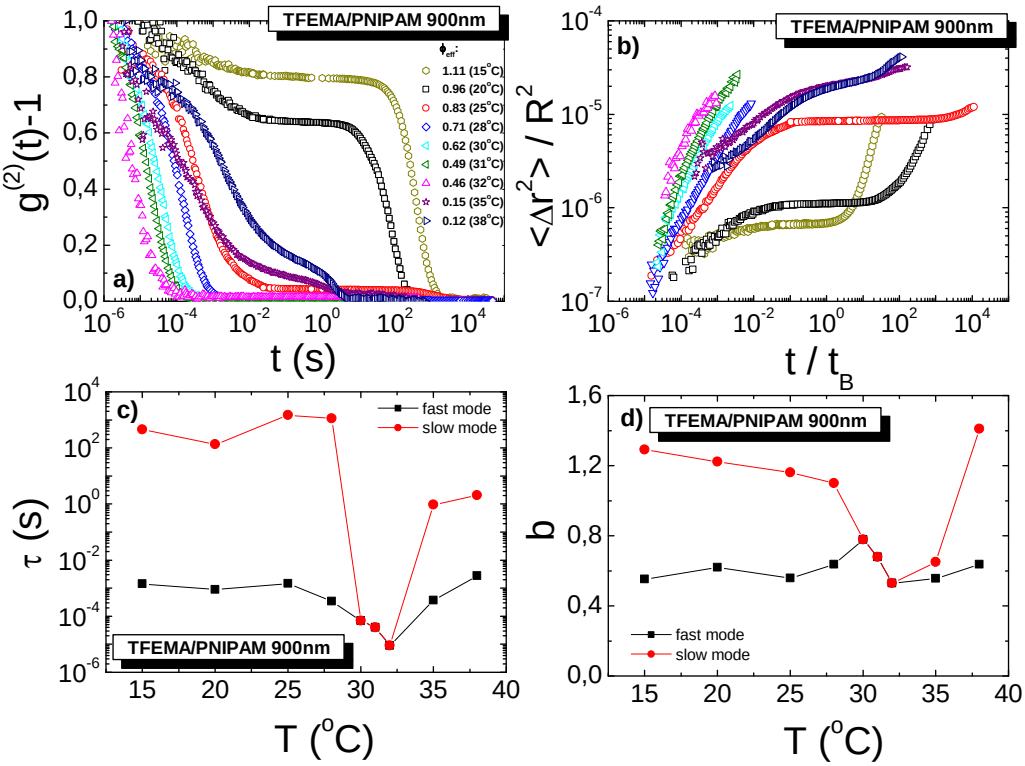

Fig. 5.15 – *a) Intermediate scattering function for various temperatures and various effective volume fractions of concentrated sample c=0.07g/ml - TFEMA/PNIPAM 900nm, b) mean square displacement, measured by DWS, c) temperature dependence of relaxation time and d) stretching exponent extracted by KWW fitting of intermediate scattering function.*

Fig. 5.16a displays the evolution of dynamics of a glassy suspension (c=0.07g/ml) of the system TFEMA/PNIPAM 500nm upon temperature increase. Similar to the larger system, the probed intermediate scattering functions are monitored once steady state is reached. This system exhibits a similar behavior to hybrid microgels TFEMA/PNIPAM 900nm, presenting a non-ergodic plateau, at temperatures below the LCST, where the sample is in glassy state. Increasing the temperature close to the LCST, there is a glass-to-liquid transition, whereas at even higher temperatures aggregation takes place which is quite weak as observed in confocal microscopy images as well (see fig. 5.13).

Fig. 5.16b displays the evolution of the mean square displacement with time for various temperatures. For the calculation of the MSD, we estimated the transport mean free path for TFEMA/PNIPAM 500nm with the technique that we reported before ($l^* = 35\mu m$). The behaviour of microgels with smaller is similar to the larger ones. At temperatures below the LCST, at intermediate times there is the presence of a plateau which signals that the sample is glassy; at short and long times the behaviour is diffusive. At LCST, the behaviour is liquid-like with MSD increasing linearly in time. As we have already seen in confocal microscopy, for TFEMA/PNIPAM 500nm at temperatures above the LCST, the attractive interactions are weak and compete the weak electrostatic ones, resulting in a slight slowing down to the MSD.

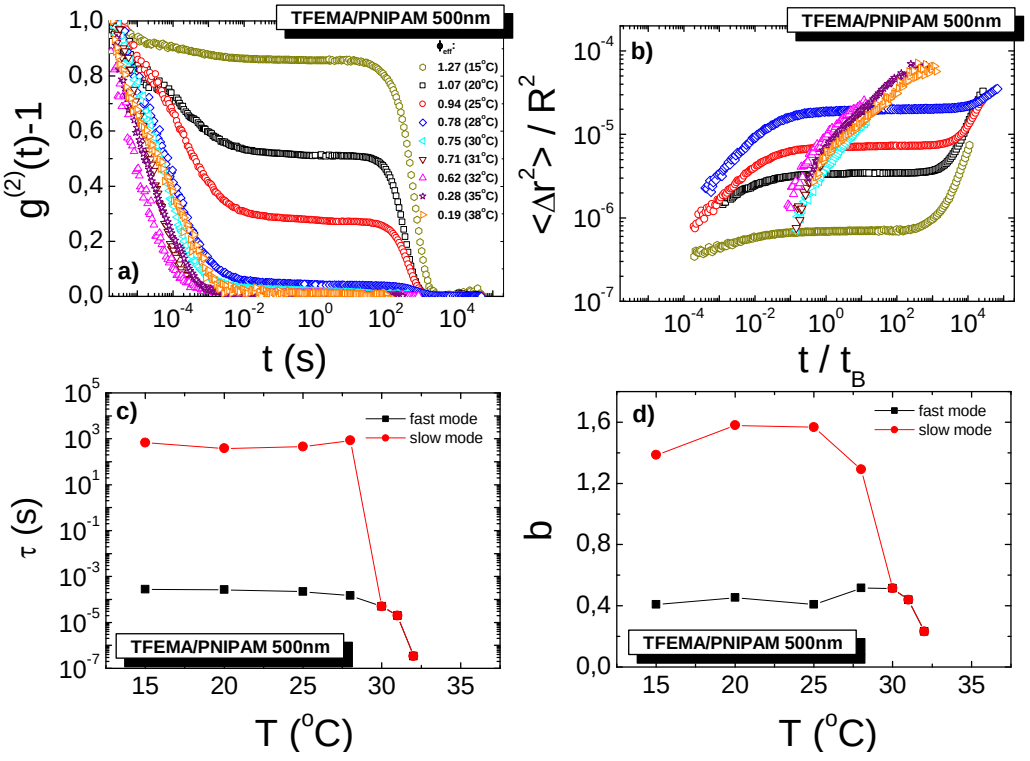

Fig. 5.16 – *a) Intermediate scattering function of concentrated sample c=0.07g/ml of TFEMA/PNIPAM 500nm, b) mean square displacement, measured by DWS, c) temperature dependence of relaxation time and d) stretching exponent extracted by KWW fitting of intermediate scattering function.*

Fig. 5.16c and 5.16d present the response of the relaxation time and the stretching exponent respectively as a function of temperature for the sample c=0.07g/ml of TFEMA/PNIPAM 500nm. Both values are obtained by the intensity

correlation functions with KWW model. At temperature below the LCST, both relaxation time and stretching exponent are almost constant for both fast and slow mode, whereas close to the LCST, they both decrease. At temperatures above the LCST, the correlation functions were hard to be fitted.

5.3.3 Rheometry

Rheometry was used for studying thoroughly the glass to liquid and gel transition by determining the temperature dependence of the linear viscoelastic moduli as well as the non-linear mechanical properties. All rheological measurements carried out with a strain-controlled ARES rheometer with a force rebalance transducer 100FRTN1 in a cone-plate geometry d=25mm with a cone-angle of 0.04 degrees and truncation 0.05mm. Accurate and fast temperature control was achieved by Peltier elements placed at the lower plate.

A specific experimental protocol was followed for all measurements in order to avoid the contribution of any loading history effects. The sample was first heated at T=30^{o}C in order to get liquefied, fill properly the gap and erase all memory effects. Then the temperature was brought back to desired temperature and stabilized before starting the measurement. For eliminating solvent evaporation a homemade trap was used, which “sealed” the sample by a low-molecular poly(dimethylsiloxane) of low viscosity (5cP).

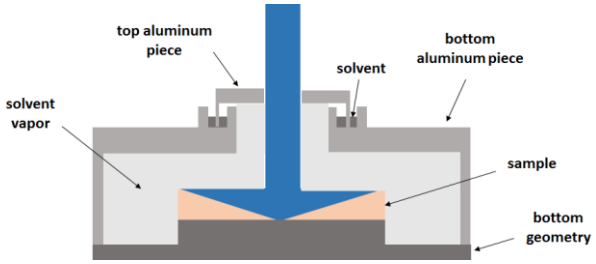

Fig. 5.17 – *Schematic representation of the homemade trap used in measurements with TA ARES strain-controlled rheometer.*

5.3.3.1 Linear Viscoelasticity (temperature and frequency dependence)

In order to follow the temperature dependence of the linear viscoelastic moduli of the concentrated suspensions of TFEMA/PNIPAM 900nm (0.0845g/ml) and

TFEMA/PNIPAM 500nm (0.071g/ml) used in DWS and CLSM, we fixed both frequency (ω=1rad/s) and strain amplitude (γ=0.5%) applied to the samples and slowly increased the temperature.

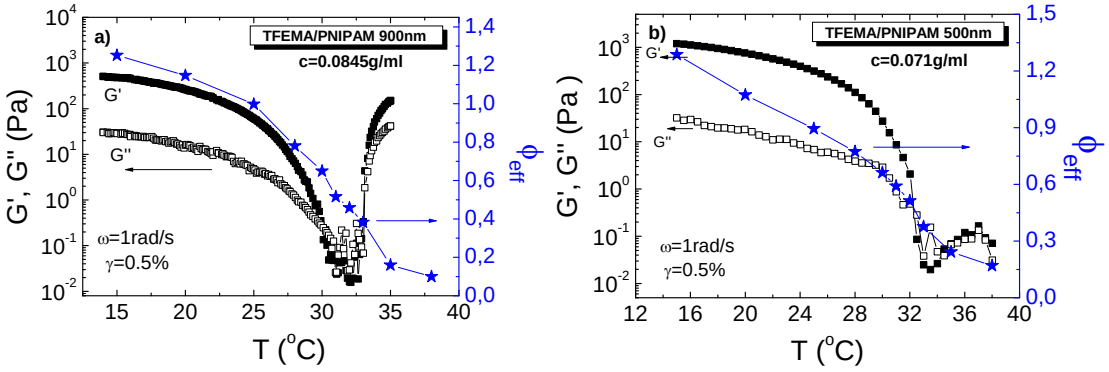

Fig. 5.18 – *Left axis: Storage (black full squares) and Loss (black open squares) moduli as a function of temperature. Right axis: effective volume fraction φ_{eff} (blue full stars) as a function of temperature for concentrated samples a) c=0.0845g/ml / TFEMA/PNIPAM 900nm and b) c=0.071g/ml / TFEMA/PNIPAM 500nm.*

Both systems exhibit a similar behavior with the storage modulus G' being higher than the loss modulus G'' at temperatures below the LCST, corresponding to a typical solid-like behavior. However, increasing the temperature the difference between the moduli gets progressively smaller and at the LCST the loss modulus dominates over the storage one indicating a liquid-like behavior. Increasing further the temperature, repulsive interactions switch to attractive and a sudden increase of storage modulus is observed, which is related to the existence of re-entrance from liquid to solid-like behavior. The solid-like behavior at low volume fraction which is followed by the existence of attractive interaction is related to formation of percolated network, which is consistent to what we observed through DWS and CLSM techniques. As we have already observed at DWS and CLSM, the network formation for the system TFEMA/PNIPAM 500nm is quite weak.

Below, we analyze the frequency dependence of the viscoelastic moduli at a constant strain amplitude γ=0.5%, for various temperatures for the same concentrations for both TFEMA/PNIPAM 900nm (0.0845g/ml) and TFEMA/PNIPAM 500nm (0.071g/ml).

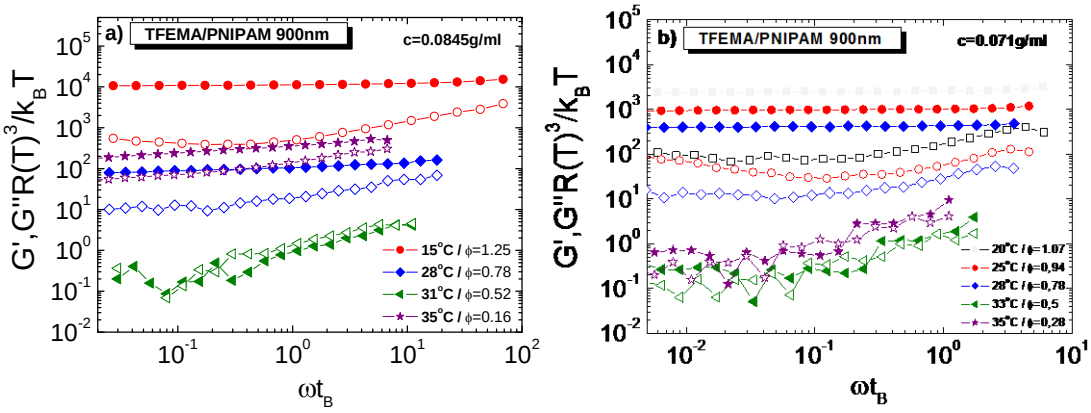

Fig. 5.19 *– Frequency dependence of storage (full symbols) and loss (open symbols) moduli for various temperatures (volume fractions) for concentrated samples a) c=0.0845g/ml / TFEMA/PNIPAM 900nm and b) c=0.071g/ml / TFEMA/PNIPAM 500nm.*

At low temperatures, both systems exhibit a dominant storage modulus G' over a wide range of frequencies, a condition which, as we already mentioned, corresponds to solid-like behavior for a quiescent sample. More specifically, G' presents a plateau with a slightly increasing slope, which may be attributed to increased particle motions at small frequencies compared to the higher ones, whereas G'' exhibits a minimum, which is related to the transition between the in cage and the out-of-cage relaxation times of the particles of the specific size (Van Megen and Underwood 1993, Mason and Weitz 1995). We should also mention that the long-time relaxation times are not observed in the experimental window, since are found at much lower frequencies. For the large microgels the minimum of G'' appeared at lower frequency (ω=1rad/s) than the smaller ones at (ω=2rad/s). The frequency ω is set by $1/t_B$, where t_B is the characteristic time of the faster relaxation process that takes place in a colloidal glass due to the caging of the individual particles (Pusey and van Megen 1987). The characteristic time t_B depends on the size of the particles ($t_B=R^2/D$). Hence, for large particle the t_B is greater, since they need more time to explore their cage.

At temperature T≈31°C, the G'' dominates depicting a liquid regime. At T=35°C, G' is becoming higher than G'' again, which indicates the existence of re-

entrance from liquid to solid-like behavior by switching from repulsive to attractive interactions.

5.3.3.2 Transient shear

Fig. 5.20 shows the measured stress versus strain in step-rate experiments for three different applied shear rates (0.05, 0.1 and $0.5s^{-1}$) and temperatures for both studied systems. The experimental data are plotted in log-log so that the transient response of all the probed states are clearly observed. In both systems, the stress initially increases starting from a finite value for each temperature, then passes through a maximum and reaches a final steady-state plateau. The initial stress increase reflects an energy storage mechanism that is related to the entropic elasticity of the cage of a colloidal glass and the entropic elasticity of a percolated network. The initial stress increase up to about 3-5% for system TFEMA/PNIPAM 900nm and 8-9% for TFEMA/PNIPAM 500nm, depending on the temperature is given by linear response.

At higher strains, a stress maximum is appeared due to subsequent energy dissipation mechanism which finally leads to plastic flow and a steady state stress plateau. At regime where the repulsive interactions are predominant (T<LCST), increasing the temperature, the volume fraction is decreased, leading to the increase of free volume and a less pronounced stress peak. This can be observed at both glassy and liquid-like state. At T>LCST where the attractive interactions are predominant, the onset of the formation of a percolated network results not only in the strengthening of the aforementioned stress peak, which, in this case is due to breaking of inter-cluster bonds, but also the introduction of a second one that is connected to breaking of intra-cluster bonds. For both systems, the stress maximum is not strong, contrary to hard spheres or even softer systems such as similar core-shell microgels and star-like micelles (Koumakis, Pamvouxoglou et al. 2012).

The peak value of stress in start-up flow experiments often defines the yield stress (σ_y) above which the sample flows (Carrier and Petekidis 2009). After this point the stress decreases and approaches its plateau value. For colloidal glasses

(T<LCST) the flow is related to the increase of microscopic particle motions due to out-of-cage diffusion, while for colloidal gels (T>LCST) is associated with the flow of smaller free clusters in size.

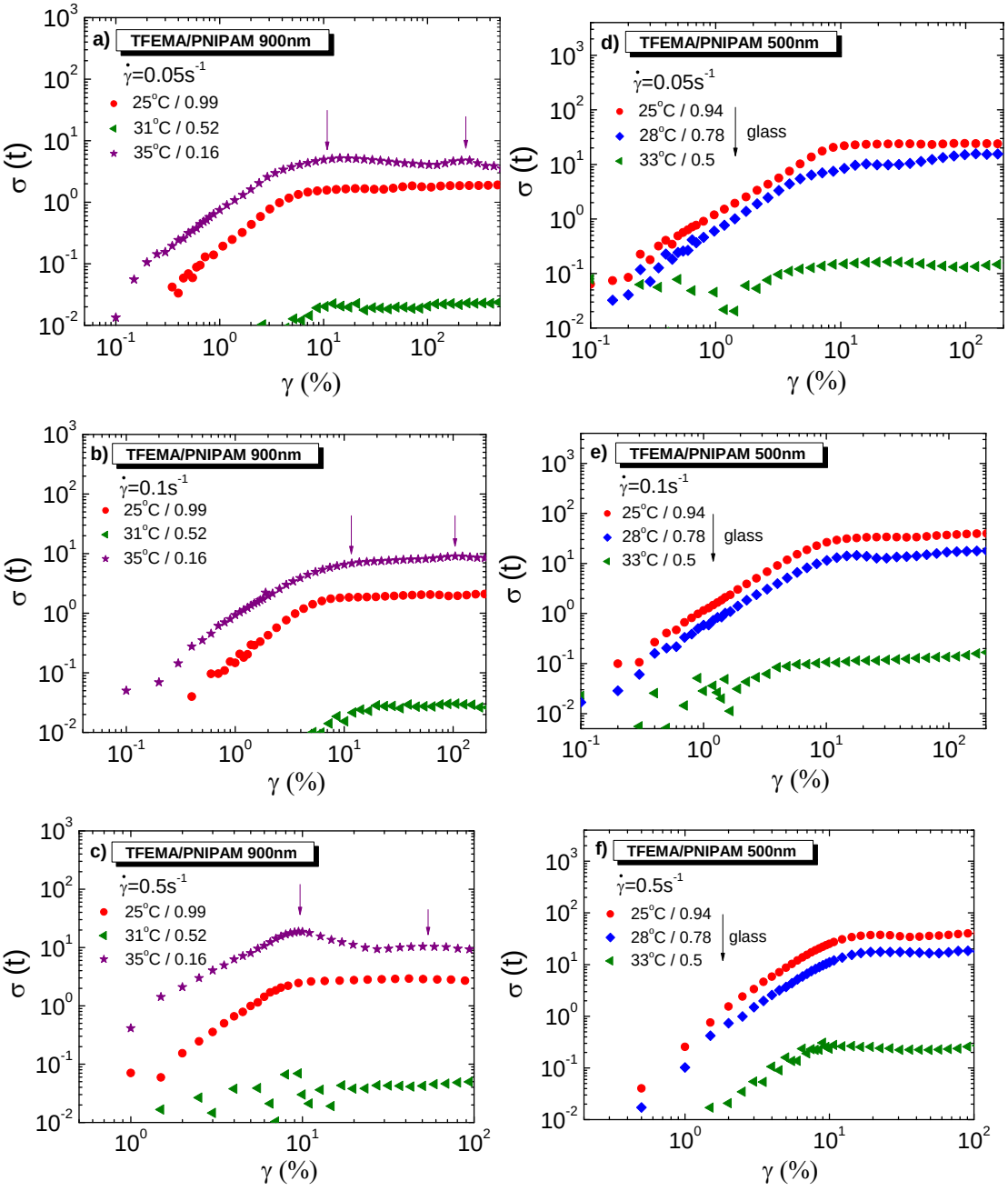

Fig. 5.20 *– Stress σ versus strain γ in log-log plots from step rate start-up experiments of systems TFEMA/PNIPAM 900nm and TFEMA/PNIPAM 500nm at various temperatures and different shear rates (0.05, 0.1 and 0.5 s^{-1}). Arrows show the double peak appeared at T>LCST.*

Fig. 5.21 depicts step rate tests for a specific temperature (T=25°C) for three different shear rates (0.05, 0.1 and 0.5s^{-1}). For both systems, we observe that the increase of the shear rates causes a rise of the stress, both at the peak and the plateau positions, while the yield strain (γ_y) moves to higher values. For hard spheres glasses, it has been previously reported that the rise of the stress is attributed to stronger elongation of the cage before yielding at larger rates. Increasing the shear rate the stress storage is also increased as Brownian motion cannot fully relax the distorted structure, leading thus to more pronounced stress overshoot. Moreover, increasing the volume fraction, the free volume decreases minimizing the cage distortion and therefore stress storage and relaxation (Koumakis, Laurati et al. 2012, Koumakis, Laurati et al. 2016). Fig. 5.21b and 5.21d display the monotonic decrease of the strain of the γ_y increasing the volume fraction and the increase of the γ_y increasing the shear rate applied.

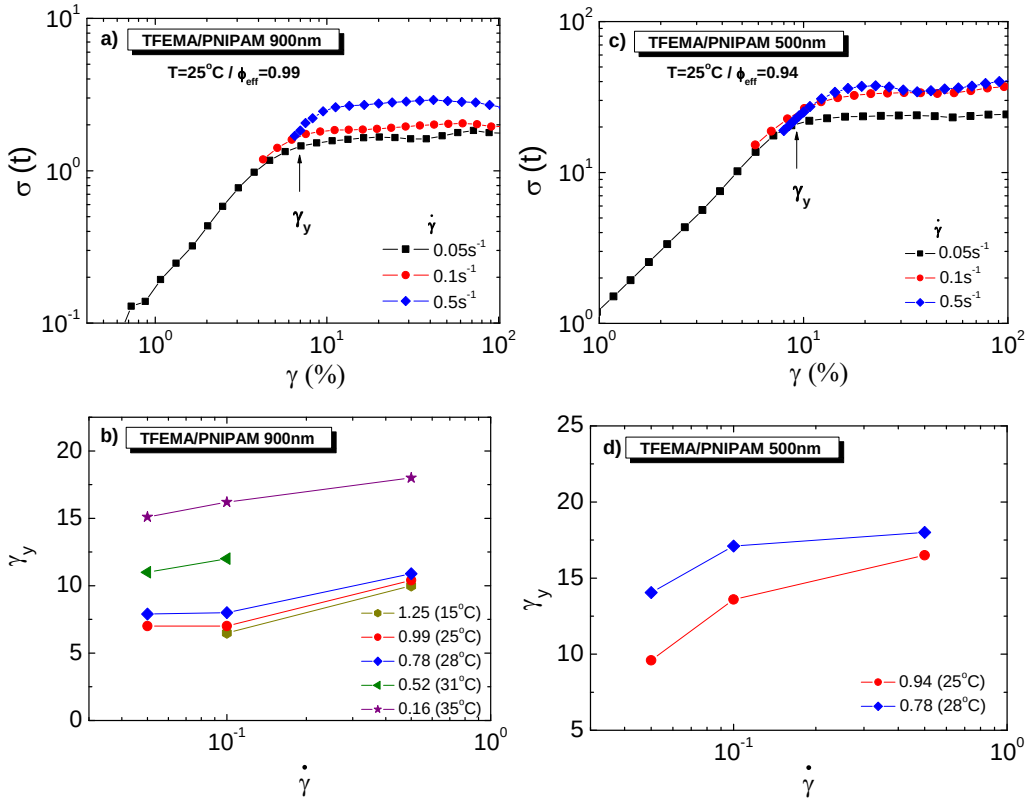

Fig. 5.21 *– a) and c) stress σ versus strain γ for T=25°C at different shear rates (0.05, 0.1 and 0.5s^{-1}) for both TFEMA/PNIPAM 900nm and TFEMA/PNIPAM 500nm systems, b) and d) strain at the yield strain versus shear rate for various volume fractions.*

5.3.3.3 Non – linear Viscoelasticity

In this section, studying the nonlinear response of both soft thermosensitive microgel systems at different temperatures, we extract information about how the applied strain affects their yielding behavior.

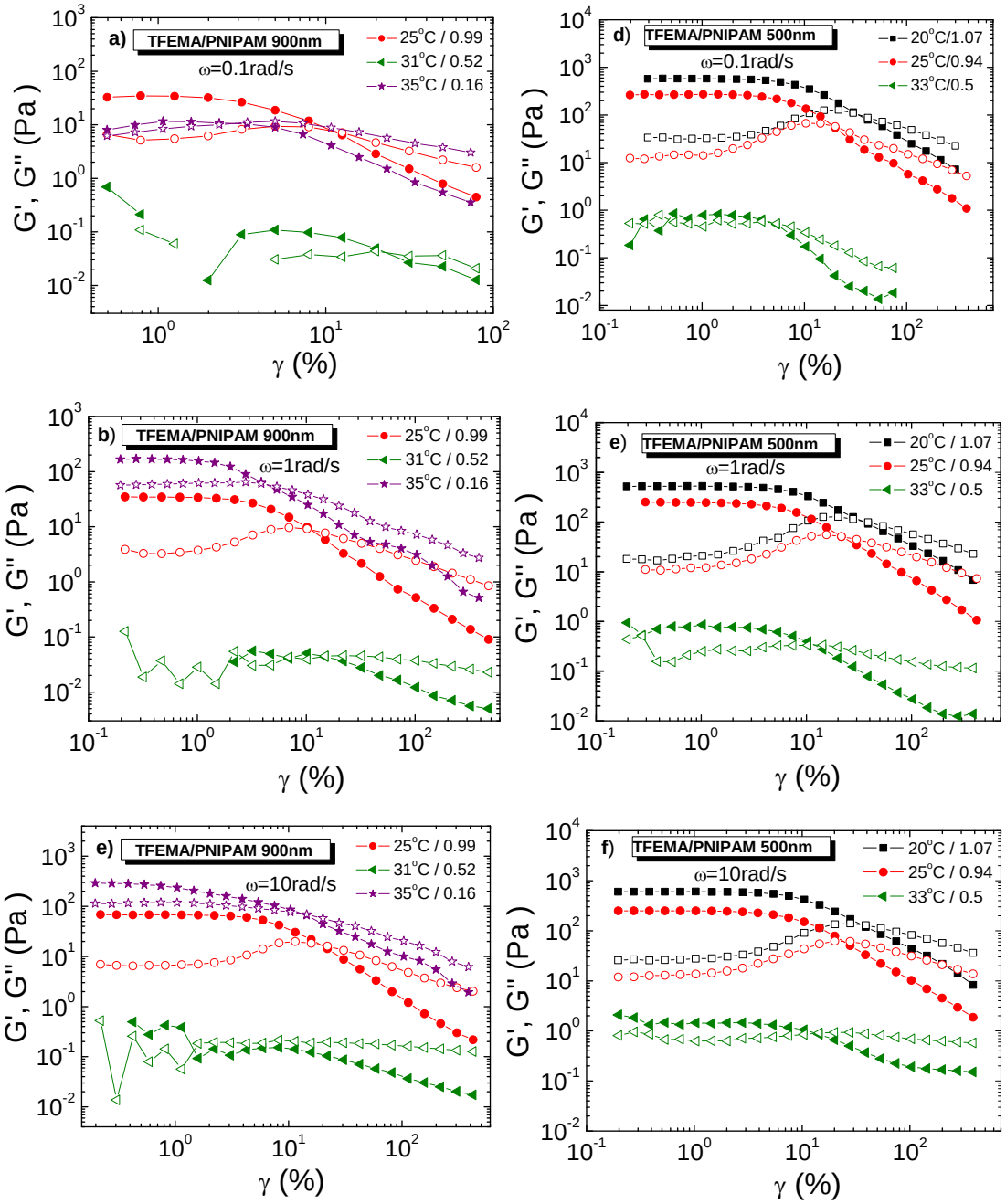

***Fig. 5.22** – Dynamic Strain Sweeps for various temperatures for TFEMA/PNIPAM 900nm at a) 0.1rad/s, b) 1rad/s and c) 10rad/s and TFEMA/PNIPAM 500nm at d) 0.1rad/s, e) 1rad/s and f) 10rad/s.*

Non-linear tests include Dynamic Strain Sweeps (DSS) were performed at different frequencies (0.1, 1, 10rad/s) and various temperatures (various effective volume fractions) from low to high strain amplitudes (fig. 5.22).

Both systems present a common general behavior in agreement with a large number of previous studies (Derec, Ducouret et al. 2003, Le Grand and Petekidis 2008, Pham, Petekidis et al. 2008). At low strain amplitudes there is the linear viscoelastic regime, which exhibits a solid-like response with G'>G''. For glassy state, the linear regime is related to the slight deformation of the cage formed by the neighbor particles. Increasing the strain amplitude, the elastic modulus G' starts to decrease, while the viscous one G'' passes through a peak before decrease as well. One way to determine the yield strain γ_y (G'=G'') is the crossover point beyond which the viscous stress is higher than the elastic one, marking the break of the cage formed by the neighbor particles and the transition from a viscoelastic solid to a viscoelastic liquid. At all frequencies probed, the crossover strain is at $\gamma_y \approx 10\%$, which agrees with the breakage of the cage of the repulsive glasses. The peak of G'' represents the maximum energy dissipation around yielding where it is expected that a large number of cages break and particle rearrangements are important (Petekidis, Moussaid et al. 2002, Koumakis, Pamvouxoglou et al. 2012).

At temperature T≈31°C, the system TFEMA/PNIPAM 900nm is a liquid rendering difficult the measurement of G' and G'' moduli at all frequencies applied due to weak torque signal.

For TFEMA/PNIPAM 900nm at temperature T=35°C, where we have the formation of network we observe the existence of two yielding points at ω=1rad/s. One at $\gamma_y \approx 5\%$ is connected to the breakage of inter-cluster bond, whereas a second one at higher strains $\gamma_y \approx 100\%$ where particles break apart. Both crossover points reflect correspondent length-scales; lower strains for bond-scale and higher ones for cluster-scale. At frequencies ω=0.1 and 10rad/s the two yielding points are weaker than at ω=1rad/s.

For system TFEMA/PNIPAM 500nm, increasing the temperature, we observe a continuous weakening of the glass until T=33°C, where the torque signal was too

low marking a liquid-like behavior. The measurements of moduli at temperatures above the LCST was not possible. We should mention that the rheological measurements are in agreement with DWS and confocal microscopy techniques.

For both systems the yield strain γ_y varies for different volume fractions and for frequencies ω=0.1 and 1rad/s increases monotonically increasing the volume fraction (Tables 5.d and 5.e). At ω=10rad/s the change is not monotonic and ranges between γ_y=12 and 17% depending on the volume fraction for TFEMA/PNIPAM 900nm, whereas for TFEMA/PNIPAM 500nm ranges between γ_y=13 and 49%.

TFEMA/PNIPAM 900nm				
ω=0.1rad/s				
T (°C) / ϕ_{eff}	**15°C / 1.25**	**25°C / 0.99**	**28°C / 0.78**	**35°C / 0.16**
γ_y	13%	11%	9%	3%
$G' \sim \gamma^{\nu}$	$G' \sim \gamma^{-1.5}$	$G' \sim \gamma^{-1.35}$	$G' \sim \gamma^{-1.25}$	$G' \sim \gamma^{-1.29}$
$G'' \sim \gamma^{\xi}$	$G'' \sim \gamma^{-0.72}$	$G'' \sim \gamma^{-0.78}$	$G'' \sim \gamma^{-0.79}$	$G'' \sim \gamma^{-0.55}$
ν/ξ	2.08	1.73	1.58	2.3
ω=1rad/s				
T (°C) / ϕ_{eff}	**15°C / 1.25**	**25°C / 0.99**	**28°C / 0.78**	**35°C / 0.16**
γ_y	12.5%	11%	9%	4.5%
$G' \sim \gamma^{\nu}$	$G' \sim \gamma^{-1.22}$	$G' \sim \gamma^{-1.2}$	$G' \sim \gamma^{-1.22}$	$G' \sim \gamma^{-1.42}$
$G'' \sim \gamma^{\xi}$	$G'' \sim \gamma^{-0.69}$	$G'' \sim \gamma^{-0.64}$	$G'' \sim \gamma^{-0.6}$	$G'' \sim \gamma^{-0.79}$
ν/ξ	1.77	1.88	2.03	1.8
ω=10rad/s				
T (°C) / ϕ_{eff}	**15°C / 1.25**	**25°C / 0.99**	**28°C / 0.78**	**35°C / 0.16**
γ_y	12%	16%	17%	13%
$G' \sim \gamma^{\nu}$	$G' \sim \gamma^{-1.2}$	$G' \sim \gamma^{-1.5}$	$G' \sim \gamma^{-1.43}$	$G' \sim \gamma^{-1.54}$
$G'' \sim \gamma^{\xi}$	$G'' \sim \gamma^{-0.62}$	$G'' \sim \gamma^{-0.75}$	$G'' \sim \gamma^{-0.66}$	$G'' \sim \gamma^{-0.96}$
ν/ξ	1.94	2	2.16	1.6

Table 5.d – *Values of the strain amplitude γ_c (G'=G'') and power laws in shear-thinning regime for TFEMA/PNIPAM 900nm at 0.1, 1 and 10rad/s.*

TFEMA/PNIPAM 500nm				
ω=0.1rad/s				
T (°C) / ϕ_{eff}	20°C / 1.07	25°C / 0.94	28°C / 0.78	33°C / 0.5
γ_y	33%	21%	20%	5%
$G' \sim \gamma^{\nu}$	$G' \sim \gamma^{-1.21}$	$G' \sim \gamma^{-1.25}$	$G' \sim \gamma^{-1.96}$	$G' \sim \gamma^{-1.56}$
$G'' \sim \gamma^{\xi}$	$G'' \sim \gamma^{-0.73}$	$G'' \sim \gamma^{-0.95}$	$G'' \sim \gamma^{-1.1}$	$G'' \sim \gamma^{-0.89}$
ν/ξ	1.66	1.3	1.8	1.75
ω=1rad/s				
T (°C) / ϕ_{eff}	20°C / 1.07	25°C / 0.94	28°C / 0.78	33°C / 0.5
γ_y	29%	21%	20%	12%
$G' \sim \gamma^{\nu}$	$G' \sim \gamma^{-0.99}$	$G' \sim \gamma^{-1.46}$	$G' \sim \gamma^{-1.37}$	$G' \sim \gamma^{-1.04}$
$G'' \sim \gamma^{\xi}$	$G'' \sim \gamma^{-0.66}$	$G'' \sim \gamma^{-0.8}$	$G'' \sim \gamma^{-0.72}$	$G'' \sim \gamma^{-0.37}$
ν/ξ	1.5	1.83	1.9	2.8
ω=10rad/s				
T (°C) / ϕ_{eff}	20°C / 1.07	25°C / 0.94	28°C / 0.78	33°C / 0.5
γ_y	35%	24%	31%	13%
$G' \sim \gamma^{\nu}$	$G' \sim \gamma^{-1.19}$	$G' \sim \gamma^{-1.36}$	$G' \sim \gamma^{-1.3}$	$G' \sim \gamma^{-0.69}$
$G'' \sim \gamma^{\xi}$	$G'' \sim \gamma^{-0.7}$	$G'' \sim \gamma^{-0.8}$	$G'' \sim \gamma^{-0.58}$	$G'' \sim \gamma^{-0.19}$
ν/ξ	1.7	1.7	2.2	3.6

Table 5.e – *Values of the strain amplitude γ_y (G'=G'') and power laws in shear-thinning regime for TFEMA/PNIPAM 500nm at 0.1, 1 and 10rad/s.*

Fig. 5.23 presents the yield strain γ_y at the crossover point (G'=G'') as a function of frequency for various temperatures for both systems. We observe that for both systems, the crossover transition shifts to higher strains as the frequency increases, which is more pronounced in attractive systems. Increasing the frequency, Brownian motions become less effective in assisting particles to escape from either their cages (in the case repulsive glass) or their attractive bonds (in the case of attractive gel) (Laurati, Egelhaaf et al. 2011). At T=35°C, the presence of attractive interactions leads to the formation of clusters. As a result, the length scales due to clustering are higher and then the yield strain needed for breaking the inter-cluster bonds is increased.

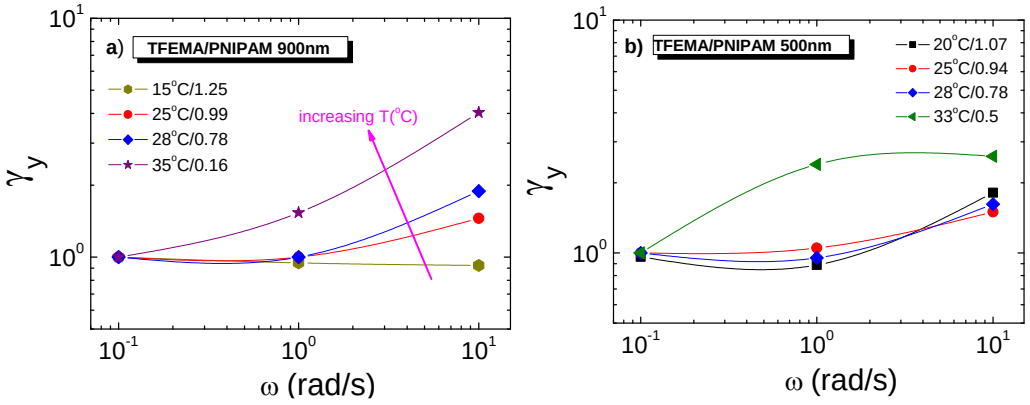

Fig. 5.23 *– Yielding point position γ_y (G'=G'') as a function of ω for various temperatures for a) TFEMA/PNIPAM 900nm and b) TFEMA/PNIPAM 500nm.*

At strains above the yield strain, where the material shows a viscoelastic liquid-like behavior, both the storage and the loss moduli exhibit a power law dependence with strain amplitude. Tables 5.d and 5.e summarize the values for the exponents v and ξ for various frequencies and temperatures for both systems. The exponents v and ξ are similar to what other experimental studies extracted (Mason and Weitz 1995, Mason, Lacasse et al. 1997, Derec, Ducouret et al. 2003). Moreover, the ratio of v/ξ is around 2, a value which agrees with theoretical predictions (Miyazaki, Wyss et al. 2006).

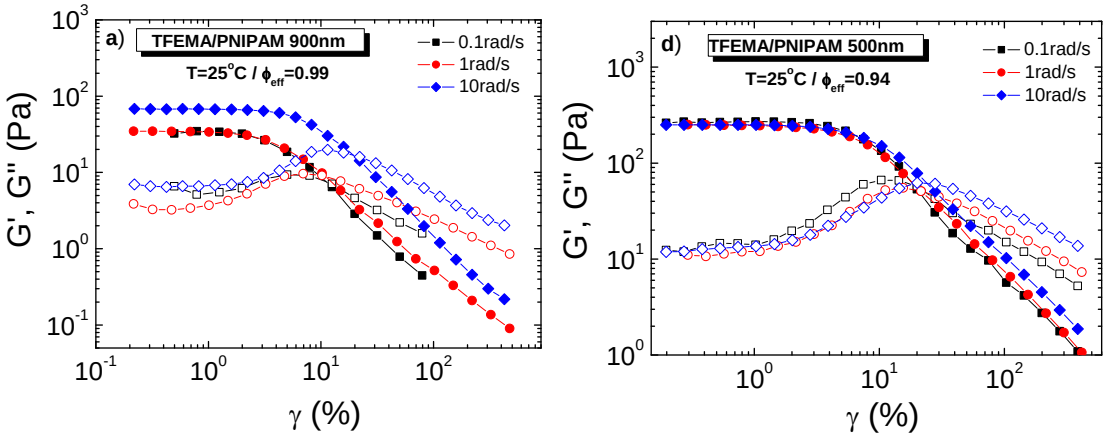

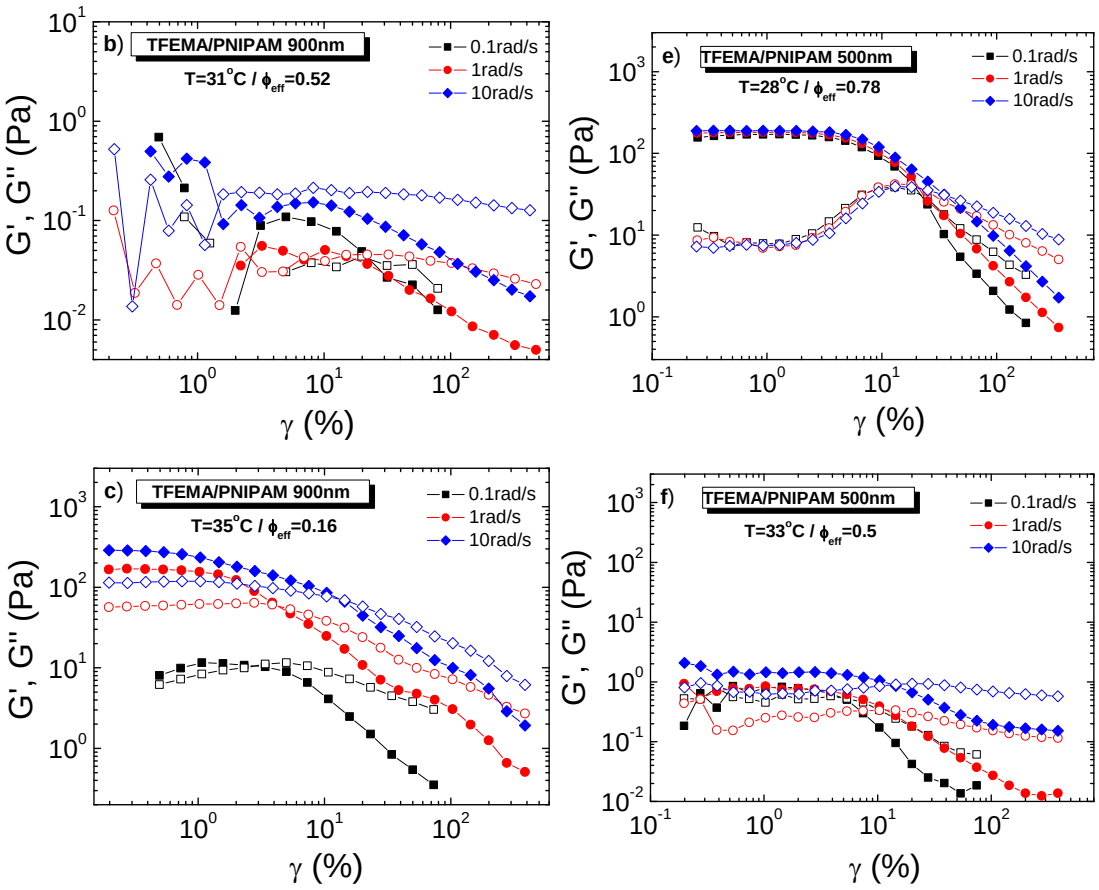

Fig. 5.24 – *Frequency dependence of Dynamic Strain Sweeps for a) 25°C, b) 31°C and c) 35°C for TFEMA/PNIPAM 900nm and d) 25°C, e) 28°C and f) 33°C for TFEMA/PNIPAM 500nm.*

Another way to present the DSS experiments in fig. 5.22 is by plotting the DSS for each volume fraction at different frequencies. In this way, we examined more clearly, the impact of frequency on yielding of both microgel systems at fixed temperatures.

Large Amplitude Oscillatory Shear (LAOS):

Large Amplitude Oscillatory Shear (LAOS) measurements consists of a popular method to investigate the nonlinear viscoelastic response of a system beyond the first harmonic approximation, which gives G' and G'' and is the standard output of most rheometers. Higher order harmonic contributions are accessed by collecting the full time-dependent stress signal during the application of a sinusoidal strain of large amplitude with strain amplitude γ and frequency ω (Philippoff 1966,

Dealy and Wissbrun 1990, Wilhelm, Maring et al. 1998, Cho, Hyun et al. 2005, Ewoldt, Hosoi et al. 2008). The nonlinear contributions in the signal can be extracted following different approaches (Ewoldt, Hosoi et al. 2008, Hyun, Wilhelm et al. 2011).

Fourier transform (FT) analysis is one of the oldest and the most common used techniques for analysis of LAOS experimental data, but it is difficult to establish a direct relation between the nonlinear response and the physical interpretation of material behavior. The periodic signal is expressed as a Fourier series (Wilhelm, Maring et al. 1998). The magnitude of the nonlinearity can be quantified by the ratio of the amplitude of the higher harmonics and the one of the fundamental first harmonic, as shown for many different systems (Wilhelm, Reinheimer et al. 1999, Daniel, Hamley et al. 2001, Langela, Wiesner et al. 2002, Schlatter, Fleury et al. 2005, Le Grand and Petekidis 2008, Carrier and Petekidis 2009).

More specifically, in strain-controlled LAOS deformation, the imposed oscillatory strain, $\gamma = \gamma_o \sin(\omega t)$, subjects the sample to a corresponding strain rate $\dot{\gamma} = \omega\gamma_o \cos(\omega t)$. The viscoelastic stress response to this input deformation can be analyzed by decomposition into the higher harmonics of the frequency (Fourier analysis) as:

$$\sigma(t) = \sigma_e(t) + \sigma_v(t) = \gamma_o \sum_{n-1}^{\infty} G_n^{'} \sin(n\omega t) + \gamma_o \sum_{n-1}^{\infty} G_n^{''} \cos(n\omega t) = \gamma_o \sum_{n-1}^{\infty} G_n^{*} \sin(n\omega t - \delta_n) \quad (5.5)$$

where n is an odd number due to symmetry conditions that denotes the number of higher harmonic present in the response (Bird, Armstrong et al. 1987); since the stress shows symmetry with respect to strain reversal, e.g. $\sigma(\gamma, \dot{\gamma}) = -\sigma(-\gamma, -\dot{\gamma})$, no even harmonics should be present in the equation σ(t). $G_n^{'}$ and $G_n^{''}$ are the moduli of each harmonic while δ_n is the phase difference of each harmonic from the phase of the applied strain. The stress response for individual harmonics is then written:

$$\sigma_n(t) = \gamma_o \left(G_n^{'} \sin(n\omega t) + G_n^{''} \cos(n\omega t)\right) = \gamma_o G_n^{*} \sin(n\omega t - \delta_n) \quad (5.6)$$

The stress response is also separated into elastic and viscous stresses which are described as parametric curves (Lissajous curves) of the oscillating stress versus strain (elastic Lissajous curves) or alternatively stress versus strain rate (viscous Lissajous curves) (Cho, Hyun et al. 2005, Ewoldt, Hosoi et al. 2008).

Moreover, the intensity of each harmonic is given by the expression:

$$I_n = \sqrt{G_n^{'2} + G_n^{''2}} \tag{5.7}$$

Thus, we can quantify the nonlinear behavior using the intensity ratios of the higher harmonics to the first. When the ratio I_n/I_1 shows a value close to zero, the state is mainly linear, whereas when the ratio is higher, nonlinearities become important too. All odd higher harmonics show similar dependencies on the strain amplitude γ and frequency ω with the amplitudes of the third harmonics considerably exceeding the other higher harmonics. So, we focus on the ratio I_3/I_1 in order to describe the nonlinear behavior.

The physical understanding of the higher harmonic components of the stress response is of great importance and can be obtained by representing the individual curves of the decomposed elastic stress σ' and viscous stress σ'' with an orthogonal set of polynomial functions, such as the Chebyshev polynomials of the first kind (Ewoldt, Hosoi et al. 2007, Ewoldt, Hosoi et al. 2008, Hyun, Wilhelm et al. 2011) as described by Cho et al. (Cho, Hyun et al. 2005). Chebyshev functions that can be used to create the elastic and viscous stresses as follows:

$$\sigma'(\bar{x}) = \gamma_o \sum_{n=odd} e_n(\omega, \gamma_o) T_n(\bar{x}) \tag{5.8}$$

$$\sigma''(\bar{y}) = \dot{\gamma}_o \sum_{n=odd} v_n(\omega, \gamma_o) T_n(\bar{y}) \tag{5.9}$$

where $T_n(\ )$ is the *nth*-order Chebyshev polynomial of the first kind, $\bar{x} = \gamma(t)/\gamma_o$ and $\bar{y} = \dot{\gamma}(t)/\dot{\gamma}_o$ with $\dot{\gamma}_o$ the maximum in-cycle shear rate and $e_n(\omega,\gamma_o)$ and $v_n(\omega,\gamma_o)$ are the elastic and viscous Chebyshev coefficients of order *n*, respectively.

The LAOS experiments allow us to probe the strain stiffening and/or strain softening behavior and the shear thickening and/or shear thinning one. The third-order coefficients, e_3 and v_3, are used to classify the response in terms of strain stiffening/softening ($e_3>0$ and $e_3<0$ respectively) and shear thickening/thinning ($v_3>0$ and $v_3<0$ respectively) and (see fig. 5.25). The elastic Chebyshev coefficients are connected with the local elastic non-linear coefficients calculated at specific points within the period as Ewoldt et al. have been reported (Ewoldt, Hosoi et al. 2008):

$$G_L^{'} = \left.\frac{\sigma}{\gamma}\right|_{\gamma=\pm\gamma_0} = \sum_{n-odd} G_n^{'}(-1)^{(n-1)/2} = e_1 + e_3 + \ldots \tag{5.10}$$

and

$$G_M^{'} = \left.\frac{d\sigma}{d\gamma}\right|_{\gamma=0} = \sum_{n-odd} nG_n^{'} = e_1 - 3e_3 + \ldots \tag{5.11}$$

where $G_L^{'}$ is the large-strain modulus or secant modulus at the maximum imposed strain and $G_M^{'}$ is the minimum-strain elastic modulus or tangent modulus at zero instantaneous strain (γ=0). Under large strains (fast flow), colloids tend to form complex microstructures due to increased strain deformation that result in increased modulus. In LAOS experiments, for large imposed strain amplitude, $G_L^{'} > G_M^{'}$ with the material being strain stiffening within a given cycle.

Shear thickening occurs in colloidal suspensions subjected to strong viscous flows and is accompanied by a rapid or even discontinuous increase of the viscosity due to large distortion of the particle distribution and increased energy dissipation. On the contrary, shear thinning occurs when strong viscous flows fluidize the local

microstructure due to shear-induced ordering of the particles, with the shear viscosity decreasing (Barnes 1989, Ackerson 1990). The viscous Chebyshev coefficients are connected with the shear viscosity as follows:

$$\eta_M^{'} = \left.\frac{d\sigma}{d\dot{\gamma}}\right|_{\dot{\gamma}=0} = \frac{1}{\omega}\sum_{n-odd} nG_n^{"}(-1)^{(n-1)/2} = v_1 - 3v_3 + \ldots \tag{5.12}$$

and

$$\eta_L^{'} = \left.\frac{\sigma}{\dot{\gamma}}\right|_{\dot{\gamma}=\pm\dot{\gamma}_0} = \frac{1}{\omega}\sum_{n-odd} G_n^{"} = v_1 + v_3 + \ldots \tag{5.13}$$

where $\eta_L^{'}$ and $\eta_M^{'}$ are the instantaneous dynamic viscosities at the largest and smallest shear rates, respectively.

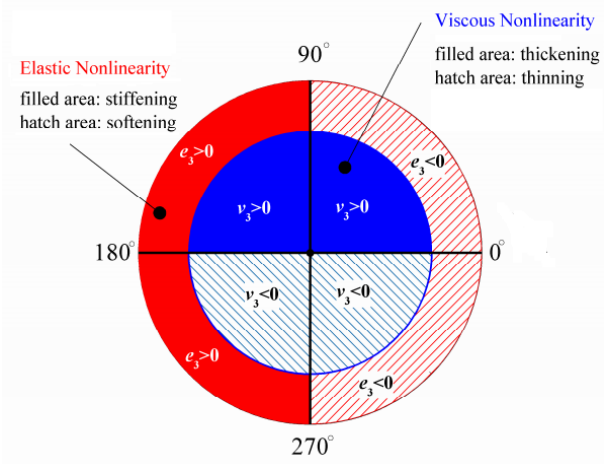

Fig. 5.25 – *Schematic diagram summarizing the interpretation of the third-order Chebyshev coefficients. Adapted from (Hyun, Wilhelm et al. 2011).*

Ewoldt et al. (Ewoldt, Hosoi et al. 2008, Ewoldt, Winter et al. 2010) also defined dimensionless indexes of nonlinearity:

$$S = \frac{G_L^{'} - G_M^{'}}{G_L^{'}} \tag{5.14}$$

and

$$T = \frac{\eta_L^{'} - \eta_M^{'}}{\eta_L^{'}} \qquad (5.15)$$

The elastic nonlinearity is strain-stiffening when S>0 and is strain-softening when S<0. When T>0, the behavior is intra-cycle shear-thickening and shear-thinning when T<0 (Laurati, Egelhaaf et al. 2014).

Poulos et al. proposed a simpler way to classify the non-linear response of systems based on the framework of Ewoldt et al. . According to this simpler method, the total stress response $\sigma_{total}(t,\omega)$ can be decomposed into the first harmonic response $\sigma_1(t,\omega)$, which is directly extracted by rheometer's software:

Lissajous figures:

The onset of a nonlinear stress response to oscillatory shear can be visualized by Lissajous figures for both systems, in which the stress response is plotted as a function of either strain amplitude or shear rate in order to highlight the elastic (stress vs strain amplitude) and viscous (stress vs shear rate) parts of the response, respectively. Fig. 5.26 and fig. 5.27 the LAOS response for TFEMA/PNIPAM 900nm and TFEMA/PNIPAM 500nm respectively at three frequencies (0.1, 1 and 10rad/s).

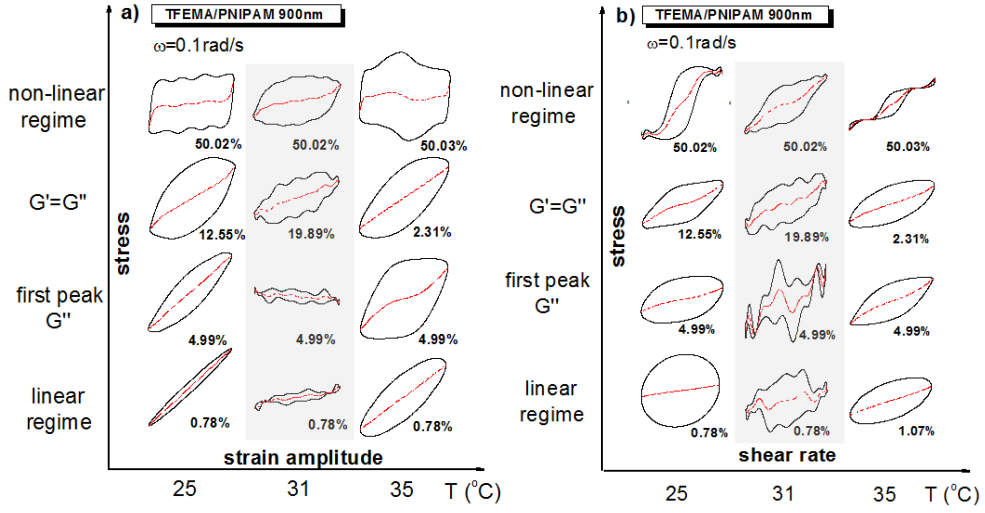

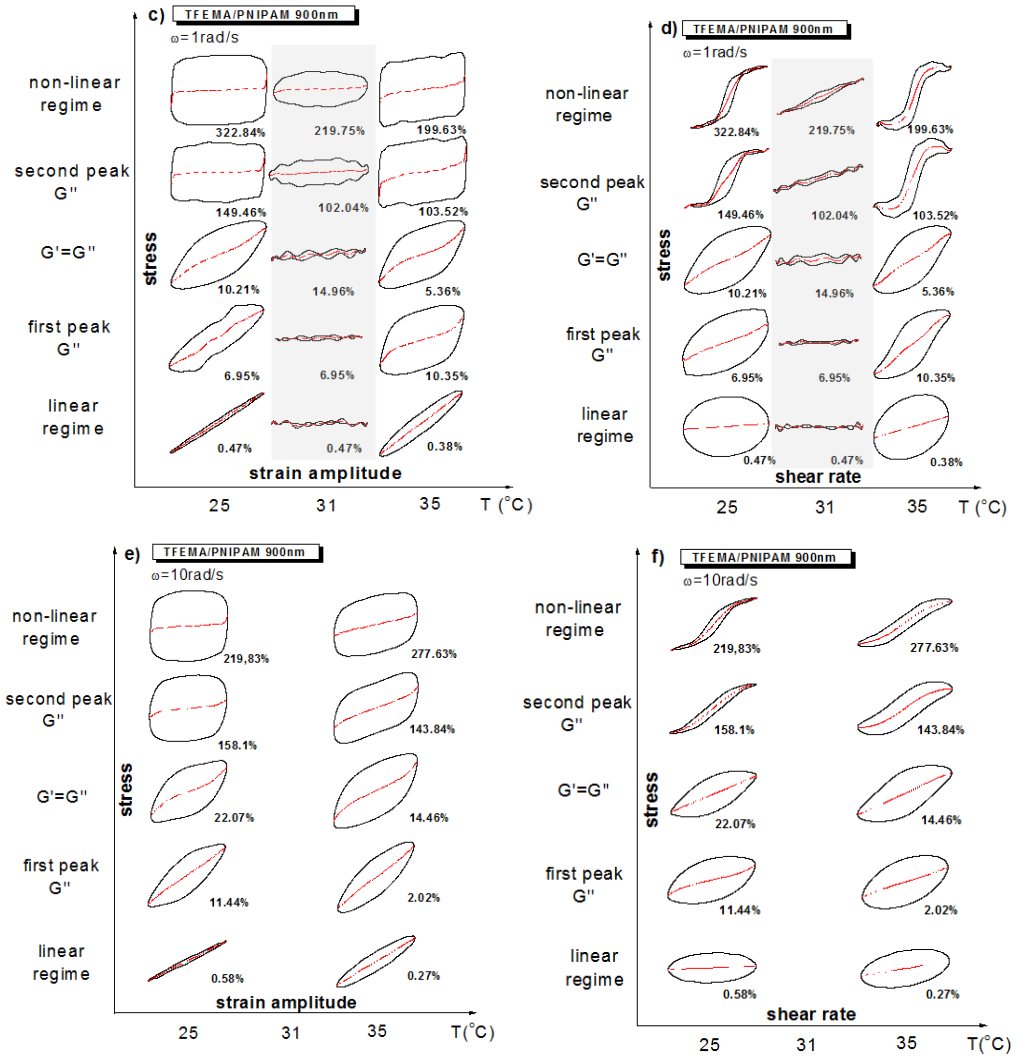

Fig. 5.26 *- Elastic and viscous Lissajous curves map for different strains for TFEMA/PNIPAM 900nm at frequencies 0.1, 1 and 10rad/s; a) The solid lines are the normalized total stress response and the dotted lines are the elastic stress response as a function of the normalized strain and b) the viscous stress response as a function of the normalized strain rate.*

For the system TFEMA/PNIPAM 900nm, in the linear regime, where the stress response is sinusoidal, the Lissajous figures are elliptical, while any deviation from this shape indicates the contribution of higher harmonic components. Three different states were investigated (glassy/25°C, liquid/31°C and gel/35°C) in various strain regimes. For ω=1rad/s, at low strains (γ=0.47%) we observe the linear regime, where the elastic and viscous Lissajous figures for both glass and gel samples are elliptical, indicating a linear response of the system, with the elastic contribution to

stress (red dashed lines at fig. 5.26a, 5.26c and 5.26e) being a straight line, the slope of which is equal to G' and its value is in agreement with the one obtained by DSS or DFS in the linear regime. Similarly the intracycle viscous stress (red dashed lines at fig. 5.26b, 5.26d and 5.26f) is also straight line at low strain amplitudes with their slope being equal to G''/ω. For T=31^{o}C, that we are close to liquid state the experimental data suffer from noise indicating that we measure below the torque resolution of the instrument.

As the strain amplitude increases, the Lissajous curves are progressively distorted due to stress response which is no longer sinusoidal. For T=25^{o}C, where the interparticle interactions are repulsive, increasing the strain amplitude the increasingly rectangular shape indicates the extension of the flow regime over a larger fraction of the cycle. This rectangular shape is similar to what is reported for various repulsive systems such as PMMA hard spheres (Koumakis, Pamvouxoglou et al. 2012), microgels (Brader, Siebenbürger et al. 2010, Koumakis, Pamvouxoglou et al. 2012, Siebenbürger, Fuchs et al. 2012), star-like micelles (Renou, Stellbrink et al. 2010, Koumakis, Pamvouxoglou et al. 2012, Poulos, Stellbrink et al. 2013) and multi-arm star polymers (Rogers, Erwin et al. 2011). For the attractive state (T=35^{o}C), we observe a weak stress overshoot at large strains (fig.5.26c), where the second peak of G'' is detected, which indicates the breaking of intra-clusters bonds. A similar overshoot but even weaker, we also observe for T=25^{o}C at the second peak of G'', which is connected with the break of the cage structure by the applied flow.

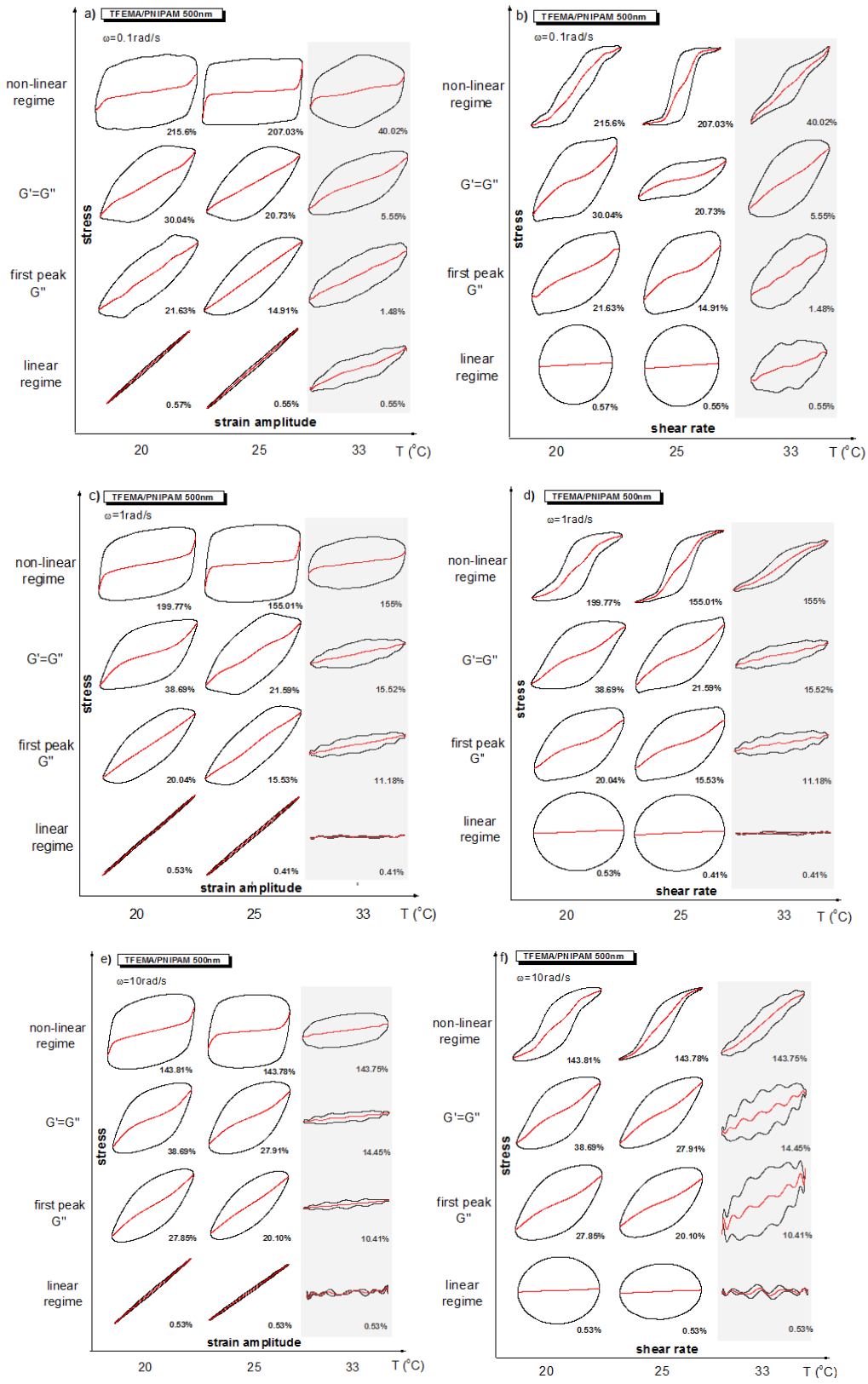

Fig. 5.27 - *Elastic and viscous Lissajous curves map for different strains γ for TFEMA/PNIPAM 500nm at frequency ω=0.1, 1 and 10rad/s; a) The solid lines are the normalized total stress response and the*

dotted lines are the elastic stress response as a function of the normalized strain and b) the viscous stress response as a function of the normalized strain rate.

Similarly for the smaller particles (fig. 5.27), three different temperatures in the repulsive regime were investigated (T=20, 25 and 33^{o}C), at three different frequencies (0.1, 1 and 10rad/s) and various strain regimes. In the linear regime, for T=20 and 25^{o}C and all frequencies probed, the elastic and viscous Lissajous figures are elliptical, whereas for T=33^{o}C, where we are getting closer to the transition to a viscoelastic liquid, the Lissajous plots are fuzzy due to torque resolution issues. Increasing the strain amplitude, the shape of the curves changes, with the elastic and viscous stress contributions to the total stress denoting that we are already in the nonlinear regime. The square-like Lissajous loop in the elastic representation is similar to what is reported for various repulsive systems (Renou, Stellbrink et al. 2010, Koumakis, Pamvouxoglou et al. 2012).

For both systems, the qualitative behavior is the same at all frequencies applied. However, increasing the frequency the Lissajous curves become smoother.

Fourier transform analysis:

As we already highlighted, in order to quantify the nonlinear behavior we can use the intensity ratios of the higher harmonics to the first one. The linear regime is signaled when the ratio I_n/I_1 is close to zero, whereas the onset of nonlinearities is marked with higher values of this ratio.

For TFEMA/PNIPAM 900nm, for all frequencies (0.1, 1 and 10rad/s) the strain dependence of the ratio I_3/I_1 shows that for both glass and gel states, already at γ=1% the third harmonic contributions become significant (fig. 5.28a-5.28f) and thus the stress response is nonlinear, which is in agreement with the DSS experimental results. For glassy state increasing the strain, the ratio I_3/I_1 increases continuously and saturates at around γ=100%. This increase reflects an increasingly pronounced plastic response. For gel (35^{o}C), for frequencies 1 and 10rad/s, increasing the strain amplitude, the ratio I_3/I_1 increases as well and we observe two saturation points at around γ=5% and γ=100%, which are connected to the two yielding points that

reflect the breakage of inter-cluster bonds and the breakage of bonds between particles respectively. For ω=1rad/s at γ=39% and for ω=10rad/s at γ=11%, we observe an abrupt increase of the ratio I_3/I_1. In both glass and gel states the results are consistent to the DSS experiments. At large strain amplitudes, we observe a small decrease of I_3/I_1 for both glass and gel states, which is attributed to the approach toward a simpler liquid-like response, as also observed in hard-sphere glasses (Koumakis, Pamvouxoglou et al. 2012), concentrated microgel dispersions (Le Grand and Petekidis 2008, Carrier and Petekidis 2009, Koumakis, Pamvouxoglou et al. 2012), multiarm star polymers (Rogers, Erwin et al. 2011) and star-like micelles (Poulos, Stellbrink et al. 2013). In the liquid state (31°C), the trend of the ratio I_3/I_1 is not clear due to the fact that we are close to the torque resolution of the instrument.

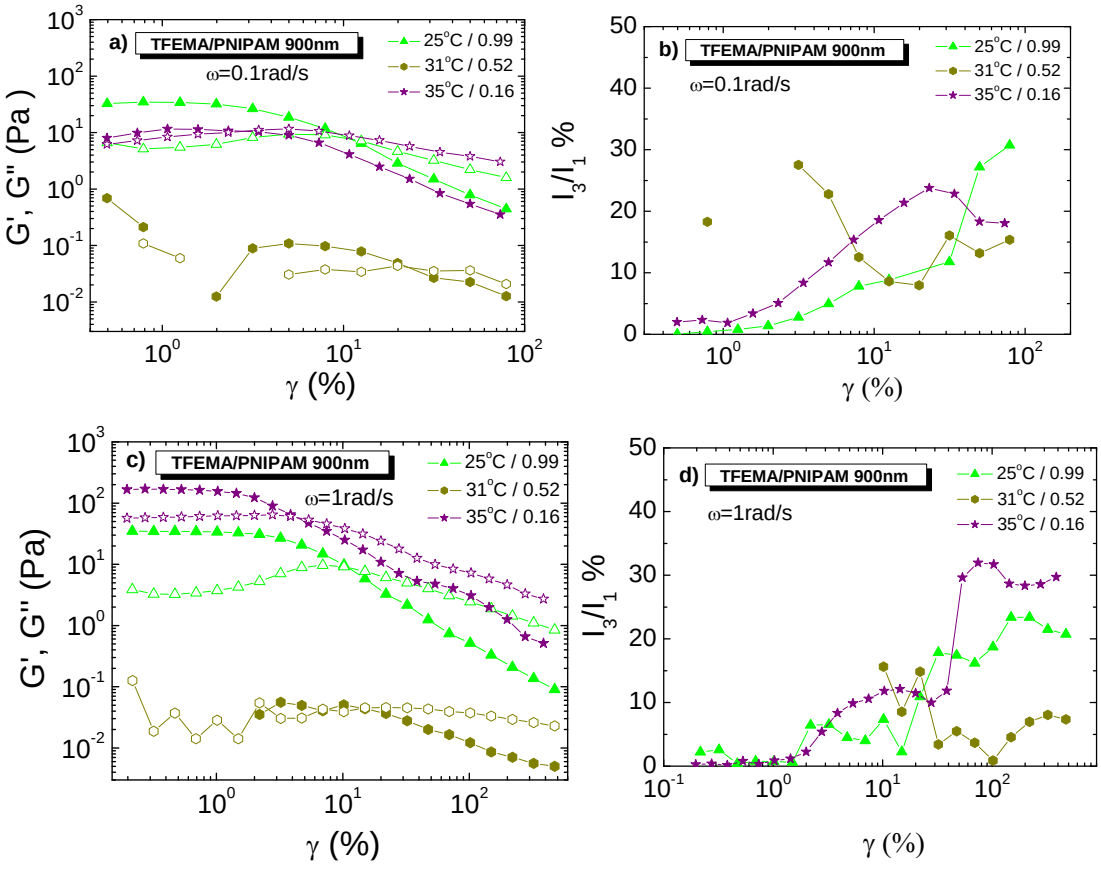

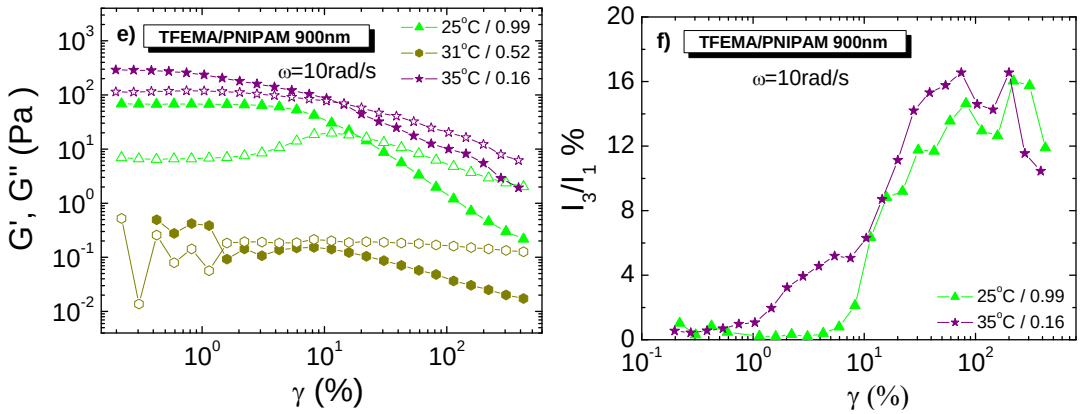

Fig. 5.28 *– a) DSS for various temperatures for 0.1, 1 and 10rad/s for TFEMA/PNIPAM 900nm and b) FT analysis results as indicated for the same system, showing the amplitude of the third harmonic divided by that of the first, I_3/I_1, as a function of strain amplitude* γ.

Fig. 5.29 displays the strain dependence of the ratio I_3/I_1 for TFEMA/PNIPAM 500nm, at frequencies 0.1, 1 and 10rad/s. Similarly to larger particles, at temperatures 20 and 25°C, for all frequencies probed, increasing strain, the ratio I_3/I_1 increases continuously as well and saturates at around γ=100%, denoting the plastic response for glassy regime. At T=33°C, the system is close to transition from a viscoelastic solid to a viscoelastic liquid. At ω=0.1rad/s, I_3/I_1 presents an increase at around γ=10%, which is followed by a decrease, an abrupt increase at around γ=100% and saturation around γ=300%. At 1 and 10rad/s, at low strain amplitudes there are torque issues, which become less pronounced increasing the strain amplitude. For both 1 and 10rad/s, at γ=10%, I_3/I_1 increases continuously and finally saturates at around γ=100%.

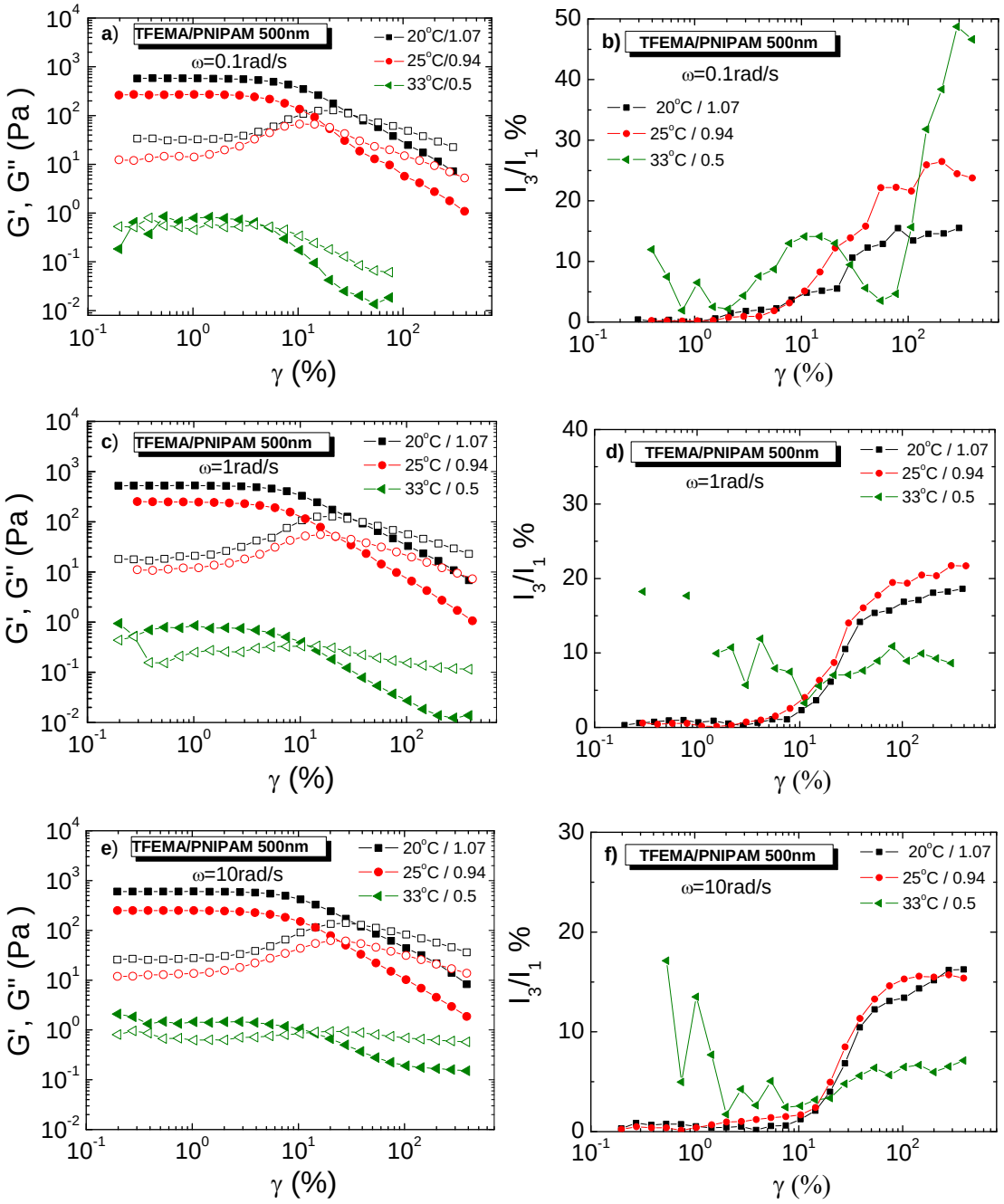

Fig. 5.29 *– a) DSS for various temperatures for 0.1, 1 and 10rad/s for TFEMA/PNIPAM 500nm and b) FT analysis results as indicated for the same system, showing the amplitude of the third harmonic divided by that of the first, I_3/I_1, as a function of strain amplitude* γ.

Stress expansion using Chebyshev polynomials:

As already mention, the use of Chebyshev coefficients allows decomposition of the stress response into purely elastic and viscous components. Here, we focus at the third order coefficients $e_3 = -G_3^{'}$ and $v_3 = G_3^{"}/\omega$, since they are significantly

larger than higher order contributions. By comparing absolute values of e_3 and v_3 and the related S and T nonlinearity indexes, which are extracted based on the raw stress response, we can evaluate the relative contribution of both the elastic and viscous in-cycle responses.

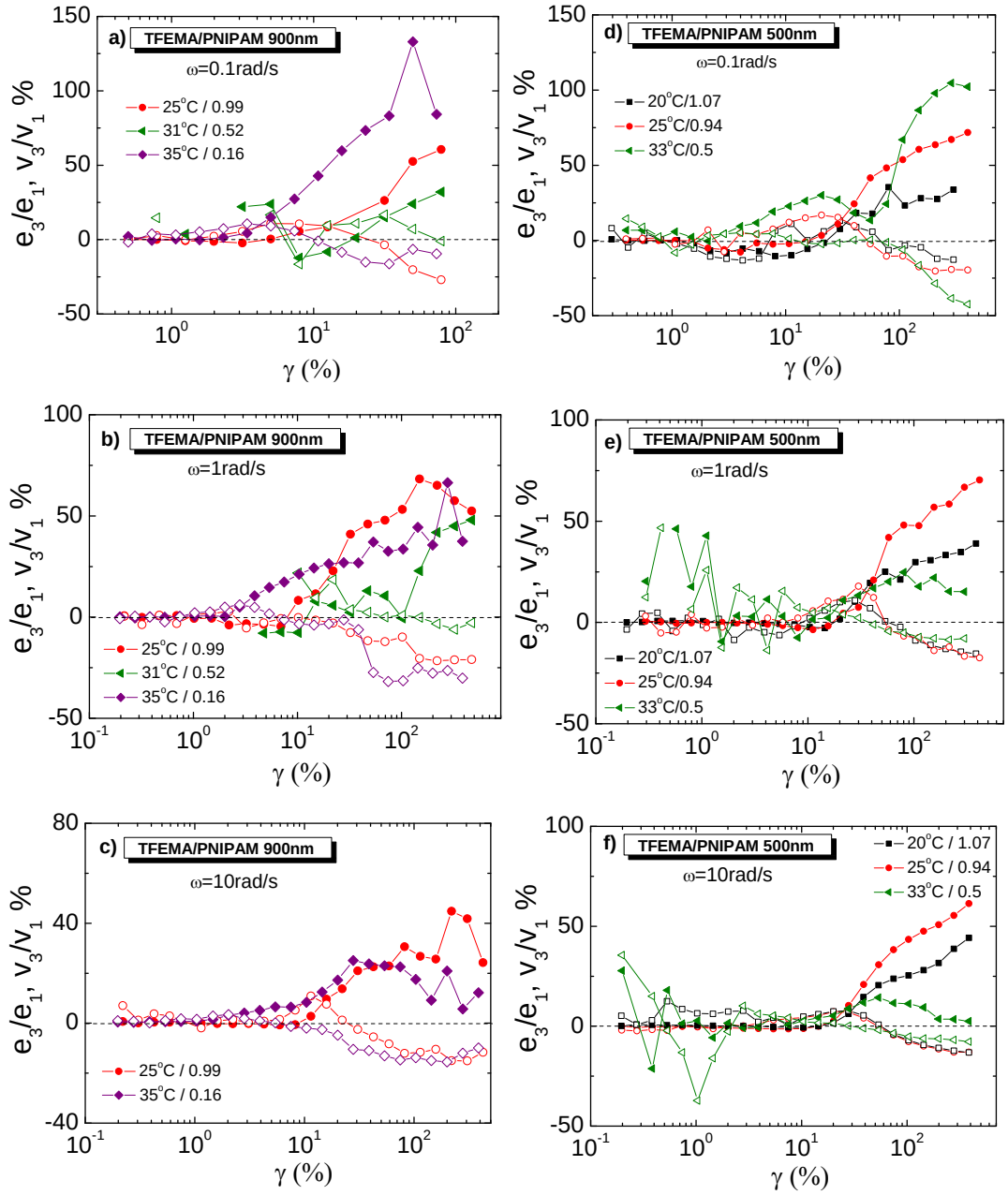

Fig. 5.30 *– Relative third order elastic, e_3/e_1 (full symbols) and viscous, v_3/v_1 (open symbols) Chebyshev coefficients vs γ for different temperatures for TFEMA/PNIPAM 900nm (a), b) and c)), and TFEMA/PNIPAM 500nm (d), e) and f)).*

Fig. 5.30 display e_3/e_1 and v_3/v_1 as a function of the applied strain at frequencies 0.1, 1 and 10rad/s for both systems. For the TFEMA/PNIPAM 900nm, in the linear regime of the glassy state (25^{o}C) of ω=1rad/s (fig.5.30b), no contribution from higher order intracycle elastic or viscous stresses is detected. Increasing the strain amplitude above about 1%, v_3/v_1 starts to increase as well revealing a shear thickening contribution, whereas no elastic contribution is observed. This fact coincides with the increase of G'' in DSS, which is related to the increased energy dissipation, reflecting the purely viscous origin of the nonlinearity at these strains. Increasing the strain above 2%, e_3/e_1 starts to increase strongly denoting a strain stiffening non-linear behavior. Simultaneously, v_3/v_1 decreases and above γ=10% becomes negative, marking the onset of a shear thinning nonlinear viscous response. Between strains 2%<γ<10%, the sample displays both elastic and viscous nonlinearities attributed to strain stiffening and shear thickening respectively. At even higher strains, both the elastic and viscous Chebyshev coefficients reach almost a plateau similarly with the ratio I_3/I_1 seen at fig. 5.28d. At T=31^{o}C, the system has a liquid-like behavior and the signal is quite weak due to torque issues. For gel state (35^{o}C) and ω=1rad/s (fig.5.30b), the sample exhibits a similar behavior to the glass state. The linear regime extends up to γ=1% with no detection of both elastic and viscous contributions, whereas at strains above 2%, e_3/e_1 increases sharply reflecting a strain stiffening character, while v_3/v_1 drops and become negative at strains above 7% signaling a shear thinning response. At around γ=20%, we observe that both coefficients reach a first plateau which is followed by a second one at around 40% strain. The existence of two plateau is attributed to two length-scale yielding processes that take place for gels similarly to what we saw in DSS experiments. As we have already reported, the first yielding process is connected to the breakage of the bonds between clusters (Zaccone, Wu et al. 2009, Koumakis and Petekidis 2011, Laurati, Egelhaaf et al. 2011). Since gels is an arrested state, the breakage of bonds implies an increased energy dissipation and a reduced elastic response which is connected to strain softening. When the bonds between clusters break, restructuring of the gel structure is possible which leads to stronger gel networks

and strain stiffening in average. The second yielding process corresponds to the final yielding and the fluidization of the sample, with shear thinning nonlinear response dominating. Between strains 2%<γ<10%, the system exhibits both elastic and viscous behavior connected to strain stiffening and shear thickening respectively. Similar behaviors to what we detected for all temperatures for ω=1rad/s, we observe for frequencies 0.1 and 10rad/s as well.

System TFEMA/PNIPAM 500nm (fig. 5.30d-f) exhibits an analogous behavior with the system TFEMA/PNIPAM 900nm at glassy regime for ω=1rad/s. For T=20^{o}C and 25^{o}C (fig.5.30e), the linear regime extends up to strain amplitudes 8%. Increasing further the strain amplitude, e_3/e_1 increases and nonlinearities are attributed to strain stiffening. In parallel, v_3/v_1 increases until γ=26% corresponding to shear thickening (coincides with the maximum of G'' from DSS), then drops and become negative at around γ=60% indicating shear thinning viscous response. At higher strains, both Chebyshev coefficients saturate around 100% strain similarly to FT analysis. At T=33^{o}C that we are close to liquid-like behavior, at low strains the signal is too weak due to torque issues. However, at higher strains displays a similar but weaker response compared to repulsive regime (20 and 25^{o}C). Analogous responses we also observed for frequencies 0.1 and 10rad/s as well.

Fig. 5.31 depicts an alternative way of plotting the third order Chebyshev coefficients for both systems, at various temperatures and frequencies.

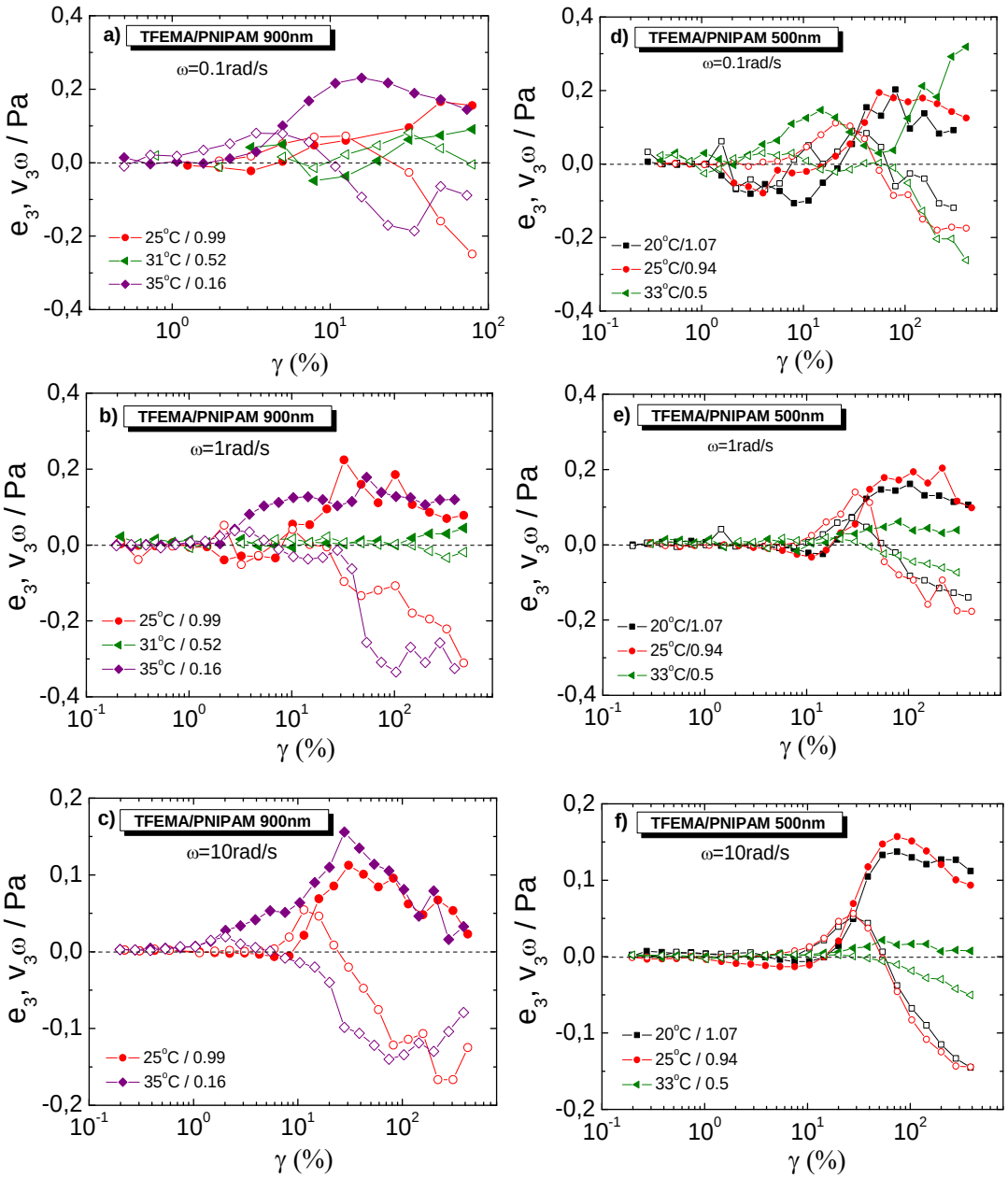

Fig. 5.31 *- Absolute values of the strain hardening/softening, e_3 (full symbols), and shear thickening/thinning, v_3 (open symbols) coefficients, vs γ for different temperatures for TFEMA/PNIPAM 900nm (a), b) and c)), and TFEMA/PNIPAM 500nm (d), e) and f)).*

Fig. 5.32 presents the strain-stiffening ratio S and shear-thickening ratio T for different frequencies and temperatures for both systems. For system TFEMA/PNIPAM 900nm, at temperatures T=25 and 35°C, which correspond to glassy and gel regime respectively, at all frequencies and strain amplitudes probed, the nonlinearity index S>0, reflecting the strain stiffening of the system for all strain

spectra. However, the nonlinearity index T exhibits a different behavior. At low strain amplitudes the nonlinearity index T>0, denoting shear thickening of the sample. At strain around 10%, T<0 indicating a shear thinning behavior. Finally, at 31°C, the response is random due to the viscoelastic liquid-like behavior.

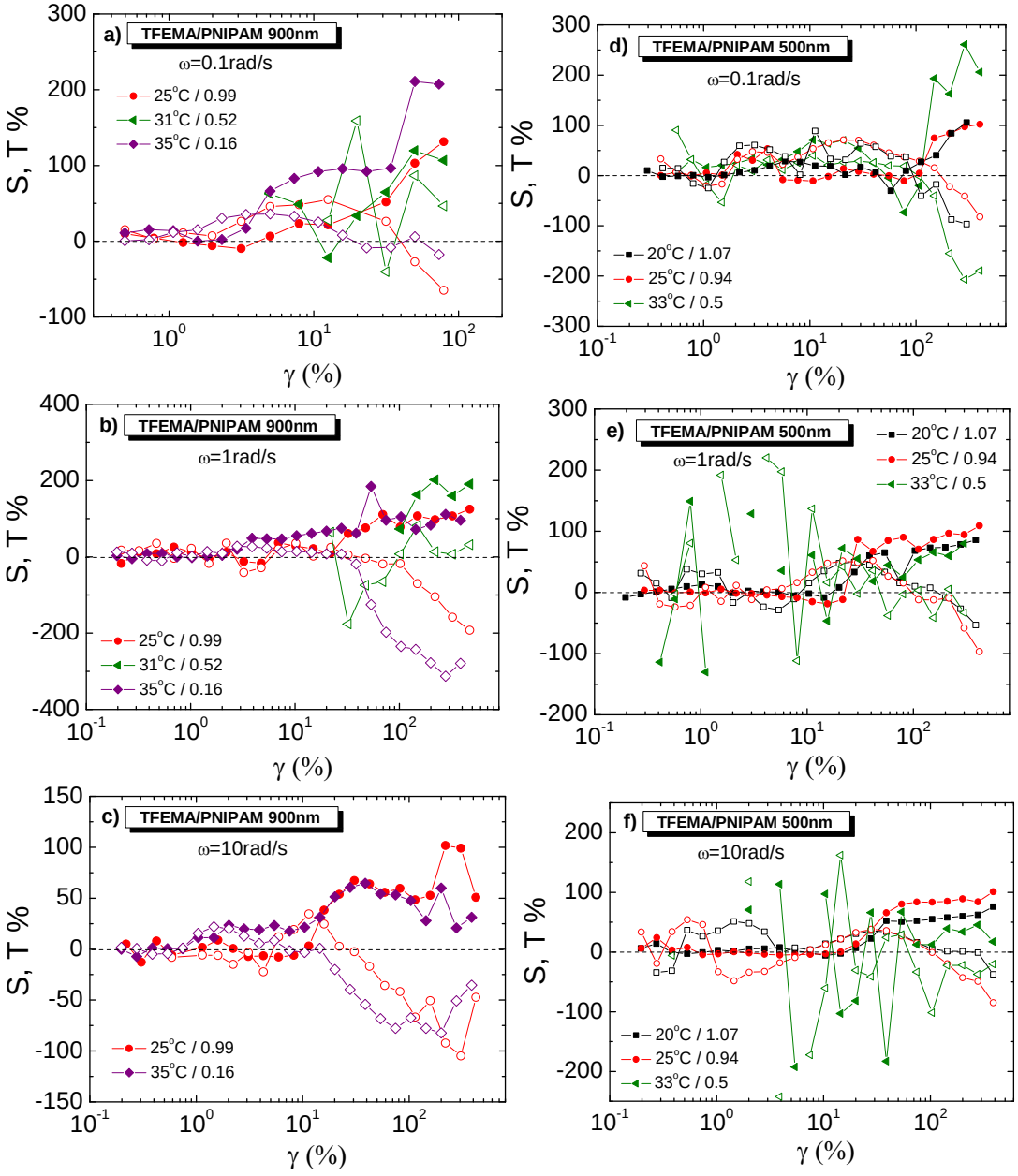

Fig. 5.32 *– Dimensionless indexes of nonlinearity, S (full symbols) and T (open symbols) vs γ for different temperatures for TFEMA/PNIPAM 900nm (a), b) and c)), and TFEMA/PNIPAM 500nm (d), e) and f)).*

For system TFEMA/PNIPAM 500nm, at 20 and 25^{o}C, which correspond to glassy regime, the indexes S and T show a similar behavior to what we observed for system TFEMA/PNIPAM 900nm, with S>0, while T>0 at low strains and T<0 at higher ones, with the difference that the transition from positive to negative values of index T takes place at γ>10%. At 33^{o}C, the behavior is arbitrary.

5.4 Conclusions

Structure, dynamics and mechanical properties of two different hybrid core-shell microgel systems investigated by employing various experimental methods such as scattering techniques, rheology and confocal microscopy. Both systems consist of a rigid TFEMA core of similar size and a PNIPAM shell of similar cross-linking density but different shell size and therefore different softness. Dynamic light scattering in dilute suspensions revealed shrinking of 57% for the softer system whereas about 46% for the less soft. Static light scattering in various dilute suspensions was used for the estimation of the interparticle interactions expressed by second virial coefficient. For temperatures below the LCST the interactions are repulsive, while they switch in attractive for temperatures above the LCST. In concentrated regime, the tune of the interactions, upon temperature changes, allows switching between glass, liquid and gel state. The structure and dynamics of each physical state was explored by using confocal microscopy and diffusive wave spectroscopy respectively. Linear and non-linear rheology was also employed for investigating the viscoelastic properties of the different physical states. Moreover, the application of these techniques revealed that the larger in size system is characterized by stronger both repulsive and attractive interactions, at repulsive and attractive regimes respectively, comparing to the smaller one. More specifically, at LCST the larger system in size presents a clear solid-liquid transition, which is quite weak for the smaller one. Finally, at temperatures above the LCST the attractive interactions induced by PNIPAM in the softer system lead to the formation of a percolated network and a strong liquid-solid transition, whereas in the less soft

system the weak attractive attractions fail to form a network and therefore lead to a “sea” of floating clusters.

References:

Ackerson, B. J. (1990). "Shear induced order and shear processing of model hard sphere suspensions." Journal of Rheology **34**(4): 553-590.

Appel, J., et al. (2015). "Temperature Controlled Sequential Gelation in Composite Microgel Suspensions." Particle & Particle Systems Characterization **32**(7): 764-770.

Appel, J., et al. (2016). "Mechanics at the glass-to-gel transition of thermoresponsive microgel suspensions." Soft Matter **12**(9): 2515-2522.

Ballauff, M. and Y. Lu (2007). ""“Smart” nanoparticles: preparation, characterization and applications." Polymer **48**(7): 1815-1823.

Barnes, H. (1989). "Shear-thickening (“Dilatancy”) in suspensions of nonaggregating solid particles dispersed in Newtonian liquids." Journal of Rheology **33**(2): 329-366.

Bird, R. B., et al. (1987). "Dynamics of polymeric liquids. Vol. 1: Fluid mechanics."

Bockstaller, M., et al. (2001). "Characterization of association colloids of amphiphilic poly (p-phenylene) sulfonates in aqueous solution." Macromolecules **34**(18): 6353-6358.

Bonham, J., et al. (2014). "Non-aqueous microgel particles: synthesis, properties and applications." Soft Matter **10**(47): 9384-9398.

Brader, J. M., et al. (2010). "Nonlinear response of dense colloidal suspensions under oscillatory shear: Mode-coupling theory and Fourier transform rheology experiments." Physical Review E **82**(6): 061401.

Brown, W. (1993). Dynamic light scattering: the method and some applications, Oxford University Press, USA.

Buscall, R. (1994). "An effective hard-sphere model of the non-Newtonian viscosity of stable colloidal dispersions: Comparison with further data for sterically stabilised latices and with data for microgel particles." Colloids and Surfaces A: Physicochemical and Engineering Aspects **83**(1): 33-42.

Carrier, V. and G. Petekidis (2009). "Nonlinear rheology of colloidal glasses of soft thermosensitive microgel particles." Journal of Rheology (1978-present) **53**(2): 245-273.

Chen, Y.-L. and K. S. Schweizer (2004). "Microscopic theory of gelation and elasticity in polymer–particle suspensions." The Journal of Chemical Physics **120**(15): 7212-7222.

Cho, K. S., et al. (2005). "A geometrical interpretation of large amplitude oscillatory shear response." Journal of Rheology (1978-present) **49**(3): 747-758.

Cloitre, M., et al. (2000). "Rheological aging and rejuvenation in microgel pastes." Physical review letters **85**(22): 4819.

Crassous, J. J., et al. (2008). "Shear stresses of colloidal dispersions at the glass transition in equilibrium and in flow." The Journal of Chemical Physics **128**(20): 204902.

Crassous, J. J., et al. (2006). "Thermosensitive core-shell particles as model systems for studying the flow behavior of concentrated colloidal dispersions." The Journal of Chemical Physics **125**(20): 204906.

Daniel, C., et al. (2001). "Non-linear rheology of a face-centred cubic phase in a diblock copolymer gel." Rheologica Acta **40**(1): 39-48.

Dealy, J. M. and K. F. Wissbrun (1990). "Melt rheology and its role in plastics processing: Theory and applications." New York: Van Nostram Reynhold.

Deike, I., et al. (2001). "Rheology of thermosensitive latex particles including the high-frequency limit." Journal of Rheology **45**(3): 709-720.

Derec, C., et al. (2003). "Aging and nonlinear rheology in suspensions of polyethylene oxide–protected silica particles." Physical Review E **67**(6): 061403.

Dingenouts, N., et al. (1998). "Observation of the Volume Transition in Thermosensitive Core− Shell Latex Particles by Small-Angle X-ray Scattering." Macromolecules **31**(25): 8912-8917.

Ewoldt, R. H., et al. (2008). "New measures for characterizing nonlinear viscoelasticity in large amplitude oscillatory shear." Journal of Rheology **52**(6): 1427-1458.

Ewoldt, R. H., et al. (2008). "New measures for characterizing nonlinear viscoelasticity in large amplitude oscillatory shear." Journal of Rheology (1978-present) **52**(6): 1427-1458.

Ewoldt, R. H., et al. (2007). "Rheological fingerprinting of complex fluids using large amplitude oscillatory shear (LAOS) flow." ANNUAL TRANSACTIONS-NORDIC RHEOLOGY SOCIETY **15**: 3.

Ewoldt, R. H., et al. (2010). "Large amplitude oscillatory shear of pseudoplastic and elastoviscoplastic materials." Rheologica Acta **49**(2): 191-212.

Gan, D. and L. A. Lyon (2001). "Interfacial Nonradiative Energy Transfer in Responsive Core–Shell Hydrogel Nanoparticles." Journal of the American Chemical Society **123**(34): 8203-8209.

Gasser, U., et al. (2001). "Real-space imaging of nucleation and growth in colloidal crystallization." Science **292**(5515): 258-262.

Gilányi, T., et al. (2000). "Characterisation of monodisperse poly (N-isopropylacrylamide) microgel particles." Physical Chemistry Chemical Physics **2**(9): 1973-1977.

Hunter, G. L. and E. R. Weeks (2012). "The physics of the colloidal glass transition." Reports on Progress in Physics **75**(6): 066501.

Hyun, K., et al. (2011). "A review of nonlinear oscillatory shear tests: Analysis and application of large amplitude oscillatory shear (LAOS)." Progress in Polymer Science **36**(12): 1697-1753.

Kodger, T. E. and J. Sprakel (2013). "Thermosensitive Molecular, Colloidal, and Bulk Interactions Using a Simple Surfactant." Advanced Functional Materials **23**(4): 475-482.

Koumakis, N., et al. (2012). "Yielding of hard-sphere glasses during start-up shear." Physical review letters **108**(9): 098303.

Koumakis, N., et al. (2016). "Start-up shear of concentrated colloidal hard spheres: Stresses, dynamics, and structure." Journal of Rheology **60**(4): 603-623.

Koumakis, N., et al. (2012). "Direct comparison of the rheology of model hard and soft particle glasses." Soft Matter **8**(15): 4271-4284.

Koumakis, N. and G. Petekidis (2011). "Two step yielding in attractive colloids: transition from gels to attractive glasses." Soft Matter **7**(6): 2456-2470.

Langela, M., et al. (2002). "Microphase reorientation in block copolymer melts as detected via FT rheology and 2D SAXS." Macromolecules **35**(8): 3198-3204.

Laurati, M., et al. (2011). "Nonlinear rheology of colloidal gels with intermediate volume fraction." Journal of Rheology (1978-present) **55**(3): 673-706.

Laurati, M., et al. (2014). "Plastic rearrangements in colloidal gels investigated by LAOS and LS-Echo." Journal of Rheology **58**(5): 1395-1417.

Laurati, M., et al. (2007). "Asymmetric poly (ethylene-alt-propylene)-poly (ethylene oxide) micelles: A system with starlike morphology and interactions." Physical Review E **76**(4): 041503.

Le Grand, A. and G. Petekidis (2008). "Effects of particle softness on the rheology and yielding of colloidal glasses." Rheologica Acta **47**(5-6): 579-590.

Likos, C., et al. (1998). "Star polymers viewed as ultrasoft colloidal particles." Physical review letters **80**(20): 4450.

Liu, R., et al. (2009). "Thermoresponsive copolymers: from fundamental studies to applications." Colloid and Polymer Science **287**(6): 627-643.

Mason, T., et al. (1997). "Osmotic pressure and viscoelastic shear moduli of concentrated emulsions." Physical Review E **56**(3): 3150.

Mason, T. and D. Weitz (1995). "Linear viscoelasticity of colloidal hard sphere suspensions near the glass transition." Physical review letters **75**(14): 2770.

Mason, T. G. and D. A. Weitz (1995). "Linear Viscoelasticity of Colloidal Hard Sphere Suspensions near the Glass Transition." Physical Review Letters **75**(14): 2770-2773.

Mattsson, J., et al. (2009). "Soft colloids make strong glasses." Nature **462**(7269): 83-86.

Miyazaki, K., et al. (2006). "Nonlinear viscoelasticity of metastable complex fluids." EPL (Europhysics Letters) **75**(6): 915.

Mohanty, P. S., et al. (2014). "Effective interactions between soft-repulsive colloids: Experiments, theory, and simulations." The Journal of Chemical Physics **140**(9): 094901.

Neal, B., et al. (1998). "Molecular origins of osmotic second virial coefficients of proteins." Biophysical journal **75**(5): 2469-2477.

Neal, B., et al. (1999). "Why is the osmotic second virial coefficient related to protein crystallization?" Journal of Crystal Growth **196**(2): 377-387.

Paloli, D., et al. (2013). "Fluid–solid transitions in soft-repulsive colloids." Soft Matter **9**(11): 3000-3004.

Pelton, R. and P. Chibante (1986). "Preparation of aqueous latices with N-isopropylacrylamide." Colloids and Surfaces **20**(3): 247-256.

Petekidis, G., et al. (2002). "Rearrangements in hard-sphere glasses under oscillatory shear strain." Physical Review E **66**(5): 051402.

Pham, K., et al. (2008). "Yielding behavior of repulsion-and attraction-dominated colloidal glasses." Journal of Rheology **52**(2): 649-676.

Philippoff, W. (1966). "Vibrational measurements with large amplitudes." Transactions of the Society of Rheology **10**(1): 317-334.

Poulos, A. S., et al. (2013). "Flow of concentrated solutions of starlike micelles under large-amplitude oscillatory shear." Rheologica Acta **52**(8-9): 785-800.

Prasad, V., et al. (2007). "Confocal microscopy of colloids." Journal of Physics: Condensed Matter **19**(11): 113102.

Pusey, P. (1991). Liquids, freezing and the glass transition, North-Holland: Amsterdam.

Pusey, P. (2008). "Colloidal glasses." Journal of Physics: Condensed Matter **20**(49): 494202.

Pusey, P. N. and W. Van Megen (1986). "Phase behaviour of concentrated suspensions of nearly hard colloidal spheres." Nature **320**(6060): 340-342.

Pusey, P. N. and W. van Megen (1987). "Observation of a glass transition in suspensions of spherical colloidal particles." Physical review letters **59**(18): 2083.

Renou, F., et al. (2010). "Yielding processes in a colloidal glass of soft star-like micelles under large amplitude oscillatory shear (LAOS)." Journal of Rheology **54**(6): 1219-1242.

Rogers, S. A., et al. (2011). "A sequence of physical processes determined and quantified in LAOS: Application to a yield stress fluid." Journal of Rheology (1978-present) **55**(2): 435-458.

Rogers, S. A., et al. (2008). "Aging, yielding, and shear banding in soft colloidal glasses." Physical review letters **100**(12): 128304.

Royall, C. P., et al. (2008). "Direct observation of a local structural mechanism for dynamic arrest." Nature materials **7**(7): 556-561.

Saunders, B. R. and B. Vincent (1999). "Microgel particles as model colloids: theory, properties and applications." Advances in colloid and interface science **80**(1): 1-25.

Scheffold, F., et al. (2010). "Brushlike interactions between thermoresponsive microgel particles." Physical review letters **104**(12): 128304.

Schild, H. G. (1992). "Poly (N-isopropylacrylamide): experiment, theory and application." Progress in Polymer Science **17**(2): 163-249.

Schlatter, G., et al. (2005). "Fourier transform rheology of branched polyethylene: experiments and models for assessing the macromolecular architecture." Macromolecules **38**(15): 6492-6503.

Senff, H. and W. Richtering (1999). "Temperature sensitive microgel suspensions: Colloidal phase behavior and rheology of soft spheres." The Journal of chemical physics **111**(4): 1705-1711.

Senff, H. and W. Richtering (2000). "Influence of cross-link density on rheological properties of temperature-sensitive microgel suspensions." Colloid & Polymer Science **278**(9): 830-840.

Senff, H., et al. (1999). "Rheology of a temperature sensitive core− shell latex." Langmuir **15**(1): 102-106.

Sessoms, D. and I. Bischo (2009). "erger, L. Cipelletti and V. Trappe." Philos. Trans. R. Soc., A **367**: 5013-5032.

Siebenbürger, M., et al. (2012). "Core–shell microgels as model colloids for rheological studies." Soft Matter **8**(15): 4014-4024.

Stieger, M., et al. (2004). "Structure formation in thermoresponsive microgel suspensions under shear flow." Journal of Physics: Condensed Matter **16**(38): S3861.

Stieger, M., et al. (2004). "Are thermoresponsive microgels model systems for concentrated colloidal suspensions? A rheology and small-angle neutron scattering study." Langmuir **20**(17): 7283-7292.

Stieger, M., et al. (2004). "Small-angle neutron scattering study of structural changes in temperature sensitive microgel colloids." The Journal of Chemical Physics **120**(13): 6197-6206.

Valente, J. J., et al. (2005). "Colloidal behavior of proteins: effects of the second virial coefficient on solubility, crystallization and aggregation of proteins in aqueous solution." Current pharmaceutical biotechnology **6**(6): 427-436.

Van Megen, W. and S. Underwood (1993). "Glass transition in colloidal hard spheres: Mode-coupling theory analysis." Physical review letters **70**(18): 2766.

Velev, O., et al. (1998). "Protein interactions in solution characterized by light and neutron scattering: comparison of lysozyme and chymotrypsinogen." Biophysical journal **75**(6): 2682-2697.

Vlassopoulos, D. and M. Cloitre (2014). "Tunable rheology of dense soft deformable colloids." Current Opinion in Colloid & Interface Science **19**(6): 561-574.

Weitz, D., et al. (1993). "Diffusing-wave spectroscopy: The technique and some applications." Physica Scripta **1993**(T49B): 610.

Weitz, D. A., et al. (1993). "Diffusing-wave spectroscopy: The technique and some applications." Physica Scripta **1993**(T49B): 610.

Wilhelm, M., et al. (1998). "Fourier-transform rheology." Rheologica Acta **37**(4): 399-405.

Wilhelm, M., et al. (1999). "High sensitivity Fourier-transform rheology." Rheologica Acta **38**(4): 349-356.

Wolfe, M. and C. Scopazzi (1989). "Rheology of swellable microgel dispersions: Influence of crosslink density." Journal of colloid and interface science **133**(1): 265-277.

Wu, C. and S. Zhou (1995). "Laser light scattering study of the phase transition of poly (N-isopropylacrylamide) in water. 1. Single chain." Macromolecules **28**(24): 8381-8387.

Wu, J., et al. (2003). "Interparticle potential and the phase behavior of temperature-sensitive microgel dispersions." Macromolecules **36**(2): 440-448.

Wu, J., et al. (2003). "Phase behavior of thermally responsive microgel colloids." Physical review letters **90**(4): 048304.

Yunker, P. J., et al. (2014). "Physics in ordered and disordered colloidal matter composed of poly (N-isopropylacrylamide) microgel particles." Reports on Progress in Physics **77**(5): 056601.

Zaccarelli, E. (2007). "Colloidal gels: equilibrium and non-equilibrium routes." Journal of Physics: Condensed Matter **19**(32): 323101.

Zaccone, A., et al. (2009). "Elasticity of arrested short-ranged attractive colloids: Homogeneous and heterogeneous glasses." Physical review letters **103**(20): 208301.

Zhang, Z., et al. (2009). "Thermal vestige of the zero-temperature jamming transition." Nature **459**(7244): 230-233.

Zimm, B. H. (1948). "Apparatus and methods for measurement and interpretation of the angular variation of light scattering; preliminary results on polystyrene solutions." The Journal of Chemical Physics **16**(12): 1099-1116.

Chapter 6

Structure, dynamics and viscoelastic properties of hybrid core-shell microgels with screened interactions

The structure and viscoelastic properties of electrostatically stabilized aqueous suspensions of microgels, with the addition of salt ions of sodium chloride (NaCl) were explored by light scattering, rheometry and optical observation techniques at quiescent state and under shear. These microgels consist of a rigid trifluorethyl methacrylate (TFEMA) core, onto which a thermosensitive Poly(N-isopropylacrylamide) shell is affixed. At temperatures above the LCST, the increase of the ionic strength leads to a competition between the long-range screened electrostatic repulsions and the short-range attractions. However, at sufficiently high ionic strength, this delicate balance of these opposing forces can be appropriately controlled leading to the interesting clustering phenomena.

6.1 Introduction

For low ionic strength suspensions of microgels, increasing the temperature, the particle size decreases, because the solvent quality decreases due to an increasing preference for the PNIPAM chains to form intramolecular hydrogen bonds (Appel, de Lange et al. 2015). Above the lower critical solution temperature (LSCT), this behavior induces attractive interaction between polymer chains of the microgel driving to phase separation from the aqueous solution. However, this internal attraction at low ionic strength does not entail colloidal instability as the particles are electrostatically stabilized at their periphery (Appel, de Lange et al. 2015).

Increasing the ionic strength, the electrostatic interactions can be screened. This leads to an interplay between electrostatic repulsion that can be controlled by salt concentration and attractive interactions which can be tuned by temperature. At sufficiently high salt concentrations, a critical aggregation temperature T_a emerges, at which attractive interactions become sufficiently strong to overcome the screened electrostatic repulsive interactions leading to particle clustering.

In this chapter, we explore structure, dynamics and viscoelastic properties of thermosensitive hybrid microgels where electrostatic repulsive interactions are screened after the addition of monovalent salt ions of sodium chloride (NaCl)

6.2 Materials

We used temperature-sensitive composite core-shell particles which consists of a fluorescently labeled (Nile red) trifluorethyl methacrylate (TFEMA) core of 85nm radius, around which a Poly(*N*-isopropylacrylamide) shell is affixed. In the shell of the microgels, NIPAM is copolymerized by 5%wt. N, N'-methylenebis(acrylamide) (MBAM), TFEMA/PNIPAM, which introduces thermo-responsive behavior. The total size of the particles is around D~880nm at T=20^{o}C. The particles are electrostatically stabilized in aqueous solutions by sulfonate groups at their periphery, remnant from the radical initiator potassium persulfate (Appel, de Lange et al. 2015). Increasing the temperature, the PNIPAM network at the shell shrinks as the solvent quality becomes bad. For the effective screening of the electrostatic repulsive interactions

we used monovalent salt ions of sodium chloride (NaCl) in two different concentrations (20mM and 50mM).

6.3 Results - Discussion

6.3.1 Particle Characterization

Dynamic Light Scattering (DLS) used to measure the intensity fluctuations of the scattered light in two different ionic strength suspensions of dilute solutions (20mM and 50mM of monovalent salt NaCl) for various temperatures and extract the diffusion coefficient via the Stokes-Einstein-Sutherland relation $R_H = k_B T / 6\pi\eta D$ (Berne and Pecora 2000, Schärtl 2007).

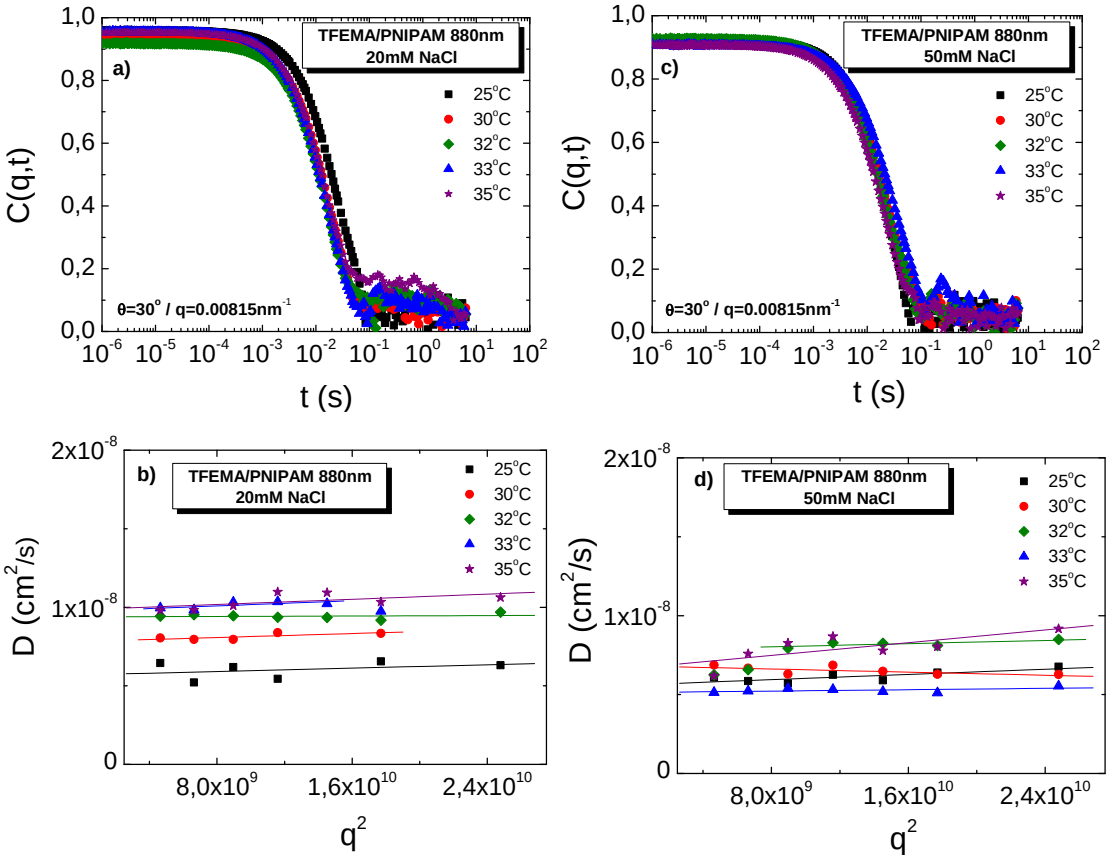

Fig. 6.1 *– Correlation functions for ϑ=30° (q=0.00815nm^{-1}) for various temperatures for TFEMA/PNIPAM particles at salt concentrations a) 20mM and c) 50mM of NaCl and the diffusion coefficient for various temperatures for b) 20mM and d) 50mM of NaCl.*

Fig. 6.1a and 6.1c depict the autocorrelation functions C(q,t) at θ=30° (q=0.00815nm^{-1}) for various temperatures at NaCl concentrations of 20mM and 50mM, whereas 6.1c and 6.1d present the diffusion coefficients for the same temperatures and salt concentrations.

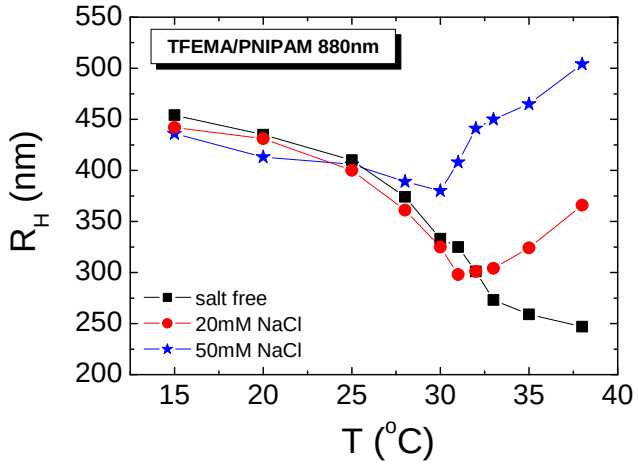

Fig. 6.2 – *Hydrodynamic radius R_H as a function of temperature for salt-free solutions and salt solutions of 20mM and 50mM of NaCl.*

Fig. 6.2 shows the temperature dependence of the hydrodynamic radius R_H for 20mM and 50mM of NaCl, which is directly compared with the experimental data for the same system at low ionic strength (salt-free solution). As we have already mentioned, for salt-free solutions the LCST is the critical temperature that the solvent quality changes and repulsive interactions switch to attractive, while the particle size decreases with increasing temperature; for this system, the LCST is at 32°C. For sufficiently high ionic strengths, we observe the aggregation temperature T_a at which attractive interactions become quite strong marking the onset of particle aggregation. Increasing the salt concentration, the aggregation temperature T_a appears at lower temperature; T_a=31°C for salt concentration 20mM of NaCl, whereas T_a=30°C for salt concentration 50mM.

The second virial coefficient A_2 characterizes quantitatively the total molecular interactions between solvent and solute particles in dilute solutions, which are important to determine the thermodynamic properties of colloidal suspensions (Neal, Asthagiri et al. 1998, Valente, Payne et al. 2005). Static light

scattering (SLS) is used for the estimation of A_2 via the Zimm treatment as we already mentioned in a previous chapter (Zimm 1948, Utiyama 1972, Wilson 2003).

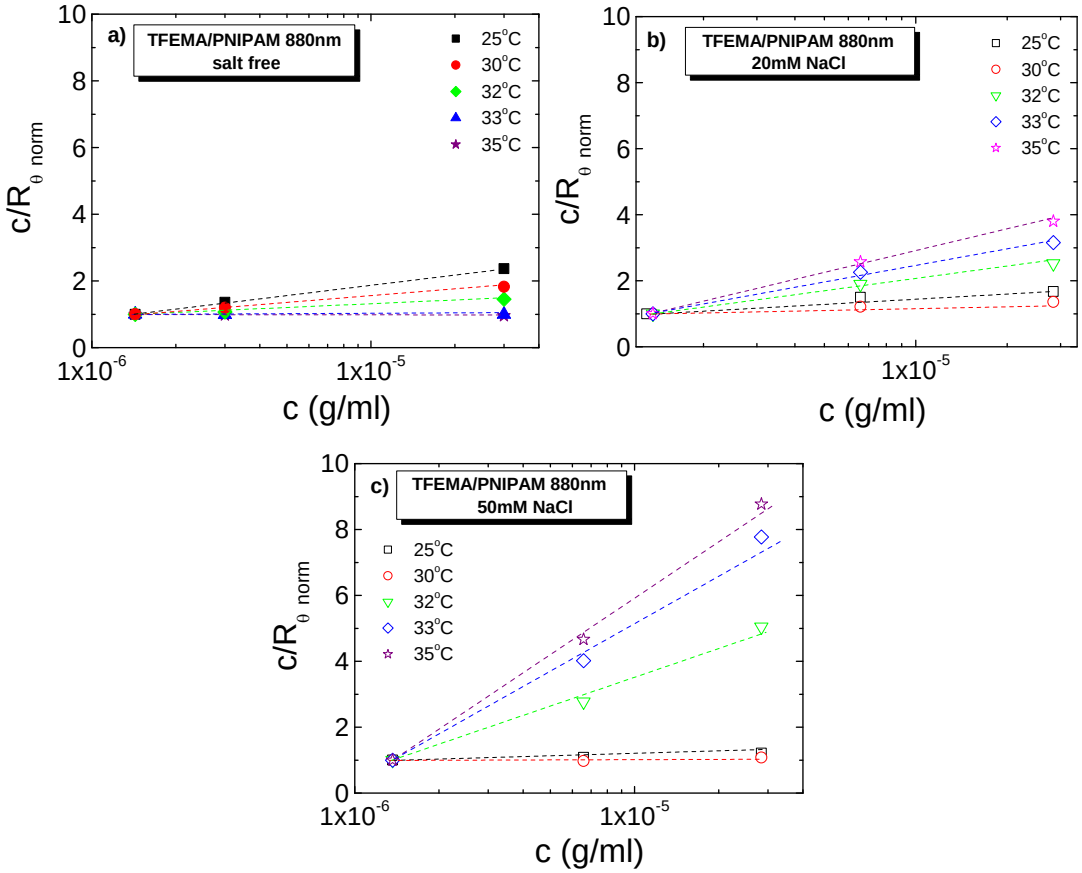

Fig. 6.3 *- Typical plots of SLS data for various temperatures for TFEMA/PNIPAM particles for a) salt-free solution, b) 20mM and c) 50mM suspensions.*

Fig. 6.3 delineates the inversed scattering intensity extracted by SLS technique as a function of particle concentration for various temperatures for all solutions probed, with and without salt. From the slope and the intercept we extract the second virial coefficient A_2 as a function of the molecular weight. As we have already mentioned, positive values of A_2 indicate repulsive intermolecular interactions, whereas negative values reflect attractive interactions (Neal, Asthagiri et al. 1999). Below the LCST, the slope of the inverse scattering intensity decreases upon increasing the salt concentration denoting that the screening of the electrostatic repulsions becomes more efficient. Above the LCST, where attractive interactions dominate, the second virial coefficient increases sharply as we increase

the salt concentration. This unexpected observation can be understood if the particles self-assemble into small clusters when the temperature is fully equilibrated forming the so-called equilibrium clusters (Groenewold and Kegel 2001, Stradner, Sedgwick et al. 2004). Equilibrium cluster formation is attributed to the interplay of strongly screened Coulomb repulsions and the significantly increased short-range attractions, which act as surface tension driving into a reduction in surface energy upon aggregation. Thus a stabilizing mechanism is provided against the formation of a percolated network (Stradner, Sedgwick et al. 2004, Stradner, Cardinaux et al. 2006). Fig. 6.4 presents the temperature dependence of the second virial coefficient as a function of M_w, where we can clearly observe the vast increase of the A_2.

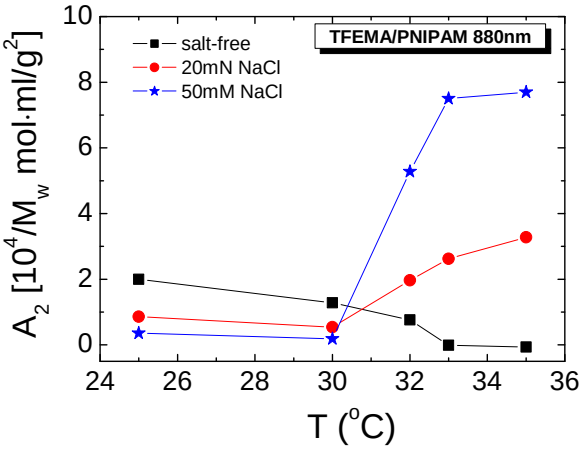

Fig 6.4 – *Estimation of second virial coefficient A_2 through the experimental SLS data for various temperatures for salt-free and salt suspensions of 20mM and 50mM of NaCl.*

The thermoresponsive hybrid microgel particles of our study are permeable. Therefore, the estimation of the effective volume fraction ϕ_{eff}, which one may consider that can be easily determined by its temperature dependence size is not trivial. As we already reported in a previous chapter, in order to estimate the effective volume fraction of the particle, we measure the relative viscosity η_{rel} for a series of dilute solutions and then we calculate the ϕ_{eff} through the method described by Senff et al. using the Batchelor-Einstein's expression $\eta_{rel} = 1 + 2.5\phi_{eff} + 5.9\phi_{eff}^2$ (Senff, Richtering et al. 1999, Senff and Richtering 2000, Deike, Ballauff et al. 2001). The viscosity measurements were performed by a

LOVIS/DMA 4100M viscometer by Anton Paar. The relative viscosity as a function of the mass concentration for the salt-free solution and two different NaCl concentrations (20mM and 50mM) are shown at different temperatures in fig. 6.5. Due to the screening of the electrostatic repulsions it was impossible to fit the experimental data according to Batchelor-Einstein's expression. Moreover, for temperatures above the LCST the viscosity increases sharply rendering difficult any viscosity measurements in higher mass concentrations. This fact supports the existence of equilibrium clusters which increase by increasing the ionic strength. However, under the assumption that the TFEMA/PNIPAM 880nm particles with 20mM NaCl have similar size to salt-free TFEMA/PNIPAM 880nm until 30°C (see fig. 6.2) we can assume that the effective volume fraction of the TFEMA/PNIPAM 880nm with 20mM NaCl at 20°C is $\phi_{eff@20^oC} \approx 1.1$ (c=0.097g/ml).

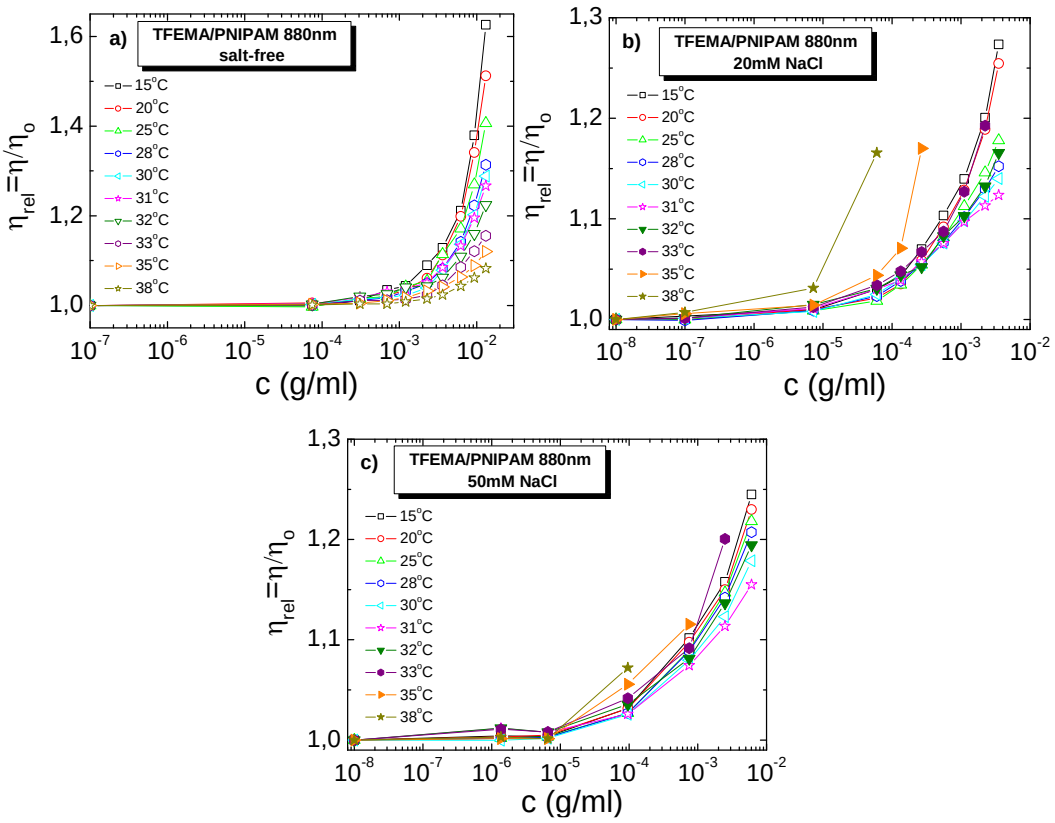

Fig. 6.5 – *Relative viscosity η_{rel} as a function of mass concentration for various temperatures for a) salt-free and salt concentrations b) 20mM and c) 50mM of NaCl.*

6.3.2 Rheometry at quiescent state

Rheometry used for the investigation of the temperature dependence of the linear and non-linear viscoelastic properties of core-shell microgels. All rheological tests carried out with a strain-controlled ARES rheometer with a force rebalance transducer 100FRTN1 in a cone-plate geometry d=25mm with a cone-angle of 0.04 degrees and truncation 0.05mm. Accurate and fast temperature control was achieved by Peltier elements placed at the lower plate. Before each rheological test, the sample was rejuvenated in order to erase any stress history effects by using a specific protocol consisting of heating at T=31^{o}C where the sample is liquefied and fills properly the gaps. For eliminating the solvent evaporation a homemade trap was used, which "sealed" by a low-molecular poly(dimethylsiloxane) of low viscosity (5cP).

6.3.2.1 Linear Viscoelasticity (temperature and frequency dependence)

Below, we present the temperature and the frequency dependence of the viscoelastic moduli of the concentrated suspension of TFEMA/PNIPAM 880nm (c=0.097g/ml - $\phi_{eff@20^oC}\approx1.1$) with salt concentration 20mM of NaCl. For the temperature dependence test, we imposed a fixed frequency (ω=1rad/s) and strain amplitude (γ=0.5%) and slowly increased the temperature (fig. 6.6a), whereas for the frequency sweeps we kept constant the strain amplitude at γ=0.5% at four different temperatures, while varying the frequency (fig. 6.6b). Fig. 6.6a shows the temperature dependence data, for TFEMA/PNIPAM 880nm with 20mM NaCl at c=0.097g/ml ($\phi_{eff@20^oC}\approx1.1$), where we observe that for temperatures below the LCST, the elastic modulus is higher than the viscous one indicating a solid-like behavior. As temperature increases, both viscoelastic moduli decrease and their difference becomes progressively smaller. Around the LCST, the viscous modulus becomes larger indicating a liquid-like behavior. Increasing the temperature above the LCST, the weak repulsive interactions switch to attractive ones leading to a re-entrance from liquid to solid-like response due to the formation of a percolated network. A salt-free suspension of TFEMA/PNIPAM 880nm of slightly higher mass

concentration (c=0.107g/ml - $\phi_{eff@20^oC}$=1.23) is also presented in fig. 6.6a for comparison. We observe that the three different states are also detected in the salt-free solution but they are slightly shifted to lower temperatures due to the screening of electrostatic repulsions; the LCST also shifts from around 33°C to 30°C. Moreover, the cluster formation at temperatures above the LCST is stronger in the sample with 20mM NaCl which is consistent with the equilibrium clusters detected at this temperature range by light scattering and viscometry.

Fig. 6.6b exhibits the frequency sweeps performed for various temperatures below and above the LCST. As we already mentioned in chapter 5, at temperatures below the LCST, microgels show a glassy behavior with G' presenting a plateau with a slightly increasing slope, related to an enhanced motion of microgel particles at low frequencies compared to high ones, while G'' shows a minimum that is related with the transition of the particles between the in cage and the out-of-cage relaxation (Van Megen and Underwood 1993, Mason and Weitz 1995). Close to the LCST the response is liquid-like with the torque being really low and G''>G'. At temperatures above the LCST, the effective volume fraction is decreasing due to shrinkage of the particles, but the interactions are strongly attractive resulting in the formation of a percolated network, which leads to a solid-like behavior.

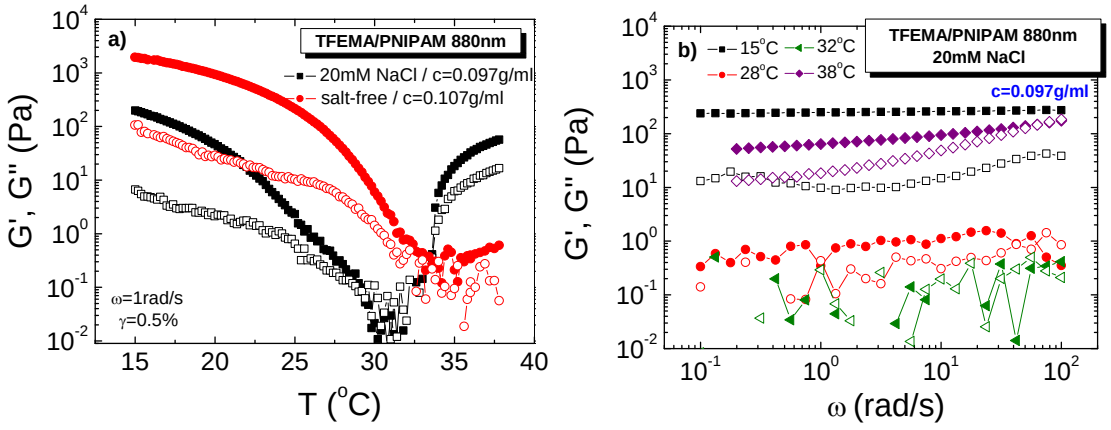

Fig. 6.6 – *a) Temperature dependence and b) frequency dependence of the elastic (black full square) and viscous (black open square) moduli for concentrated sample c=0.097g/ml TFEMA/PNIPAM 880nm with 20mM of NaCl.*

6.3.2.2 Oscillatory shear – Nonlinear Viscoelasticity

The nonlinear response provides information about how the applied strain affects the yielding behavior of colloidal systems. Hence, Dynamic Strain Sweeps (DSS) were performed at various frequencies (0.1, 1, 10rad/s) and various temperatures from low to high strain amplitudes for TFEMA/PNIPAM 880nm containing 20mM of NaCl (c=0.097g/ml - $\phi_{eff@20^oC}\approx1.1$).

Fig. 6.7 shows typical dynamic strain sweeps where the elastic and viscous moduli, G' and G'', are plotted as a function of the strain amplitude at three different frequencies. At low strain amplitudes (linear viscoelastic regime) microgels exhibit a solid-like response with G'>G''. As strain amplitudes increase, for repulsive regime (T>LCST) the elastic modulus decreases, whereas the viscous one reaches a maximum before it starts decreasing as well. The yielding point is marked by the yield strain γ_γ at G'=G'', beyond which the material shows a viscoelastic liquid-like behavior with both the storage and the loss moduli exhibiting a power law decrease with strain amplitude. Increasing the temperature, the system exhibits a transition from a repulsive glass to liquid and consequently to gel as discussed above. From the dynamic strain sweep data, in the attractive regime (T>LCST) we observe that the yielding point is located in much higher strain amplitude ($\gamma_\gamma\approx60\%$) comparing to temperature regime below the LCST ($\gamma_\gamma\approx10$-20%). Furthermore, for T>LCST we observe that the viscoelastic moduli do not exhibit a power law decrease with strain amplitude beyond the yielding point which marks the onset of the terminal flow, denoting either a multiple yielding procedure which does not complete within the experimental window or a yield behavior of a suspension with heterogeneities.

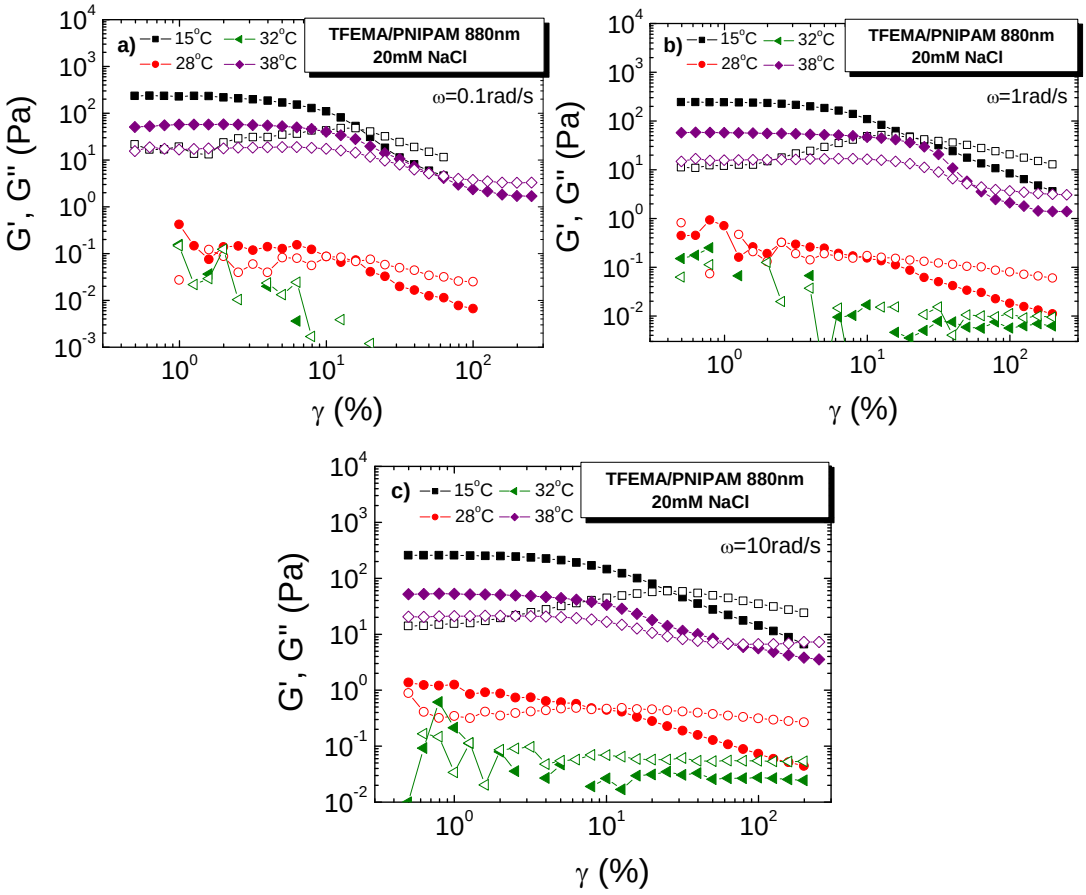

Fig. 6.7 *– Dynamic Strain Sweeps for various temperatures for TFEMA/PNIPAM 880nm with 20mM of NaCl at a) 0.1rad/s, b) 1rad/s and c) 10rad/s.*

Flow curves (steady rate sweeps) are also performed from high to low rates in order to further study the flow behavior of the various states for TFEMA/PNIPAM 880nm with 20mMof NaCl (fig. 6.8). For temperatures below the LCST, flow curves show the typical response of a soft solid-like material exhibiting a shear thinning behavior at high shear rates, where stress shows a sub-linear increase with shear rate and the emergence of a yield stress plateau at low shear rates. The flow curves can be fitted with the Herschel-Bulkley model $\sigma = \sigma_0 + k\dot{\gamma}^n$ (Koumakis, Pamvouxoglou et al. 2012), where k is the consistency index and n the flow index. Both parameters k and n for various temperatures are summarized in Table 6.a.

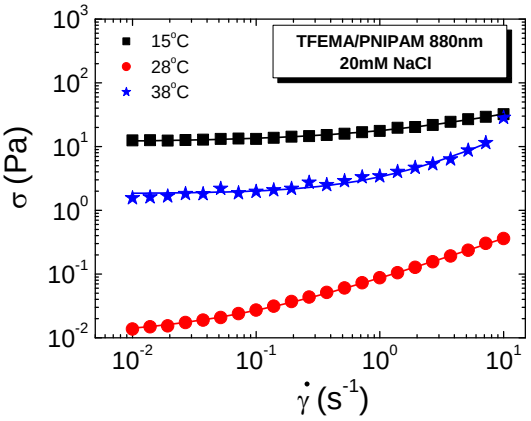

Fig. 6.8 *– Steady state shear stress as a function of rotational shear rate (flow curve) for various volume fractions as indicated. The solid curves represent the fitting of experimental data with Herschel-Bulkley model.*

T (°C)	k	n
15	5.96	0.55
28	0.074	0.68
38	1.52	0.92

Table 6.a *– Characteristic values of k and n for Herschel-Bulkley model of TFEMA/PNIPAM 880nm in 20mM of NaCl.*

6.3.3 Rheo – confocal visualization

Rheo-confocal microscopy which combines two independent techniques (confocal microscopy with rheology) was performed simultaneously, in order to directly visualize any structural or morphological changes induced by shear and deformation forces on TFEMA/PNIPAM 880nm with 20mM of NaCl and c=0.097g/ml ($\phi_{eff@20^oC}\approx1.1$).

When a colloidal suspension is subjected to flow, the microstructure rearranges as the suspension is driven out of equilibrium (Mewis and Wagner 2012). The shear-induced behaviour of a suspension depends on the effective volume fraction, interparticle interactions, particle shape (Glotzer and Solomon 2007), the character of the particle surface and the ratio of shearing to thermal motions, characterized by the Peclet number $Pe = \dot{\gamma} t_B = 6\pi\eta\dot{\gamma}R^3 / k_B T$ (Kulkarni and Morris

2009, Xu, Rice et al. 2013). Colloidal dispersions near HS interactions develop anisotropic amorphous structures at low shear rates, whereas at high ones, clustering due to strong hydrodynamic forces results in shear thickening.

The confocal rheometer system, used for the investigation of TFEMA/PNIPAM 880nm with 20mM of NaCl under mechanical deformation, consists of a stress-controlled MCR302 rheometer of Anton Paar mounted on VT-Eye confocal system of VisiTech. The geometry we used is a roughened 40mm cone and plate geometry with truncation 0.07mm. A homemade trap was also used in order to minimize the solvent evaporation.

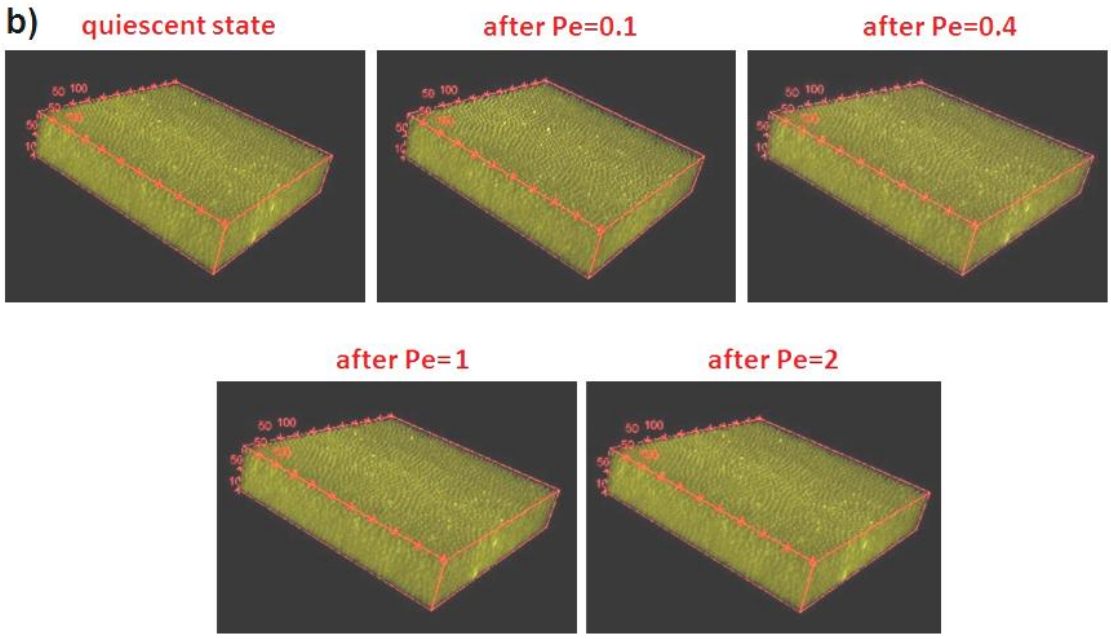

Fig. 6.10 *– a) 2D confocal images of TFEMA/PNIPAM 880nm of 20mM of NaCl at the glass bottom and b) 3D representation of z-scan under quiescent conditions and under shear for c=0.097g/ml at 20°C.*

Firstly, 2D confocal scanning recorded the sample's microstructure at quiescent state and under different shear rates. The visualization of TFEMA/PNIPAM system is quite challenging since the sample is highly concentrated (c=0.097g/ml – $\phi_{eff@20^oC} \approx 1.1$) and optically dense, resulting in significant multiple scattering. Moreover, only the core of the particles is labelled by Nile red dye, whose size (d~180nm) is below the objective's resolution, prohibiting clear detection deep in the bulk of the sample. Therefore, we could visualize the sample's structure only near the glass bottom and up to 2μm depth. For all temperatures and shear rates applied, we observed that the structure near the glass bottom remains unaffected over time, denoting the existence of no-slip conditions during the rheo-confocal tests. Fig. 6.10a shows the 2D confocal images near the glass bottom both at rest and under pre-shear conditions for T=20°C, where we observed that the structure formed did not change. Furthermore, full 3D videos with additional scanning (fig. 6.10b) were performed 400s after the cessation of every shear applied (pre-shearing) in order to visualize the structure formed once a steady state is reached. These 3D videos which were performed up to 10μm depth with a step of stack of

images every 0.1μm, indicate a quite homogeneous particle distribution of the sample which was unaffected despite the pre-shear. However, the quality of the video is not good with the particles look quite hazy due to the interplay of the strong multiple scattering and small labelled core size.

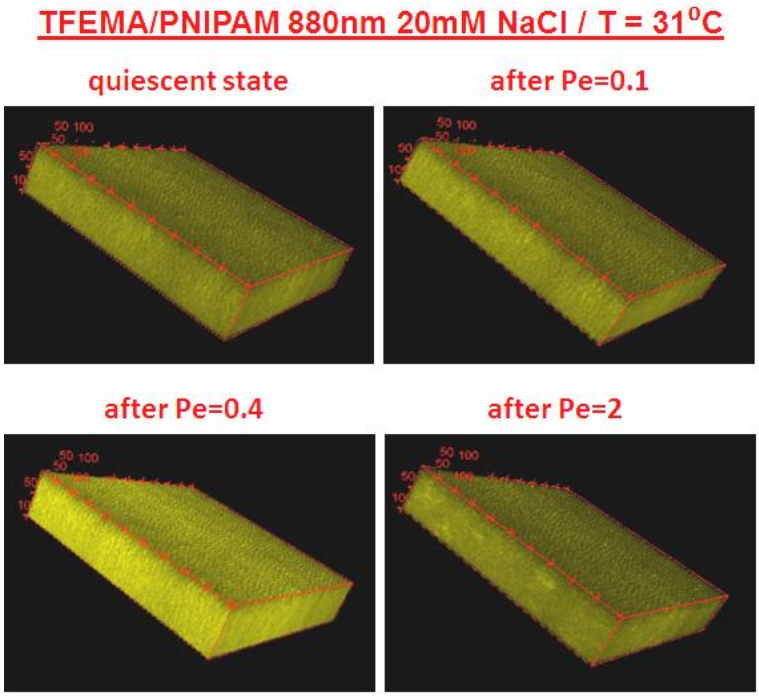

Fig. 6.11 *–3D representation of z-scan under quiescent conditions and under shear for c=0.097g/ml at 31°C.*

Approaching the LCST (~30°C) (fig. 6.11), the levels of the structure which acquired by the 3D scanning, look even hazier than the case of 20°C denoting the faster particle motion which corresponds to a liquid-like behavior.

Next, for temperatures above the LCST (36°C), confocal 3D z-scans at rest show strong heterogeneities of the structure which is characterized by large clusters in random positions in the bulk and smaller aggregates close to the glass bottom. Then, we monitored the particle motion over time under the application of various Pe numbers. The transition from quiescent state to Pe=0.05 and 0.1 revealed an increasingly more difficult particle flow denoting the formation of a stiffer structure increasing the shear rate. Increasing further the shear rate at intermediate and higher Pe numbers (0.4, 1 and 2, 4 and 10), the particle flow became easier reflecting

a progressive collapse of the heterogeneities without reaching a homogeneous suspension. Moreover, at these Pe range, moving deeper in the sample the flow seemed to be higher comparing to closer to the glass bottom giving the impression of a velocity gradient moving from the bottom to the glass. However, we did not realize any experimental investigation in order to determine this velocity gradient. We also observe that after the cessation of shear rates Pe=4 and 10, the clusters continue to flow for a couple of seconds due to inertia, before the system freeze again.

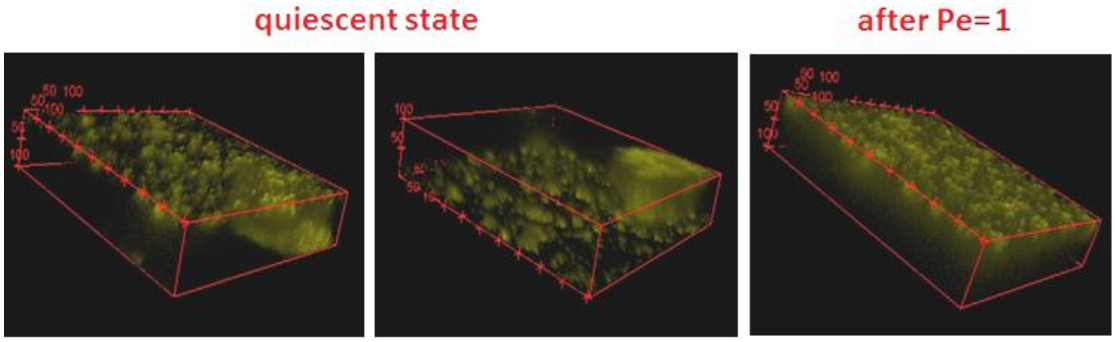

Fig. 6.12 *– 3D representation of z-scan under quiescent conditions and under shear for c=0.097g/ml 36°C.*

Fig. 6.13a shows dynamic frequency sweeps for temperature 36°C, which were performed 400s after the cessation of various shear rates, in order to explore the effect of pre-shear on the viscoelastic moduli. We observe that applying pre-shear Pe=0.05 or 0.1 the sample became stronger with the moduli being around one order magnitude higher compared to the not pre-sheared state. Increasing the Pe number the moduli weakens towards less heterogeneous suspensions without liquefying not even after the application of Pe=10. The trend of the viscoelastic moduli upon increasing the shear, is more obvious in fig. 6.12b where the viscoelastic moduli are presented for ω=1rad/s.

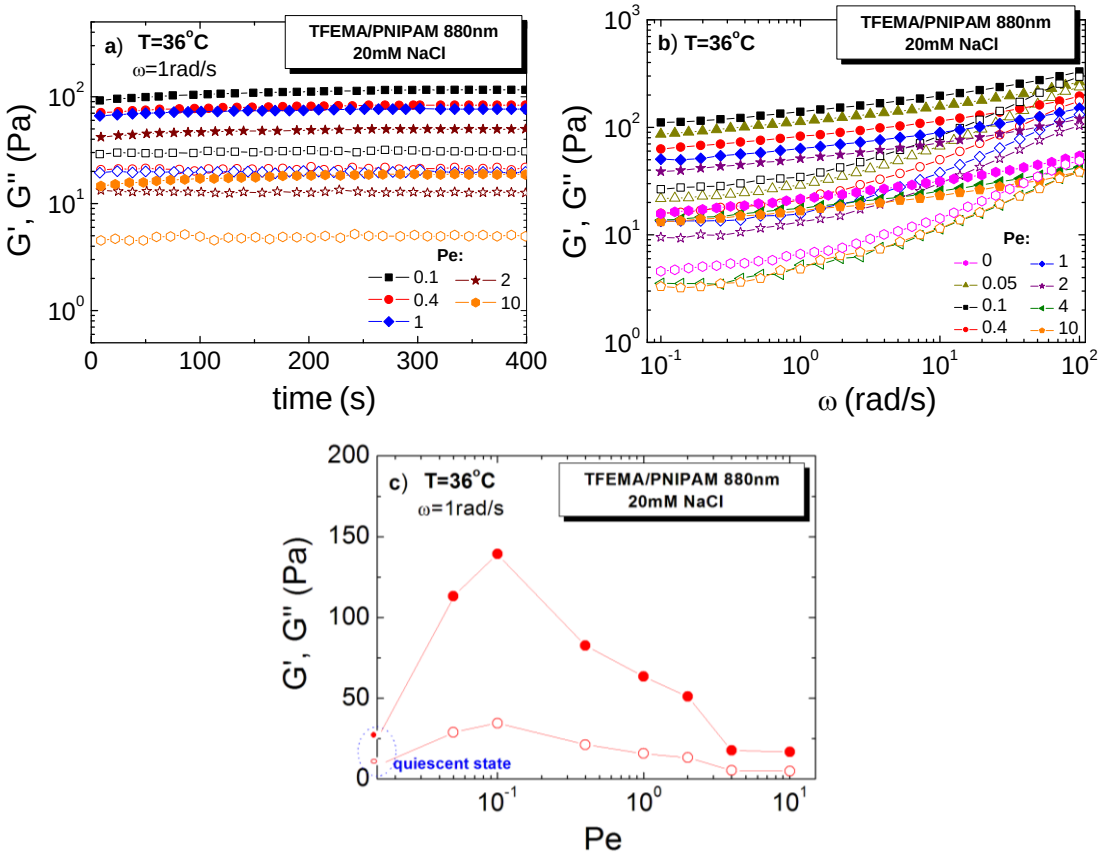

Fig. 6.13 *– a) Dynamic time sweep data at ω=1rad/s and b) frequency dependence of storage (full symbols) and loss (open symbols) moduli after the application of various Peclet numbers for 36°C and c) the storage (full symbols) and loss (open symbols) moduli at ω=1rad/s.*

Start-up shear experiments (step rate tests) were also performed at various shear rates (Pe= 0.1, 0.4, 1 and 2) and temperatures (below, close and above the LCST), where a constant shear rate is applied from rest and the subsequent stress response is monitored until steady-state is reached. Start-up experiments are simpler than oscillatory strain sweeps, as the shear rate remains constant throughout the test, and constitute more suitable tests in examining the time dependence of the non-linear response. As it has been reported in numerous studies of soft materials such as polymers and colloids (Derec, Ducouret et al. 2003, Letwimolnun, Vergnes et al. 2007, Carrier and Petekidis 2009, Boukany, Hemminger et al. 2010), a stress overshoot is observed, after an initial elastically dominated response, which reflects the yield stress above which the sample flows. For 20°C (fig. 6.9a) and 31°C (fig. 6.9b) we observe that the increase of the shear rate causes a rise

of the stress, both at the peak and the steady state plateau, while the yield strain move to higher values. For hard spheres glasses, this rise of the stress and the increase of the yield strain are related to stronger elongation of the cage before yielding, which also involves larger storage of elastic energy (Koumakis, Laurati et al. 2012, Koumakis, Laurati et al. 2016).

At T=36°C, where the attractive interactions are dominant, we observe a complex non-monotonic behavior where increasing the Pe from 0.05 to 1 the stress overshoot rises, whereas for higher Pe weakens. However, at all shear rates applied, the yield strain shifts to higher values with increasing the shear rate (or Pe). Moreover, at all shear rates applied the elastic response does not start from the same point and increases with increasing the strain amplitude. This behavior indicates the presence of strong heterogeneities before each start-up test, which every time lead to different structural rearrangements. Fig. 6.9d shows the correspondent stress relaxation tests, where the steady shear flow that the samples undergo, is abruptly stopped and the stress gradually decays. After the application of low Pe we observe a stress relaxation plateau does not decay at zero, denoting that the internal stresses do not fully relax due to strong structural heterogeneities. However, after the application of high Pe, the stress relaxation plateau approaches zero, indicating the almost full relaxation of the internal stresses.

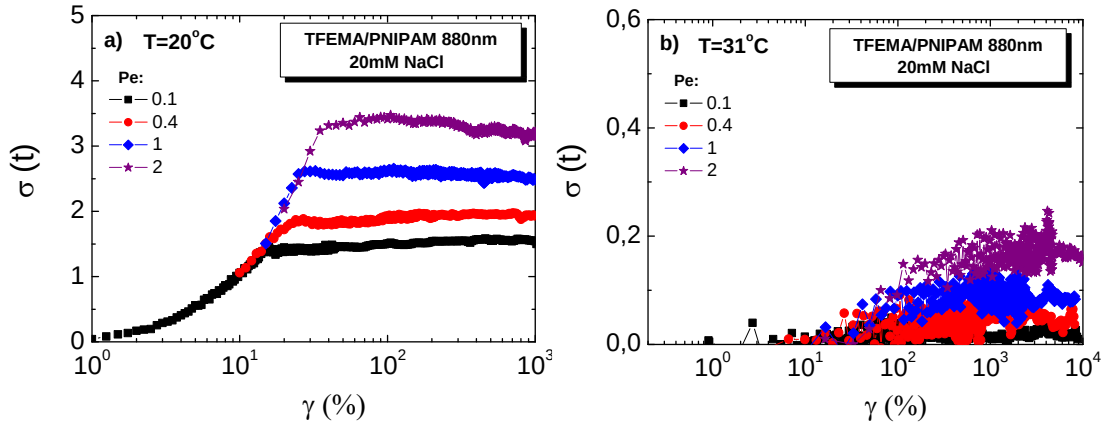

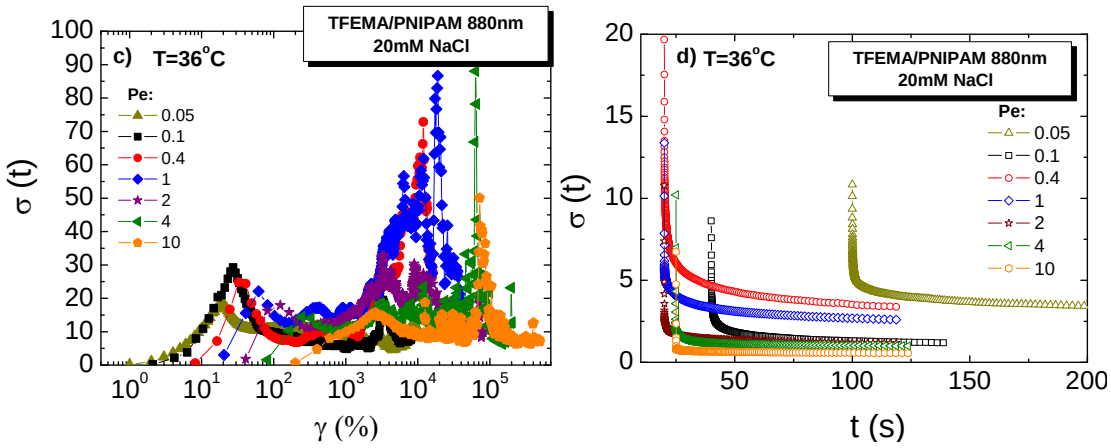

Fig. 6.9 *– Stress σ versus strain γ in ln-log plots from step rate start-up experiments of systems TFEMA/PNIPAM 880nm with 20mM of NaCl for various Pe for temperatures a) 20°C, b) 31°C, c) 36°C and d) stress relaxation for various Pe at 36°C.*

6.3.4 Rheo – imaging visualization

In order to get a better insight into the shear-induced large length-scale structures microgels at temperatures above the LCST, we also performed rheo-imaging with a lower magnification (4.25x) using a Point Grey Grasshopper 14S3 CCD camera taking snapshots with a step of 10s. During imaging, we used a parallel plate-plate geometry where both plates are made of glass. The upper plate has 40mm diameter, while the measurement were taken with a truncation 0.10mm.

At first, the sample was rejuvenated in order to erase any stress history effects by using the same protocol as before, which consists of heating at T≈31°C where the sample melts and fills properly the gap. Then, we explore the evolution of the structure upon changing the temperature from 20 to 36°C at rest and hence following the transition from repulsive to attractive interactions (fig. 6.14). Therefore, we were taking snapshots every 10s for 25mins, while a DTS test at constant strain amplitude γ=0.5% and frequency ω=1rad/s was performed in order to monitor the evolution of linear viscoelastic moduli and determine when an equilibrium state is reached. We observe that after quenching temperature from the LCST to T=20°C, the sample is homogeneous. Once the temperature was increased and was equilibrated at T=36°C, heterogeneous in size and shape clusters appear which become larger and larger as the time passes. These might be actually

indication of macro-phase separation. Moreover, the temperature increase leads to large refractive index variations and hence strong optical contrast that allows better visual detection of the clusters.

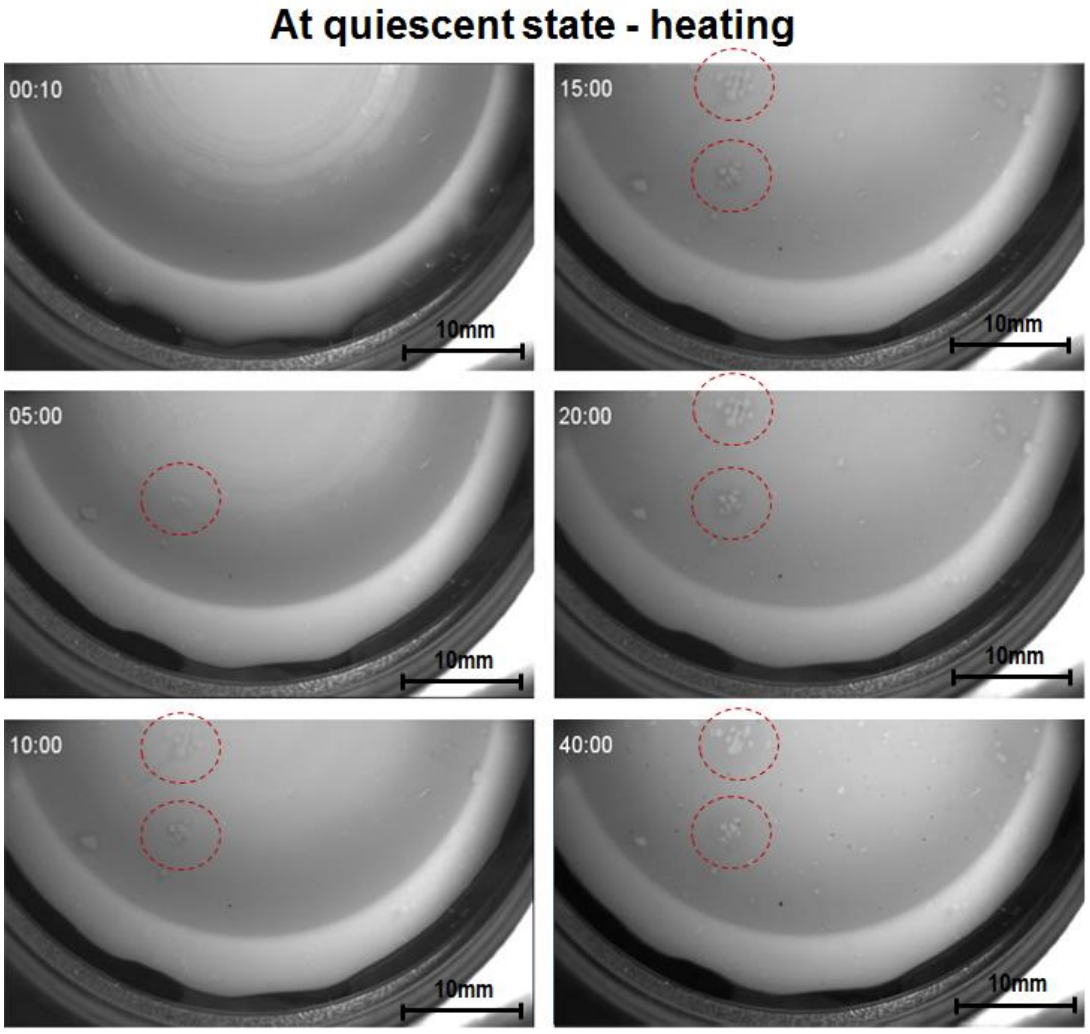

Fig. 6.14 *– Bottom plate images during heating (from 20 to 36°C) at quiescent state for the TFEMA/PNIPAM with 20mM of NaCl.*

At T=36°C we imposed shear flow for various Peclet numbers, while we were imaging for 40mins. At low shear rate (Pe=0.05), the suspension develops a string-like structure along the shear flow direction which becomes stronger with time (edge effects) (fig. 6.15).

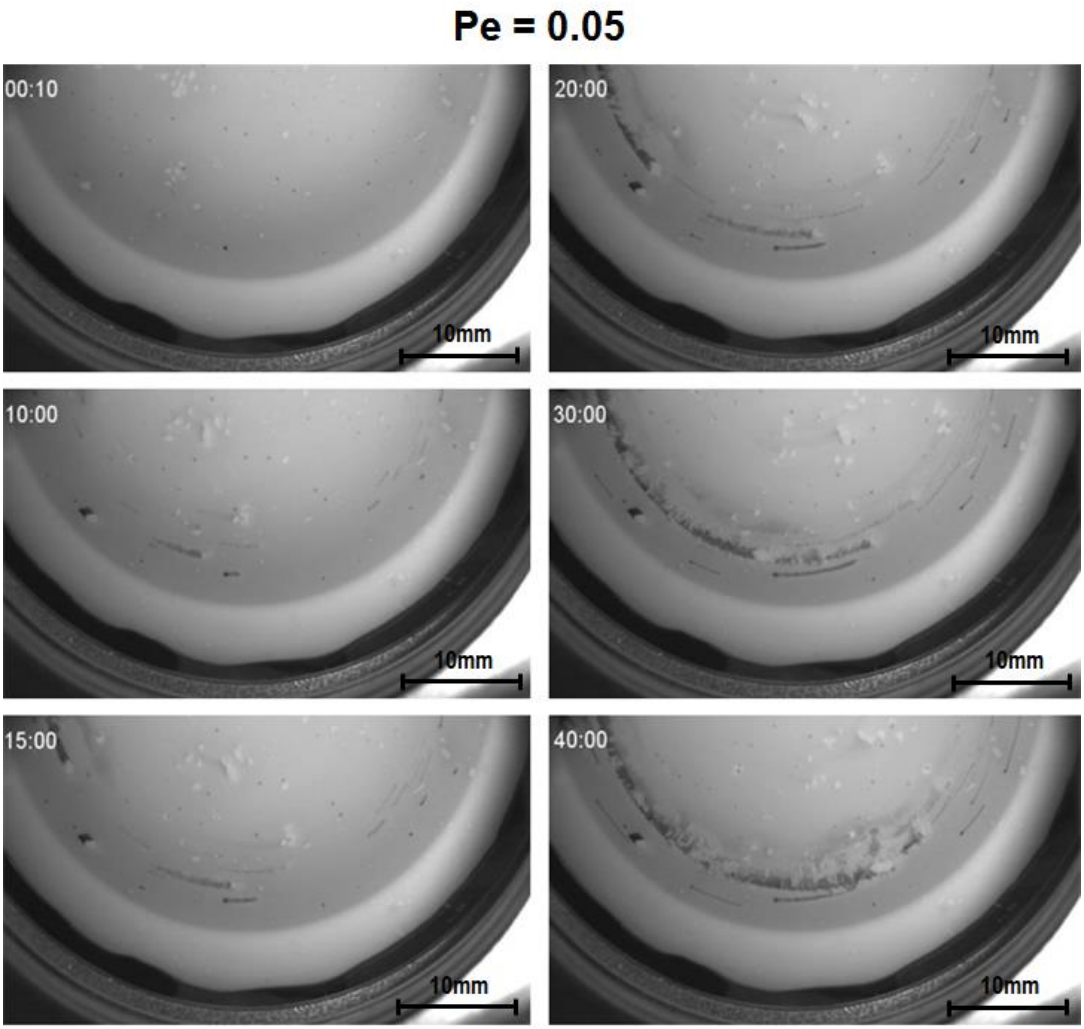

Fig. 6.15 *– Bottom plate images for TFEMA/PNIPAM with 20mM of NaCl for Pe=0.05 at 36°C.*

For intermediate shear rates (e.g. Pe=0.4) at 36°C, the string-rolling structure becomes more pronounced. As the time passes, we observe that the structure collapses with the clusters being pushed along the vorticity direction towards the periphery of the geometry (fig. 6.16).

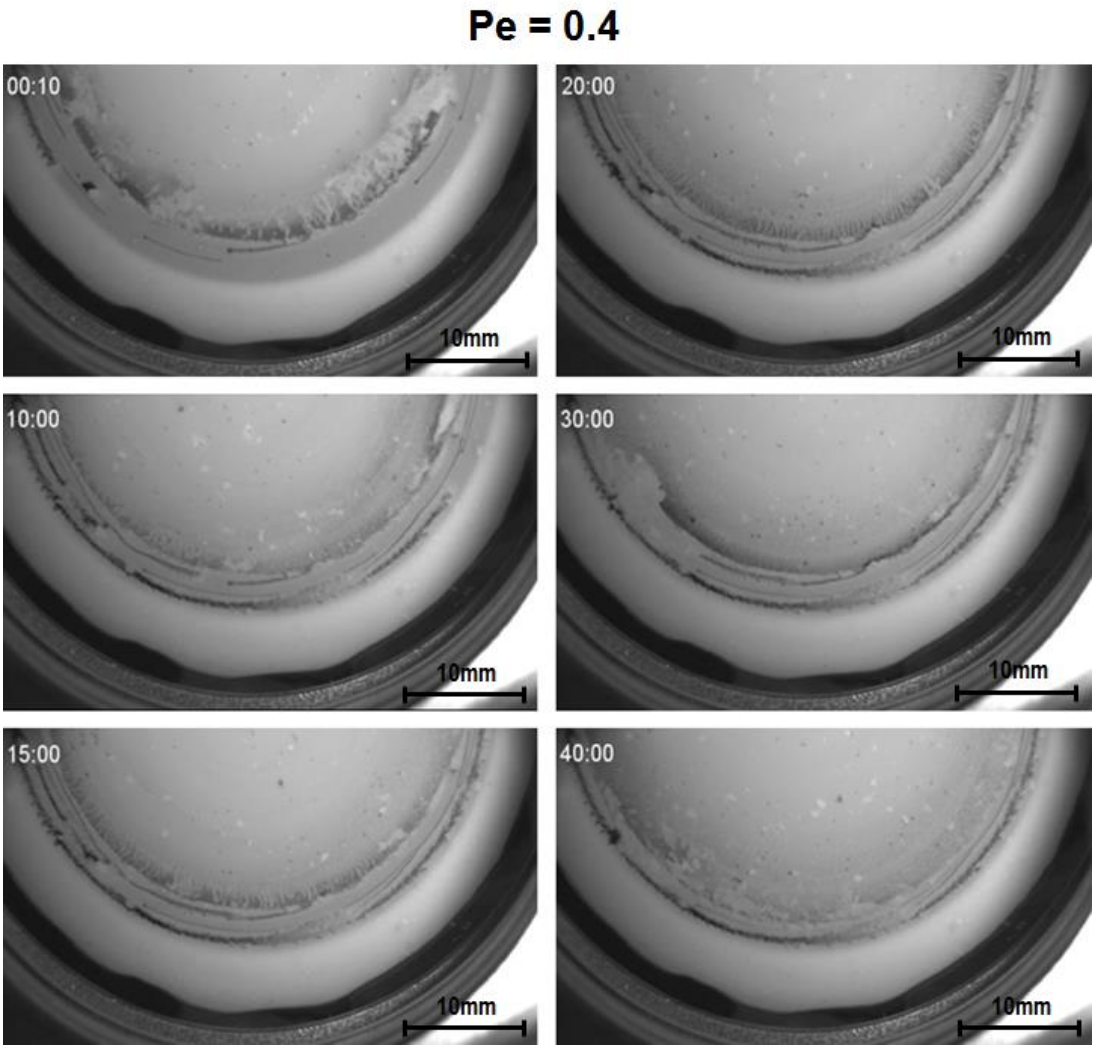

Fig. 6.16 *– Bottom plate images for TFEMA/PNIPAM with 20mM of NaCl for Pe=0.4 at 36°C.*

For even higher shear rates (Pe=10), the clusters which are accumulated in the periphery start to detach as time passes and mix along the shear flow. However, the suspension does not get completely homogeneous (fig. 6.17).

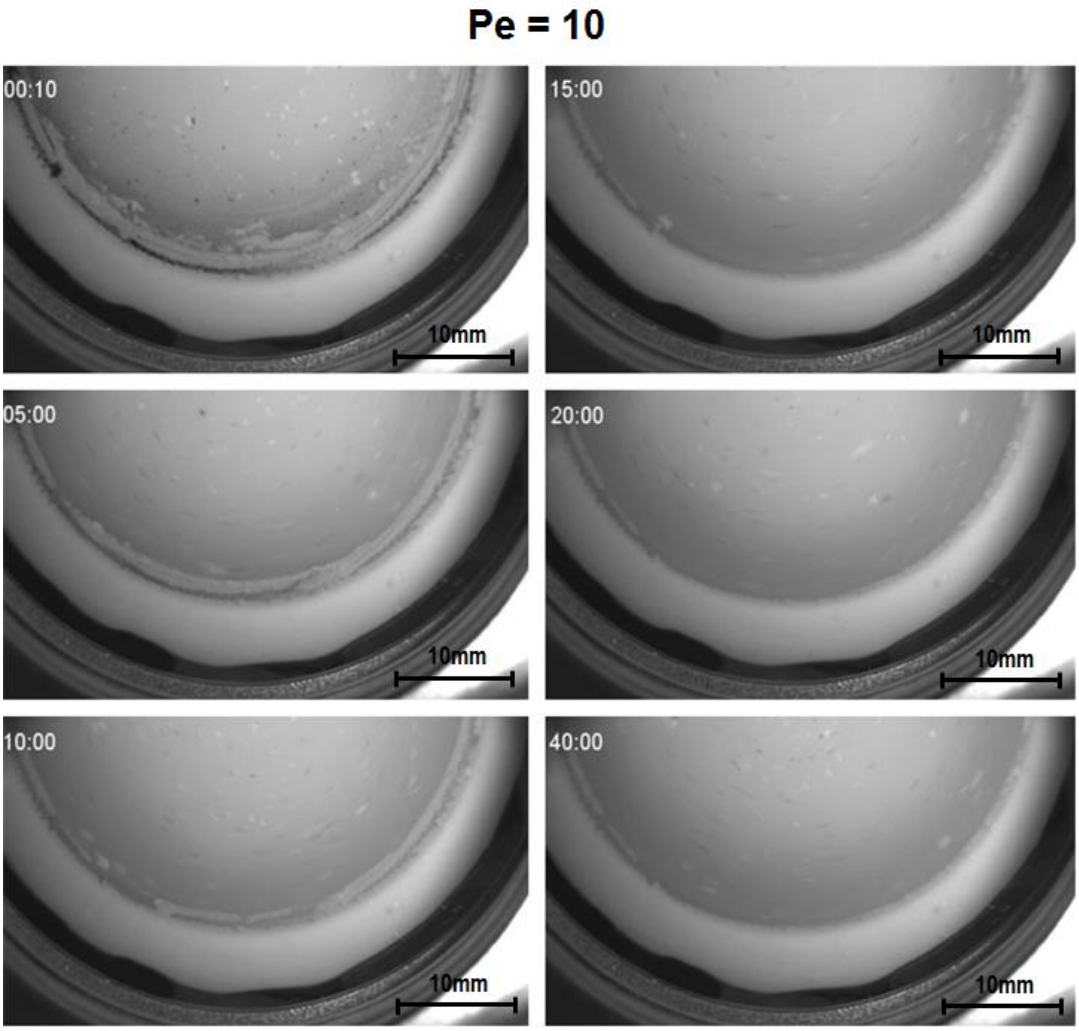

Fig. 6.17 *– Bottom plate images for TFEMA/PNIPAM with 20mM of NaCl for Pe=10 at 36°C.*

Finally, we cooled down the temperature where we observe that once the temperature equilibrated back at 20°C, the sample seems to get homogeneous again (fig. 6.18).

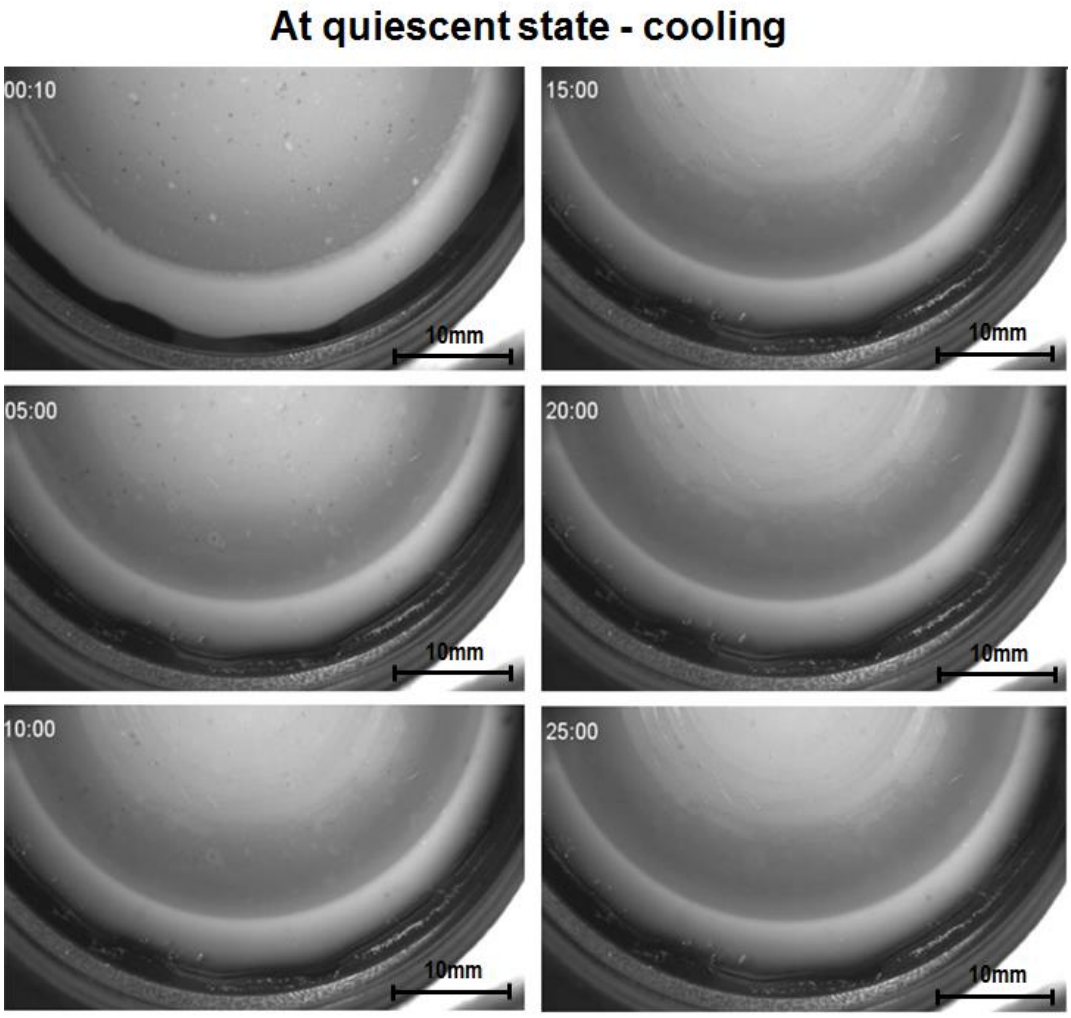

Fig. 6.18 *– Bottom plate images during cooling (from 36 to 20°C) at quiescent state for TFEMA/PNIPAM with 20mM of NaCl at 36°C.*

6.4 Conclusions

In this chapter, we explore the influence of monovalent salt ions of NaCl on structure and viscoelastic properties of electrostatically stabilized aqueous suspensions of core-shell microgels of TFEMA/PNIPAM. At first, we used light scattering in dilute regime in order to characterize the particle size and determine the hydrodynamic radius for 20mM and 50mM of NaCl, while the evaluation of the A_2 revealed the range of the interparticle interactions. For both salt concentrations, we identify the aggregation temperature T_a, above which the attractive interactions become sufficiently large to induce clustering, which eventually would lead to phase separation. However, the aggregation temperature strongly depends on the ionic

strength with the T_a decreasing as the salt concentration increases. At temperatures above the LCST, the competition between long-range screened electrostatic repulsions and short-range attractions provides an efficient way to stabilize clusters whose shape and size result from the subtle balance between these opposing forces. Equilibrium cluster formation is delineated in the second virial coefficient estimation which unexpectedly increases increasing the salt concentration and in capillary viscometry tests, where the viscosity increases extremely rendering difficult the viscosity measurements.

Linear and non-linear rheological measurements were performed for concentrated suspension (c=0.097g/ml / $\phi_{eff@20^oC}$≈1.1) of ionic strength of 20mM of NaCl. Increasing the temperature we gradually tuned the interactions from repulsive to attractive and switched between glassy, liquid and phase separation regime.

Rheo-confocal measurements on the same sample allowed direct determination of microstructure during and after the cessation of shear. Observation deep in the bulk was problematic due to small core size, which consists the only labelled (Nile red dye) part of the particles, while there is also significant multiple scattering. However, at T=36^{o}C, the visual indication of phase separation and the formation of equilibrium clusters is possible. Furthermore, the dynamic frequency sweeps which were performed after the cessation of the shear, reveals strengthening of the moduli for pre-shear with shear rates up to Pe=0.1, whereas a weaker response for pre-shear with higher shear rates.

Finally, in order to obtain more information about the large length-scale structure, especially at T=36^{o}C, we used low magnification imaging under shear, where we observe formation of regions that may indicate phase separation. Under flow, we notice shear-dependent assembly of log-rolling colloidal strings parallel to the confining geometry. Imposing higher shear rate, the suspension does not homogenize, except for pre-shear with Pe=10, where some homogenization is achieved. However, the shrinking and swelling of the microgel particle in the heating and cooling cycle are completely reversible.

References:

Appel, J., et al. (2015). "Temperature Controlled Sequential Gelation in Composite Microgel Suspensions." Particle & Particle Systems Characterization **32**(7): 764-770.

Berne, B. J. and R. Pecora (2000). Dynamic light scattering: with applications to chemistry, biology, and physics, Courier Corporation.

Boukany, P. E., et al. (2010). "Molecular imaging of slip in entangled DNA solution." Physical review letters **105**(2): 027802.

Carrier, V. and G. Petekidis (2009). "Nonlinear rheology of colloidal glasses of soft thermosensitive microgel particles." Journal of Rheology (1978-present) **53**(2): 245-273.

Deike, I., et al. (2001). "Rheology of thermosensitive latex particles including the high-frequency limit." Journal of Rheology **45**(3): 709-720.

Derec, C., et al. (2003). "Aging and nonlinear rheology in suspensions of polyethylene oxide–protected silica particles." Physical Review E **67**(6): 061403.

Glotzer, S. C. and M. J. Solomon (2007). "Anisotropy of building blocks and their assembly into complex structures." Nature materials **6**(8): 557.

Groenewold, J. and W. K. Kegel (2001). "Anomalously large equilibrium clusters of colloids." The Journal of Physical Chemistry B **105**(47): 11702-11709.

Koumakis, N., et al. (2012). "Yielding of hard-sphere glasses during start-up shear." Physical review letters **108**(9): 098303.

Koumakis, N., et al. (2016). "Start-up shear of concentrated colloidal hard spheres: Stresses, dynamics, and structure." Journal of Rheology **60**(4): 603-623.

Koumakis, N., et al. (2012). "Direct comparison of the rheology of model hard and soft particle glasses." Soft Matter **8**(15): 4271-4284.

Kulkarni, S. D. and J. F. Morris (2009). "Ordering transition and structural evolution under shear in Brownian suspensions." Journal of Rheology **53**(2): 417-439.

Letwimolnun, W., et al. (2007). "Stress overshoots of organoclay nanocomposites in transient shear flow." Journal of non-newtonian fluid mechanics **141**(2-3): 167-179.

Mason, T. and D. Weitz (1995). "Linear viscoelasticity of colloidal hard sphere suspensions near the glass transition." Physical review letters **75**(14): 2770.

Mewis, J. and N. J. Wagner (2012). Colloidal suspension rheology, Cambridge University Press.

Neal, B., et al. (1998). "Molecular origins of osmotic second virial coefficients of proteins." Biophysical journal **75**(5): 2469-2477.

Neal, B., et al. (1999). "Why is the osmotic second virial coefficient related to protein crystallization?" Journal of Crystal Growth **196**(2): 377-387.

Schärtl, W. (2007). Light scattering from polymer solutions and nanoparticle dispersions, Springer Science & Business Media.

Senff, H. and W. Richtering (2000). "Influence of cross-link density on rheological properties of temperature-sensitive microgel suspensions." Colloid & Polymer Science **278**(9): 830-840.

Senff, H., et al. (1999). "Rheology of a temperature sensitive core− shell latex." Langmuir **15**(1): 102-106.

Stradner, A., et al. (2006). "A small-angle scattering study on equilibrium clusters in lysozyme solutions." The Journal of Physical Chemistry B **110**(42): 21222-21231.

Stradner, A., et al. (2004). "Equilibrium cluster formation in concentrated protein solutions and colloids." Nature **432**: 492.

Utiyama, H. (1972). "Calibration and correction factors." Light Scattering from Polymer Solutions. MB Huglin, editor. Academic Press, London.

Valente, J. J., et al. (2005). "Colloidal behavior of proteins: effects of the second virial coefficient on solubility, crystallization and aggregation of proteins in aqueous solution." Current pharmaceutical biotechnology **6**(6): 427-436.

Van Megen, W. and S. Underwood (1993). "Dynamic-light-scattering study of glasses of hard colloidal spheres." Physical Review E **47**(1): 248.

Wilson, W. W. (2003). "Light scattering as a diagnostic for protein crystal growth—A practical approach." Journal of structural biology **142**(1): 56-65.

Xu, X., et al. (2013). "Influence of interlayer exchanges on vorticity-aligned colloidal string assembly in a simple shear flow." The Journal of Physical Chemistry Letters **4**(19): 3310-3315.

Zimm, B. H. (1948). "Apparatus and methods for measurement and interpretation of the angular variation of light scattering; preliminary results on polystyrene solutions." The Journal of Chemical Physics **16**(12): 1099-1116.

Chapter 7

Orthogonal Superposition Rheometry of core-shell microgels

Here, we examine the mechanisms of flow in suspensions of soft particles well above glass transition using Orthogonal Superposition Rheometry (OSR). A small amplitude oscillatory shear flow is superimposed orthogonally onto a well-developed steady shear flow, which allows probing the full linear viscoelastic spectra of sheared core-shell jammed microgels. The characteristic crossover frequency ω_c, deduced from the viscoelastic spectrum, provides information about the shear induced structural relaxation, which is connected to the microscopic yielding mechanism of cage breaking. The shear rate evolution of the crossover frequency is used to achieve a superposition of all spectra and get a better insight of the flow mechanism. Despite their inherent softness, the hybrid core-shell microgels exhibit similarities with hard sphere-like flow behavior, with the main difference that for the microgels the transition from a glassed to a jammed state introduces a volume fraction dependence of scaling of ω_c with shear rate.

7.1 Introduction

The microstructure of complex soft materials, such as polymeric or colloidal viscoelastic fluids, is strongly affected even by weak mechanical perturbations (Mewis and Wagner 2012). Shear flow consists of such an external perturbation and its interplay with microstructure and rheological behavior constitute an intriguing subject that has received much attention (De Silva, Poulos et al. 2011, Eberle and Porcar 2012, Koumakis, Pamvouxoglou et al. 2012, Lettinga, Holmqvist et al. 2012, López-Barrón, Porcar et al. 2012, Mewis and Wagner 2012, Koumakis, Brady et al. 2013, Amann, Denisov et al. 2015, Snijkers, Pasquino et al. 2015).

Colloidal hard spheres have been used as model systems to study phase behavior, state transitions and flow response of both ordered and glassy states (Koumakis, Schofield et al. 2008, Koumakis, Laurati et al. 2012). For hard spheres the glass transition occurs at volume fractions above $\phi_g \approx 0.58$, due to entropic caging of particles induced by the presence of their first neighbors (Pusey 1991, Van Megen and Underwood 1994, Cheng, Chaikin et al. 2001, El Masri, Brambilla et al. 2009).

The mechanisms of yielding and flow of hard sphere colloidal glasses have been studied through experiments and simulations, for both steady (Petekidis, Vlassopoulos et al. 2004, Schall, Weitz et al. 2007, Besseling, Isa et al. 2010, Chikkadi, Wegdam et al. 2011, Koumakis, Laurati et al. 2012, Siebenbürger, Ballauff et al. 2012) and oscillatory shear flow (Petekidis, Moussaid et al. 2002, Miyazaki, Wyss et al. 2006, Brader, Siebenbürger et al. 2010, Koumakis, Brady et al. 2013). Furthermore, Jacob et al. (Jacob, Poulos et al. 2015) studied the viscoelastic spectra of hard sphere glasses under steady shear flow and the shear rate dependence of structural relaxation using Orthogonal Superposition Rheometry, the experimental technique reported in this chapter. Except for hard sphere glasses, there are similar measurements of softer particles that exhibit deformability, such as microgels, or interpenetrability, such as polymer grafted colloids and multiarm stars (Cloitre, Borrega et al. 2003, Erwin, Cloitre et al. 2010, Seth, Mohan et al. 2011, Truzzolillo, Vlassopoulos et al. 2014, Vlassopoulos and Cloitre 2014). Similarly, non-linear rheology in connection with microstructural evolution has been explored in several

soft glasses under shear (Le Grand and Petekidis 2008, Siebenbürger, Fuchs et al. 2009, Mohan, Pellet et al. 2013).

In this chapter, we investigate the effect of steady shear on the viscoelastic behavior of sheared hybrid core-shell microgels well above glass transition through Orthogonal Superposition Rheometry (OSR). Orthogonal superposition rheometry (OSR) combines two deformation modes, steady shear in one direction and small amplitude oscillatory shear applied simultaneously and orthogonally to the steady shear. In this way, small amplitude orthogonal frequency sweeps interrogate the sample and extract its viscoelastic spectra under steady shear (Simmons 1966, Vermant, Walker et al. 1998, Kim, Mewis et al. 2013, Jacob, Poulos et al. 2015).

First, we determined the characteristic crossover frequency ω_c, which provides a direct measure of the shear induced structural relaxation that is attributed to the microscopic yielding mechanism of cage breaking. We further used the shear rate dependence of the crossover frequency to investigate if a scaling of the viscoelastic spectra can be achieved (Jacob, Poulos et al. 2015).

7.2 Materials and methods

We used temperature-sensitive soft core-shell particles consisting of a fluorescently labeled (Nile red) trifluorethyl methacrylate (TFEMA) core of 85nm radius onto which a Poly(*N*-isopropylacrylamide) shell is affixed. The composition of the microgel shell determines the thermosensitive behavior of the hybrid particle (Liu, Fraylich et al. 2009). As we have already mentioned in former chapter, the hybrid particles, TFEMA/PNIPAM 880nm, are synthesized in a two step-procedure according to the process described by Appel et al. (Appel, de Lange et al. 2015). The crosslinking density of the shell is 5%wt. The particles are electrostatically stabilized in aqueous suspensions by sulfonate groups at the periphery of the particles. Dynamic light scattering is used in the dilute regime in order to extract the hydrodynamic radius of the particles, which is R_H=440nm at T=20^{o}C. Capillary viscometry is used to deduce the effective volume fraction ϕ_{eff} of colloidal

suspensions by measuring the relative viscosity η_{rel} of dilute suspensions as a function of particle concentration, as described in former chapter.

Orthogonal Superposition Rheometry is performed at various rotational rates and three different effective volume fractions well above glass transition (ϕ_{eff}=0.99, 1.13 and 1.27 at T=20^{o}C), using an ARES-G2 (TA) rheometer with a modified normal force control loop, equipped with an open bottom double wall Couette geometry (Vermant, Moldenaers et al. 1997, Kim, Mewis et al. 2013). Steady shear flow is imposed in the tangential direction, whereas oscillatory motion vertically. Here, we explored tangential steady shear rates ranging from 10^{-3} to $10s^{-1}$.

7.3 Results - Discussion

First, we investigate the flow behavior under constant steady shear of the system TFEMA/PNIPAM 880nm. Fig. 7.1 shows the flow curves (steady state shear stress vesus shear rate) for various volume fractions. These show the typical response expected for soft yield-stress materials with a shear-thinng behaviour at high shear rates, where stress shows a sub-linear increase with shear rate and the detection of a yield stress plateau at low shear rates. The flow curve shown in fig. 7.1a can be fitted with the Herschel-Bulkley model ($\sigma = \sigma_0 + k\dot{\gamma}^n$) in agreement with similar earlier studies (Cloitre, Borrega et al. 2003, Bécu, Manneville et al. 2006, Ballesta, Besseling et al. 2008, Erwin, Cloitre et al. 2010, Koumakis, Pamvouxoglou et al. 2012). Table I shows the values of k and n for various volume fractions. The consistency factor, k, is a simple constant of proportionality, that increases with increasing volume fraction. The flow index exponent, n, describes the shear-thinning behavior and shows an insignificant change with volume fraction with value less than one. In fig. 7.1b, we plot the normalized flow curves. The shear rate is scaled by the local relaxation time t_B, while the stress is scaled by the experimental yield stress (σ_y) that consists the lowest stress for which a stationary state is achieved. At low shear rates (up to $\sigma/\sigma_y \approx 10^{-2}$), all the flow curves collapse onto a universal curve which is well represented by the Herschel-Bulkley model. At low shear rates, rearranging particles relax back to local equilibrium before the flow induces a new

rearrangement. Thus, the stress remains of the order of the yield stress. However, at high shear rates, the flow induces continuoulsy rearrangements. Then the stress increases due to viscous dissipation connected with interparticle friction (Cloitre, Borrega et al. 2003).

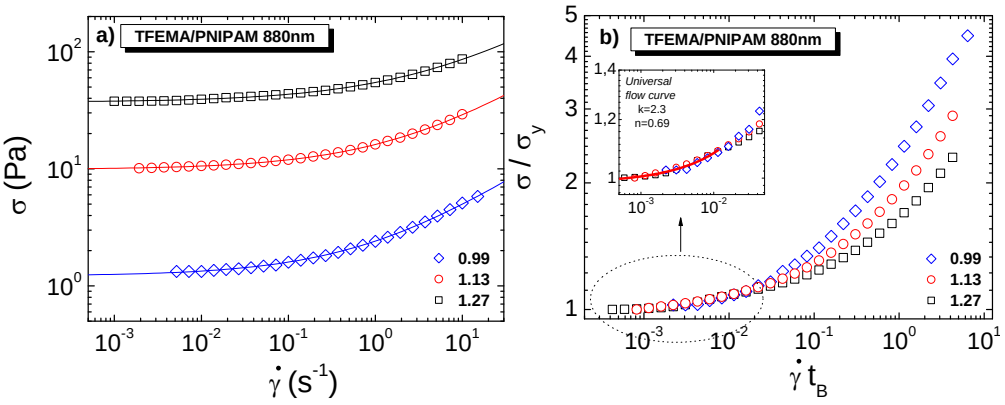

Fig. 7.1 *– a) Steady state shear stress as a function of rotational shear rate (flow curve) for various volume fractions as indicated. The solid curves represent the fitting of experimental data with Herschel-Bulkley model, b) Normalized flow curves for various volume fractions, and Inset: universal flow curve at low shear rates.*

φ_{eff}	k	n
1.27	17.5	0.45
1.13	6.3	0.48
0.99	1.2	0.51

Table I *- The consistency k and shear thinning exponent n values obtaind by fitting experimental data of fig. 7.1 with Herschel-Bulkley model.*

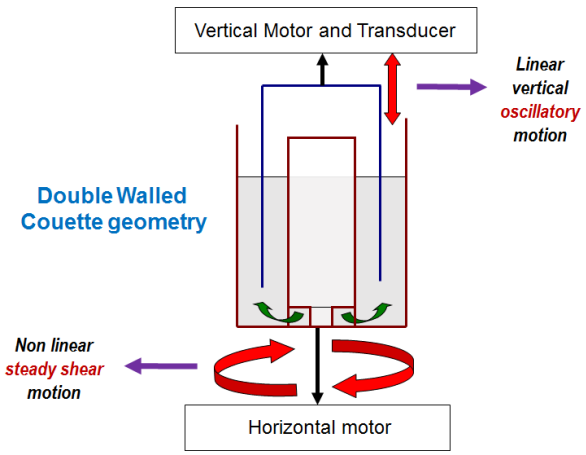

Fig. 7.2 *– Double-wall Couette cell for Orthogonal Superposition Rheometry.*

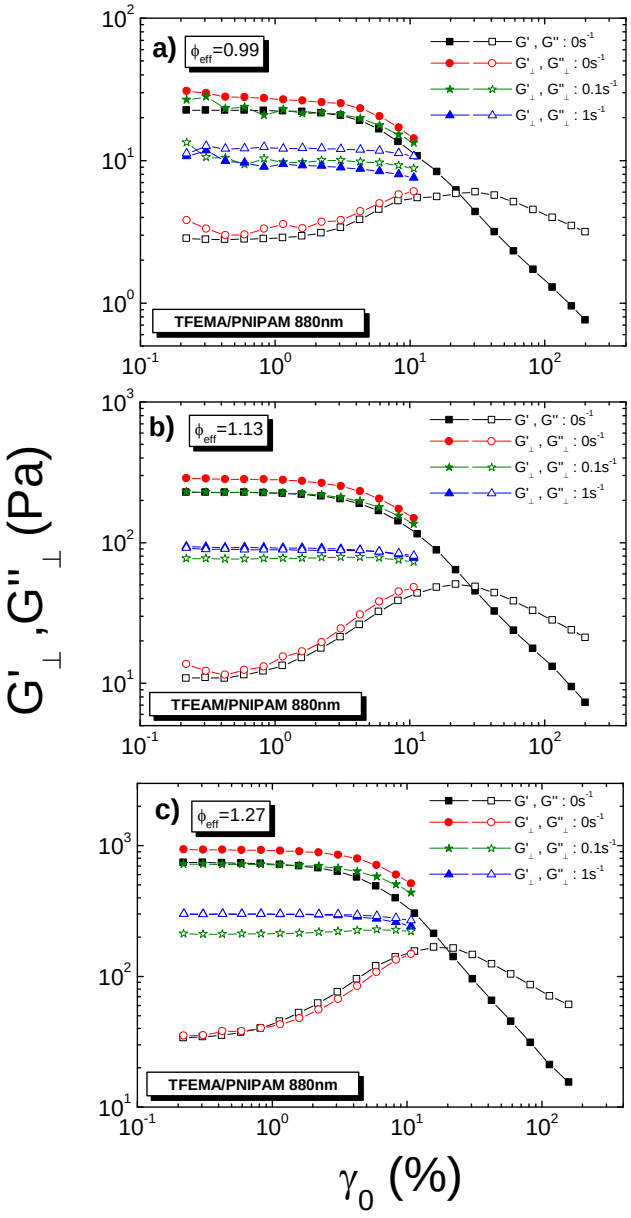

Fig. 7.3 *– Orthogonal dynamic strain sweeps (ODSS) showing the elastic (solid symbols) and viscous (open symbols) moduli at frequency of ω=10 rad/s under steady shear flow for various shear rates as indicated at φ_{eff} a) 0.99, b) 1.13 and c) 1.27 of TFEMA/PNIPAM 880nm. The parallel dynamic strain sweeps (black curves) are also shown for the comparison.*

The extent of the linear viscoelastic regime in the orthogonal direction is determined by performing dynamic strain sweep tests. Fig. 7.3 presents the orthogonal dynamic strain sweeps at rest as well as for rotational shear rates of 0.1 and 1s^{-1} at the fixed frequency of 10rad/s. The rotational dynamic strain sweep is also depicted for comparison. The rotational dynamic strain sweep experiments

exhibit the typical features for yielding as seen in many colloidal systems; the decrease of G' with increasing strain amplitude and the simultaneous appearance of a peak in G'' at approximately 10% strain amplitude as well as the constant power law slopes at high strains with G' having roughly twice the slope of G''. With no shear, the orthogonal dynamic strain sweep exhibits similar response to the parallel one. As expected, the onset of non-linearity begins at around 1% strain, with higher volume fraction showing an earlier onset. Increasing the shear rate, the system tends to liquefy leading to the extension of the linear regime to larger values. For instance, for ϕ_{eff}=1.27 the linear regime at rest extends to approximately 0.3%, whereas at shear $0.1s^{-1}$ increases to 1.5% and at $1s^{-1}$ to 3%. In dynamic strain sweeps, the peak of loss moduli represents the maximum energy dissipation around yielding where it is expected that a large number of cages break and particle rearrangements are important (Petekidis, Moussaid et al. 2002, Koumakis, Laurati et al. 2012). Here, we observe that increasing the shear there, the peak disappears indicating a more gradual energy dissipation before yielding.

Orthogonal dynamic frequency sweeps, at the selected low strain amplitude in linear regime, were performed once a steady state was reached typically after 200s for the highest to 2000s for the lowest shear rates. The waiting time used each time corresponds to a total strain of γ>1. Fig. 7.4 shows both the orthogonal and parallel frequency sweeps at rest for all the volume fractions measured. The measured DFS experiments represent the typical behaviour of colloidal suspensions above glass transition where the storage modulus G' dominates the loss modulus G'' over a wide range of frequencies. The storage modulus G' presents a plateau with a slightly increasing slope, which is due to increased particle motions at small frequencies compared to the high ones, where the motion is restricted due to caging effect. The loss modulus G'' exhibits a minimum, which is related to the transition between the in-cage and the out-of-cage relaxation times of the particles (Van Megen and Underwood 1993, Mason and Weitz 1995). For all volume fractions, the difference between the orthogonal and the tangential measurement is up to 20% which is within the setup limits (Colombo, Kim et al. 2017).

The tangential experimental data can be compared with the Kramer-Kronig relation for linear viscoelastic materials (Stuart 1955, Booij and Thoone 1982):

$$G''(\omega) \cong \frac{\pi}{2}\left(\frac{dG'(u)}{d\ln u}\right)_{u=\omega} \tag{7.1}$$

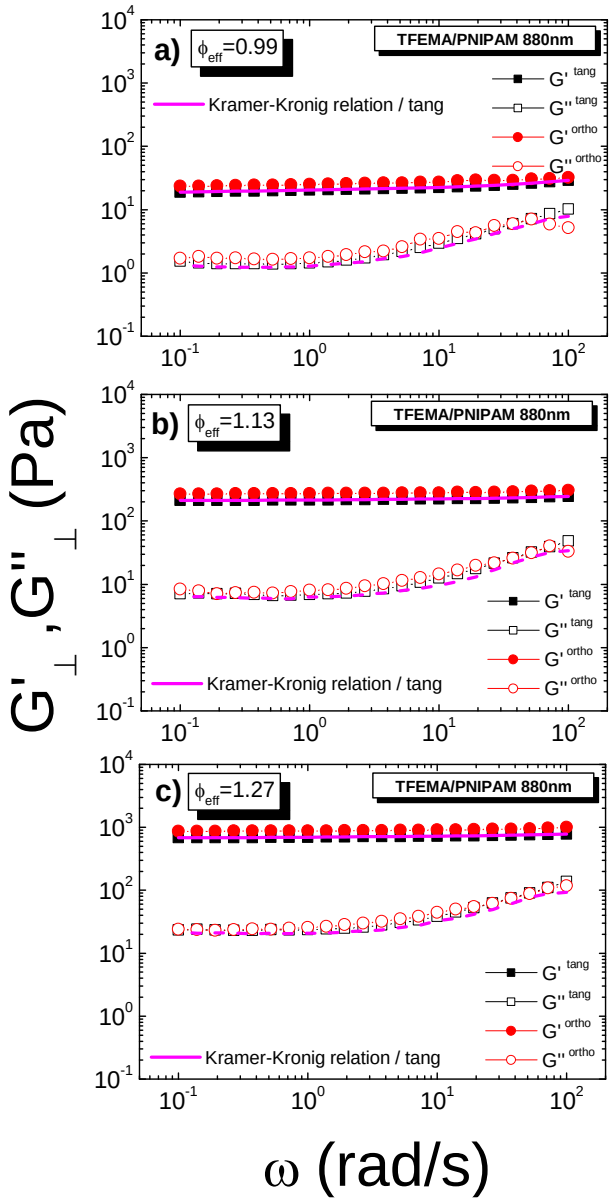

Fig. 7.4 *- Orthogonal and parallel frequency sweeps preformed in the linear viscoelastic regime at φ_{eff} a) 0.99, b) 1.13 and c) 1.27 of TFEMA/PNIPAM 880nm at quiescent state. Dark yellow and blue curves represent the generalized Maxwell model fit to each pair of orthogonal and tangential G'(ω) and G''(ω) data respectively. Magenta curves represent the Kramer-Kronig relation for tangential experimental data.*

From dynamic frequency sweeps we can extract the plateau modulus G'_p, which is located in the minimum of loss modulus around a frequency ω_m (Pellet and Cloitre 2016). Fig. 7.5 presents the plateau modulus as a function of effective particle volume fraction. For TFEMA/PNIPAM 880nm, increasing the effective volume fraction, a change of the slope is observed. This change in the plateau modulus probably signifies a transition from glassy to jammed state as has been reported by Pellet et al. (Pellet and Cloitre 2016) as a mechanical signature of glass to jammed transition. The tangential storage modulus for different volume fractions for the system TFEMA/PNIPAM 900nm (explored thoroughly in chapter 5) is presented for comparison, where we also observe the change of the slope.

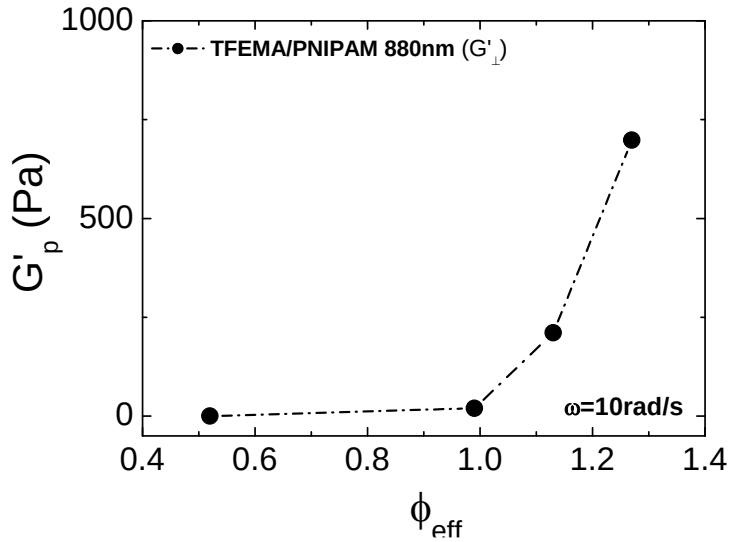

Fig. 7.5 *– Variations of plateau modulus at rest for TFEMA/PNIPAM 880nm and TFEMA/PNIPAM 900nm (reported at chapter 5) as a function of effective volume fraction.*

Apart from the quiescent situation, orthogonal dynamic frequency sweeps (ODFS) were also performed under various rotational shear rates $\dot{\gamma}$ ranging from 0.001s^{-1} to 10s^{-1}. Fig. 7.6 depicts the evolution of $G_\perp^{'}$ and $G_\perp^{''}$ at various rotational shear rates for different volume fractions. Increasing the shear rate, the flow induces microstructural changes in the system, which results in speeding up of the internal relaxation dynamics.

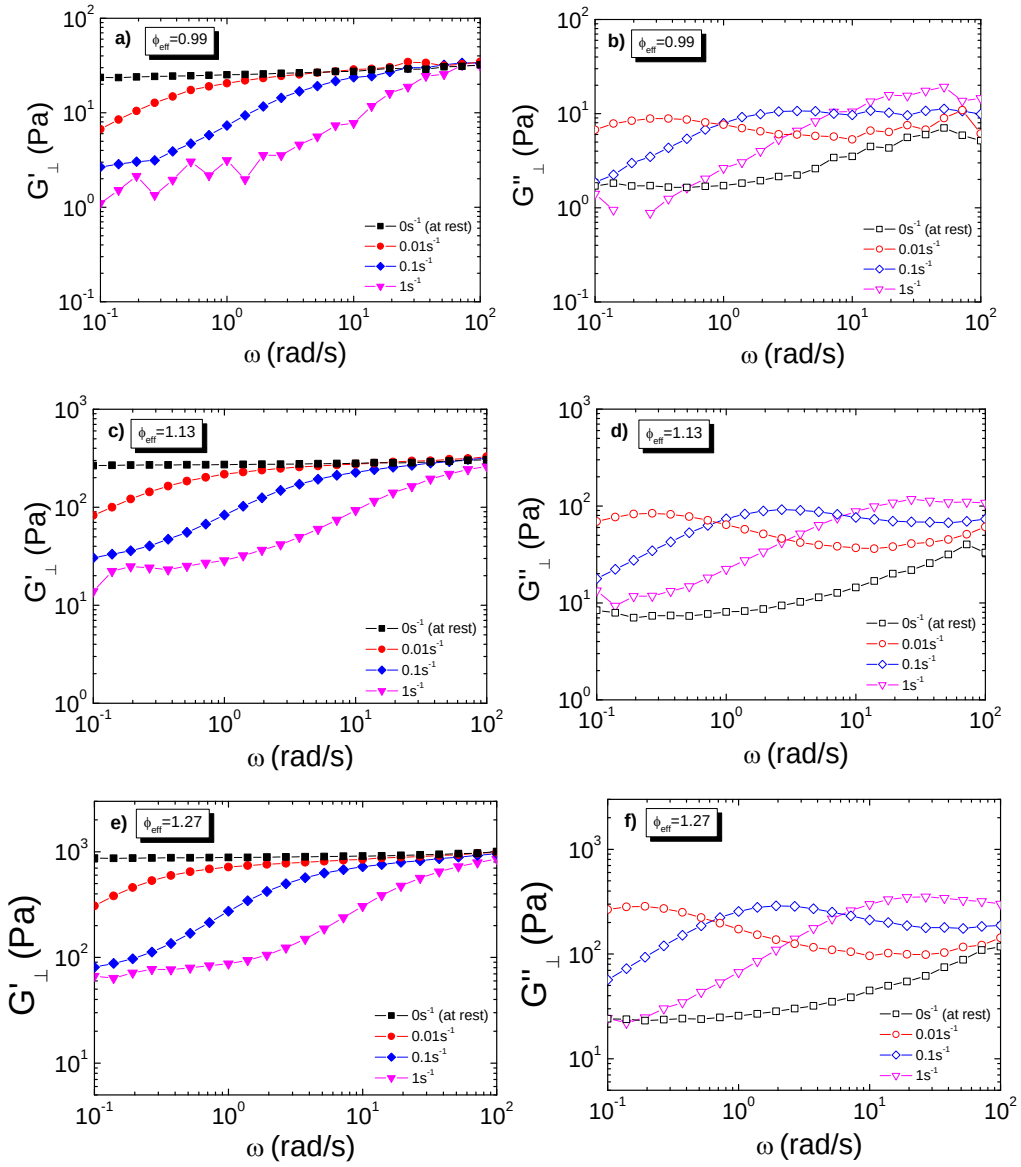

Fig. 7.6 *– Storage and loss moduli from orthogonal frequency sweeps at volume fraction 0.99 (a) $G_{\perp}^{'}$, b) $G_{\perp}^{"}$), 1.13 (c) $G_{\perp}^{'}$ and d) $G_{\perp}^{"}$) and 1.27 (e) $G_{\perp}^{'}$ and f) $G_{\perp}^{"}$) at T=20°C for various shear rates.*

Fig. 7.7 shows comparison graphs for various rotational shear rates for the three different volume fractions measured. We observe that even at the lowest shear rate measured ($\dot{\gamma} = 0.01s^{-1}$), the ODFS shows a discernible change from the DFS at rest, with the elastic modulus $G_{\perp}^{'}$ decreasing and the viscous modulus $G_{\perp}^{"}$ increasing over the whole frequency range. This fact is consistent with the idea that the rotational shear rate partially fluidizes the initially glassy sample. Moreover, both $G_{\perp}^{'}$ and $G_{\perp}^{"}$ increase as the effective volume fraction increases for all the applied

shear rates. At shear rate 0.01s^{-1}, we detect the emergence of a crossover frequency, inside the experimental frequency window (fig. 7.7b), which moves to higher frequencies with increasing shear rate. Above a certain shear rate, a second crossover frequency is observed at lower frequencies. These two crossover frequencies represent two structural relaxation timescales ($t_c=1/\omega_c$) related to two different length-scales. In the case of HS glasses, high frequency crossover is related to the shear-induced out-of-cage displacements, while the low frequency crossover to the formation of larger length scale structures or aggregates probably formed due to the interplay of shearing with lubrication hydrodynamics interactions (hydro-clusters) (Brady and Bossis 1985, Bender and Wagner 1996). Hybrid microgels though consist of shells surrounding the cores defined by repulsive thermodynamic forces, which modify the lubrication interactions, minimizing the probability of hydro-clustering (Melrose and Ball 2004). As shear is increased, we observe that both the high and low crossover frequency ω_c move to higher frequencies, denoting the speed-up of the internal dynamics which is manifested by ω_c. Moreover, above the high frequency crossover, the Kramer-Kronig relation is applied successfully, whereas below the low ω_c the fitting is not satisfactory.

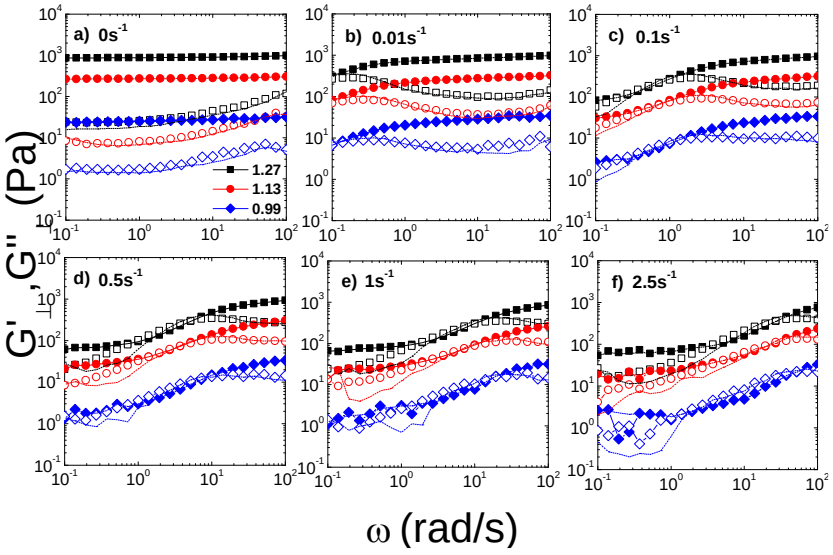

Fig. 7.7 *– Orthogonal dynamic frequency sweeps obtained for different rotational shear rates from a) 0s^{-1} to f) 2.5s^{-1} (rest) at φ_{eff} =0.99, 1.13 and 1.27 of TFEMA/PNIPAM 880nm. Curves represent the Kramer-Kronig predictions.*

Fig. 7.8 presents the relaxation times measured from the low and high frequency crossovers as a function of dimensionless rotational Péclet number ($Pe = \dot{\gamma} t_B = \dot{\gamma} R^2 / D_O$), which relates the shear rate of a flow to the particle's diffusion rate. Then, direct comparison of microgel suspensions with HS glasses can be achieved by normalizing both the relaxation times and the shear rate by the Brownian time. The short-time relaxation, which corresponds to high frequency crossover, shows almost a linear decrease with Pe similar to HS glasses ($tc_1 \sim t_B^{-1}$) (Fig. 7.8a). Increasing shear rate (Pe≈1), the fluid structure becomes anisotropic, as particles rearrange in order to reduce their interparticle interactions so as to flow with less resistance (Wagner and Brady 2009). For HS glasses this particle rearrangement is associated with the shear assisted particle escape from their cage and hence the reduction of the short-time relaxation (Jacob, Poulos et al. 2015). Here, we observe that the short-time relaxation exhibits a non-monotonic dependence on particle volume fraction in contrast with HS glasses where the relaxation time was found to be independent of particle volume fraction. This non-monotonic dependence of short-time relaxation on particle volume fraction could be indication of a transition from a glassy state to a jammed state, similarly to the change of the slope of the plateau modulus with particle effective volume fraction (see fig. 7.5). The long-time relaxation, which corresponds to low frequency crossover, shows a power law decrease with Pe (Fig. 7.8b). In the case of HS glasses, Brownian dynamics simulations, which do not take into account the hydrodynamic interactions (HI) between particles, exhibit only high frequency crossover (Jacob, Poulos et al. 2015). Hence, the low frequency crossover detected only in experiments was associated to formation of clusters which is more prominent at high shear rates. However, the microscopic origin of this structural relaxations is not clear yet. The above assumption needs to be thoroughly examined by experiments that are capable of providing detailed information on the microscopic structure, such as simultaneous rheometry and confocal measurements and by computer simulations where full HI are included.

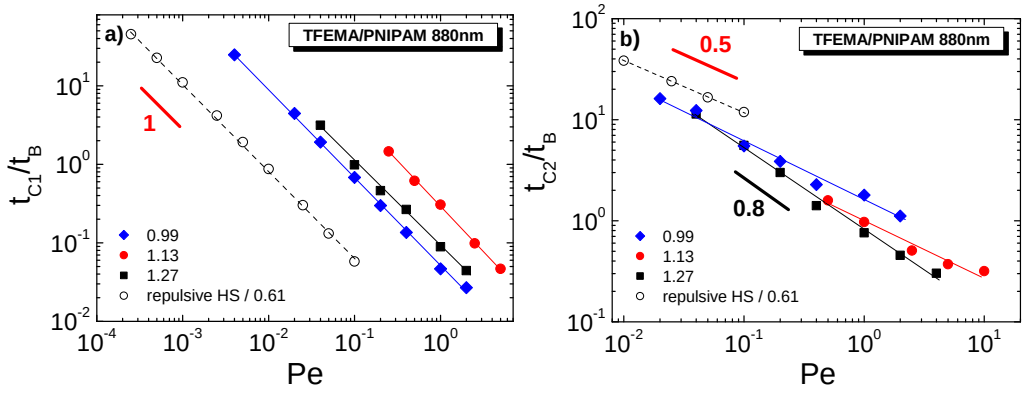

Fig. 7.8 *– Normalized relaxation time calculated for a) high (t_{c1}/t_B) and b) low ω_c (t_{c2}/t_B) for various effective particle volume fractions as indicated. The results for HS glass with φ_{eff} =0.61 is shown for comparison.*

A scaling of the moduli as a function of frequency for the different steady state shear rates was produced by shifting the experimental data in the x- (frequency) and y- (modulus) axes by factors, α and b, respectively, in a way that the crossover frequencies ω_c for all shear rates coincide. In the regime where the crossover frequencies ω_c is not measurable, the shift is performed in a way that the rest of the viscoelastic spectra matches. The scaling results for core-shell microgel glasses at T=20°C are presented in the fig. 7.9a, b and c for effective volume fractions ϕ_{eff}=0.99, 1.13 and 1.27 respectively. Hence, a scaled map of the dynamics of the microgels through a shear rate-orthogonal frequency superposition (SROFS) is obtained. In all the measurements for the three different volume fractions, two distinct frequency regimes are detected which are separated by the crossover frequency ω_c. At regime $\omega>\omega_c$, which corresponds to short-time scales, the elastic moduli $G_\perp^{'}$ superimpose for all shear rates, whereas the loss modulus $G_\perp^{''}$ increases as shear rate is increased (see arrows in fig. 7.9). In contrast, for $\omega<\omega_c$ related to long-time scales, $G_\perp^{'}$ shows a decrease with increasing shear rate, whereas $G_\perp^{''}$ shows a rather good superposition for all shear rates explored here. In the case of HS glasses, deviation of $G_\perp^{''}$ from scaling detected at high frequency has been related to shear-induced reduction of short-time in-cage motions. Shear deforms cages leading into structural anisotropy with particles being accumulated more in the compression

axis while are pushed out in the extension axis which restricts the short-time in-cage particle diffusion (Koumakis, Laurati et al. 2012, Koumakis, Laurati et al. 2016). In contrast, the deviation of $G_{\perp}^{'}$ at low frequency has been related to the formation of hydro-clusters, which is quite controversial for core-shell particles. Hence, for soft-hybrid microgels this deviation at low frequency perhaps is connected to the partial interpenetration of the chains in the outer part of the particles.

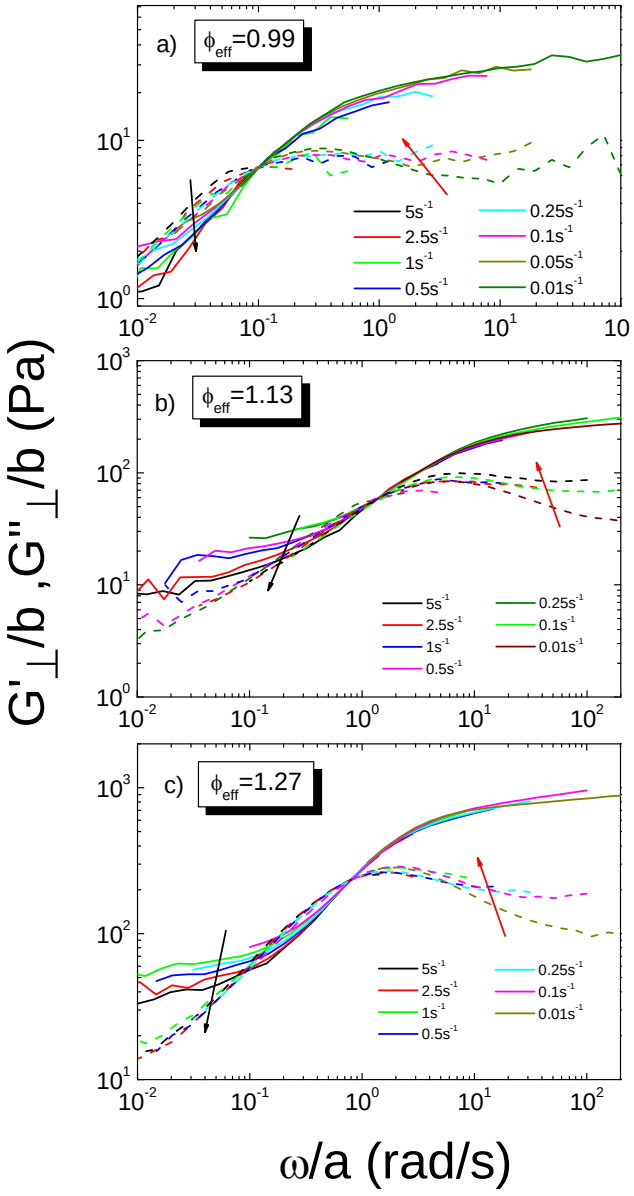

Fig. 7.9 *– Superposition of orthogonal dynamic frequency sweeps for microgels at various rotational shear rates for shear rates 0.01s^{-1} to 5s^{-1} for volume fractions a) 0.99, b) 1.13 and c) 1.27.*

The horizontal and vertical scaling factors used in obtaining the scaling data of figure 7.9 are shown in the fig. 7.10. The horizontal (frequency) shift factor reflects the shear rate dependence of the transition from the in-cage to out-of-cage motion and exhibits a linear dependence on the shear rate, similarly to HS glasses. Wyss et al. (Wyss, Miyazaki et al. 2007) though reported the strain-rate frequency superimposition of hydrogel suspensions, where the frequency shift factor presents a sub-linear power law dependence with an exponent of 0.9. Moreover, the frequency shift factor of hybrid microgels exhibits a non-monotonic change with the effective volume fraction, similarly with the behavior of the ω_c. This non-monotonic dependence could be attributed to the transition from a glassy state to a jammed one, as it is evident by a significant change in the elastic modulus with particle volume fraction (see fig. 7.5). On the contrary, repulsive hard sphere (HS) glasses present a volume fraction independent shear rate dependence of the shift factor α (Jacob, Poulos et al. 2015). Moreover, for core-shell microgels the slope of the horizontal shift factor is almost constant and slightly higher comparing to the unit, which is the reported slope for hard spheres (Jacob, Poulos et al. 2015).

For HS glasses, the vertical shift factor b reflects the effect of shear on the free volume inside the cage and is directly connected to elasticity. Increasing the shear rate, the short-time in-cage motion of the particles is slowed down. When converted to viscoelastic moduli, using the generalized Stokes-Einstein relation (Mason 2000), the decreased in-cage motion corresponds to stronger elasticity and thus $G_{\perp}^{'}$ is higher. Furthermore, for lower effective volume fractions, a loosely packed cage is able to deform more under shear before breaking due to higher in-cage free volume, which is also reflected to shear dependence of the modulus shift factor (Jacob, Poulos et al. 2015). On the contrary, at higher volume fractions, a tightly packed cage cannot deform much under shear due to smaller in-cage free volume with the modulus shift factor being close to unit (Jacob, Poulos et al. 2015). The behavior of vertical shift factor for hybrid microgels is analogous to HS one, with the difference that even at jammed state, microgels exhibit shear rate dependence

which is probable related to their ability to partially interpenetrate each other and easily deform when they are jammed.

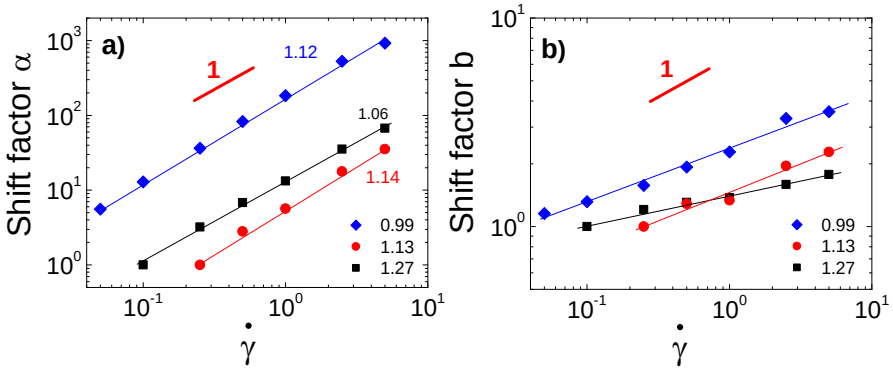

Fig. 7.10 *– a) The horizontal (frequency) shift factor α and b) the vertical (modulus) shift factor b used for SROFS analysis for 0.99, 1.13 and 1.27.*

7.4 Conclusions

Orthogonal Superposition Rheometry (OSR) was employed to study shear-induced microstructural changes of soft hybrid core-shell microgels. The orthogonal superposition moduli, extracted during steady state flow at various shear rates, provide information about the mechanism of flow under shear at three different effective volume fractions well above glass transition. At rest, hybrid microgels exhibit a typical behavior of colloidal glass with G'>G'' in a wide frequency range. Under steady shear flow, in all the probed volume fractions, two crossover frequencies are observed, which move monotonically to higher values increasing the shear rate applied and represent two structural relaxation timescales ($t_c=1/\omega_c$) related to two different length-scales; high frequency crossover is related to the shear-induced out-of-cage displacements, while the low frequency crossover to the formation of larger length scale structures.

Scaling of the viscoelastic spectrum was realized by using shift factors α and b. Both shift factors show a power law dependence on the shear rate. The frequency shift factor, which is directly connected to ω_c, exhibits an almost linear dependence that is similar to the repulsive hard spheres' behaviour despite the soft character of the hybrid core-shell microgels. This can be attributed to the crosslinked shell that exists in the outer part of the particles, which prohibits full chain interpenetration

allowing only a partial one, and its ability to deform. Contrary to HS behaviour, the frequency shift factor for microgels presents volume fraction dependence, which is probably connected to the transition from a jammed state to a glassy one. The modulus shift factor, which is connected to elasticity and expresses the in-cage free volume, shows a shear rate dependence both at glassy and jammed state. This behaviour differs for HS, where at lower volume fractions, shear affects the vertical shift factor, due to increased free volume inside a loosely packed cage. However, at higher volume fractions, a tightly packed cage cannot deform under shear before breaking, rendering the factor b shear independent.

7.5 Appendix

Orthogonal Superposition Rheometry (OSR) was also performed in various temperatures below, close and above the LCST for the effective volume fraction ϕ_{eff}=1.13.

Firstly, we explored the flow behavior under constant steady shear at various temperatures (20, 32 and 38^{o}C). Fig. 7.11 depicts the flow curves (steady state shear stress vesus shear rate) for various temperatures, whereas Table II presents the values of k and n extracted by fitting the experimental data with the Herschel-Bulkley model. The consistency factor k decreases from temperature transition 20 to 32^{o}C, which corresponds to transition from a stronger solid-like behavior to a weaker one in repulsive regime. Then increasing the temperatures above the LCST, where the interparticle interactions are attractive, we observe a strengthen of the response and hence of the consistency factor k. However, the flow index exponent n presents an increase and then a decrease for the same transitions.

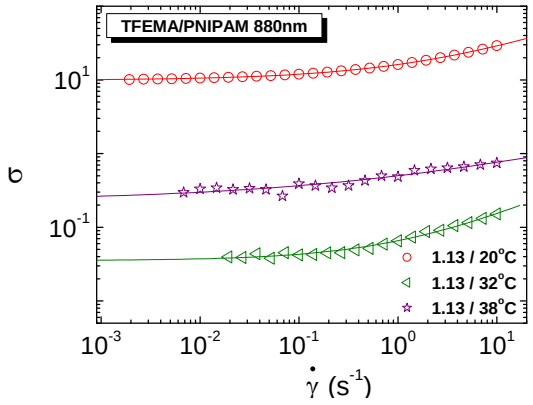

Fig. 7.11 *– Steady state shear stress as a function of rotational shear rate (flow curve) for various temperatures for φ_{eff}=1.13 of TFEMA/PNIPAM 880nm. The solid curves represent the fitting of experimental data with Herschel-Bulkley model.*

T (°C)	***k***	***n***
20	6.3	0.48
32	0.03	0.59
38	0.27	0.29

Table II *- The consistency k and shear thinning exponent n values obtaind by fitting experimental data of fig. 7.11 with Herschel-Bulkley model*.

Afterwards, we performed dynamic frequency sweeps at rest in rotational direction, at a low strain amplitude in linear viscoelastic regime following the same protocol as before; tests were performed once a steady state was reached typically after 200s for the highest to 2000s for the lowest shear rates. The waiting time used each time corresponds to a total strain of γ>1. For T=20°C, DFS test reveals the typical behaviour of colloidal suspensions above glass transition where the storage modulus G' dominates the loss modulus G'' over a wide range of frequencies. The loss modulus G'' exhibits a minimum, which is related to the transition between the in-cage and the out-of-cage relaxation times of the particles (Van Megen and Underwood 1993, Mason and Weitz 1995). Increasing the temperature at T=32°C, which is close to the LCST we observe a much weaker colloidal glass. Increasing further at T=38°C, the attractive interactions contribute to the formation of a percolated network expressed by a stronger solid-like behaviour.

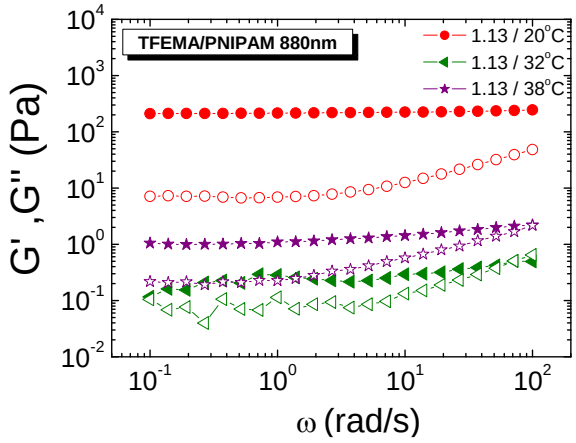

Fig. 7.12 *- Orthogonal and parallel frequency sweeps preformed in the linear viscoelastic regime at various temperatures for φ_{eff}=1.13 of TFEMA/PNIPAM 880nm at quiescent state.*

References:

Amann, C. P., et al. (2015). "Shear-induced breaking of cages in colloidal glasses: Scattering experiments and mode coupling theory." The Journal of Chemical Physics **143**(3): 034505.

Appel, J., et al. (2015). "Temperature Controlled Sequential Gelation in Composite Microgel Suspensions." Particle & Particle Systems Characterization **32**(7): 764-770.

Ballesta, P., et al. (2008). "Slip and flow of hard-sphere colloidal glasses." Physical review letters **101**(25): 258301.

Bécu, L., et al. (2006). "Yielding and flow in adhesive and nonadhesive concentrated emulsions." Physical review letters **96**(13): 138302.

Bender, J. and N. J. Wagner (1996). "Reversible shear thickening in monodisperse and bidisperse colloidal dispersions." Journal of Rheology **40**(5): 899-916.

Besseling, R., et al. (2010). "Shear banding and flow-concentration coupling in colloidal glasses." Physical review letters **105**(26): 268301.

Booij, H. and G. Thoone (1982). "Generalization of Kramers-Kronig transforms and some approximations of relations between viscoelastic quantities." Rheologica Acta **21**(1): 15-24.

Brader, J. M., et al. (2010). "Nonlinear response of dense colloidal suspensions under oscillatory shear: Mode-coupling theory and Fourier transform rheology experiments." Physical Review E **82**(6): 061401.

Brady, J. F. and G. Bossis (1985). "The rheology of concentrated suspensions of spheres in simple shear flow by numerical simulation." Journal of Fluid Mechanics **155**: 105-129.

Cheng, Z., et al. (2001). "Phase diagram of hard spheres." Materials & Design **22**(7): 529-534.

Chikkadi, V., et al. (2011). "Long-range strain correlations in sheared colloidal glasses." Physical review letters **107**(19): 198303.

Cloitre, M., et al. (2003). "Glassy dynamics and flow properties of soft colloidal pastes." Physical review letters **90**(6): 068303.

Colombo, G., et al. (2017). "Superposition Rheology and Anisotropy in Rheological Properties of Sheared Colloidal Gels." Journal of Rheology.

De Silva, J., et al. (2011). "Rheological behaviour of polyoxometalate-doped lyotropic lamellar phases." The European Physical Journal E: Soft Matter and Biological Physics **34**(1): 1-9.

Eberle, A. P. and L. Porcar (2012). "Flow-SANS and Rheo-SANS applied to soft matter." Current Opinion in Colloid & Interface Science **17**(1): 33-43.

El Masri, D., et al. (2009). "Dynamic light scattering measurements in the activated regime of dense colloidal hard spheres." Journal of Statistical Mechanics: Theory and Experiment **2009**(07): P07015.

Erwin, B. M., et al. (2010). "Dynamics and rheology of colloidal star polymers." Soft Matter **6**(12): 2825-2833.

Jacob, A. R., et al. (2015). "Convective cage release in model colloidal glasses." Physical review letters **115**(21): 218301.

Kim, S., et al. (2013). "Superposition rheometry of a wormlike micellar fluid." Rheologica Acta **52**(8-9): 727-740.

Koumakis, N., et al. (2013). "Complex oscillatory yielding of model hard-sphere glasses." Physical review letters **110**(17): 178301.

Koumakis, N., et al. (2012). "Yielding of hard-sphere glasses during start-up shear." Physical review letters **108**(9): 098303.

Koumakis, N., et al. (2016). "Start-up shear of concentrated colloidal hard spheres: Stresses, dynamics, and structure." Journal of Rheology **60**(4): 603-623.

Koumakis, N., et al. (2012). "Direct comparison of the rheology of model hard and soft particle glasses." Soft Matter **8**(15): 4271-4284.

Koumakis, N., et al. (2008). "Effects of shear induced crystallization on the rheology and ageing of hard sphere glasses." Soft Matter **4**(10).

Le Grand, A. and G. Petekidis (2008). "Effects of particle softness on the rheology and yielding of colloidal glasses." Rheologica Acta **47**(5-6): 579-590.

Lettinga, M., et al. (2012). "Nonlinear behavior of nematic platelet dispersions in shear flow." Physical review letters **109**(24): 246001.

Liu, R., et al. (2009). "Thermoresponsive copolymers: from fundamental studies to applications." Colloid and Polymer Science **287**(6): 627-643.

López-Barrón, C. R., et al. (2012). "Dynamics of melting and recrystallization in a polymeric micellar crystal subjected to large amplitude oscillatory shear flow." Physical review letters **108**(25): 258301.

Mason, T. and D. Weitz (1995). "Linear viscoelasticity of colloidal hard sphere suspensions near the glass transition." Physical review letters **75**(14): 2770.

Mason, T. G. (2000). "Estimating the viscoelastic moduli of complex fluids using the generalized Stokes–Einstein equation." Rheologica Acta **39**(4): 371-378.

Mason, T. G. and D. A. Weitz (1995). "Linear Viscoelasticity of Colloidal Hard Sphere Suspensions near the Glass Transition." Physical Review Letters **75**(14): 2770-2773.

Melrose, J. R. and R. C. Ball (2004). "Continuous shear thickening transitions in model concentrated colloids—The role of interparticle forces." Journal of Rheology **48**(5): 937-960.

Mewis, J. and N. J. Wagner (2012). Colloidal suspension rheology, Cambridge University Press.

Miyazaki, K., et al. (2006). "Nonlinear viscoelasticity of metastable complex fluids." EPL (Europhysics Letters) **75**(6): 915.

Mohan, L., et al. (2013). "Local mobility and microstructure in periodically sheared soft particle glasses and their connection to macroscopic rheology." Journal of Rheology **57**(3): 1023-1046.

Pellet, C. and M. Cloitre (2016). "The glass and jamming transitions of soft polyelectrolyte microgel suspensions." Soft Matter **12**(16): 3710-3720.

Petekidis, G., et al. (2002). "Rearrangements in hard-sphere glasses under oscillatory shear strain." Physical Review E **66**(5): 051402.

Petekidis, G., et al. (2004). "Yielding and flow of sheared colloidal glasses." Journal of Physics: Condensed Matter **16**(38): S3955.

Pusey, P. (1991). Liquids, freezing and the glass transition, North-Holland: Amsterdam.

Schall, P., et al. (2007). "Structural rearrangements that govern flow in colloidal glasses." Science **318**(5858): 1895-1899.

Seth, J. R., et al. (2011). "A micromechanical model to predict the flow of soft particle glasses." Nature materials **10**(11): 838.

Siebenbürger, M., et al. (2012). "Creep in colloidal glasses." Physical review letters **108**(25): 255701.

Siebenbürger, M., et al. (2009). "Viscoelasticity and shear flow of concentrated, noncrystallizing colloidal suspensions: Comparison with mode-coupling theory." Journal of Rheology **53**(3): 707-726.

Simmons, J. (1966). "A servo-controlled rheometer for measurement of the dynamic modulus of viscoelastic liquids." Journal of Scientific Instruments **43**(12): 887.

Snijkers, F., et al. (2015). "Perspectives on the viscoelasticity and flow behavior of entangled linear and branched polymers." Journal of Physics: Condensed Matter **27**(47): 473002.

Stuart, H. A. (1955). Die Physik der Hochpolymeren: Bd. Ordnungszustände und Umwandlungserscheinungen in festen hochpolymeren Stoffen, bearb. von W. Brenschede, et al, Springer.

Truzzolillo, D., et al. (2014). "Depletion gels from dense soft colloids: Rheology and thermoreversible melting." Journal of Rheology **58**(5): 1441-1462.

Van Megen, W. and S. Underwood (1993). "Glass transition in colloidal hard spheres: Mode-coupling theory analysis." Physical review letters **70**(18): 2766.

Van Megen, W. and S. Underwood (1994). "Glass transition in colloidal hard spheres: Measurement and mode-coupling-theory analysis of the coherent intermediate scattering function." Physical Review E **49**(5): 4206.

Vermant, J., et al. (1997). "Orthogonal superposition measurements using a rheometer equipped with a force rebalanced transducer." Review of scientific instruments **68**(11): 4090-4096.

Vermant, J., et al. (1998). "Orthogonal versus parallel superposition measurements." Journal of non-newtonian fluid mechanics **79**(2): 173-189.

Vlassopoulos, D. and M. Cloitre (2014). "Tunable rheology of dense soft deformable colloids." Current Opinion in Colloid & Interface Science **19**(6): 561-574.

Wagner, N. J. and J. F. Brady (2009). "Shear thickening in colloidal dispersions." Physics Today **62**(10): 27-32.

Wyss, H. M., et al. (2007). "Strain-rate frequency superposition: a rheological probe of structural relaxation in soft materials." Physical review letters **98**(23): 238303.

Summary and Perspectives

Structure and dynamics of ellipsoidal particles in dilute regime

In chapter 3, FESEM, DLS and DDLS were used for the characterization of the size, shape and the determination of the hydrodynamic properties for both salt-free aqueous solutions of various aspect ratios of PS spheroids and suspensions containing monovalent salt ions. FESEM and LS technique were quite consistent for the extracted size values. The SLS experimental data of the polarized scattered intensity were successfully described by the corresponding theoretical predictions for ellipsoids. To the contrary, the theory of depolarized scattering intensity fails to describe the correspondent data. Moreover, the estimated translational diffusion coefficients exhibit satisfactory agreement with the theory developed by Perrin. However, the predictions for the rotational diffusion coefficient overestimates the diffusion of particles of smaller aspect ratios (ρ=1.8 and 2.3), whereas describes successfully the systems of higher aspect ratios (ρ=3 and 6.9).

SLS technique was also used for the study of the interparticle interactions through the determination of the second virial coefficient A_2 for salt-free solutions, and its variation upon the addition of salt. Finally, we noticed that the long-range electrostatic interactions contribute to the formation of a "pseudo-organized" structure at volume fraction $\varphi=10^{-5}$, which disappear after the addition of monovalent salt ions.

Based on the above findings, one can propose future studies to elucidate open problems. For example, a comparative investigation with PMMA spheroids, for both salt-free and salt dilute solutions, could reveal the influence of the volume fraction on the interparticle interactions. An extension of the study in concentrated regime for PS spheroids, could also inform us about the formation or not of organized structures at higher volume fractions.

Structure and dynamics of soft core-shell particles from dilute to glassy regime

The structure and dynamics of soft core-shell colloids, which consists of PMMA chains of different molecular weight grafted on a silica core, were examined in chapter 4. In dilute regime, we characterized the particle size and the interparticle interactions and we determined the effective volume fraction. In concentrated suspensions, 3D Dynamic Light Scattering technique is used for eliminating the undesirable multiple scattering effects due to refractive index mismatch between particles and solvent and extracting single scattering. The structural properties deviate from hard spheres probably due to form factor changes that do not allow us to measure properly the S(q).

Dynamic properties were also investigated revealing the single exponential behaviour of the electric field correlation function until volume fraction 0.56c/c, where a second and slower mode appears and is related to the out-of-cage diffusion process. Furthermore, the concentration dependence of the estimated structural diffusion coefficient was also explored, exhibiting a minimum around the peak position of the S(q), which was compared with theoretical predictions for hard spheres. The random close packing volume fraction of this soft system was finally determined around* $\Phi_{RCP} \approx 0.95$*, which is much higher than the RCP of hard spheres.*

In the glassy regime, where dynamics are kinetically arrested and aging phenomena take place, we used Multispeckle Dynamic Light Scattering technique (MSDLS). The slowest relaxation time of the intermediate scattering function of glassy suspensions increases with time. For both P2-41k and P2-126k systems, the structural rearrangements led in creation of larger free volume locally via ordering of the particles and a glass-crystal re-entrant transition. However, for 0.68c/c of the system P2-126k, this transition was detected after 6 months from rejuvenation due to high polydispersity, while the crystal growth was inhomogeneous probably due to size segregation. In this direction, we could complete the thorough investigation of the dynamics of this polydisperse systems at 0.68c/c*, through the determination of intermediate scattering function after the crystal growth in the sample.*

Structure, dynamics and mechanical properties of thermoresponsive core-shell microgels

Here (chapter 5), we examined the structure, dynamics and viscoelastic properties of electrostatically stabilized aqueous suspensions of two different core-shell microgel systems, which consist of similar core size and crosslinking density of the shell, but different shell size and therefore different softness.

In the dilute regime, dynamic light scattering was used in order to determine the temperature dependence of hydrodynamic radius, revealing higher shrinking ability for the softer system comparing to the harder one. The interparticle interactions were also quantified by performing static light scattering in various dilute suspensions and calculating the second virial coefficient. For temperatures below the LCST the interactions are repulsive, while they switch to attractive for temperatures above the LCST.

In the concentrated regime, tuning of the interactions by temperature, allows switching between glass, liquid and gel states. For the investigation of structure and dynamics of each physical state we used confocal microscopy and diffusive wave spectroscopy. Moreover, the viscoelastic properties of the different physical states were explored by performing linear and non-linear rheology. These techniques revealed that the larger particles exhibit stronger repulsive and attractive interactions compared to the smaller.

Structure, dynamics and viscoelastic properties of hybrid core-shell microgels with screened interactions

In chapter 6, we studied the structure, dynamics and viscoelastic properties of electrostatically stabilized aqueous suspensions of core-shell microgels of TFEMA/PNIPAM, after the addition of monovalent salt ions of NaCl. Light scattering was used in dilute regime in order to extract the hydrodynamic radius for suspensions of 20mM and 50mM of NaCl and estimate the range of the interparticle interactions. Both salt concentrations are sufficiently high, revealing the characteristic aggregation temperature T_a, above which attractive interactions become sufficiently

large to induce clustering. The existence of equilibrium clusters for temperatures above the LCST is also delineated in capillary viscometry tests, where the viscosity increases extremely fast with volume fraction.

Linear and non-linear rheological measurements were also performed for concentrated suspension of ionic strength only of 20mM of NaCl. Increasing the temperature we gradually tuned the interactions from repulsive to attractive and switched between different states, similarly with chapter 5. Rheo-confocal microscopy at the same concentrated sample were performed to visualize the structure under shear. The observation deeply in the bulk was impossible due to the fact that only the core of the particles is labelled by Nile red dye, whose size is below the objective's resolution. However, from dynamic frequency sweeps performed at T=36^{o}C, we observed that imposing low Pe the moduli increase compared to the quiescent state. At higher Pe, the aggregated structure tends to weaken. Supplementary tests with imaging under shear supported the existence of heterogeneous clusters at T=36^{o}C. Under flow, we also observed shear-dependent assembly of log-rolling colloidal strings parallel to the confining geometry. The homogenization of the suspension failed to take place even by imposing high Pe, but was succeeded by cooling down to the temperature of 20^{o}C.

Orthogonal Superposition Rheometry of soft core-shell microgels

Orthogonal Superposition Rheometry (OSR) was employed, in this chapter, to study shear-induced microstructural changes of three different effective volume fractions well above glass transition of soft core-shell microgels. At rest, hybrid microgels exhibit a typical behavior of colloidal glass with G'>G'' in a wide frequency range. Under steady shear conditions, in all the probed volume fractions, two crossover frequencies appear, which move monotonically to higher values increasing the shear rate applied and represent two structural relaxation timescales related to two different length-scales.

Afterwards, we tried to achieve scaling of the viscoelastic spectrum by using shift factors α and b, with both of them exhibiting a power law dependence on the

shear rate. Moreover, the microgel system, despite its soft character, presents hard sphere-like behaviour that is attributed to the crosslinked shell, which prohibits full chain interpenetration allowing only a partial one and its ability to deform. Except for the shear dependence, the frequency shift factor shows volume fraction dependence as well, which is probably connected to the transition from a jammed state to a glassy one. The modulus shift factor shows a shear rate dependence both at glassy and jammed state.

Following the above work, BD simulations could be a useful tool to understand colloidal glasses under shear since the contribution of hydrodynamic interactions is also taken into consideration. Moreover, creep deformation tests of microgel colloidal glasses could access experimentally low frequency response.

Apart from salt-free suspensions, orthogonal superposition rheometry could be also performed at salty ones. Then experiments in the attractive regime could be also feasible, since the viscoelastic moduli at temperatures above the LCST would be stronger and thus torque issues would not be faced anymore.